APPLIED COMPUTATIONAL ELECTROMAGNETICS SOCIETY JOURNAL

Advances in Analysis, Design and Control of Switched Reluctance Machines

Guest Editors:

Chen Hao, School of Electrical Engineering, China University of Mining and Technology, China
Antonino Musolino, Department of Energy, System, Territory and Construction Engineering, University of Pisa, Italy
Yan Wenju, School of Electrical Engineering, China University of Mining and Technology, China

September 2025
Vol. 40 No. 9
ISSN 1054-4887

The ACES Journal is abstracted in INSPEC, in Engineering Index, DTIC, Science Citation Index Expanded, the Research Alert, and to Current Contents/Engineering, Computing & Technology.

The illustrations on the front cover have been obtained from the ARC research group at the Department of Electrical Engineering, Colorado School of Mines

Published, sold and distributed by: River Publishers, Alsbjergvej 10, 9260 Gistrup, Denmark

SEPTEMBER 2025 REVIEWERS

Atef Elsherbeni
Chen Hao
Lukasz Knypinski
Ningxin Liu
Zhiming Liu
Antonino Musolino
Peixin Niu
Heshmat Noori
Qing Wang
Yan Wenju

THE APPLIED COMPUTATIONAL ELECTROMAGNETICS SOCIETY JOURNAL

Vol. 40 No. 9 September 2025

TABLE OF CONTENTS

Introduction to the Special Issue

Advances in Analysis, Design and Control of Switched Reluctance Machines

Welcome to the special issue of the *Applied Computational Electromagnetics Society (ACES) Journal*. This special issue brings together a collection of state-of-the-art research findings aimed at improving the key performance metrics of reluctance machines—namely, power density, efficiency, and torque ripple

Through these contributions, the issue seeks to showcase advancements that help bridge the performance gap between reluctance machines and IPMSMs.

Guest Editors:

Chen Hao, School of Electrical Engineering, China University of Mining and Technology, China

Antonino Musolino, Department of Energy, System, Territory and Construction Engineering, University of Pisa, Italy

Yan Wenju, School of Electrical Engineering, China University of Mining and Technology, China

Multi-objective Optimization Design of Modular Linear Rotary Switched Reluctance Machine Based on the Taguchi Method

Hao Chen[1,2,3], Cheng Liu[1], Xing Wang[2], Shudong Hou[3], Antonino Musolino[4], and Nurkhat Zhakiyev[5]

[1]School of Electrical Engineering
China University of Mining and Technology, Xuzhou 221116, China
hchen@cumt.edu.cn, Chengliu97@cumt.edu.cn

[2]Shenzhen Research Institute
China University of Mining and Technology, Shenzhen 515100, China
3512@cumt.edu.cn

[3]Nexus Intelligent Equipment (Zhejiang) Co. Ltd.
Zhejiang, China
njdr2007@126.com

[4]Department of Energy, System, Territory and Construction Engineering (DESTEC)
University of Pisa, 56122 Pisa, Italy
antonino.musolino@unipi.it

[5]Department of Science and Innovation
Astana IT University, Astana, Kazakhstan
nzhakiyev@gmail.com

***Abstract* –** In order to combine the advantages of modularity for motor power density enhancement, this paper proposes a three-phase modular linear rotary switched reluctance machine (MLRSRM) with both segmented stator and rotor. In order to increase the torque characteristics of the motor, this paper proposes a multi-objective optimization design of MLRSRM based on the Taguchi method. The static average electromagnetic torque and electromagnetic thrust of the motor are taken as the optimization objectives, and the four ontological parameters (stator pole arc, rotor pole arc, rotor module radial depth and rotor module edge width) that have a greater impact on the MLRSRM optimization objectives are selected. The Taguchi method is used to optimize the motor, determine the optimized structural parameters and verify them by finite element analysis software. The finite element simulation results demonstrate the effectiveness of the described optimization method on the structural design of the MLRSRM. This paper has certain theoretical significance and reference value for the optimal design of MLRSRM.

***Index Terms* –** Finite element analysis, modular linear rotary switched reluctance machine, structural optimization, Taguchi method.

I. INTRODUCTION

In the context of the global energy crisis and the growing importance of energy conservation and emission reduction, the development process of modern industry and technology, many scientific and technological cutting-edge fields of electric drive control and other operations require multiple degrees of freedom of precise movement, the form of movement of the mechanical system is becoming more and more complex [1]. The traditional multi-motor drive system has a large energy loss due to the existence of multiple transmission links. Two-degree-of-freedom motors directly realize two motions in a single motor structure, reducing intermediate transmission components and thus reducing energy loss. Two-degree-of-freedom motors are able to meet the needs of complex motion while reducing energy waste, which is in line with the development trend of efficient energy use [2].

The switched reluctance motor (SRM) has a relatively simple construction with convex pole structures for both the stator and rotor, without complex windings and permanent magnets. In two-degree-of-freedom motor applications, this simple structure is conducive to reducing the size and weight of the motor, increasing the power density, making the motor more compact and

Submitted On: December 1, 2024
Accepted On: July 14, 2025

https://doi.org/10.13052/2025.ACES.J.400901

easier to install and integrate into a variety of equipment, especially suitable for occasions with stringent space requirements. By controlling the on angle, off angle, current amplitude and other parameters of the stator winding current, the torque, speed and steering of the SRM can be flexibly adjusted to achieve a variety of different mechanical characteristics and operation modes. In two-degree-of-freedom motor control, this high degree of control flexibility meets the requirements for precise control of linear and rotary motions in different application scenarios and allows for easy implementation of a variety of complex control strategies [3–5].

SRMs are strongly coupled, multivariable controlled nonlinear systems whose performance metrics are usually conflicting with each other, so when choosing the number of optimization objectives, multiple objectives need to be optimized at the same time to ensure that the best system performance is output. At present, many experts and scholars have introduced various types of optimization algorithms for different optimization objectives into the optimal design of the motor body. A multi-objective optimization strategy (MOS) and shape optimization of 8/6 SRM based on a Gaussian process regression (GPR) model is proposed in [6], and a GPR model based on the finite element method (FEM) is developed to perform multi-objective analysis of the main design parameters of the SRM, which improves output power and efficiency performance of the SRM. A design methodology for a SRM for 80 kW battery electric vehicle (BEV) propulsion applications is presented in [7]. The design methodology first determines motor geometry and then performs a sensitivity analysis of motor performance considering various motor parameters. A multi-objective genetic algorithm is then used to optimize the SRM conduction angle to improve torque density and reduce torque pulsations. Due to the problems of small starting torque and large torque pulsation in conventional 12/14 hybrid stator pole type bearingless switched reluctance motors (BSRMs), a BSRM based on a stepped rotor structure is designed in [8], and simulated annealing particle swarm optimization (SAPSO) algorithm is proposed, which uses the response surface method instead of finite element calculation, and combines the mathematical model with the SAPSO algorithm for the motor's structural parameters are optimized. In order to improve the torque performance and vibration characteristics of a permanent magnet assisted SRM, a multi-objective optimization design method of permanent magnet assisted SRM based on non-dominated sorting genetic algorithm III (NSGA-III) iterative optimization strategy is proposed in [9]. A three-phase SRM with 18 stator poles and 12 rotor poles (18/12) is introduced, which is designed for electric vehicles [10]. Ant Lion Optimization (ALO) is used to optimize the torque ripple of the motor, and the results of the optimization problem are compared with the initial machine. In order to enhance the dynamic performance of SRM, a novel ON/OFF optimization method based on linesearch is introduced to overcome the limitations of the traditional annealing-based ON/OFF optimization in [11]. The proposed method converges to the optimal solution faster than the traditional annealing-based ON/OFF method. An optimization algorithm consisting of genetic algorithm (GA) and finite element analysis (FEA) is used to determine the optimum rotor geometry to maintain the average torque while minimizing torque pulsations and tangential vibrations in the stator in [12].

To address the above research status, this paper proposes a multi-objective optimal design of the torque characteristics of a three-phase two-degree-of-freedom switched reluctance generator based on Taguchi's optimization algorithm. In this paper, the key structural parameters of the motor stator and rotor are selected as design variables, and the orthogonal experimental matrix is established with the static torque and static thrust of the motor as the optimization objectives. The time-step FEM is used to solve the orthogonal experimental matrix, and the results of the experimental matrix are analyzed to obtain the proportion of the influence of each optimization variable on each optimization objective. According to the optimization objectives, the best combination of design variables is selected. Torque characteristics of the motor after parameter optimization are simulated and analyzed using finite element simulation software, and the simulation results prove the effectiveness of the described optimization method.

Section II of this paper describes the structure and geometry of the proposed motor. The multi-objective optimization design process based on Taguchi's algorithm is given in section III, and section IV concludes.

II. PROPOSED MODULAR LINEAR ROTARY SWITCHED RELUCTANCE MACHINE (MLRSRM)

The cross-section and 3D model of the proposed three-phase modular linear rotary SRM are shown in Fig. 1. There are no permanent magnets on the stator and rotor of the machine. The stator and rotor are made of silicon steel sheets laminated with high magnetic permeability, and their operation follows the principle of minimum reluctance, which means that the magnetic flux is always closed along the path of minimum reluctance, and the rotor is pulled to rotate by magnetic gravity. There is a centralized winding on the convex pole of the stator, and the two windings opposite to the axis are connected in series to form a phase winding, which in turn excites the rotor to rotate. Neighboring stator and moving rings

arranged in the axial direction are spaced apart by a certain distance and, due to the difference in the staggered positions of the stator and moving rings, the moving rotor will be subjected to the axial magnetic pull of the stator ring in the axial direction to make a continuous linear motion. The stator-rotor segmented structure reduces the weight of the machine, and it also effectively reduces the wind resistance when the machine is rotating.

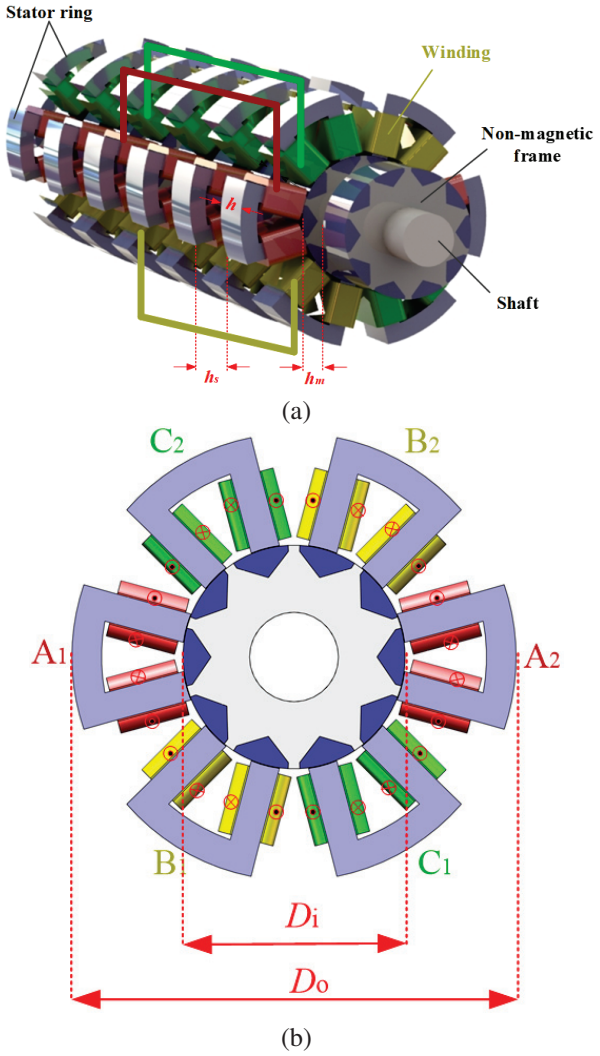

Fig. 1. 3D structure of the proposed MLRSRM: (a) overall view and (b) cross-section view.

The design of the basic dimensions of the structure of the MLRSRM can be referred to the design method of the rotary generator for wind power generation and the linear generator for wave power generation. If the linear unit is not considered, according to the design theory of the rotary motor, the main size expression of the rotating unit is [13]:

$$D_i^2 l = C_1 \frac{P_R}{\cos\varphi_R n}. \tag{1}$$

D_i is the inner diameter of the stator, l is the axial length of the stator, P_R is the power of the rotating part, $\cos\varphi_R$ is the power factor, n is the rotational speed and C_1 is a constant as shown in (2):

$$C_1 = \frac{6.1 \times k_{E1}}{\alpha_R k_{M1} k_{dp1} A_R B_R}. \tag{2}$$

k_{E1} is the calculation coefficient of air gap potential, α_R is the effective pole-arc coefficient, k_{M1} is the waveform coefficient of air gap magnetic field, k_{dp1} is the winding coefficient, A_R is the line load, B_R is the maximum value of air gap flux density.

If the rotary unit is not considered, the main dimensional formula of the linear unit can be derived from the main dimensional formula of the rotary unit. This is shown in (3):

$$\frac{(D_i + D_o) h_s l}{h_m} = C_2 \frac{P_L}{\cos\varphi_L v}. \tag{3}$$

D_o is the outer diameter of the stator, $\lambda = D_i/D_o$, according to the design experience, λ usually takes the value of 0.4∼0.7, the value of λ in this paper is taken as 0.5. h_s is the thickness of the stator spacer ring, and h_m is the thickness of the movable spacer ring. In order to ensure continuous power generation during linear motion, the value of h_s/h_m is designed to be 0.75 in this paper, P_L is the linear part of the power, $\cos\varphi_L$ is the power factor, v is the speed, and C_2 is a constant, as shown in (4):

$$C_2 = \frac{6.1 \times \pi k_{E2}}{60 \times \alpha_L k_{M2} k_{dp2} A_L B_L}. \tag{4}$$

k_{E2} is the calculation coefficient of air gap potential, α_L is the effective pole-arc coefficient, k_{M2} is the waveform coefficient of air gap magnetic field, k_{dp2} is the winding coefficient, A_L is the line load, B_L is the maximum value of air gap flux density.

Based on the theoretical calculation results of some key dimensions above, combined with some design experiences of switched reluctance rotary motors and switched reluctance linear motors, the key dimensional parameters of the proposed MLRSRM in this paper can be obtained. The key structural parameters of the MLRSRM are shown in Table 1.

Table 1: Key structural parameters of MLRSRM

Item	Value
Stator inner diameter D_i	150.8 mm
Stator outer diameter Do	300 mm
Stator ferromagnetic ring thickness h	90 mm
Stator spacer ring thickness h_s	150 mm
Mover ferromagnetic ring thickness h	90 mm
Mover spacer ring thickness h_m	90 mm
Air gap thickness g	0.4 mm
Stator/rotor pole arc	30°/28°

III. MULTI-OBJECTIVE OPTIMIZATION DESIGN BASED ON THE TAGUCHI METHOD

The Taguchi method was firstly proposed and applied in the field of quality management by Japanese scholars. Due to the scientific, systematic and efficient nature of the algorithm, it has gradually been expanded and deepened and applied to scientific research and industrial applications such as robust design, tolerance design and parameter optimization design [15–19]. It has been studied and applied in researching the design and optimization of motor parameters [20–24].

The core technique of the Taguchi method is to first use orthogonal tables for experimental design and then analyze the experimental results to obtain the optimal combination of structural parameters through the signal-to-noise ratio, mean, variance and other indicators. Ultimately, the purpose of obtaining the optimal motor size scientifically and reliably through a small number of experiments is achieved. In this paper, the flowchart of MLRSRM multi-objective and multi-parameter optimization using the Taguchi method is shown in Fig. 2.

A. Determine the optimization objective and the range of design variables

For the linear rotary SRM designed in this paper, whether it is used as electric or power generation, it is required that the motor torque/power density should be as high as possible, outputting higher electromagnetic torque in rotary motion and higher electromagnetic thrust in linear motion. Considering that the operation principles of the two motions are the same, this paper takes rotary motion as an example to establish a mathematical model of the electromagnetic and mechanical relationships in SRMs. The electromagnetic torque of the motor can be obtained by using its magnetic co-energy for the partial derivation of the motor at any running point x, and the equation is as follows [14]:

$$T_x(i,\theta) = \left.\frac{\partial W'_m(i,\theta)}{\partial \theta}\right|_{i=const}. \tag{5}$$

T_x is the instantaneous electromagnetic torque of the motor, θ is the relative position of the motorized motor, i is the winding current and W'_m is the winding magnetic co-energy. The winding magnetic co-energy is the result of integrating the winding magnetic chain over the current:

$$W'_m(i,\theta) = \int_0^i \psi(i,\theta)di. \tag{6}$$

ψ is the motor winding magnetic chain.

Equation (6) is integrated and averaged over one operating cycle. Based on the assumption of symmetry of the windings of each phase, the average SRM output torque is obtained as:

$$T = \frac{mN_r}{2\pi}\int_0^{2\pi/N_r} T_x(\theta, i(\theta))\mathrm{d}\theta. \tag{7}$$

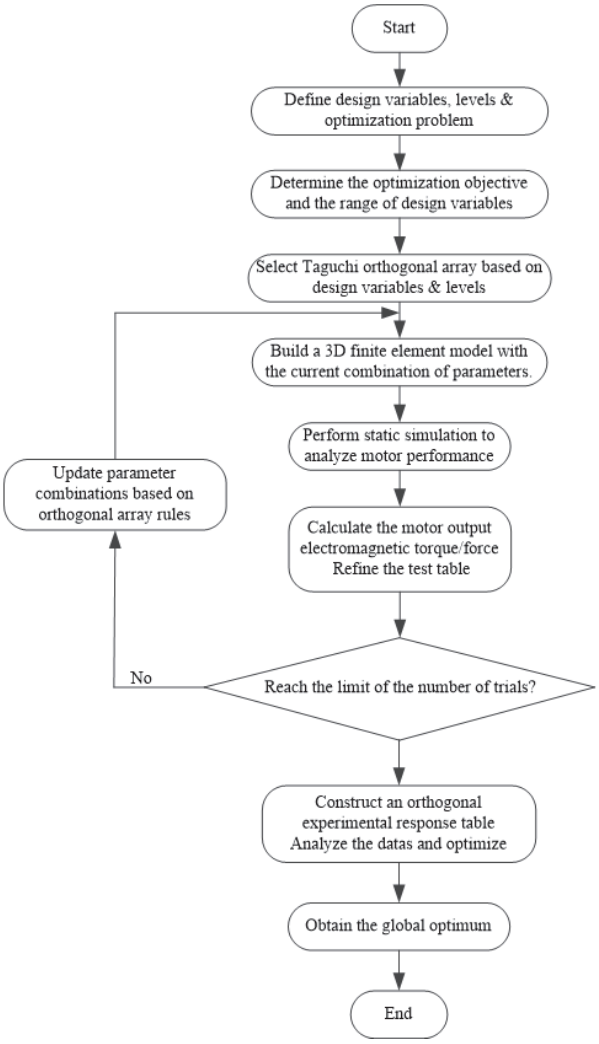

Fig. 2. Flow chart of parameter optimization design based on the Taguchi method.

m is the number of phases of the SRM, N_r is the number of rotor poles.

After the initial dimensioning in Table 1, geometrical optimization of the structural parameters of the proposed motor is required in order to have a higher output torque. Therefore, a sensitivity analysis is carried out in this section to obtain the optimum parameters of the proposed MLRSRM. These parameters help to produce maximum electromagnetic torque/thrust. Based on the design experience and the structural characteristics of the MLRSRM, the sensitivity analysis is carried out for the four structural parameters, namely, stator pole arc α, rotor pole arc β, rotor module radial depth h_1, and rotor module edge width h_2, in turn, as shown in Fig. 3.

In this paper, a multi-objective optimization of the torque performance of the MLRSRM is carried out, which requires that the output/electromagnetic torque of

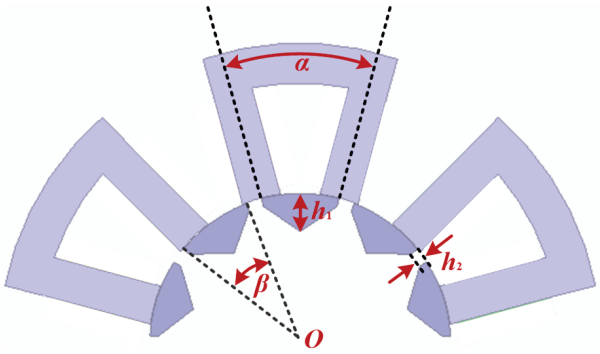

Fig. 3. Stator-rotor construction parameters of MLRSRM.

the motor is as high as possible in both rotary and linear motions. The optimization objectives are chosen as the following two torque indicators: average electromagnetic torque T_{avg} and average electromagnetic thrust F_{avg}. The stator pole arc α, rotor pole arc β, rotor module radial depth h_1 and rotor module edge width h_2 in the previous section are taken as the design variables, and an orthogonal test matrix is established by selecting the appropriate test level values in the annex of the original parameters of the motor. The design variables and their level values are shown in Table 2.

Based on the static torque of the motor at different angles obtained by the FEM, the static average torque of the motor can be obtained by (8):

$$T_{avg} = \frac{1}{n}\sum_{i=1}^{n} T_i. \tag{8}$$

T_i is the static torque value of the motor at a specific angle and n is the number of sampling points in the finite element calculation. Calculation of the static average thrust is obtained in the same way.

Table 2: Different level values for each design variable

Design Variable	Level 1	Level 2	Level 3	Level 4
α °	26	27	28	29
β °	27	28	29	30
h_1 mm	14	16	18	20
h_2 mm	1	3	5	7

B. Orthogonal test design

Based on the four design variables (each with four levels) selected in Table 2, an $L_{16}(4^4)$ orthogonal array was constructed following Taguchi's experimental design methodology. Compared with the full factorial design, this approach requires only 16 experimental trials to comprehensively evaluate parameter effects, enabling simultaneous optimization of both torque and thrust objectives while dramatically reducing computational load.

Using the time-step FEM, the MLRSRM with 16 different parameter combinations is modeled separately as a three-dimensional finite element in the electromagnetic field finite element simulation software. Based on the winding excitation of the motor, the motor boundary conditions are set and the model is reasonably dissected. Static simulation under rated operating conditions is performed for each finite element model. The average torque and average thrust corresponding to different parameter combinations of the MLRSRM are obtained. The 4-factor and 4-level Taguchi orthogonal test table and test results are shown in Table 3.

Table 3: Taguchi orthogonal test table and MLRSRM test results

Test Number	Test Matrix				Test Result	
	α°	β°	h_1 mm	h_2 mm	T_{avg} Nm	F_{avg} Nm
1	26	27	14	1	41.3	134.0
2	26	28	16	3	42.1	141.5
3	26	29	18	5	42.3	149.5
4	26	30	20	7	41.1	153.8
5	27	27	16	5	41.7	140.5
6	27	28	14	7	40.3	146.7
7	27	29	20	1	44.7	141.0
8	27	30	18	3	43.2	149.7
9	28	27	18	7	41.6	141.0
10	28	28	20	5	43.4	147.2
11	28	29	14	3	41.8	147.5
12	28	30	16	1	43.1	141.0
13	29	27	20	3	43.0	138.0
14	29	28	18	1	43.1	137.1
15	29	29	16	7	40.2	148.6
16	29	30	14	5	39.5	151.5

In order to analyze the influence of the parameter changes of the motor design variables on the optimization objectives and the proportion, a statistical analysis of the experimental data is carried out, according to the orthogonal test table established above and the FEA results in Table 3, to obtain the proportion of the influence of all design variables on each optimization objective. Analysis of mean and variance are carried out first.

The average value of the finite element simulation results of each optimization objective can be calculated by equation (8), and the results are shown in Table 4:

$$m = \frac{1}{n}\sum_{i=1}^{n} S_i. \tag{9}$$

m is the average value of the experiment, n is the number of experiments and S_i is the optimization objective value for the i^{th} time.

Table 4: Mean value of the optimization objective

	T_{avg} Nm	F_{avg} Nm
m	42.0	144.3

The average value of the simulation results for each optimization objective under different optimization factors taking different level values can be calculated, taking the average electromagnetic torque T_{avg} of α under level 1 as an example, and the equation obtained is:

$$m_{\alpha 1}(T_{avg}) = \frac{1}{4}\left(T_{avg}(1) + T_{avg}(2) + T_{avg}(3) + T_{avg}(4)\right). \tag{10}$$

In addition, in order to facilitate the analysis, a multi-objective optimization function is introduced to measure the importance of each variable, and the weight factor is used to evaluate the comprehensive consideration of each factor on the optimization objective. The multi-objective function equation is:

$$F_{\text{obj}} = \omega_1 \frac{T_{\text{avg}}}{\max(T_{\text{avg}})} + \omega_2 \frac{F_{\text{avg}}}{\max(F_{\text{avg}})}. \tag{11}$$

ω_1 and ω_2 are the weight factors of average torque and average thrust, respectively. In this paper, the values of ω_1 and ω_2 are both 0.5.

Referring to the above calculations, the average values of the average electromagnetic torque T_{avg} and the average electromagnetic thrust F_{avg} can be obtained for each design variable taken at different levels. The results are shown in Table 5.

Table 5: Optimization value of structural parameters

Design Variable	Level	T_{avg} Nm	F_{avg} Nm	F_{obj}
α°	1	41.7	144.7	0.969
	2	42.5	144.5.	0.978
	3	42.5	144.2	0.977
	4	41.4	143.8	0.963
β°	1	41.9	138.4	0.951
	2	42.2	143.1	0.970
	3	42.2	146.7	0.982
	4	41.7	149.0	0.984
h_1 mm	1	40.7	144.9	0.958
	2	41.8	142.9	0.964
	3	42.6	144.3	0.978
	4	43.0	145.0	0.985
h_2 mm	1	43.1	138.3	0.964
	2	42.5	144.2	0.977
	3	41.7	147.2	0.978
	4	40.8	147.6	0.969

According to the average value of each optimization objective in Table 4 and the average value of each design variable under different levels of motor performance index in Table 5, the variance (SS) of the optimized design variable under each motor performance index and its weight of influence on the performance of each motor can be calculated by (12):

$$SS = \frac{1}{n}\sum_{i=1}^{n}(m_X(S_i) - m(S))^2. \tag{12}$$

X is design variable, S is the optimization objective, $m_X(S_i)$ is the average value of an optimization objective at level i, and $m(S)$ is the average value of the optimization objective. The obtained calculation results are shown in Table 6.

Table 6: Effect of each design variable on the performance index of different motors

Design Variable	T_{avg} Nm		F_{avg} Nm	
	SS	Percentage	SS	Percentage
α°	0.22	12.33%	0.1	0.33%
β°	0.05	2.67%	16.0	52.29%
h_1 mm	0.79	44.57%	0.7	2.29%
h_2 mm	0.72	40.43%	13.8	45.10%
Total	1.78	100%	30.6	100%

From Table 6, it can be seen that the rotor module radial depth h_1 and rotor module edge width h_2 have a greater effect on the average electromagnetic torque T_{avg}. The rotor pole arc β and rotor module edge width h_2 have a greater effect on the average electromagnetic thrust F_{avg}. Therefore, level 4 is best selected for h_1 and β. Since the effect of stator pole arc α on the average electromagnetic thrust F_{avg} is very small, α is best selected at level 2. For the rotor module edge width h_2, considering the large T_{avg} and F_{avg} at the same time, either level 2 or 3 is suitable. In order to verify the above analysis, the experimental results of the simulation combination are quantified by the objective function F_{obj}. The size of the value directly reflects the influence of the corresponding parameter level on the objective function. Larger values indicate stronger parameter sensitivity. Combined with the results of F_{obj} calculation in Table 5, the optimal parameter level value combination for multi-objective optimization is finally determined to be $\alpha(2)$ $\beta(4)$ h_1 (4) h_2 (3), at which time the objective function results in the maximum with the optimal design effect. The calculation results of the objective function F_{obj} are consistent with the above analysis.

C. Comparison of finite element simulation

The parameter values and performance indexes before and after optimization are shown in Table 7, and finite element simulation is performed on the data in Table 7. The simulation results are shown in Fig. 4. Figure 4 shows the waveforms of static electromagnetic torque and static electromagnetic thrust before and

after optimization. It can be seen that after the multi-objective optimization based on the Taguchi method, the electromagnetic torque and electromagnetic thrust of the MLRSRM increase significantly, compared with the average electromagnetic torque of 40.2 Nm and the average electromagnetic thrust of 140.2 Nm before optimization, the average electromagnetic torque and the average electromagnetic thrust of the optimized MLRSRM are 43.5 Nm and 148.6 Nm, which are increased by 8.2% and 6.0%, respectively.

Table 7: Comparison of results before and after optimization

	α °	β °	h_1 mm	h_2 mm	T_{avg} Nm	F_{avg} Nm
Before Optimization	30	28	22	3	40.2	140.2
After Optimization	27	30	20	4	43.5	148.6

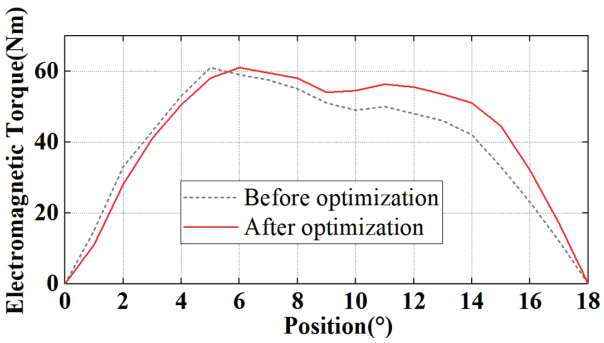

(a)

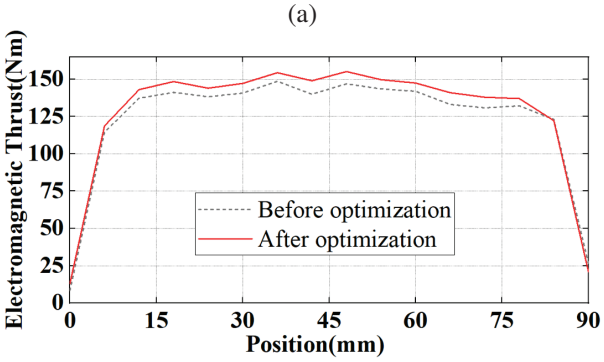

(b)

Fig. 4. Comparison of static torque and static thrust before and after optimization: (a) rotary motion and (b) linear motion.

A three-dimensional static model of the motor was constructed in FEA software, and the simulation accuracy was improved by manual mesh refinement. Taking a stator ferromagnetic ring cell as an example, the mesh profile is shown in Fig. 5. Compared with the inner region of the stator-rotor core, the surface of the core close to the air gap is used with a more precise mesh dissection. Specifically, the optimization process implemented by the proposed method consumes less than one day, which is far shorter than the tens of days required by the approach that combines intelligent algorithms with FEA methods. All these iterative operations are carried out on a workstation equipped with Intel Core i7-13650HX and 32-GB memory.

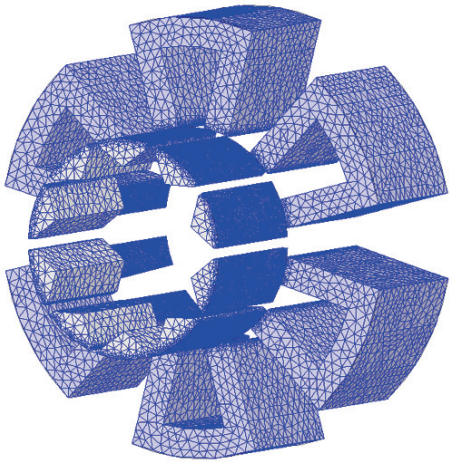

Fig. 5. Mesh division diagram of the MLRSRM.

IV. CONCLUSION

In this paper, a three-phase two-degree-of-freedom modular switched reluctance machine (MLRSRM) with a simple structure is presented. A multi-objective optimization design of torque performance based on the Taguchi method is proposed for the structural characteristics and torque characteristics of the proposed MLRSRM. The motor optimization objectives are determined as the static average electromagnetic torque in rotary motion and the static average electromagnetic thrust in linear motion. The key dimensions of the rotor structure selected reasonably are the optimization parameters. The Taguchi experimental method is used to optimize the parameters and obtain the optimized rotor structure parameter combinations and finite element analysis of the motor after optimization. Compared with before optimization, the electromagnetic torque and electromagnetic thrust of the optimized motor are increased by 8.2% and 6.0%, respectively. The effectiveness of Taguchi method in multi-objective optimization of linear rotary SRMs is verified. Future improvements include combining intelligent algorithms, such as genetic algorithms, to improve multi-objective trade-off accuracy and extending experimental validation to actual prototype testing to supplement the reliability of simulation data.

ACKNOWLEDGMENT

This work is supported by the National Natural Science Foundation of China International (regional) cooperation and exchange projects NSFC-RSF under Grant W2412064, the Shenzhen Collaborative Innovation Special Plan International Cooperation Research Project under Grant GJHZ20240218114300002 and the 2023 China-CEEC University Joint Education Program (2023304).

REFERENCES

[1] H. Chen, R. Nie, and X. Li, "A transverse-flux single-phase tubular switched reluctance linear machine with 4 poles," *IEEE Transactions on Applied Superconductivity*, vol. 31, no. 8, pp. 1-4, Nov. 2021.

[2] G. Zhang, R. Nie, J. Si, C. Gan, and Y. Hu, "Optimal design of a novel double-stator linear-rotary flux-switching permanent-magnet generator for offshore wind-wave energy conversion," in *2021 IEEE Energy Conversion Congress and Exposition*, Vancouver, BC, Canada, pp. 4300-4305, 2021.

[3] R. Nie, J. Si, P. Wang, Z. Li, J. Liang, and C. Gan, "Optimization design of a novel permanent magnet linear-rotary generator for offshore wind-wave combined energy conversion based on multi-attribute decision making," *IEEE Transactions on Energy Conversion*, pp. 1-17, Feb. 2024.

[4] W. Ding, H. Fu, and Y. Hu, "Characteristics assessment and comparative study of a segmented-stator permanent-magnet hybrid-excitation SRM drive with high-torque capability," *IEEE Transactions on Power Electronics*, vol. 33, no. 1, pp. 482-500, Jan. 2018.

[5] R. Nie, J. Si, Y. Jia, P. Wang, S. Xu, J. Liang, and C. Gan, "Comprehensive comparison of mover-PM and stator-PM linear-rotary generators for wind-wave combined energy conversion system," *IEEE Transactions on Industry Applications*, pp. 1-14, May 2024.

[6] J. Zhang, J. Liu, and L. Gei, "Multi-objective optimization of switched reluctance motor based on Gaussian process regression model," in *2024 IEEE 10th International Power Electronics and Motion Control Conference*, Chengdu, China, pp. 4020-4025, 2024.

[7] O. Zayed, M. Omar, M. Bakr, M. Narimani, A. Emadi, and B. Bilgin, "Switched reluctance motor design for an EV propulsion application," in *IECON 2021 – 47th Annual Conference of the IEEE Industrial Electronics Society*, Toronto, ON, Canada, pp. 1-6, 2021.

[8] Z. Xu, Q. Yu, H. Wang, Y. Zhang, and T. Yi, "Optimal design of hybrid stator pole type bearingless switched reluctance motor with simulated annealing particle swarm optimization algorithm," in *2022 IEEE 5th International Electrical and Energy Conference*, Nanjing, China, pp. 3422-3427, 2022.

[9] Y. Geng, C. Huang, H. Yuan, and Y. Wu, "Optimization of a permanent magnet-assisted switching reluctance motor based on the iterative optimization strategy of NSGA-III," in *2023 IEEE 6th International Electrical and Energy Conference*, Hefei, China, pp. 3733-3738, 2023.

[10] T. Sharifi, V. M. Khales, and M. Mirsalim, "Torque ripple minimization for a switch reluctance motor using the Ant Lion Optimization algorithm," in *2022 13th Power Electronics, Drive Systems, and Technologies Conference*, Tehran, Islamic Republic of Iran, pp. 207-211, 2022.

[11] M. Abdalmagid, M. H. Bakr, and A. Emadi, "A linesearch-based algorithm for topology and generative optimization of switched reluctance machines," *IEEE Transactions on Transportation Electrification*, vol. 9, no. 3, pp. 3849-3866, Sep. 2023.

[12] S. E. M. Mohammadi, P. Chen, M. Moallem, B. Fahimi, and M. Kiani, "An alternate rotor geometry for switched reluctance machine with reduced torque ripple," *IEEE Transactions on Energy Conversion*, vol. 38, no. 2, pp. 939-947, June 2023.

[13] M. Pourkarimi, U. Demır, and M. C. Akuner, "Neural network approach for E-motor development," in *2022 8th International Conference on Control, Decision and Information Technologies*, Istanbul, Turkey, pp. 1091-1095, 2022.

[14] W. Yan, W. Wang, H. Li, H. Chen, F. Yu, D. Zhao, and H. Yang, "Performance analysis of a novel axial radial flux segmental rotor switched reluctance motor," *IEEE Transactions on Transportation Electrification*, vol. 10, no. 1, pp. 1031-1042, Mar. 2024.

[15] S.-I. Kim, J.-Y. Lee, Y.-K. Kim, J.-P. Hong, Y. Hur, and Y.-H. Jung, "Optimization for reduction of torque ripple in interior permanent magnet motor by using the Taguchi method," *IEEE Transactions on Magnetics*, vol. 41, no. 5, pp. 1796-1799, May 2005.

[16] X. Jia and G. Lu, "An improved random Taguchi's method based on swarm intelligence and dynamic reduced rate for electromagnetic optimization," *IEEE Antennas and Wireless Propagation Letters*, vol. 18, no. 9, pp. 1878-1881, Sep. 2019.

[17] X. Dong, Z. Q. Zhu, D. Liang, L. Mao, X. Qiu, S. Li, and L. Zheng, "Taguchi-based preprocess strategy for fast evaluating worst case cogging torque due to PM tolerance interactions," *IEEE Transactions on Transportation Electrification*, vol. 11, no. 1, pp. 4097-4110, Feb. 2025.

[18] J. Yang, J. Chen, Z. Cai, W. Yan, W. Liu, J. Zhang, J. Qiao, G. Yang, and C. Zhang, "Design and optimization of a novel permanent magnet linear motor with the same number of poles and slots," *IEEE Transactions on Industry Applications*, vol. 61, no. 1, pp. 16-24, Jan.-Feb. 2025.

[19] J. Chen, K. Liu, Z.-Q. Zhu, H. Cai, S. Zhou, D. Wei, Y. Chen, and D. Zhang, "Torque improvement of interior permanent magnet synchronous machine by axial-assisted magnets," *IEEE Transactions on Transportation Electrification*, vol. 11, no. 1, pp. 3480-3490, Feb. 2025.

[20] S. Jiang, J. Wang, B. Zhou, Y. Zhao, M. Gao, S. Miao, L. Xu, and X. Xu, "Design and electromagnetic–thermal analysis of doubly salient electromagnetic machine for more electric engine based on excitation compensation," *IEEE Transactions on Transportation Electrification*, vol. 11, no. 1, pp. 3311-3322, Feb. 2025.

[21] Y. Wang, M. Zhao, Y. Huang, X. Jia, and M. Lu, "Torque performance optimization of a novel hybrid PMSM with eccentric Halbach based on improved Taguchi method," *IEEE Transactions on Instrumentation and Measurement*, vol. 73, pp. 1-12, 2024.

[22] M. T. B. Tarek, A. W. Bandarkar, and Y. Sozer, "Design, optimization, and development of an axial flux interior permanent magnet motor with a novel flux barrier," *IEEE Transactions on Industry Applications*, vol. 60, no. 4, pp. 6103-6112, July-Aug. 2024.

[23] F. Siddique, S. Shastri, and B. Singh, "Computational investigation of modeling coupled optimization techniques for MCSRM driving EV," *IEEE Transactions on Energy Conversion*, vol. 39, no. 3, pp. 1793-1803, Sep. 2024.

[24] F. Liu, X. Wang, and H. Wei, "Electromagnetic performance analysis, prediction, and multiobjective optimization for U-type IPMSM," *IEEE Transactions on Industrial Electronics*, vol. 71, no. 9, pp. 10322-10334, Sep. 2024.

Hao Chen (SM'08) received the B.S. and Ph.D. degrees from the Department of Automatic Control, Nanjing University of Aeronautics and Astronautics, Nanjing, China, in 1991 and 1996, respectively. In 1998, he became an Associate Professor with the School of Information and Electrical Engineering, China University of Mining and Technology, Xuzhou, where he has been a Professor since 2001. From 2002 to 2003, he was a Visiting Professor at Kyungsung University, Busan, Korea. Since 2008, he is an Adjunct Professor at the University of Western Australia, Perth, Australia. He is the author of one book and has authored more than 190 papers. He is the holder of 14 US Patents, 23 Australian Patents, one Danish Patent, seven Canadian Patents, three South African Patents, 10 Russian Patents, 44 Chinese Invention Patents and six Chinese Utility Model Patents. His current research interests include motor control, linear launcher, electric vehicles, electric traction, servo drives and wind power generator control.

Chen was the recipient of both the Prize of Science and Technology of Chinese Youth and the Prize of the Fok Ying Tong Education Foundation for Youth Teachers in both 2004. He was awarded the first prize in the Science and Technology advanced of Province and Ministry once, the second prize in the Science and Technology advanced of Province and Ministry seven times, and the third prize in the Science and Technology advanced of Province and Ministry 14 times. He became the Chinese New Century Hundred-Thousand Ten-Thousand Talents Engineering National Talent in 2007 and won the Government Especial Allowance of People's Republic of China State Department in 2006.

Cheng Liu received the B.S. degree in electrical engineering and automation from Hubei University of Technology, Wuhan, Hubei, China, in 2020, and the M.S. degree in electrical engineering from Hubei University of Technology, Wuhan, Hubei, in 2023. He is currently pursuing a Ph.D. degree in electrical engineering at China University of Mining and Technology, Xuzhou. His research interests include switched reluctance motor design control, ocean wave power generation, and electric vehicles.

Xing Wang received the B.S. degree from China University of Mining and Technology, Xuzhou Jiangsu, China, in 1996, and M.S. degree from China University of Mining and Technology, Xuzhou Jiangsu, in 1999. In 2007, she became an Associate Professor with China University of Mining and Technology, Xuzhou. She is a holder of four US Patents, nine Australian Patents, two Canadian Patents, four Russian Patents, 12 Chinese Invention Patents, three Chinese Utility Model Patents, and has authored 15 papers.

Shudong Hou founded Nanjing Enchuan New Energy Power System Co. Ltd. In September 2022, he won third prize in the high-level talent entrepreneurship competition in Zaozhuang, Shandong. In 2024, he founded Nexus Intelligent Equipment (Zhejiang) Co. Ltd. and serves as its chairman. He has presided over the research, development, production and sales of motor and controller systems for many years.

Antonino Musolino received his Ph.D. degree in electrical engineering from the University of Pisa, Pisa, Italy, in 1994. He is currently a Full Professor of electrical machines at the University of Pisa. He has co-authored more than 130 papers published in international journals/conferences. He holds three international patents in the field of magnetorheological devices. His current research activities are focused on linear electromagnetic devices, motor drives for electric traction, and the development of analytical and numerical methods in electromagnetics. Musolino was involved in the organization of several international conferences, where he has served as the session chairman and an organizer, and as a member of the editorial board.

Nurkhat Zhakiyev received the bachelor's degree in physics and computer science in 2005, the master's degree in applied mathematics from M. Utemisov West Kazakhstan State University, Kazakhstan, in 2007, and the Ph.D. degree in physics from L. N. Gumilyov Eurasian National University (ENU), in 2015. He is currently working at Astana IT University. His research interests include energy system modeling, smart grid and networks, smart city and optimization modeling.

Multi-objective Optimization Design of a DSSRM with U-type Modular Segmental-stator Structure

Xing Wang[1,2,3], Hao Chen[1,2,3,4,5], Fengyuan Yu[4], Wenju Yan[4], Jianfei Pan[6], and Yassen Gorbounov[7]

[1]International Joint Research Center of Central and Eastern European Countries
on New Energy Electric Vehicle Technology and Equipment
Xuzhou 221008, China
3512@cumt.edu.cn, hchen@cumt.edu.cn

[2]International Cooperation Joint Laboratory of New Energy Power Generation
and Electric Vehicles of Jiangsu Province Colleges and Universities
Xuzhou 221008, China

[3]Jiangsu Province Foreign Expert Workshop
on New Energy Power Generation and Electric Transportation
Xuzhou 221008, China

[4]School of Electrical Engineering
China University of Mining and Technology, Xuzhou 221116, China
cumt_yfy@163.com, yanwenju09@126.com

[5]Shenzhen Research Institute
China University of Mining and Technology, Shenzhen 518057, China

[6]School of Electromechanical and Control Engineering
Shenzhen University, Shenzhen 518054, China
pjf@szu.edu.cn

[7]Department of Informatics
New Bulgarian University, Sofia 1618, Bulgaria
y.gorbounov@mgu.bg

Abstract **–** A U-type modular double stator switched reluctance motor (DSSRM) which has the merit of high-power density is optimized in this paper. Taking average torque, torque smoothing coefficient and efficiency as objectives, sensitivity analysis on DSSRM is investigated and discussed to select significant geometric variables. On the basis of the initial structural parameters, the multi-objective optimization design is processed by adopting a fuzzy iteration optimization algorithm with weight determination. After the determination of decision result of each structure parameter, the best dimension scheme of the DSSRM is concluded. Moreover, the final scheme proves to perform better than the initial scheme by finite element (FE) analysis. Finally, a prototype motor is manufactured and the experimental results validate the improvement of the DSSRM performance.

Index Terms **–** Double stator structure, multi-objective optimization, switched reluctance motor, U-type modular structure.

I. INTRODUCTION

The switched reluctance motor (SRM) and its control system, after decades of development, is firmly established. Its inherent merits such as simple, sturdy, durable structure and high reliability contributes to its excellent running performance and high performance/cost ratio.

However, several problems like electromagnetic torque characteristic and large torque ripple still prevent the SRM from becoming a mainstream motor. Thus, many newly designed SRMs are proposed to enhance torque performance and efficiency or to reduce

Submitted On: December 19, 2024
Accepted On: May 29, 2025

https://doi.org/10.13052/2025.ACES.J.400902

torque ripple, such as double stator switched reluctance motor (DSSRM) [1–6], segmented-rotor SRM [7] and segmented-stator SRM [8–9]. Researchers from the University of Texas at Arlington in the USA presented a concentric DSSRM structure and analyzed its principle and electromagnetic force [1]. The DSSRM structure has a higher torque density because of its larger available winding area than a conventional SRM.

The comprehensive performance of a DSSRM, including design methods [2], mechanical vibration characteristic [3], thermal modeling [4] and rotor shape investigation [5] have been explored and discussed. A 100 kw DSSRM prototype was manufactured to verify that it has the same performance as the permanent magnet motor and, furthermore, has advantages in cost performance [6]. In addition, some scholars have studied the segmental SRM structure [7–9]. The core mass and magnetic flux leakage of a segmental structure are reduced without the connection of a yoke part, thereby improving the efficiency and torque density of the motor. Researchers found that the combination of these structures can further improve the performance of an SRM.

A novel segmented-rotor modular 12/14 DSSRM is presented in [10]. Torque output capability is improved and torque ripple is reduced compared to a conventional 12/8 nonsegmented-rotor DSSRM. Researchers from China University of Mining and Technology presented a novel SRM topology combining U-type modular stator and double stator structure. The decoupling characteristics of the inner and outer motors were verified and the winding configuration scheme was analyzed and discussed in [11].

Besides devising novel structures, conducting optimization design can also improve the performance of the motor [12–22]. In [12], a comprehensive framework for multi-objective design optimization of SRM was proposed to synchronously achieve five key objectives for low-speed electric vehicles application. Paolo Di Barba from University of Pavia in Italy has done a lot of research on benchmark TEAM multi-objective Pareto optimization [13–14]. The particular shape of the Pareto front was established and the design space was thoroughly searched on the basis of considering field uniformity and sensitivity [13]. The TEAM benchmark of magnetic devices under AC conditions was studied and the model for evaluating the quality of the magnetic field produced by distributed windings was proposed and verified [14].

To shorten computational time in multi-objective optimization problems, researchers from McGill University in Canada stated that applying sensitivity analysis is a useful tool to reduce the number of variables, while conflict analysis can reduce the number of objectives [15]. Both sensitivity analysis and conflict analysis were incorporated into the proposed strategy to optimize a fractional slot concentrated winding machine in [16]. In [17], employing finite element (FE) sensitivity analysis, seven initial design variables were reduced to four important variables in the optimization process of a double-sided linear permanent magnet motor. Moreover, sensitivity analysis was also employed to eliminate relatively insignificant geometric variables of SRM optimization problem [18–21]. Amoros and Andrada [18] presented a sensitivity analysis method of the influence to structural parameters on the average electromagnetic force of a double-sided linear SRM. The comprehensive sensitivity analysis was verified to be an effective method for optimizing the linear SRM. In [19], the average torque, average torque per copper loss, and average torque per lamination volume were selected to be optimized objectives, while the stator and rotor pole angles are chosen as the optimization variables, thus a four-phase outer-rotor SRM for electric vehicles was optimized. In [22], a combined weighting method based on the fuzzy optimization iteration was proposed and employed to optimize a single-phase tubular linear SRM.

The main contributions are as follows: (a) investigating the influence of the geometric parameters on the performance of DSSRM in detail by applying sensitivity analysis. Since the modular segmental-stator DSSRM structure has more geometric size parameters than the conventional SRM topology, the sensitivity indices of design variables are more essential to be calculated and analyzed; (b) optimizing the structural parameters to reduce torque ripple and further improve electromagnetic torque performance of the DSSRM by employing a fuzzy iteration optimization algorithm with weight determination.

This paper is organized as follows. The DSSRM structure is introduced in section II and sensitivity analysis is done in section III. Multi-objective optimization is conducted by applying a weight determination iteration algorithm in section IV. The optimal scheme is verified by experiment in section V.

II. STRUCTURE OF DSSRM

The structure of 16/18/18/16 U-type modular DSSRM is shown in Fig. 1. It can be seen that the proposed DSSRM is composed of segmental outer stator, rotor and segmental inner stator. The number of U-shaped outer stator segment, rotor outer salient pole, rotor inner salient pole and U-shaped inner stator segment is 8, 18, 18, 8, respectively.

Based on general design experience and parameter selection principle, the initial dimension parameter values of DSSRM are selected and presented in Table 1. It should be noted that the center lines of the rotor inner and outer teeth are staggered at a certain mechanical angle to

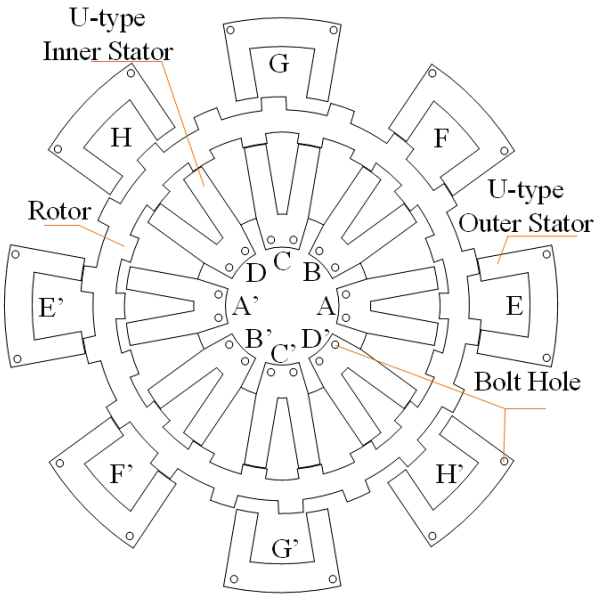

Fig. 1. Structure and winding distribution of DSSRM.

Table 1: Initial geometry size of DSSRM

Item	Variable	Value
Outer diameter of outer stator	D_{so}	220 mm
Outer stator yoke height	b_{syo}	9 mm
Outer stator pole angle	β_{so}	7.5°
Outer air gap length	g_o	0.3 mm
Rotor outer diameter	D_{ro}	175 mm
Rotor outer pole angle	β_{ro}	7.5°
Rotor inner pole angle	β_{ri}	7.5°
Rotor outer pole length	h_{ro}	7 mm
Rotor inner pole length	h_{ri}	7.2 mm
Rotor yoke height	b_{ry}	10 mm
Rotor inner diameter	D_{ri}	127.2 mm
Inner air gap length	g_i	0.3 mm
Inner stator yoke height	b_{syi}	7 mm
Inner stator pole angle	β_{si}	7.5°
Staggered mechanical angle of the rotor inner and outer teeth	θ	2.5°
Outer stator winding turns	N_o	88
Inner stator winding turns	N_i	68
Shaft radius	D_{sh}	45 mm
Lamination thickness	L	70 mm

reduce the torque ripple of the motor and the staggered mechanical angle is defined as θ. According to Table 1, the FE model of DSSRM is established in FLUX software and the performance is analyzed. Figure 2 illustrates the FE model and magnetic field distribution of the DSSRM. When a 12.5 A current is applied to A-phase winding of inner stator and G-phase winding of outer stator simultaneously, Fig. 2 (c) gives the flux density distribution at outer stator aligned position, and Fig. 2 (d) shows it at inner stator aligned position.

For the modular segmental-stator DSSRM, the design objective is to maximize the average static electromagnetic torque T_{avg}, maximize the torque smoothing coefficient τ, and maximize the efficiency η simultaneously. Average torque refers to the average value of the electromagnetic torque over a complete electrical cycle (the rotor has turned one pole pitch) and is obtained by integrating and averaging the instantaneous electromagnetic torque:

$$T_{avg} = \frac{1}{\theta_r}\int_0^{\theta_r} T_{em} d\theta, \tag{1}$$

where θ_r denotes the rotor pole pitch and T_{em} is the electromagnetic torque. Likewise, τ is the torque smoothing coefficient of DSSRM which can be described as:

$$\tau = \frac{T_{avg}}{T_{max} - T_{min}}, \tag{2}$$

where T_{max} is the maximum static electromagnetic torque and T_{min} is the minimum static electromagnetic torque.

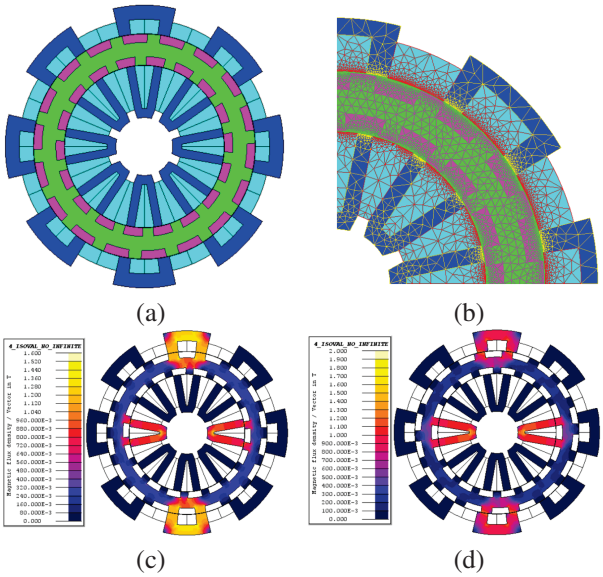

Fig. 2. FE model and magnetic field distribution of DSSRM: (a) FE model, (b) mesh map, (c) flux density distribution at outer stator aligned position, and (d) flux density distribution at inner stator aligned position.

III. COMPREHENSIVE SENSITIVITY ANALYSIS

In the process of structural design and optimization of an electrical machine, various geometric parameters are often under consideration for adjustment. It is

necessary to analyze the sensitivity of each geometric variable parameter to structural characteristic variation. Then, the relative influence of the geometric size parameters, such as inner and outer stator and rotor pole angles, on the performance of the DSSRM is analyzed and discussed. According to the calculated comprehensive sensitivity index, five significant sensitive design variables are selected for the next multi-objective optimization process.

In this paper, eight variable parameters are selected for sensitivity analysis, namely rotor inner pole angle β_{ri}, inner stator pole angle β_{si}, rotor outer pole angle β_{ro}, outer stator pole angle β_{so}, rotor yoke height b_{ry}, inner stator yoke height b_{syi}, outer stator yoke height b_{syo} and the staggered mechanical angle θ. During this analysis, the sensitivity of the eight geometric parameters is conducted while the other geometric parameters remain unchanged. Generally, the sensitivity of design variables to the objects is indicated by a sensitivity index, which can be expressed as [17]:

$$S_{ni} = \frac{\partial f}{\partial z_i}\Big|_{\mathrm{NOP}} \frac{z_i}{f} \approx \frac{\Delta f/f}{\Delta z_i/z_i}, \tag{3}$$

where f represents the function of design objectives and z_i is the design variable. The sensitivity analysis results concerning the eight geometric variable parameters are illustrated in Fig. 3.

As shown in Fig. 4, the sensitivity results of each parameter vary greatly while the eight variables lead to a growth of geometric times in sample size for multi-objective optimization.

Thus, the sensitivity index $G(n_i)$ is introduced to measure the significance of each variable [17]. Weight coefficient is applied to evaluate each variable comprehensively considering three optimization objectives and $G(n_i)$ is expressed as:

$$G(n_i) = w_1 \left|S_{T_{\mathrm{avg}}}\right| + w_2 \left|S_\tau\right| + w_3 \left|S_\eta\right|. \tag{4}$$

It should be noted that w_1, w_2 and w_3 represent the weight of the average torque, the torque smoothing coefficient and the efficiency, respectively, which satisfy $w_1+w_2+w_3 = 1$. In this paper, w_1 is selected as 0.5, while the value of w_2 and w_3 are selected to be 0.3 and 0.2.

According to (4), the comprehensive sensitivity indices of eight design parameters are calculated as listed in Table 2. The negative sensitivity indices in Table 2 mean that the optimization objectives will come down with the increase of design variables, while the positive sensitivity indices indicate that the optimization objectives will rise with the increase of design parameters. It should be noted that the absolute value of the sensitivity index of the design parameters directly represents their influence on the design objectives. The design parameter with higher absolute value of sensitivity index indicates that the design parameter has a relatively larger influence on the optimization objective. The influence of each design variable on the three design objectives is analyzed and discussed.

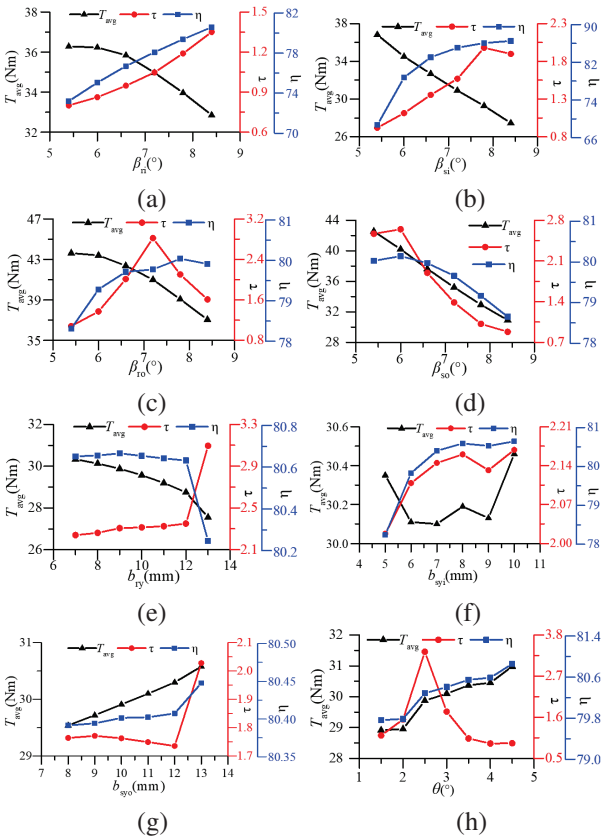

Fig. 3. Sensitivity analysis results: (a) rotor inner pole angle, (b) inner stator pole angle, (c) rotor outer pole angle, (d) outer stator pole angle, (e) rotor yoke height, (f) inner stator yoke height, (g) outer stator yoke height, (h) staggered angle of rotor inner and outer teeth.

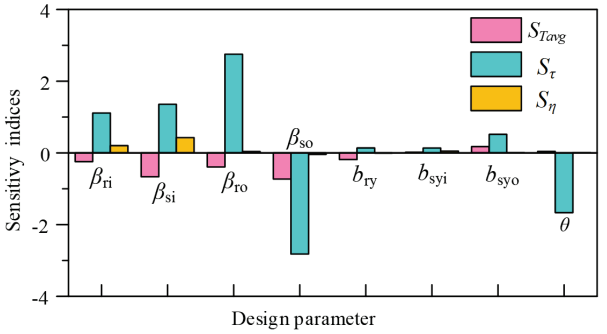

Fig. 4. Sensitivity indices of design parameters to the optimization objectives.

For the average torque T_{avg}, the most sensitive design variable is the outer stator pole angle β_{so}, and its sensitivity index is -0.729. The inner stator yoke height

Table 2: Sensitivity of design variables

Design Parameter	Optimization Objective			$G(n_i)$
	$S_{T_{avg}}$	S_τ	S_η	
β_{ri}	−0.244	1.114	0.204	0.493
β_{si}	−0.665	1.357	0.426	0.8009
β_{ro}	−0.391	2.752	0.038	0.9934
β_{so}	−0.729	−2.819	−0.04	1.1493
b_{ry}	−0.187	0.14	−0.006	0.1186
b_{syi}	0.02	0.137	0.052	0.0647
b_{syo}	0.177	0.519	0.004	0.2277
θ	0.042	−1.664	0.006	0.5178

b_{syi} is the least sensitive design variable due to the sensitivity index of 0.02. Moreover, all the pole angles of stator and rotor (rotor inner pole angle β_{ri}, inner stator pole angle β_{si}, rotor outer pole angle β_{ro} and outer stator pole angle β_{so}) have significant influence on the average torque of DSSRM. Variation of the stator and the rotor pole angles directly affects the length of the air gap at the unaligned position. Hence, variation of the unaligned inductance further affects the electromagnetic torque of DSSRM, which is mentioned in [19, 20].

It can be observed that the sensitivity indices of pole angles of the outer stator and outer rotor on average torque is larger than that of the inner stator and inner rotor. Note that the total mechanical torque of DSSRM is obtained by the superposition of torque generated by inner and outer motors and they have strong decoupling characteristics. However, the power of the outer motor is greater than the inner motor due to the larger dimensions of the outer motor. Therefore, the influence of the pole angles in outer motor on average torque is greater than the inner stator and inner rotor pole angles.

Additionally, after simple analysis, the most sensitive design variable to the torque smoothing coefficient τ is the outer stator pole angle β_{so}, and its sensitivity index is −2.819. Rotor yoke height b_{ry} is the least sensitive design variable because it has the smallest sensitivity index absolute value of 0.14 within the eight design parameters.

Similar with the average torque, all the pole angles of stator and rotor (β_{so}, β_{ro}, β_{si} and β_{ri}) significantly influence the torque smoothing coefficient. In addition, the staggered mechanical angle of inner and outer rotor θ is another significant sensitive parameter to torque smoothing coefficient. It should be noted that total mechanical torque is obtained by the superposition of torque generated by inner and outer motors. The staggered mechanical angle θ directly affects the staggering degree of the two torque waveforms. Hence, θ has little influence on the average torque, but has great influence on the torque smoothing coefficient.

It can also be observed that the sensitivity indices of the pole angles of the outer stator and outer rotor on the torque smoothing coefficient is larger than that of the inner stator and inner rotor. Note that the torque output capability of the outer motor is superior to the inner motor due to the larger dimensions of the outer motor.

It can be observed that no design variable has a sensitivity index absolute value greater than 0.5. In other words, the eight design variables selected in this paper have relatively small effects on the efficiency of the DSSRM. The phase winding turns, the rotor outer diameter and the conduction angle are the sensitive parameters that have the most significant influence on the efficiency of SRM [21].

The eight design variables are stratified into two levels in this paper. Specifically, β_{ri}, β_{si}, β_{ro}, β_{so} and θ are significant sensitive design variables compared with other variables [$G(n_i)\geq 0.3$], which are emboldened in Table 2 and will be further optimized in the next section. Meanwhile, b_{ry}, b_{syi} and b_{syo} are the nonsignificant variables which have less sensitivity on the three optimization objectives [$G(n_i)<0.3$]. Figure 5 illustrates the complete optimization process of the proposed method.

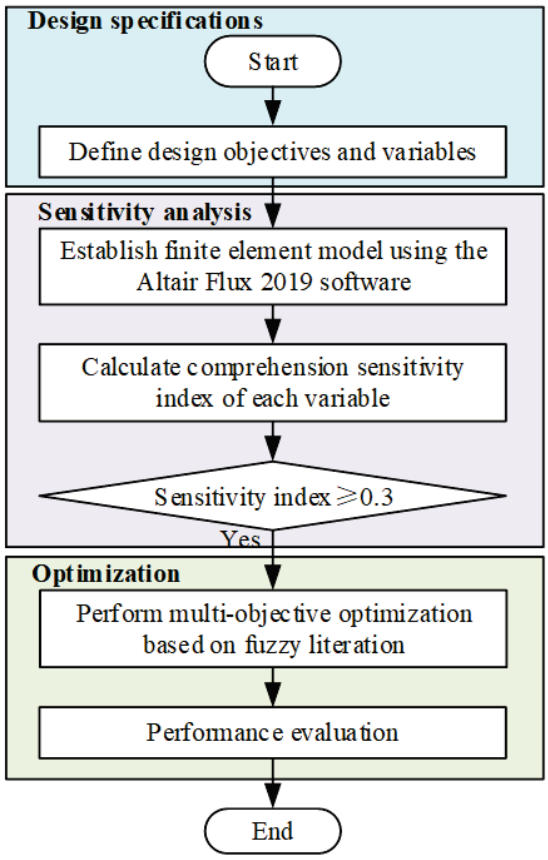

Fig. 5. Process of proposed optimization method.

IV. MULTI-OBJECTIVE OPTIMIZATION

This paper adopts a weight determination iteration algorithm based on vector normalization and linear transformation as the optimization method to determine optimal structural parameters of DSSRM. First, an initial decision matrix $A = (a_{ij})_{m\times n}$ can be constructed by computing the objective value within each parameter variation range, where a_{ij} is the attribute value of scheme i under index j [22]. The matrix obtained by the vector normalization method can be expressed as:

$$mi(w) = \sum_{j=1}^{m} \left(w_j r'_{ij}\right)^2. \tag{5}$$

The matrix obtained by the linear transformation method is:

$$Mi(w) = \sum_{j=1}^{m} \left(w_j r''_{ij}\right)^2. \tag{6}$$

Weight coefficient can be expressed as:

$$w = (w_1, w_2, \ldots, w_n). \tag{7}$$

The decision result of a certain optimal structure parameter can be obtained by the following formula:

$$F_i(u_i, w) = u_i^2 m(w) + (1-u_i)^2 M(w), \tag{8}$$

where u_i is the adjustment coefficient of the matrix $m_i(w)$ and 1-u_i is the adjustment coefficient of the matrix $M_i(w)$.

It should be noted that the selected index weight and adjustment coefficient should make the sum of decision results minimum. The weight calculation problem can be converted to the following nonlinear optimization model:

$$\max\{F_i(u_i, w)\} \quad \begin{cases} 0 \le u_i \le 1 \\ \sum_{j=1}^{m} w_j = 1 \\ w_j \ge 0 \end{cases}. \tag{9}$$

To facilitate the solution, the Lagrange function can be constructed as:

$$L(u_i, \lambda) = \sum_{i=1}^{n} F_i(u_i, w) + \lambda\left(\sum_{j=1}^{m} w_j - 1\right). \tag{10}$$

By solving this formula, the following result can be obtained:

$$\begin{cases} u_i = \left[1 + \dfrac{\sum_{j=1}^{m} w_j^2 (r'_{ij})^2}{\sum_{j=1}^{m} w_j^2 (r''_{ij})^2}\right]^{-1} \\ w_j = \left(\sum_{k=1}^{m} \dfrac{\sum_{i=1}^{n} \left[u_i^2 (r'_{ij})^2 + (1-u_i^2)(r''_{ij})^2\right]}{\sum_{i=1}^{n} \left[u_i^2 (r'_{ik})^2 + (1-u_i^2)(r''_{ik})^2\right]}\right)^{-1} \end{cases}. \tag{11}$$

The flow chart of the fuzzy iteration algorithm with weight determination is illustrated in Fig. 6.

Taking the staggered angle of rotor inner and outer teeth θ as an example, the optimization process of the iteration algorithm is described in detail. While keeping other structural parameters unchanged, the average torque T_{avg}, torque smoothing coefficient τ and efficiency η under different staggered angles θ are shown in Table 3.

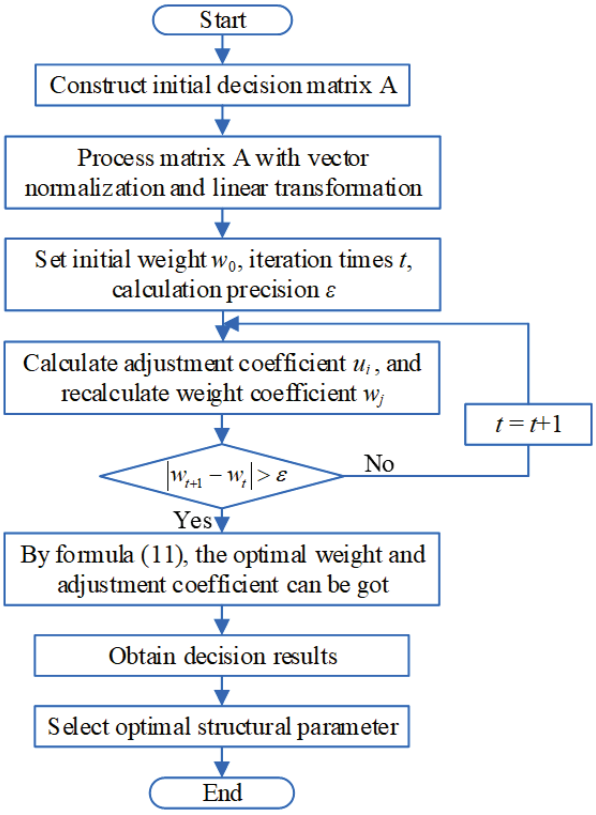

Fig. 6. Flow chart of the optimization algorithm.

Table 3: Initial decision matrix A of variable θ

Value of θ (°)	T_{avg} (Nm)	τ	η (%)
1.5	30.45	0.90	80.59
2	28.95	1.54	79.79
2.5	29.87	3.35	80.29
3	30.10	1.74	80.40
3.5	30.37	1.03	80.55

Using (5) to perform vector normalization processing on matrix A, the results are shown in Fig. 7 (a). Using (6) to perform linear transformation processing on matrix A, the results are shown in Fig. 7 (b). The initial weight is set to w_0 = (0.5, 0.3, 0.2) and, after four iterations, the optimal adjustment coefficient and optimal weight coefficient are obtained: u = (0.8155, 0.7900, 0.7213, 0.7831, 0.8112), w = (0.3068, 0.3886, 0.3046).

Finally, the obtained optimal adjustment coefficient and optimal weight coefficient are substituted into (11), and the final decision results under different staggered angles are shown in Fig. 7 (c). It can be seen that when θ is 2.5°, the decision result is the largest within the range, which is 0.0930. For each index weight and scheme adjustment coefficient, bigger decision results represent better performance of a certain decision scheme. Therefore, 2.5° is selected as the optimal size of θ.

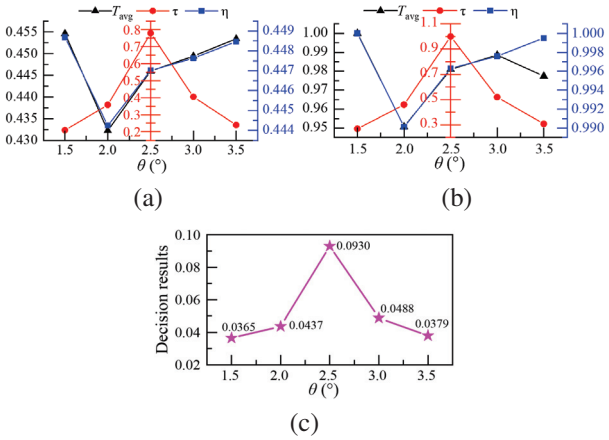

Fig. 7. Optimal process with different staggered angles as an example: (a) results of vector normalization, (b) results of linear transformation, (c) final decision results.

After the multi-objective optimization process of the five significant structural variables (one-by-one), the final decision results with β_{so}, β_{ro}, β_{si}, β_{ri} and θ are shown in Tables 4–8, and the optimal structural parameter and decision result of each variable are emboldened. It should be noted that the optimization sequence of these five parameters is determined by the comprehensive sensitivity analysis results in section III. According to the descending order rule of the comprehensive sensitivity index $G(ni)$ values, their optimization sequence is: β_{so}, β_{ro}, β_{si}, β_{ri} and θ. Additionally, based on Table 1, during the optimization process, the initial values for β_{so}, β_{ro}, β_{si}, β_{ri} and θ are all 7.5°, while the initial value for θ is 2.5°. For instance, when β_{so} is optimized for single parameter scanning, β_{ro}, β_{si} and β_{ri} are kept at 7.5° and θ is fixed at 2.5°. When β_{ro} is under optimizing, β_{si}, β_{ri} and θ remain at their respective initial values (7.5°, 7.5° and 2.5°), but β_{so} adopts its newly optimized value (6°).

The optimized geometric parameters of DSSRM are summarized in Table 9.

Table 4: Final results under different outer stator pole angle β_{so}

$\boldsymbol{\beta}_{so}$ (°)	5.4	**6**	6.6	7.2	7.8
Decision Result	0.0333	**0.0845**	0.0591	0.0453	0.0370

Table 5: Final results under different rotor outer pole angle β_{ro}

$\boldsymbol{\beta}_{ro}$ (°)	6	**6.6**	7.2	7.8	8.4
Decision Result	0.0448	**0.0707**	0.0560	0.0512	0.0431

Table 6: Final results under different inner stator pole angle β_{si}

$\boldsymbol{\beta}_{si}$ (°)	5.4	**6**	6.6	7.2	7.8
Decision Result	0.0526	**0.0616**	0.0577	0.0454	0.0493

Table 7: Final results under different rotor inner pole angle β_{ri}

$\boldsymbol{\beta}_{ri}$ (°)	6	6.6	7.2	**7.8**	8.4
Decision Result	0.0494	0.0523	0.0569	**0.0633**	0.0467

Table 8: Final results under different staggered angle θ

$\boldsymbol{\theta}$ (°)	1.5	2	**2.5**	3	3.5
Decision Result	0.0365	0.0437	**0.0930**	0.0488	0.0379

Table 9: Final key geometry size of DSSRM

Item	Variable	Value
Outer stator pole angle	β_{so}	6°
Rotor outer pole angle	β_{ro}	6.6°
Rotor inner pole angle	β_{ri}	7.8°
Inner stator pole angle	β_{si}	6°
Angle of rotor inner and outer teeth	θ	2.5°

V. SIMULATION AND EXPERIMENTAL VERIFICATION

To verify the proposed multi-objective optimization method, the DSSRM dynamic torque performance at 600 r/min and 1500 r/min in APC (angular position control) mode of the initial size and final size is compared in Fig. 8. It can be observed that the torque performance of the optimized motor is better than that of the benchmark motor at the two operating points.

The performance of the three optimization objectives at 600 r/min is compared in Table 10. It can be seen that the average torque of the DSSRM after optimization increases from 30.17 Nm to 40.99 Nm, the torque smoothing coefficient goes up from 1.78 to 2.82, and the efficiency also increases from 80.80% to 82.46%, and their growth rates are 35.86%, 58.42% and 2.05%, respectively. Hence, the three optimization objectives of the final DSSRM are all improved, but the improvement of efficiency is not as significant as the other two objectives. It should be noted that the design variables selected in this paper have relatively small effects on the efficiency of the DSSRM which has been discussed in section III.

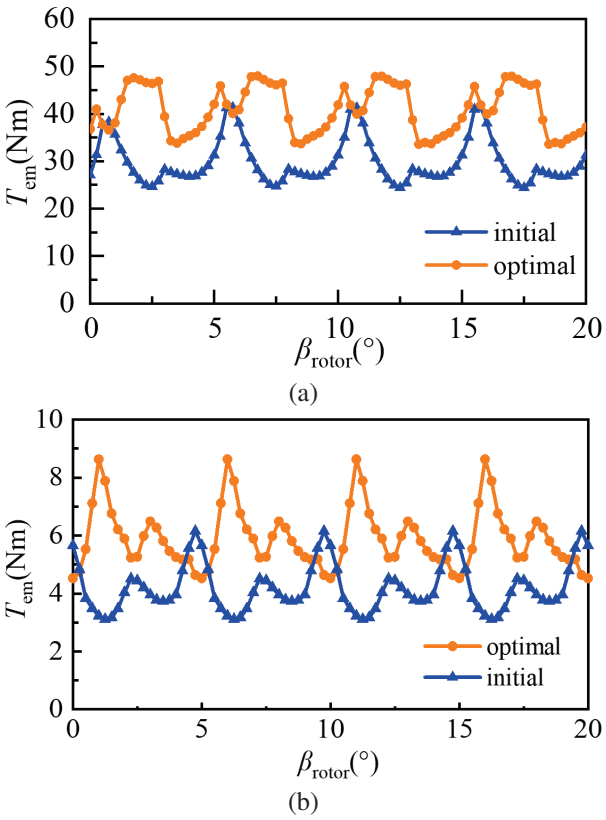

Fig. 8. Comparison of electromagnetic torque before and after optimization with APC mode: (a) at 600 r/min and (b) at 1500 r/min.

Table 10: Performance comparison of DSSRM at 600 r/min

Optimization Objective	Initial Size	Optimized Size	Percentage of Promotion (%)
T_{avg} (Nm)	30.17	40.99	35.86
τ	1.78	2.82	58.42
η (%)	80.80	82.46	2.05

In addition, to further verify the presented DSSRM and proposed multi-objective optimization method, the prototype motor experimental platform is established, which is shown in Fig. 9. The rated power of the prototype machine is the same as that of the FE model and the core material of the rotor and stator is 50DW470.

Simulated and measured flux linkage waveforms at the aligned and unaligned position of the prototype machine are shown in Fig. 10. It can be seen that the measured waveform shows good agreement with the FE simulation results, which proves that the multi-objective optimization scheme can effectively improve the performance of DSSRM.

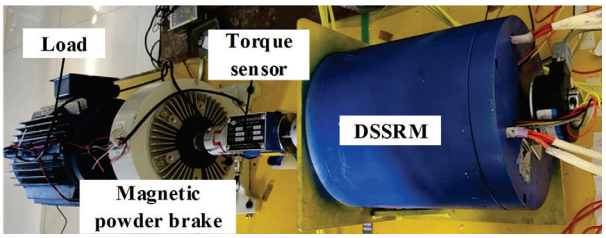

Fig. 9. DSSRM prototype experimental platform.

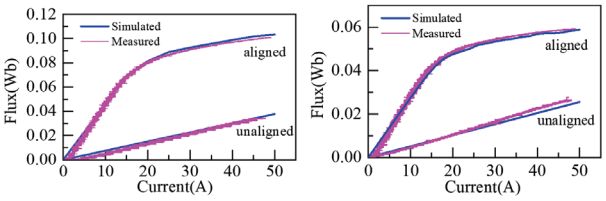

Fig. 10. Flux linkage results of experiment and simulation: (a) outer stator and (b) inner stator.

Motor speed is set to 1500 r/min. Turn-on and turn-off angles are fixed at 0° and 5°, respectively. Phase winding current waveforms of the inner and outer stators and motor torque waveforms are shown in Fig. 11. It should be noted that the measured output torque waveform is consistent with the simulation results in Fig. 8 (b), which verifies the effectiveness of the sensitivity analysis and the multi-objective optimization method.

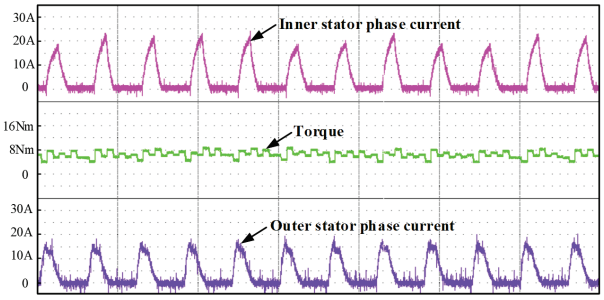

Fig. 11. Experimental results of phase current and torque at 1500 r/min.

VI. CONCLUSION

This paper introduces a multi-objective optimization design method of a high performance DSSRM. The initial scheme of the DSSRM is given first. The influence of structural parameters on the optimization objectives of the DSSRM are investigated and discussed in detail. Eight initial design variables are reduced to five significant variables in the optimization process. The final structural parameter scheme of the DSSRM is obtained by applying a weight determination iteration algorithm.

Finally, both the simulation and experimental results verify the effectiveness of the sensitivity analysis and proposed multi-objective optimization method.

ACKNOWLEDGMENT

This work is supported by the Jiangsu Science and Technology Plan Special Fund (Innovation Support Plan International Science and Technology Cooperation/ Hong Kong Macao Taiwan Science and Technology Cooperation) Project (BZ2022014), Shenzhen Basic Research Special (Natural Science Foundation) Key Project (JCYJ20220818100000001), 2022 China-CEEC University Joint Education Program (2022200), 2023 China-CEEC University Joint Education Program (2023304).

REFERENCES

[1] M. Abbasian, M. Moallem, and B. Fahimi, "Double-stator switched reluctance machines (DSSRM): Fundamentals and magnetic force analysis," *IEEE Trans. Energy Convers*., vol. 25, no. 3, pp. 589-597, Sep. 2010.

[2] M. Asgar, E. Afjei, and H. Torkaman, "A new strategy for design and analysis of a double-stator switched reluctance: Electromagnetics, FEM, and experiment," *IEEE Trans. Magn.*, vol. 51, no. 12, pp. 1-8, Dec. 2015.

[3] A. H. Isfahani and B. Fahimi, "Comparison of mechanical vibration between a double-stator switched reluctance machine and a conventional switched reluctance machine," *IEEE Trans. Magn.*, vol. 50, no. 2, pp. 293-296, Feb. 2014.

[4] N. Arbab, W. Wang, C. Lin, J. Hearron, and B. Fahimi, "Thermal modeling and analysis of a double-stator switched reluctance motor," *IEEE Trans. Energy Convers.*, vol. 30, no. 3, pp. 1209-1217, Sep. 2015.

[5] L. Maharjan, E. Bostanci, S. Wang, E. Cosoroaba, W. Cai, and F. Yi, "Comprehensive report on design and development of a 100-kW DSSRM," *IEEE Trans. Transp. Electrification*, vol. 4, no. 4, pp. 835-856, Dec. 2018.

[6] W. Wang, M. Luo, E. Cosoroaba, B. Fahimi, and M. Kiani, "Rotor shape investigation and optimization of double stator switched reluctance machine," *IEEE Trans. Magn.*, vol. 51, no. 3, pp. 1-4, Mar. 2015.

[7] R. Vandana and B. G. Fernandes, "Design methodology for high-performance segmented rotor switched reluctance motors," *IEEE Trans. Energy Convers.*, vol. 30, no. 1, pp. 11-21, Mar. 2015.

[8] S. R. Mousavi-Aghdam, M. R. Feyzi, N. Bianchi, and M. Morandin, "Design and analysis of a novel high-torque stator-segmented SRM," *IEEE Trans. Ind. Electron.*, vol. 63, no. 3, pp. 1458-1466, Mar. 2016.

[9] G. J. Li, X. Y. Ma, G. W. Jewell, and Z. Q. Zhu, "Novel modular switched reluctance machines for performance improvement," *IEEE Trans. Energy Convers.*, vol. 33, no. 3, pp. 1255-1265, Sep. 2018.

[10] M. A. J. Kondelaji and M. Mirsalim, "Segmented-rotor modular switched reluctance motor with high torque and low torque ripple," *IEEE Trans. Transp. Electrification*, vol. 6, no. 1, pp. 62-72, Mar. 2020.

[11] W. Yan, H. Chen, Y. Liu, H. Cheng, and M. Orabi, "A magnetic field decoupling double stator switched reluctance machine," *IEEE Trans. Appl. Supercond.*, vol. 31, no. 8, pp. 1-5, Nov. 2021.

[12] H. Chen, W. Yan, J. J. Gu, and M. Sun, "Multi-objective optimization design of a switched reluctance motor for low-speed electric vehicles with a Taguchi–CSO algorithm," *IEEE/ASME Trans. Mechatronics*, vol. 23, no. 4, pp. 1762-1774, Aug. 2018.

[13] P. Di Barba, M. E. Mognaschi, D. A. Lowther, and J. K. Sykulski, "A benchmark TEAM problem for multi-objective Pareto optimization of electromagnetic devices," *IEEE Trans. Magn.*, vol. 54, no. 3, pp. 1-4, Mar. 2018.

[14] P. Di Barba, F. Dughiero, M. Forzan, D. A. Lowther, M. E. Mognaschi, E. Sieni, and J. K. Sykulski, "A benchmark TEAM problem for multi-objective Pareto optimization in magnetics: The time-harmonic regime," *IEEE Trans. Magn.*, vol. 56, no. 1, pp. 1-4, Jan. 2020.

[15] G. Bramerdorfer, G. Lei, A. Cavagnino, Y. Zhang, J. Sykulski, and D. A. Lowther, "More robust and reliable optimized energy conversion facilitated through electric machines, power electronics and drives, and their control: State-of-the-art and trends," *IEEE Trans. Energy Convers.*, vol. 35, no. 4, pp. 1997-2012, Dec. 2020.

[16] R. C. P. Silva, T. Rahman, M. H. Mohammadi, and D. A. Lowther, "Multiple operating points based optimization: Application to fractional slot concentrated winding electric motors," *IEEE Trans. Ind. Electron.*, vol. 65, no. 2, pp. 1719-1727, Feb. 2018.

[17] W. Zhao, A. Ma, J. Ji, X. Chen, and T. Yao, "Multiobjective optimization of a double-side linear Vernier PM motor using response surface method and differential evolution," *IEEE Trans. Ind. Electron.*, vol. 67, no. 1, pp. 80-90, Jan. 2020.

[18] J. G. Amoros and P. Andrada, "Sensitivity analysis of geometrical parameters on a double-sided linear switched reluctance motor," *IEEE Trans. Ind. Electron.*, vol. 57, no. 1, pp. 311-319, Jan. 2010.

[19] X. D. Xue, K. W. E. Cheng, T. W. Ng, and N. C. Cheung, "Multi-objective optimization design of in-wheel switched reluctance motors in electric vehicles," *IEEE Trans. Ind. Electron.*, vol. 57, no. 9, pp. 2980-2987, Sep. 2010.

[20] Y. Zhu, W. Wei, C. Yang, and Y. Zhang, "Multi-objective optimisation design of two-phase excitation switched reluctance motor for electric vehicles," *IET Electr. Power App.*, vol. 12, no. 7, pp. 929-937, 2018.

[21] K. Diao, X. Sun, G. Lei, Y. Guo, and J. Zhu, "Multiobjective system level optimization method for switched reluctance motor drive systems using finite-element model," *IEEE Trans. Ind. Electron.*, vol. 67, no. 12, pp. 10055-10064, Dec. 2020.

[22] H. Chen, Y. Zhan, and R. Nie, "Multiobjective optimization design of single-phase tubular switched reluctance linear launcher," *IEEE Trans. Plasma Science*, vol. 47, no. 5, pp. 2431-2437, May 2019.

Xing Wang received the B.S. degree from China University of Mining and Technology, Xuzhou Jiangsu, China, in 1996, and M.S. degree from China University of Mining and Technology, Xuzhou Jiangsu, in 1999. In 2007, she became an Associate Professor with China University of Mining and Technology, Xuzhou. She is a holder of four US Patents, nine Australian Patents, two Canadian Patents, four Russian Patents, 12 Chinese Invention Patents, three Chinese Utility Model Patents, and has authored 15 papers.

Hao Chen received the B.S. and Ph.D. degrees from the Department of Automatic Control, Nanjing University of Aeronautics and Astronautics, Nanjing, China, in 1991 and 1996, respectively. In 1998, he became an Associate Professor with the School of Information and Electrical Engineering, China University of Mining and Technology, Xuzhou, where he has been a Professor since 2001. From 2002 to 2003, he was a Visiting Professor at Kyungsung University, Busan, Korea. Since 2008, he has also been an Adjunct Professor at the University of Western Australia, Perth, Australia. He is the author of one book and has also authored more than 190 papers. He is the holder of 14 US Patents, 23 Australian Patents, one Danish Patent, seven Canadian Patents, three South African Patents, 10 Russian Patents, 44 Chinese Invention Patents and six Chinese Utility Model Patents. His current research interests include motor control, linear launcher, electric vehicles, electric traction, servo drives and wind power generator control.

Chen was the recipient of both the Prize of Science and Technology of Chinese Youth and the Prize of the Fok Ying Tong Education Foundation for Youth Teachers in both 2004. He was awarded the first prize in the Science and Technology advanced of Province and Ministry once, the second prize in the Science and Technology advanced of Province and Ministry seven times, and the third prize in the Science and Technology advanced of Province and Ministry 14 times. He became the Chinese New Century Hundred-Thousand Ten-Thousand Talents Engineering National Talent in 2007 and won the Government Especial Allowance of People's Republic of China State Department in 2006.

Fengyuan Yu received the Ph.D. degree from the School of Electrical Engineering, China University of Mining and Technology, Xuzhou, China, in 2023. Since 2023, he has been a Post-Doctoral Researcher with the China University of Mining and Technology. His research interests include switched reluctance drive, special motor design, power converters and motor control.

Wenju Yan received the B.S. degree in electrical engineering and automation from the China University of Mining and Technology, Xuzhou, China, in 2013. He received the Ph.D. degree in electrical engineering from the China University of Mining and Technology, Xuzhou, in 2018. From 2019 to 2021, he was a Postdoctoral Research Fellow with China University of Mining and Technology, Xuzhou. Since 2021, he has been an associate professor at the China University of Mining and Technology, Xuzhou. His current research interests include electric vehicles, electric traction, iron loss analysis and special motor design.

Jianfei Pan graduated from the Department of Electrical Engineering of Hong Kong Polytechnic University in Hong Kong with the Ph.D. degree in 2006. Currently he is working in the College of Mechatronics and Control Engineering, Shenzhen University, China. His main research interests are wireless power transfer, electric machine design and control.

Yassen Gorbounov received his B.S., M.S. and Ph.D. degrees from the Sofia University of Technology, Sofia, Republic of Bulgaria, in 2002, 2004, and 2013, respectively. Since 2017, he has been working as an Associate Professor at the Sofia University of Technology. His current research interests include power electronics and the mining industry.

Design and Optimization of Hybrid Excitation Switched Reluctance Motors for Electric Transportation Vehicles

Qing Wang, Jiangtao Hu, Jiaxin Ding, Fengshuo Liu, Yumeng Zhu, and Yongqing Deng

Department of Electrical Engineering
Nanchang University, Nanchang 330031, China
wangq@ncu.edu.cn, 3363830583@qq.com, 1061626288@qq.com, 13767736595@163.com,
1091306318@qq.com, dengyq@ncu.edu.cn

Abstract – To improve the torque characteristic of hybrid excitation switched reluctance motors (HESRM), the structure and excitation current of HESRM are comprehensively studied. First, a novel structure is introduced to HESRM, in which pole pieces are added to the rotor salient pole to reduce output torque ripple. The effect of different structural parameters in HESRM is studied by finite element model (FEM). To evaluate the torque characteristic of the machine, mean torque and torque are chosen as key evaluation factors of HESRM. To achieve a quick and accurate optimization process, an artificial neural network (ANN) based prediction model is built according to FEM results, in which system structure is employed as input components and evaluate factors are employed as output components. Then, genetic algorithm (GA) is designed for HESRM structure optimization. With improved GA and ANN prediction models, the torque performance of HESRM can be further improved. Finally, experimental and simulation results are given to validate the accuracy of machine design.

Index Terms – Finite element analysis (FEA), genetic algorithm, hybrid excitation switched reluctance motor (HESRM), multi-objective optimization, neural network, torque performance.

I. INTRODUCTION

Compared with permanent magnet (PM) motors and synchronous motors, switched reluctance motors (SRMs) show advantages in merits such as simple structure, high fault tolerance, and wide speed range, and can be widely used in many industrial and commercial areas [1–5]. However, due to its double salient structure, SRM suffers from torque ripple and a relatively low space utility rate [6]. Thus, many scholars focus on improving the torque performance and prolonging the efficient use area of SRM.

Hybrid excitation switched reluctance motor (HESRM) is a type of double salient pole motor, whose structure is similar to traditional switched reluctance motor (TSRM). Unlike TSRM, phase windings of HESRM are excited by a sinusoidal alternating current with DC bias (i.e., phase current consists of both DC and AC components) [7]. HESRM inherits the advantages of the simple and reliable structure from TSRM and overcomes the defect of the low volume utilization rate in TSRM. In [8], the effect of distributed and centralized armature winding schemes is comprehensively studied and compared. Traditionally three-phase power inverters can be employed for HESRM control, by which the drive system achieves high power density and wide operating range. In [9], a four-phase DC-assisted bipolar switched reluctance motor is designed and optimized, by which torque ripple can be effectively reduced. By recombining DC-assisted windings and AC excitation windings introduced in [9], a sinusoidal AC with DC bias can be applied to phase windings of TSRM to improve the torque performance [10].

To reduce the torque ripple of HESRM, scholars have mainly studied two aspects: machine design and optimization [11] and control strategy design for a given motor [12]. Since the double salient structure shows high nonlinearity, it is hard to build a mathematic model for performance analysis, and finite element analysis (FEM) is thus required for most cases. In [13], stator pole arcs are optimized by FEA and the motor has more flexible pole pairs under "bipolar sine and DC bias" excitation mode. Moreover, to improve the torque performance, both mean torque and torque ripple should be considered simultaneously. Thus, multi-objective evaluations should be taken during the optimization process [14], which makes the optimization process more complex. The most commonly used optimization process has the following steps [15]: (a) Discrete torque data should be obtained by FEA; (b) According to FEA results, a fitting model should be realized on time-domain simulation platform to achieve multi-objective evaluation results; (c) According to multi-objective optimization results, the machine structure will be optimized time by time to achieve the

Submitted On: December 31, 2024
Accepted On: May 29, 2025

https://doi.org/10.13052/2025.ACES.J.400903

desired indicators. This optimization process is complicated and costs time.

To overcome the above issues, a HESRM is designed and optimized in this paper. The proposed HESRM is generated from 8/6 TSRM, and the structure is optimized to reduce torque ripple. A FEM is built to analyze the effects of structure parameters and excitation current on the torque performance of the machine. To achieve fast multi-objective optimization, a neural network is employed to establish a torque performance prediction model. To conclude, simulation and experimental results are given to verify the proposed machine structure and optimization process.

II. OPERATING PRINCIPLES OF HESRM

Figure 1 shows the topology of 8/6 HESRM. The stator and rotor present a double salient structure, phase windings are concentrated on each stator tooth, and windings on every two opposing stator teeth are connected in series. Key parameters of the HESRM are given in Table 1.

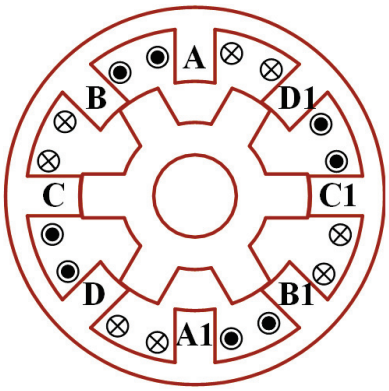

Fig. 1. Four-phase 8/6 HESRM.

Table 1: Key parameters of 8/6 HESRM

Phase windings	1.5 mm^2 copper
Turns of windings	60
Air gap	0.4 mm
Axial length	76.5 mm
Stator pole arc	20°
Rotor pole arc	22°
Rated power	200 W
Rated voltage	24 V
Rated speed	500 r/min

HESRM is excited by AC current with DC bias. The block diagram of the current control strategy is shown in Fig. 2. Main circuit topology is shown in Fig. 3. The absolute value of the reference current is determined by

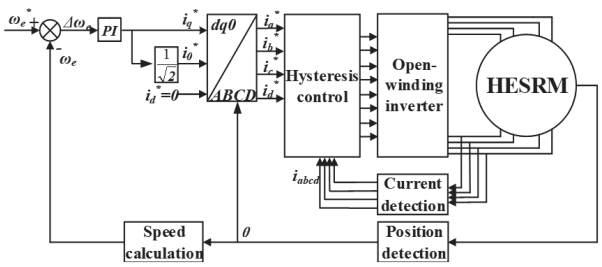

Fig. 2. Current control block diagram.

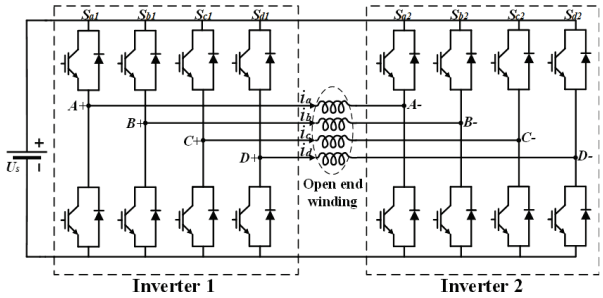

Fig. 3. Topology of the main circuit.

the speed controller. When the speed is lower than the reference speed, the absolute value of the reference current increases, generating a larger torque to increase the speed. When the speed is higher than the reference speed, the situation is the opposite. The d-axis reference current is set to 0, $i_0/i_s = 1/\sqrt{2}$. The phase of the reference value of the four-phase winding current is determined by the rotor position, and the amplitude is determined by the q-axis reference current. The transient current of each phase can be expressed by

$$\begin{cases} I_a = i_0 + i_s \cos(\omega_e t + \varphi_a) \\ I_b = i_0 + i_s \cos(\omega_e t + \varphi_b) \\ I_c = i_0 + i_s \cos(\omega_e t + \varphi_c) \\ I_d = i_0 + i_s \cos(\omega_e t + \varphi_d) \end{cases}. \quad (1)$$

i_0 is the DC bias of the sinusoidal current, i_s is the amplitude of the AC component, ω_e is the angular velocity of the AC component, and φ_k ($k = a$, b, c or d) is the phase angle.

Neglecting magnetic saturation, phase inductance of HESRM can be expressed by

$$\begin{cases} L_a = L_{dc} + L_{ac} \cos\theta_e \\ L_b = L_{dc} - L_{ac} \cos\theta_e \\ L_c = L_{dc} - L_{ac} \cos\theta_e \\ L_d = L_{dc} + L_{ac} \cos\theta_e \end{cases}. \quad (2)$$

L_k ($k = a$, b, c or d) is the self-inductance of each phase, L_{dc} and L_{ac} stand for DC component and AC component of self-inductance, respectively.

The torque equation is

$$T_{\mathrm{e}} = \frac{1}{2}\left(i_a^2\frac{\partial L_{\mathrm{a}}}{\partial \theta_{\mathrm{e}}} + i_b^2\frac{\partial L_{\mathrm{b}}}{\partial \theta_{\mathrm{e}}} + i_c^2\frac{\partial L_{\mathrm{c}}}{\partial \theta_{\mathrm{e}}} + i_d^2\frac{\partial L_{\mathrm{d}}}{\partial \theta_{\mathrm{e}}}\right). \quad (3)$$

The torque ripple can be obtained by

$$T_r = \frac{T_{max} - T_{min}}{T_{avg}}. \quad (4)$$

T_{max} is the maximum value of instantaneous torque in one stroke, T_{min} and T_{max} stand for minimum value and maximum value of instantaneous torque in one stroke, respectively. The rate of change of self-inductance will not only influence the mean torque of HESRM but also influence the torque ripple of HESRM.

III. ANALYSIS OF THE EFFECT OF STRUCTURE PARAMETERS ON TORQUE PERFORMANCE

The mutual coupling of the machine structural parameters complicates the electromagnetic analysis. Moreover, since the double salient structure shows high nonlinearity, it is hard to obtain torque characteristics with mathematic methods. Thus, a FEM is built for torque performance analysis. In FEA, a sinusoidal current with DC bias, whose RMS value is 5 A, is employed to excite phase windings, and the rate between the DC component and AC component i_0/i_s is set to 1. Transient torque performance calculated by FEM is shown in Fig. 4, where T_e represents the total torque.

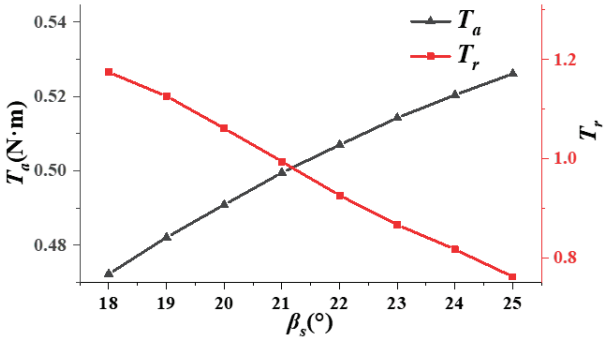

Fig. 4. Torque of the initial HESRM.

As shown in Fig. 4, since the torque decrement of the outgoing phase is higher than the torque increment of the incoming phase, the minimum torque value shows up when the electric angle comes to 5°, 20°, 35° and 50°. These electric angles show up when the stator pole and the rotor pole start to align. It is clear that if the change of inductance were suppressed, especially at the moment when this alignment starts, the change of transient torque would be reduced and the torque ripple would be thus improved. Consequently, a pole-shoe is suggested on each rotor pole, as shown in Fig. 5.

Machine structure parameters, namely stator pole arc β_s, rotor pole arc β_r, pole-shoe length $\Delta\beta_r$, and pole-shoe root height h_1 selected as optimization variables, are marked in Fig. 5. To study the effect of every structure parameter on torque performance separately, sensitivity analysis was carried out by FEM, in which excitation current remains the same as excitation current in Fig. 4.

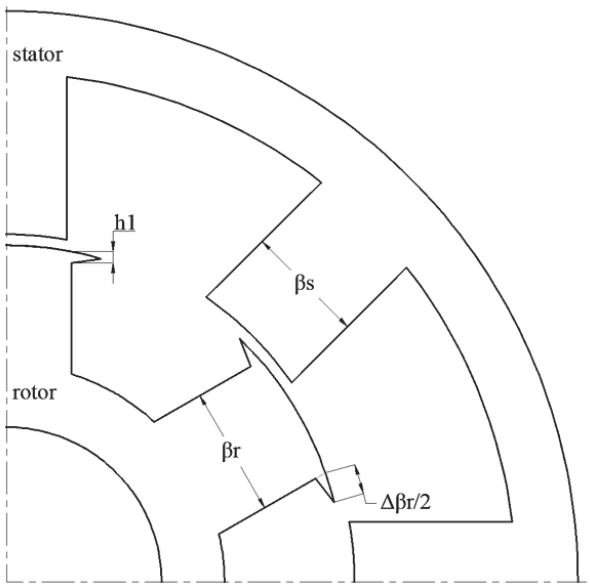

Fig. 5. Structure of proposed HESRM.

A. Sensitivity analysis on stator pole arc

We chose to fix the rotor pole arc at 23° and increase the stator pole arc from 18° to 25°. The calculated transient torque at every electric position angle is shown in Fig. 6.

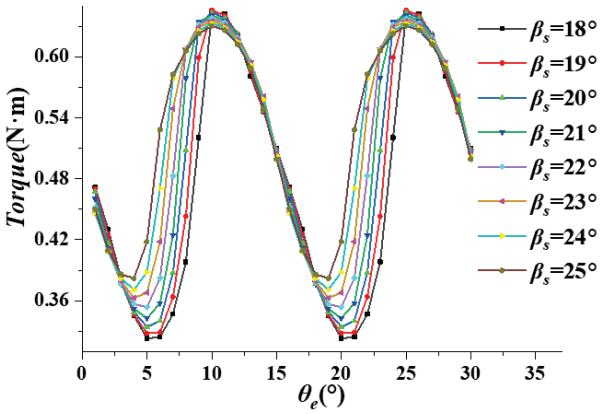

Fig. 6. Transient torque at different electric angles.

According to transient torque data in Fig. 6, mean torque in one stroke T_a and torque ripple T_r can be obtained for torque performance evaluation. The torque performance evaluation result is shown in Fig. 7.

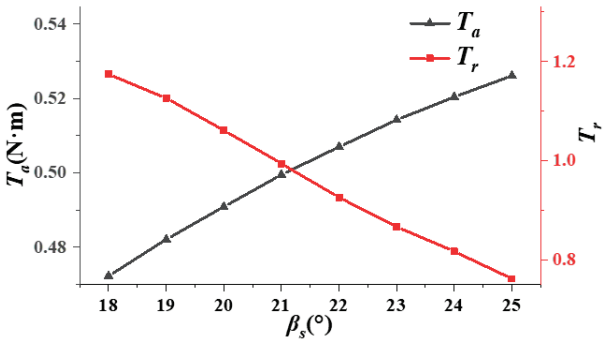

Fig. 7. Torque performance evaluation under different stator pole arcs.

As the stator pole arc increases, the average torque is increased while the torque pulsation decreases. As shown in Fig. 7, when the stator pole arc is small, the average torque is relatively low and the torque pulsation is large. Excessive stator pole arc will also result in an increased slot fullness. High slot fullness leads to dense windings in the stator slot, making the manufacture and installation of the windings more difficult. It will also lead to poor heat dissipation on phase windings. The increased phase winding temperature will also damage the reliability and life of the motor.

B. Sensitivity analysis on rotor pole arc

We chose to fix the stator pole arc at 21° and calculate torque performance under different rotor pole arcs as shown in Fig. 8.

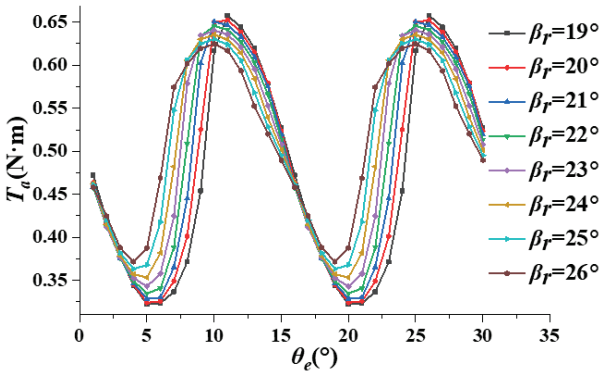

Fig. 8. Transient torque under different rotor pole arcs.

As the rotor pole arc increases, the average motor torque will increase while the torque pulsation will decrease. Therefore, a reasonable selection of the rotor pole arc positively increases the average motor torque and reduces torque pulsation. However, the overlarge rotor pole arc also leads to a decrease in motor performance, as shown in Fig. 9. The torque ripple can be increased, and the average torque will be reduced. The increment in the rotor pole arc does not change the motor slot fullness, but it requires more manufacturing materials and weight, which will increase the manufacturing cost.

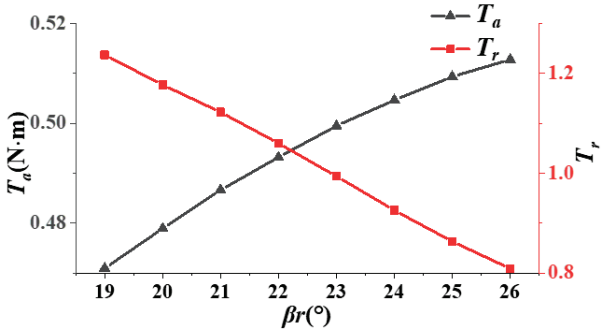

Fig. 9. Torque performance under different rotor pole arcs.

C. Sensitivity analysis on pole-shoe

We chose to fix the rotor pole arc of the motor at 23° and the stator pole arc at 21° so the effect of the pole-shoe on torque performance can be analyzed. The output torque is calculated with different pole-shoe curvatures ($\Delta\beta_r$) when the height of pole-shoe h_1 is fixed at 1.5 mm, and the calculated result is shown in Fig. 10.

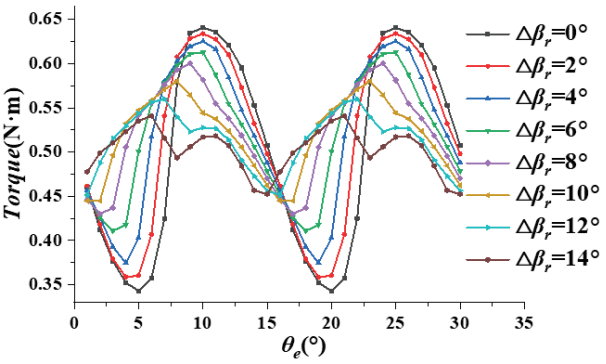

Fig. 10. Transient torque with different-length pole-shoes.

As shown in Fig. 11, the increment of $\Delta\beta_r$ is equivalent to the increase of the rotor pole arc to a certain extent. Moreover, it is more advantageous than increasing the rotor pole arc in terms of cost savings. At the

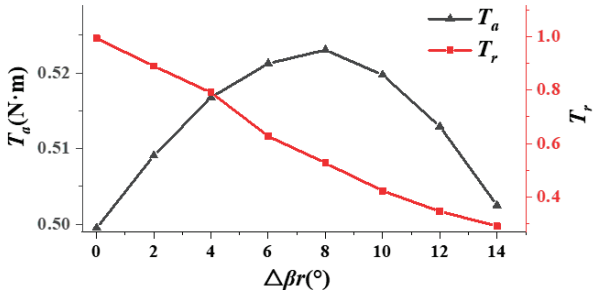

Fig. 11. Torque performance under different-length pole-shoes.

same time, it can appropriately utilize the magnetic saturation phenomenon of the pole-shoe to inhibit the torque change during commutation. As shown in Fig. 11, maximum torque will decrease while minimum torque will first increase with increment of the $\Delta\beta_r$.

Torque performance is shown in Fig. 11. As the length of the pole-shoe increases, the average torque motor will decrease while torque pulsation will first increase and then decrease. Therefore, it is important to choose the length of the pole-shoe within an appropriate range to optimize torque performance.

According to Fig. 13, the motor shows relatively

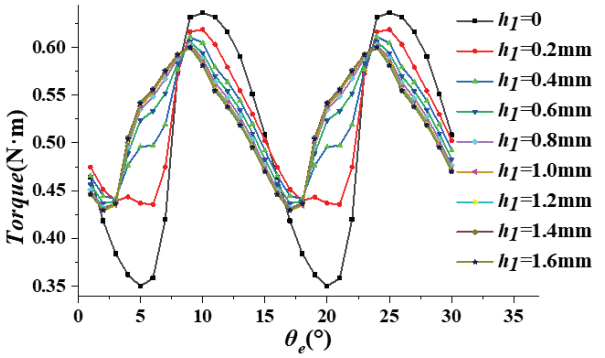

Fig. 12. Transient torque under different pole-shoe root heights.

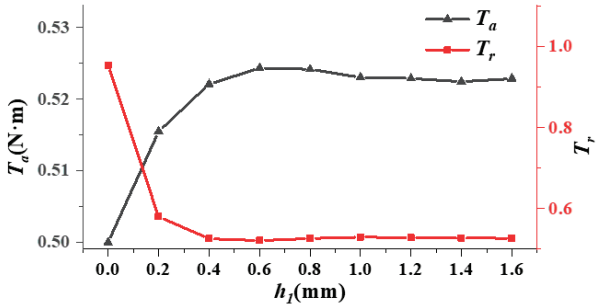

Fig. 13. Torque performance under different pole-shoe root heights.

good performance at $\Delta\beta_r = 8°$. While $\Delta\beta_r$ is fixed at 8°, torque performance under different pole-shoe root heights (h_1) is calculated and shown in Figs. 12 and 13.

As can be seen from Figs. 12 and 13, when h_1 is small, torque performance is sensitive to the increase of h_1. With the increment of h_1, magnetic saturation on the pole-shoe is relieved. When h_1 is greater than 0.6 mm, the increment of h_1 barely influences the torque performance.

D. Sensitivity analysis on the ratio of DC bias to amplitude of AC component

Composition of the phase current will directly affect the strength and distribution of the magnetic field in the machine. We chose to fix the key parameters of the machine as $\beta_s = 20°$, $\beta_r = 22°$, $\triangle\beta_r$, φ, h_1 are set as 0, RMS value of phase current is limited to 5 A. Transient torque profile under different i_0/i_s is shown in Fig. 14. Corresponding torque performance analysis is shown in Fig. 15.

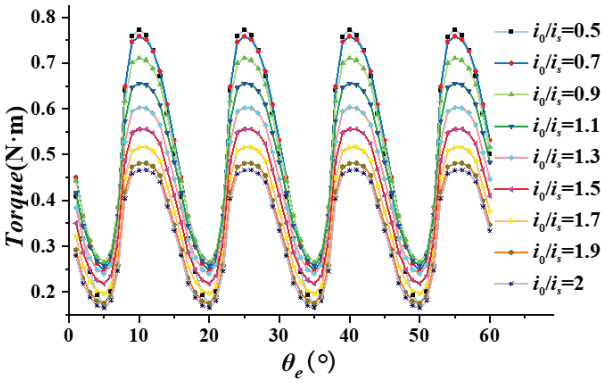

Fig. 14. Transient torque profile under different i_0/i_s.

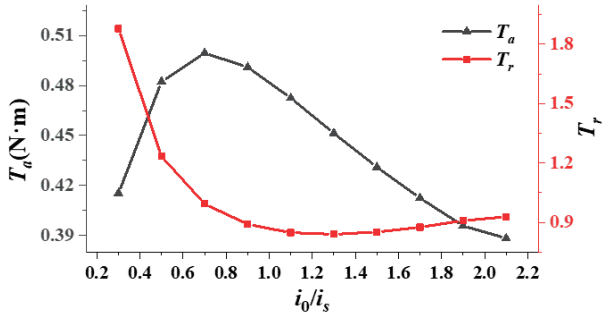

Fig. 15. Torque performance under different i_0/i_s.

As shown in Fig. 14, with the increment of i_0/i_s, maximum torque decreases continuously and minimum torque will first rise and then decrease. As shown in

Fig. 15, average torque increases and then decreases nearly linearly. Torque ripple will first decrease and then increase significantly. Change of i_0/i_s shows a significant effect on torque and average torque. According to the above analysis, the machine achieves maximum output average torque and shows good torque performance at $i_0/i_s = 0.7$. Thus, $i_0/i_s = 0.7$ can be fixed for torque performance optimization.

E. Multi-objective evaluations

Average torque and torque pulsation are selected as evaluation objectives. Key structure parameters, marked in Fig. 5, are determined through multi-objective optimization. Nonlinear optimization problems with two evaluation objectives under multiple constraints can be expressed by

$$F(\mathrm{X}) = k_1 T_a + k_2 \frac{1}{T_r}, \ \mathrm{X} \in K, \tag{5}$$

where k_1 is the weight coefficient of T_a, k_2 is the weight coefficient of T_r, X is the set of all variables, and K is the constraint condition as shown in (6). It should be noted here that both torque ripple and average torque are equally important. However, for switched reluctance motors, torque ripple is a more obvious defect and a more critical aspect for improvement. Therefore, in this paper, $k_1 = 0.6$ and $k_2 = 0.4$ are set. Researchers can flexibly select the weight coefficients they need according to the actual application requirements

$$\begin{cases} g_1(x_s) = \beta_s + \beta_r + \Delta\beta_r < 60^\circ \\ g_2(x_s) = \beta_r + \triangle\beta r \geq \beta_s \\ g_3(x_s) = \beta_s \geq \frac{2\pi}{mN_r} \\ g_4(x_s) = T_r - 1.5 < 0 \\ g_5(x_s) = 0.3 - T_{avg} < 0 \end{cases}. \tag{6}$$

According to the constraints and actual limitations, the optimization range of structural parameters is listed in Table 2. The optimization issue is a 4-factor 4-level problem, which contains a total of 16 groups of dimensions. To evaluate as many parameter combinations as possible, an artificial intelligence (AI) based torque prediction model and optimization process is proposed and explained in detail in the next section.

Table 2: Variable value range

Parameters	Range
β_r	[13,28]
β_s	[17,26]
h_1	[0.3,1.8]
$\triangle\beta_r$	[6,24]

IV. AI-BASED PERFORMANCE PREDICTION MODEL AND OPTIMIZATION

Thanks to AI techniques, complicated mathematic problems can be simplified. To solve the optimization problem, an artificial neural network (ANN) based prediction model is built for fast evaluation, and genetic algorithm (GA) is employed for multi-objective optimization. The overall flow chart is shown in Fig. 16. First, a FEM is built to obtain the average torque and torque ripple of the machine. The corresponding torque profile can be found in section II. Then, in the preliminary division, four variables are assigned equidistant, according to the optimization range, with four level values for each variable. Structural parameters are arranged and combined to establish the sample space. GA is employed to optimize the neural network to achieve an accurate predicting model. Finally, GA is employed again to generate the Pareto frontier solution with a well-constructed and trained ANN model. Solutions are evaluated by (5) and the best solution selected.

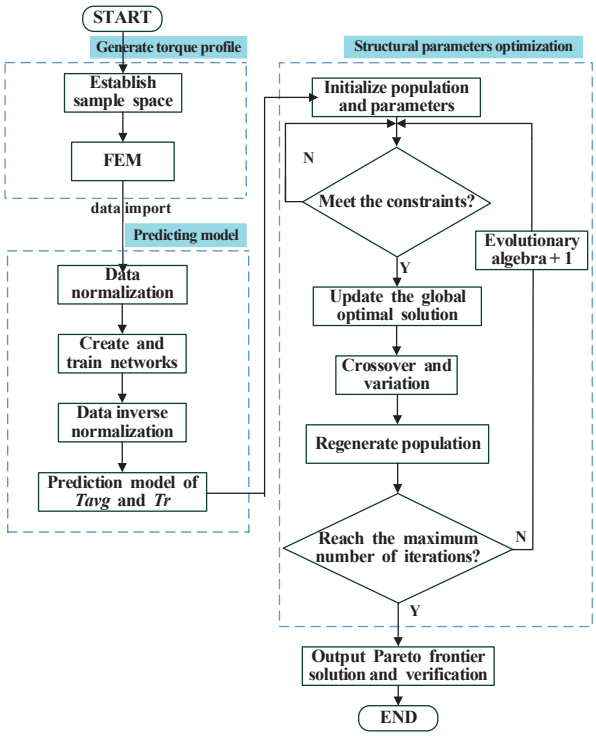

Fig. 16. Flow chart of the structural optimization process.

A. Predicting model

To construct an accurate predicting model, GA is employed to search the parameters of ANN. First, set genetic algebra, population size, and other optimization parameters. Then, set boundaries of the optimization variables according to the size of the training data and the structure of the neural network. Next, initialize the population and set the parameters of the optimization function, generate new offspring, and update chromosomes

through selection, crossover, and variation. The parameters are decoded and then trained to the neural network model. Subsequently, determine whether the average absolute error is larger, and then determine the number of iterations. If the number of iterations has reached the maximum, the training is completed and the optimized neural network model is obtained. The optimization process of the neural network model is shown in Fig. 17.

The 16 sets of orthogonal experimental data described in the previous section were substituted into the neural network optimized by the GA to establish the training and prediction models.

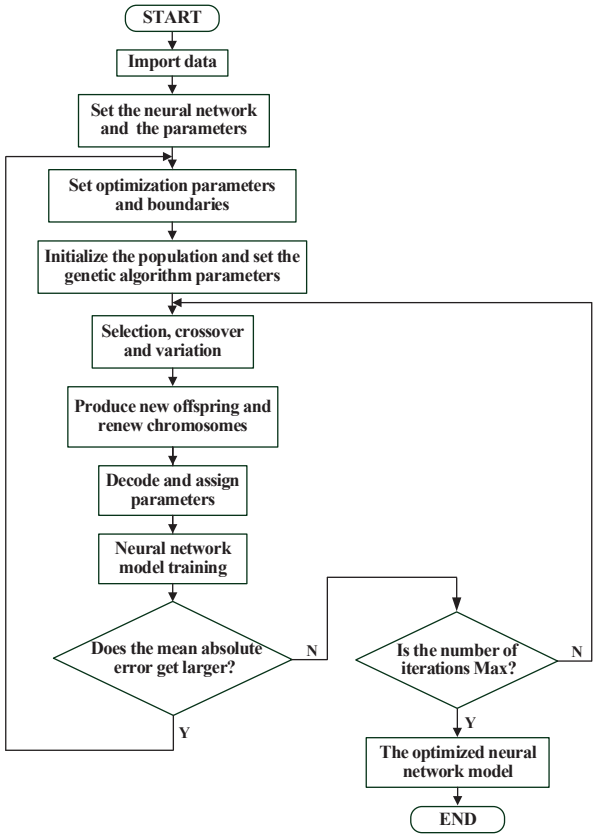

Fig. 17. Flow chart of neural network optimization.

B. Structural parameters optimization

To achieve fast and correct optimization, GA is improved by starting the optimization process with multiple starting points. This contributes to avoiding local optimal solutions and reducing the stagnation phenomenon during the search process. In this paper, the population size is set as 100, the maximum number of iterations is set as 50, the variation rate is set as 0.01, and the number of random starting points is set as 30. The Pareto frontier solution of the multi-objective optimization process is obtained after 50 iterations, and the optimization result is shown in Fig. 18.

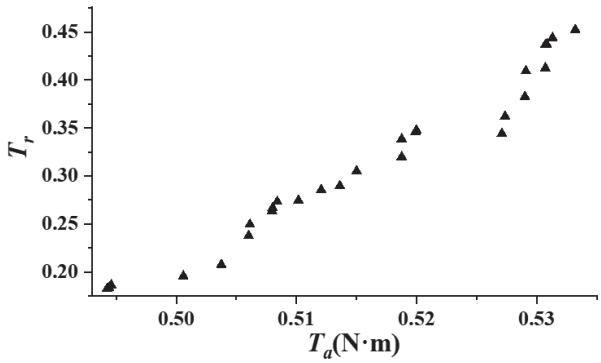

Fig. 18. Pareto frontier solutions of multi-objective optimization.

To avoid the influence of human subjective factors, a fuzzy set, which is generated according to fuzzy theory, is adopted for the final screening of Pareto frontier solutions. Let us define the subordinate function as

$$F = \begin{cases} 1 f_i \} f_i^{\min} \\ \frac{f_i^{\max} - f_i}{f_i^{\max} - f_i^{\min}} f_i^{\min} < f_i < f_i^{\max} \\ 0 f_i \sim f_i^{\max} \end{cases}, \tag{7}$$

where f_i^{max}, f_i^{min}, and f_i is the maximum, minimum, and evaluating values of the ith generations, respectively. For each non-inferior solution k in the Pareto set, the dominating function is defined as

$$\lambda_k = \sum_{i=1}^{N_{\text{obj}}} F_i^k / \left(\sum_{j=1}^{M_{\text{p}}} \sum_{i=1}^{N_{\text{obj}}} F_i^j \right), \tag{8}$$

where M_p is the number of Pareto solutions and N_{obj} is the number of optimization objectives. A higher value of λ_k indicates a better torque performance of structural parameters combination in this solution set. The value of the dominance function of the Pareto frontier solution is shown in Fig. 19.

According to Fig. 19, it can be seen that the 8th individual has the largest value of the dominance function,

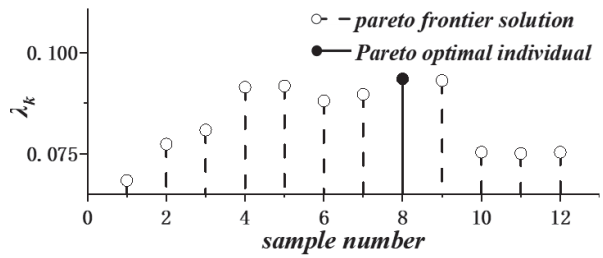

Fig. 19. Dominance function values for each Pareto frontier solution.

Table 3: Motor data before and after optimization

Parameters	Initial Value	Optimized Value
β_s (°)	21	24.2
β_r (°)	23	14.1
h_1 (mm)	0	1.75
$\triangle\beta_r$ (°)	0	20
T_a	0.50	0.52
T_r	99.4%	20.1%

and the corresponding motor parameters for the 8th individual are shown in Table 3.

The optimized data is substituted into the FEA system for verification. In Fig. 20, torque performances before and after optimization are compared. As can be seen in Fig. 20, the average torque of the optimized machine remains approximately the same while the torque ripple is reduced from 99.4% to 20.1%. Comparisons on the two concerned machines are shown in Fig. 21.

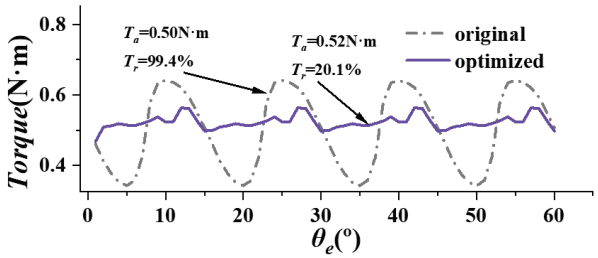

Fig. 20. Comparison of torque performance before and after optimization.

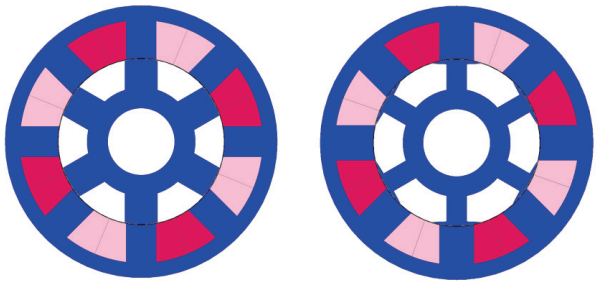

(a) (b)

Fig. 21. Structure (a) before and (b) after optimization.

V. EXPERIMENTAL VERIFICATIONS

To verify the designed and optimized HESRM, an 8/6 HESRM is made, as shown in Fig. 22. The power converter and control system are shown in Fig. 23.

The transient phase current of HESRM is shown in Fig. 24. In Fig. 25, the measured transient torque is compared with simulation results at 500 rpm, correspondingly. According to the comparison result, the transient

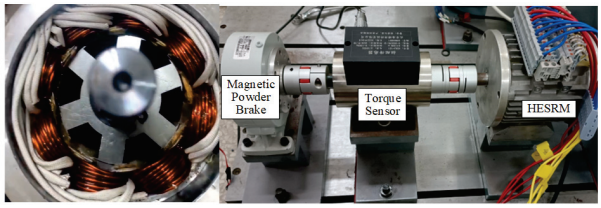

Fig. 22. Photograph of 8/6 HESRM.

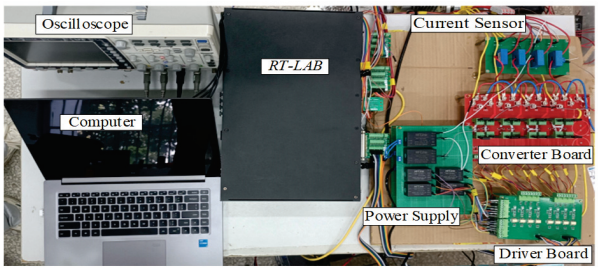

Fig. 23. Photograph of the power converter and control system for HESRM.

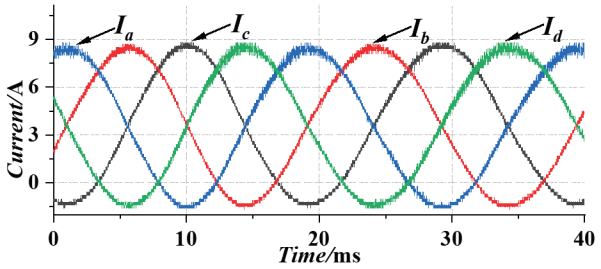

Fig. 24. Measured transient phase current.

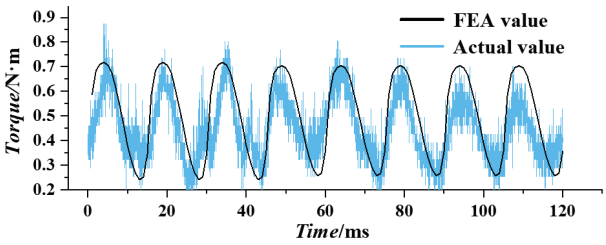

Fig. 25. Comparison of measured and calculated transient torque.

torques of the experimental and simulation results are approximately the same, which verifies the accuracy of the finite element analysis.

In Fig. 26, the effectiveness of the optimization process is verified. As shown in Fig. 26, the average torque of the initial motor is 0.47 Nm, and the torque ripple is 115%. The average torque of the optimized motor is 0.49 Nm, and the torque ripple is reduced

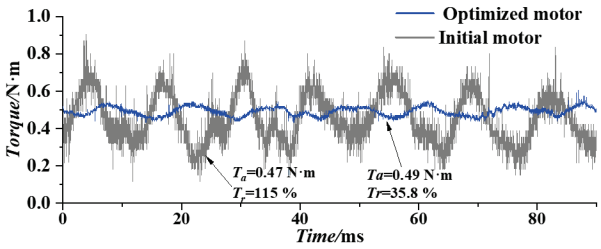

Fig. 26. Verification of the effectiveness of multi-objective optimization.

to 35.8%. The experimental results show that the optimized motor can significantly reduce torque ripple and provide smoother operation under constant average output torque. Thus, the effectiveness of the multi-objective optimization strategy proposed in this paper can be demonstrated.

VI. CONCLUSION

In this paper, a four-phase 8/6 HESRM is designed and optimized. The main contributions of this paper can be concluded as follows.

(i) The structure of SRM is optimized and the pole-shoe is introduced to improve the torque performance of the switched reluctance motor;
(ii) FEM is built and key factors that affect the torque performance are analyzed;
(iii) To achieve a fast and accurate optimization process, an optimization process is proposed. First, a FEM model is built to obtain the torque profile of the machine. Then, a systematic AI-based torque performance model is built for fast torque performance prediction. Finally, GA is introduced to optimize structural parameters with evaluation results generated by the performance predicting model.
(iv) An experimental prototype is manufactured, to verify the proposed machine structure and optimizing process. Experimental results show that the torque ripple of the prototype is reduced by 79.2% at 500 rpm, which verifies the effectiveness of the optimization method.

As a proof-of-concept, the power and torque of the studied SRM is relatively low. However, the proposed machine structure shows good torque performance and the proposed optimization process can be introduced to other motor optimization projects for further industrial and commercial applications.

REFERENCES

[1] E. Sayed, M. Abdalmagid, N. M. Sa'adeh, A. D. Callegaro, C. Goldstei, and A. Emadi, "Review of electric machines in more-/hybrid-/turboelectric aircraft," *IEEE Transactions on Transportation Electrification*, vol. 7, no. 4, pp. 2976-3005, Dec. 2021.

[2] N. Apostolidou and N. Papanikolaou, "Active power control of switched reluctance generator in more electric aircraft," *IEEE Transactions on Vehicle Technologies*, vol. 70, no. 12, pp. 12604-12616, Dec. 2021.

[3] P. J. dos Santos Neto, T. A. dos Santos Barros, E. H. Catata, and E. R. Filho, "Grid-connected SRG interfaced with bidirectional DC-DC converter in WECS," *IEEE Transactions on Energy Conversions*, vol. 36, no. 4, pp. 3261-3270, Dec. 2021.

[4] P. Yang, W. Shi, Y. Qiu, B. Li, and Y. Gan, "Enhanced efficiency of direct-drive switched reluctance motor with reconfigurable winding topology," *IEEE Access*, vol. 10, pp. 62976-62990, 2022.

[5] J. Ye, B. Bilgin, and A. Emadi, "An extended-speed low-ripple torque control of switched reluctance motor drives," *IEEE Transactions on Power Electronics*, vol. 30, no. 3, pp. 1457-1470, Mar. 2015.

[6] M. V. de Paula, T. A. d. S. Barros, H. S. Moreira, E. O. Hancco Catata, M. G. Villalva, and E. R. Filho, "A Dahlin cruise control design method for switched reluctance motors with minimum torque ripple point tracking applied in electric vehicles," *IEEE Transactions on Transportation Electrification*, vol. 7, no. 2, pp. 730-740, June 2021.

[7] P. S. Rekha and T. Vijayakumar, "Torque ripple and noise control of switched reluctance motor using an adaptive fuzzy PI control with the aid of AR algorithm," *International Journal of Power Electronics and Drive Systems*, vol. 17, no. 5, pp. 1239-1251, 2021.

[8] Y. Rao and L. Jing, "Optimization of hybrid excitation segmented rotor switched reluctance motor based on parameter sensitivity," *Journal of Electrical Engineering & Technology*, vol. 17, no. 5, pp. 2899-2907, 2022.

[9] T. Husain, Y. Sozer, and I. Husain, "DC-assisted bipolar switched reluctance machine," *IEEE Transactions on Industry Applications*, vol. 53, no. 3, pp. 2098-2109, 2017.

[10] Q. Ma, X. Cui, and L. Zhang, "Torque ripple and acoustic noise of current modulations of a pseudo-sinusoidal switched reluctance motor," *European Conference on Cognitive Ergonomics*, pp. 1-5, 2016.

[11] A. Dadpour and K. Ansari, "GA based pole shape optimization for sound noise reduction in switched

reluctance motors," *Journal of Soft Computing and Information Technology*, vol. 3, no. 4, 2015.

[12] O. Argiolas, E. Nazeraj, O. Hegazy, J. De Backer, A. Mohammadi, and J. Van Mierlo, "Design optimization of a 12/8 switched reluctance motor for electric and hybrid vehicles," in *2017 Twelfth International Conference on Ecological Vehicles and Renewable Energies (EVER),* Monte Carlo, Monaco, pp. 1-10, 2017.

[13] J. T. Shi, X. Liu, D. Wu, and Z. Q. Zhu, "Influence of stator and rotor pole arcs on electromagnetic torque of variable flux reluctance machines," *IEEE Transactions on Magnetics*, vol. 50, no. 11, pp. 1-4, 2014.

[14] B. Anvari, H. A. Toliyat, and B. Fahimi, "Simultaneous optimization of geometry and firing angles for in-wheel switched reluctance motor drive," *IEEE Transactions on Transportation Electrification*, vol. 4, no. 1, pp. 322-329, 2018.

[15] X. Sun, B. Wan, and G Lei, "Multi-objective and multiphysics design optimization of a switched reluctance motor for electric vehicle applications," *IEEE Transactions on Energy Conversion*, vol. 36, no. 4, pp. 3294-3304, 2021.

Qing Wang received the B.S. degree in automation from Northeastern University, Shenyang, China, in 2011, and the Ph.D. degree in electrical engineering from China University of Mining and Technology, Xuzhou, China, in 2017. In 2018, he became a Lecturer with the School of Information Engineering, Nanchang University, Nanchang, China, where he has been an Associate Professor since 2023. His research interests include electric vehicles, electrical motor drives, renewable energy generations, and micro-grids.

Jiangtao Hu received the B.S. degree in electrical engineering from Jiangxi University of Science and Technology, Ganzhou, China, in 2023. He is currently working toward the M.S. degree at the School of Information Engineering, Nanchang University. His research interests include power electronics and motor control.

Jiaxin Ding received the B.S. degree in Mechanical from Nanchang University, Nanchang, China, in 2020, and is currently pursuing the M.S. degree in Electrical Engineering at the School of Information Engineering, Nanchang University. His research interests include motor design and control.

Fengshuo Liu received the B.S. degree in electrical engineering from Henan Polytechnic University, Jiaozuo, China, in 2021. He is currently working toward the M.S. degree at the School of Information Engineering, Nanchang University, Nanchang, China. His research interests include switched reluctance motor and its control.

Yumeng Zhu received the B.S. degree in electrical engineering from East China Jiaotong University, Nanchang, China, in 2023. He is currently working toward the M.S. degree at the School of Information Engineering, Nanchang University. His research interests include power electronics and motor control.

Yongqing Deng received the B.S. and Ph.D. degrees from the School of Electrical Engineering, Wuhan University, Wuhan, China, in 2016 and 2021, respectively. He is currently an Associate Professor with the Information Engineering School of Nanchang University. His main research interests include high voltage and insulation technology, numerical analysis, and engineering application of electromagnetic field.

Design of Gravity Energy Storage Switched Reluctance Machine Based on Artificial Intelligence Optimization Algorithm

Wenju Yan[1,2], Xinzhu Sun[1], Jun Xin[1], Hao Chen[1], Yang Wang[1], Vuong Dang Quoc[3], and Thanh Nguyen Vu[3]

[1]School of Electrical Engineering, China University of Mining and Technology
Xuzhou 221116, China
6288@cumt.edu.cn, ts23230199p31@cumt.edu.cn, ts23230161p31ld@cumt.edu.cn, hchen@cumt.edu.cn, ts23230200p31@cumt.edu.cn

[2]Shenzhen Research Institute, China University of Mining and Technology
Shenzhen 518057, China

[3]School of Electrical Engineering, Hanoi University of Science and Technology
Hanoi, Vietnam
vuong.dangquoc@hust.edu.vn, thanh.nguyenvu@hust.edu.vn

***Abstract* –** To address the operational characteristics of gravity energy storage systems, this paper proposes an optimized design method for a switched reluctance machine (SRM) suitable for a gravity energy storage system. A novel 12/8 salient stator tooth structure is introduced to enhance performance in both energy storage and power generation modes. Four key optimization objectives are defined: average torque and torque ripple in the energy storage state, as well as generation power and efficiency in the power generation state. The influence of structural parameters on these optimization objectives is systematically analyzed and a multi-objective optimization of the structural parameters is conducted by the Multi-Objective Grey Wolf Optimizer (MOGWO) algorithm. Finite element analysis (FEA) is performed to evaluate the electromagnetic characteristics of the optimized design. The results demonstrate that the proposed SRM achieves superior performance compared to the traditional 12/8 SRM, making it well-suited for gravity energy storage applications.

***Index Terms* –** Gravity energy storage, motor and generator, multi-objective optimization, switched reluctance machine.

I. INTRODUCTION

Energy storage technology plays a pivotal role in the renewable energy sector, as it helps address the intermittency and instability of renewable energy sources while enhancing energy utilization efficiency. Compared to other energy storage methods, gravity energy storage offers significant advantages, including site flexibility, environmental friendliness, high storage capacity, long cycle life, zero self-discharge rate, deep discharge depth, fast response time, and high efficiency, making it a promising form of green energy storage. According to reports from international sources, the main configurations of gravity energy storage systems currently include piston-based gravity energy storage, mine shaft suspended gravity storage, tower crane-based concrete block energy storage, and mountain railway gravity energy storage [1–3]. Among these, mine shaft suspended gravity storage stands out for its technical advantage of repurposing abandoned resources while addressing energy supply-demand imbalances, offering broad application prospects.

The gravity energy storage motor is the core component responsible for the conversion of electrical energy and gravitational potential energy. In motoring or energy storage state, it stores gravitational potential energy and, in generating or the power generation state, it releases gravitational potential energy. Its performance directly determines the overall efficiency of the energy storage system. Compared to conventional industrial motors, energy storage motors face stricter technical requirements, such as high power and torque densities, maintaining high efficiency over a wide operating range, delivering high torque at low speeds, frequent heavy-load starts, high reliability, and excellent performance in both motoring and generating states. As a rare-earth-free motor technology [4–7], switched reluctance motors (SRMs) are particularly well-suited for applications with high-inertia operating conditions involving gravity energy storage systems. Since SRMs have the advantages

Submitted On: December 26, 2024
Accepted On: May 29, 2025

https://doi.org/10.13052/2025.ACES.J.400904

of high starting torque, low starting current, the ability to handle frequent heavy-load starts, a broad high-efficiency range, and inherent structural reliability, this paper focuses on applying SRMs in gravity energy storage.

To improve the performance of conventional SRMs, researchers frequently optimize motor structures, materials, and geometric parameters [8–11]. Specifically, substantial progress has been made in enhancing SRMs through innovative designs of stator and rotor structures. A 6/4-pole three-phase SRM featuring uniquely skew-angle rotor poles combined with sinusoidal torque-sharing control was proposed and simulated in [12]. Prasad et al. [13] introduced a linear SRM tailored for high-speed transportation systems with dual teeth on each stator pole to enhance thrust and analyzed its force ripple reduction effectiveness with finite elements. Li et al. [14] developed an axial dual-rotor segmented SRM with a new rotor profile, where rotor segment geometry was optimized to boost performance. A hollow-tooth rotor structure for a 6/2-pole SRM was designed in [15], effectively extending its acceleration range. Ma et al. [16] improved SRM vibration and noise issues by introducing rectangular slots at the stator tooth tips and optimizing the slot geometry to reduce radial forces. A magnetic decoupled dual-stator SRM with U-shaped segmented structures in both inner and outer stators was proposed in [17], and prototype experimental results confirmed the design's feasibility and performance benefits. Upadhyay and Ragavan K. [18] proposed an asymmetric stator pole design with slanted pole tips to achieve self-starting capability in both rotational directions. Diao et al. [19] designed and optimized a new SRM with different stator yoke widths to reduce saturation and unnecessary cores and improve torque density.

To tackle the challenges of low power density and efficiency in traditional SRMs, which do not consider both motoring and generating performance when designing, this paper enhances the comprehensive performance of the gravity energy storage SRM by modifying tooth structure and proposing optimization metrics and methods that simultaneously address energy storage and power generation stage. In section II, the novel gravity energy storage system and the traditional SRM initial design are introduced. The design of novel SRM suitable for gravity energy storage is presented in section III. In section IV, static electromagnetic characteristic and dynamic characteristic under energy storage stage and power generation stage are carried out. This paper is concluded with section V.

II. NOVEL GRAVITY ENERGY STORAGE SYSTEM AND MACHINE INITIAL DESIGN

The structure of the energy storage system proposed in this study is shown in Fig. 1. A single mine roadway

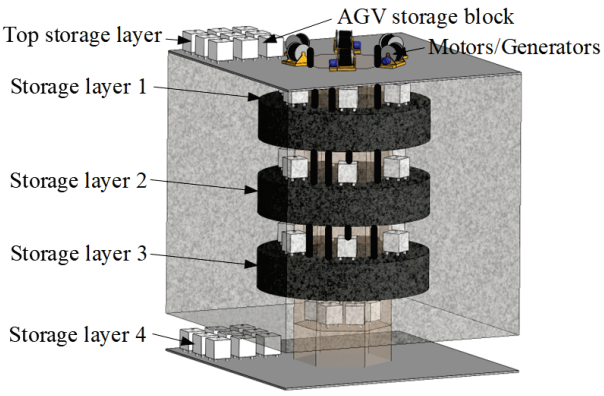

Fig. 1. Structure diagram of energy storage system for multi-energy storage motor in single well.

incorporates multiple energy storage motors, enabling coordinated control of these motors to ensure smooth and efficient operation of the motoring and generating modes. Throughout the operation of the mine track system, the speed trajectory of individual motors varies, and the speeds of the motors within a single roadway need to be coordinated to collectively achieve peak shaving, rapid response, and grid-friendly interaction functionalities for the gravity energy storage system. Figure 2 gives the storage block force analysis diagram under different stages. In energy storage stage, the force F_M is analyzed as

$$F_M = mg + f, \tag{1}$$

where m is the mass of the block, g is the gravitational acceleration and f is the friction force during its ascent.

The power of the motor P_{up} is

$$P_{up} = F_M v_{up} = (mg + f) v_{up}, \tag{2}$$

where v_{up} is the ascent speed.

In power generation stage, the reverse force F_g is

$$F_g = mg - f. \tag{3}$$

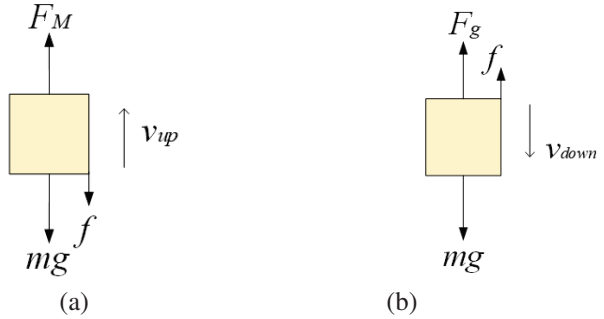

Fig. 2. Storage block force analysis diagram under different stages: (a) energy storage stage and (b) power generation stage.

The power of the generator P_g is

$$P_g = F_g v_{down}, \tag{4}$$

where v_{down} is the descent speed.

Based on the operating speed and power requirements in the motoring stage and the operating speed and power output in the generating stage, the design requirements for the motor can be determined. For this study, considering the large size and power of actual gravity energy storage systems, a prototype motor is designed. The motor has a rated power of 1.8 kW, a rated voltage of 96 V, and a rated speed of 1500 r/min. The initial dimensions of a conventional 12/8 SRM are calculated and summarized in Table 1, and the relevant structural parameters are illustrated in Fig. 3.

Table 1: Specifications range of SRM

Parameters	Symbol	Values
Stator outer diameter	D_{so}	180.0 mm
Stator pole length	p_s	20-30 mm
Stator yoke length	y_s	9.9-19.9 mm
Stator pole angle	B_s	10.0-18.0°
Rotor outer diameter	D_{ro}	99.0 mm
Rotor inner diameter	D_{ri}	30.0-50.0 mm
Rotor pole length	p_r	14.0-20.0 mm
Rotor yoke length	y_r	9.5-15.5 mm
Rotor pole angle	B_r	9.0-17.0°
Air gap length	g	0.6 mm
Number of turns per slot	N	12-16
Stack length	L	150.0 mm

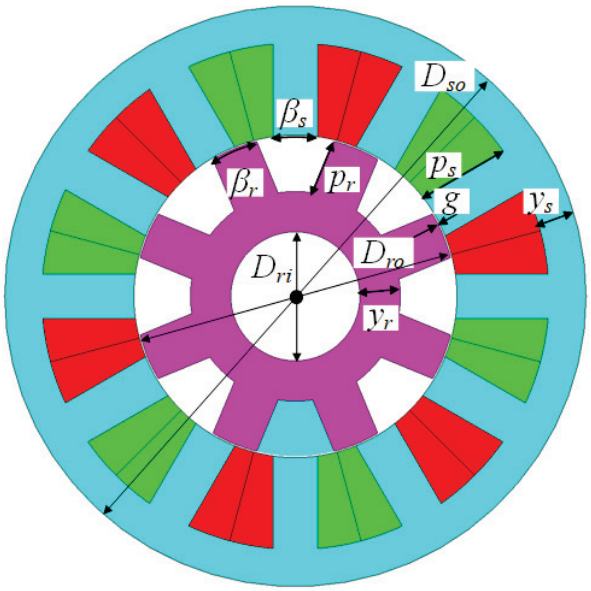

Fig. 3. Structure parameter diagram of three-phase 12/8 switched reluctance machine.

III. DESIGN OF NOVEL SWITCHED RELUCTANCE MACHINE SUITABLE FOR GRAVITY ENERGY STORAGE

A. Structure of the salient-pole SRM suitable for gravity energy storage

Assuming that the gravity energy storage SRM operates in energy storage stage during forward rotation, the rising region of the motor's inductance is utilized, as shown in Fig. 4 (a). Conversely, during reverse rotation, the motor operates in the power generation stage, utilizing the falling region of the inductance, as illustrated in Fig. 4 (b). The inductance L is calculated as

$$L = \frac{\Psi}{i}, \tag{5}$$

where ψ is the flux linkage and i is the current.

From Fig. 4, it can be observed that in the motoring state, the inductance in the turn-on interval should be minimized, while it should be maximized in the turn-off interval to produce a larger electromagnetic torque. In the generating state, the inductance during the turn-on interval should also be as low as possible to quickly establish the excitation current, while it should be as

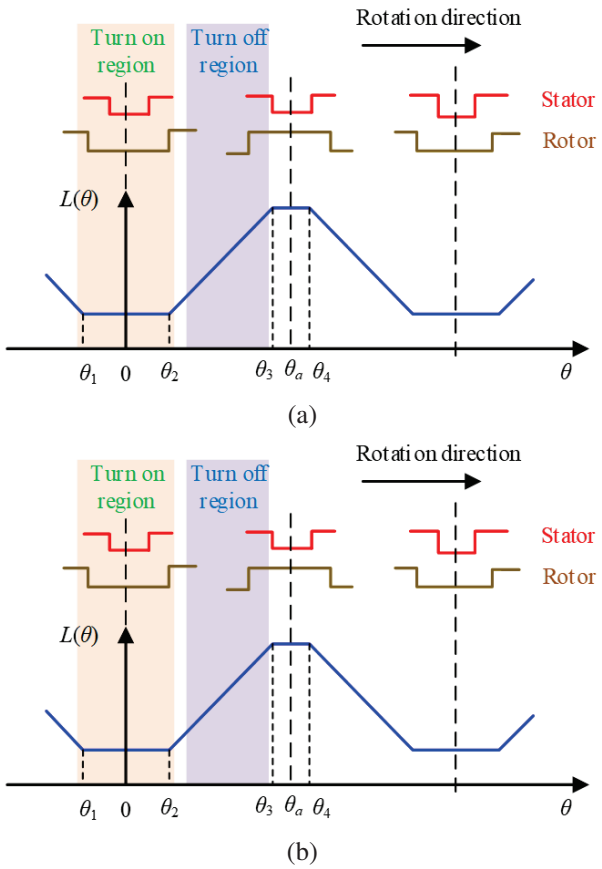

Fig. 4. The relationship between the turn-on angle, the turn-off angle and the inductance under different stages: (a) energy storage stage and (b) power generation stage.

high as possible during the turn-off interval to slow the current's decline, thereby generating more power. Based on the above analysis, the stator tooth shape can be optimized to modify the variation characteristics of the inductance with position, meeting the performance requirements of the motor in both motoring and generating states. Therefore, a novel gravity energy storage SRM is proposed in this paper, in which the three-phase 12/8 configuration is shown in Fig. 5 and the stator features a salient-pole design.

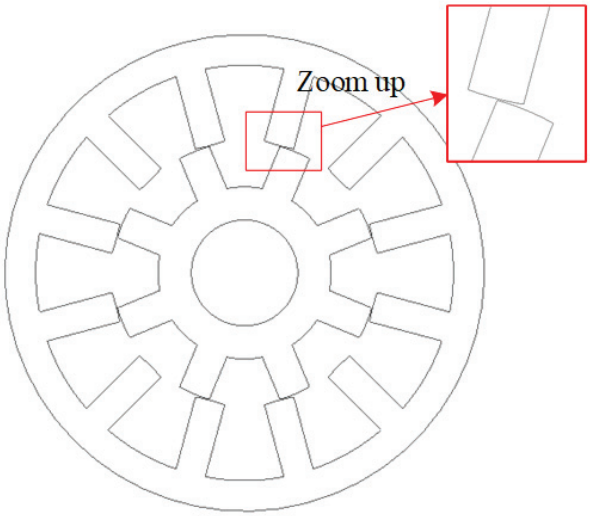

Fig. 5. Structure diagram of the new gravity energy storage switched reluctance machine.

B. Multi-objective optimal design suitable for gravity energy storage SRM

In the energy storage stage, the system must provide sufficient torque to lift the weights with minimal torque ripple to reduce mechanical impact and enhance the reliability. In the power generation phase, it must achieve high energy conversion efficiency and sufficient generating power. To meet the requirements of a gravity energy storage system in both motoring and generating stages, the average torque T_{avg} and torque ripple T_r are selected for the energy storage state, and the power generation P_o and power generation efficiency η_g are selected for the power generation state as the optimization objectives for the design of the gravity energy storage SRM. The torque ripple T_r could be defined as

$$T_r = \frac{T_{\max} - T_{\min}}{T_{\text{avg}}}, \tag{6}$$

where $T_{\max}$ and $T_{\min}$ are the maximum and minimum torque respectively. The generating efficiency η_g could be obtained as

$$\eta_g = \frac{P_o}{P_{\text{mech}}}, \tag{7}$$

where P_{mech} is the input mechanical power in the power generation state.

To meet these dual performance demands, besides fixed values for air gap length g, stator outer diameter D_{so}, and rotor outer diameter D_{ro}, the design optimizes other parameters including stator pole angle B_s, rotor pole angle B_r, stator pole length p_s, rotor pole length p_r and rotor inner diameter D_{ri}. An optimization process combining sensitivity analysis (SA), response surface (RS) modeling, and a Multi-Objective Grey Wolf Optimization (MOGWO) algorithm is proposed to address the multi-objective optimization problem of the gravity energy storage SRM.

The SA assesses the impact of each optimization parameter on the objective functions, revealing the parameters with the greatest contribution to system performance. A sensitivity index is used to quantify the influence of design variables on optimization objectives, expressed as

$$S_{n_i} = \left.\frac{\partial f}{\partial z_i}\right|_{\text{NOP}} \frac{z_i}{f} \approx \frac{\Delta f / f}{z_i / z_i}, \tag{8}$$

where f is the optimization objective function and z_i represents the optimization variable.

Weight coefficients are introduced to evaluate four sensitivity indices comprehensively and optimize performance for both motoring and generating states. A comprehensive sensitivity index $G(n_i)$ is defined as

$$G(n_i) = \omega_1 \left|S_{T_{\text{avg}}}\right| + \omega_2 \left|S_{T_r}\right| + \omega_3 \left|S_{P_o}\right| + \omega_4 \left|S_{\eta_g}\right|, \tag{9}$$

where $S_{T\text{avg}}$, S_{Tr}, S_{Po}, and $S_{\eta g}$ are sensitivity indices for T_{avg}, T_r, P_o, and η_g, respectively. The weight coefficients ω_1, ω_2, ω_3, and ω_4 satisfy $\omega_1+\omega_2+\omega_3+\omega_4=1$, with all weights set to 0.25 in this paper.

Through single-parameter scanning finite element analysis (FEA) of the optimization parameters, the absolute values of sensitivity indices and the comprehensive sensitivity indices for the four optimization objectives are obtained and shown in Table 2. To visually represent the sensitivity of each variable, the data is displayed in Fig. 6. The greater the absolute value of the sensitivity of a design variable, the more significant its impact on the optimization objectives. From Table 2 and Fig. 6, it can be observed that B_s and B_r are the design variables with comprehensive sensitivity indices exceeding 0.25, classified as significant variables since their greatest impact is on the performance of the SRM. The other three parameters, p_s, p_r, and D_{ri}, have smaller sensitivity indices, classified as insignificant variables. Local SA is limited to the changes of local variables and does not apply to the global range. Significant variables require further optimization, while insignificant variables can be fixed at their optimal values by a single-parameter scanning method. Consequently, the insignificant variables are set as constants: p_s is 24.6 mm, p_r is 19 mm,and D_{ri}

Table 2: Sensitivity indices of design parameters

Variables	$\|S_{Tavg}\|$	$\|S_{Tr}\|$	$\|S_{Po}\|$	$\|S_{\eta g}\|$	$G(n_i)$
B_r	0.1894	0.4950	0.2554	0.1834	0.2808
B_s	0.2108	0.8580	0.2722	0.0756	0.3541
p_r	0.0103	0.0171	0.0207	0.0014	0.0124
p_s	0.0874	0.0385	0.0958	0.0476	0.0673
D_{ri}	0.0002	0.0001	0.0010	0.0008	0.0005

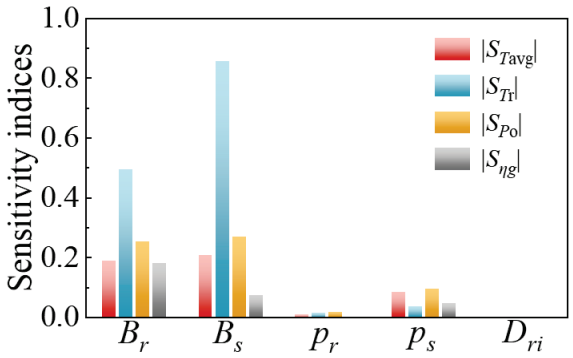

Fig. 6. Sensitivity indices of variables to the optimization objective.

is 35 mm, which will not be treated as design variables in the subsequent optimization process.

RS analysis, by constructing mathematical models, effectively reduces the number of experiments, quantitatively evaluates the interactions between design variables and reveals nonlinear relationships, which can be used in motor parameter optimization to predict objective function values, optimize parameter combinations, and significantly improve optimization efficiency and accuracy. For the two significant variables of the SRM, the Central Composite Design (CCD) experimental method is employed. CCD enhances the ability to capture interaction effects between parameters within the design space by adding center points and axial points, providing more precise model predictions and efficiently fits the RS model with fewer experimental runs. To obtain the optimal values of the two significant variables B_s and B_r, a CCD RS analysis is applied and its variable levels are shown in Table 3.

Table 3: CCD response surface analysis variable levels

Variables	Levels				
	-1.414	**-1**	**0**	**1**	**1.414**
B_r (deg)	13.586	14.0	15.0	16.0	16.414
B_s (deg)	12.586	13.0	14.0	15.0	15.414

The CCD experimental scheme included 13 different combinations. The motor output performance conducted by FEA corresponding to each experimental point is recorded. Using Design-Expert, the simulation results of the sampled points are analyzed and a quadratic regression function is fitted for the design variables and the four optimization objectives, resulting in the RS models shown in Fig. 7. The P-values of all four CCD RS experiments are less than 0.05, indicating that the two variables have a notable impact on the optimization objectives. Furthermore, the multiple correlation coefficients R^2 are all greater than 0.98. The closer the R^2 value is to 1, the better the model fits the motor performance. These results demonstrate that the RS is well fitted and the experiments are reasonable.

The MOGWO algorithm is an evolutionary algorithm inspired by the hunting behavior of grey wolf packs. It simultaneously considers multiple objective functions and introduces an external population, known as the Archive, to store non-dominated optimal solutions while eliminating numerous similar solutions. A leader selection strategy is used in MOGWO, where leaders are chosen from the Archive for guiding the hunting process, ultimately converging to a set of optimal Pareto front solutions. In this paper, MOGWO is used to further optimize significant variables to achieve optimal SRM performance, with the initial population and Archive population sizes set to 100 and iterations set to 50.

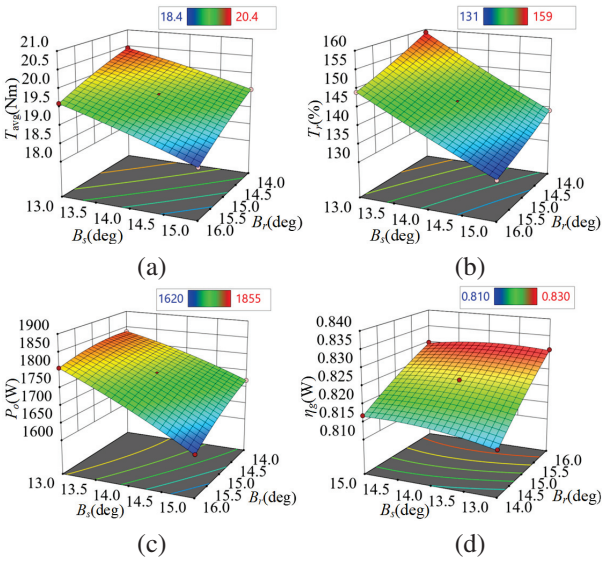

Fig. 7. Response surface of (a) Tavg, (b) Tr, (c) Po, and (d) ηg.

The Pareto solution set obtained is shown in Fig. 8, where Fig. 8 (a) illustrates the optimal solution space distribution based on T_{avg}, P_o, and η_g, and Fig. 8 (b) shows the distribution based on T_{avg} ,T_r, and η_g. After filtering out some unreasonable points, three superior solutions are selected from the set based on the performance requirements of the gravity energy storage system, and

the performance of three optimized points is listed in Table 4. A comparison reveals that although Design 1 has the lowest torque ripple, its power output and efficiency in the generating mode are relatively low. Designs 2 and 3 exhibit better overall motor performance. Ultimately, Design 2 with superior performance is chosen as the optimal size design. The values of the two significant variables in the optimal design are B_r as 15.27° and B_s as 12.84°.

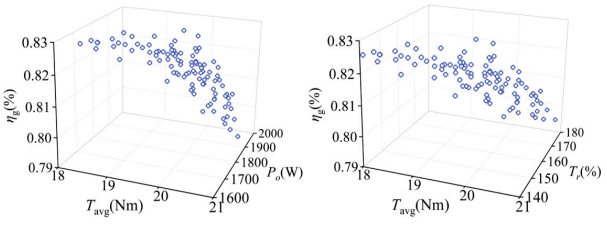

Fig. 8. The Pareto fronts obtained by MOGWO of optimization objectives: (a) T_{avg}, P_o, and η_g and (b) T_{avg}, T_r, and η_g.

Table 4: SRM performance of selected optimal designs

Variables	Initial Design	Design 1	Design 2	Design 3
B_r (deg)	14.0	13.52	15.27	14.79
B_s (deg)	13.0	14.11	12.84	13.04
T_{avg} (Nm)	20.247	20.431	20.419	20.416
T_r (%)	165.09	149.48	153.07	153.56
P_o (W)	1835.55	1853.96	1904.44	1900.04
η_g (%)	81.290	81.710	82.996	82.595

IV. SIMULATION RESULT

A. Static characteristic analysis

Based on the optimized dimensions obtained through multi-objective optimization, a finite element model of the SRM is constructed and its electromagnetic performance is analyzed. Figure 9 illustrates the magnetic density distribution at the unaligned and aligned positions when a 30 A current is applied to the A-phase winding. At the unaligned position, the magnetic density of the stator and rotor poles is approximately 0.15 T, and at the minimum air gap of the stator salient teeth the flux value decreases to 0.05 T, confirming the flux cancellation effect at the unaligned position. At the aligned position, the stator and rotor poles are aligned, with a flux density of about 1.2 T. At the stator's minimum air gap, the flux value slightly increases to around 1.4 T.

The static electromagnetic force curves for the A-phase as the current increases from 10 A to 100 A are presented in Fig. 10 (a). Across different current levels, the trend of static electromagnetic force varying

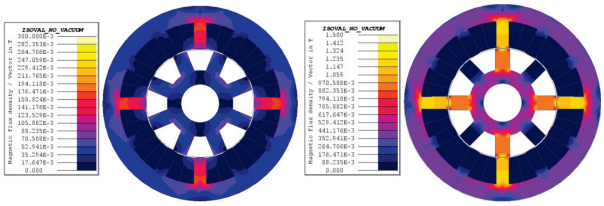

Fig. 9. Magnetic density distribution diagram of the SRM: (a) unaligned position and (b) aligned position.

with the rotor position remains consistent, and the force increases with higher current. Figure 10 (b) depicts the self-inductance curves of the A-phase winding as the current rises from 10 A to 100 A. Due to magnetic saturation, the inductance decreases with increasing current at aligned positions, and the minimum inductance is almost equal at the unaligned position. At 100 A, the maximum inductance is 1.25 mH and the minimum inductance is 0.38 mH. At 10 A, the maximum inductance is 3.08 mH, while the minimum inductance is 0.38 mH, resulting in a non-saturation maximum-to-minimum inductance ratio of 8.11.

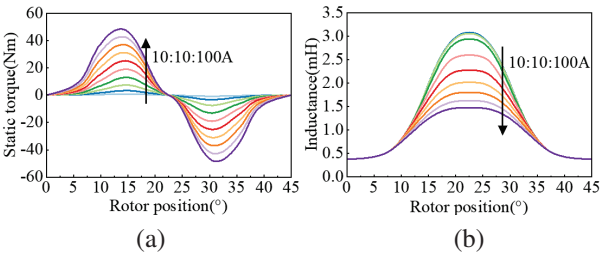

Fig. 10. Static characteristic of SRM: (a) torque characteristic and (b) inductance characteristic.

B. Dynamic characteristic analysis

1. In the energy storage stage

To verify the dynamic performance of the SRM, simulations are conducted by MATLAB/Simulink. In the energy storage stage, the motor speed is set to 1500 r/min and the conduction angle is set to 0-15°. The motoring current and torque waveforms of angle position control are given in Fig. 11. The maximum torque is 31.09 Nm, the minimum torque is 5.58 Nm, the average torque is 19.41 Nm and torque ripple is 131.43%.

2. In the power generation stage

The generating current and torque waveforms of angle position control are given in Fig. 12. The speed is set to 1500 r/min, and the generator is controlled to turn-on at 25° and turn-off at 35°. From Fig. 12, the average torque of the generator is 15.15 Nm. The generating power is the difference between the power of the power

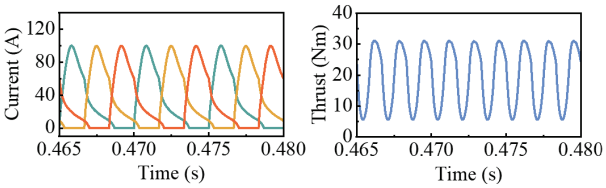

Fig. 11. Current and torque waveforms of the motor in electric state.

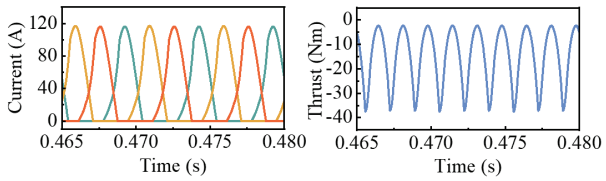

Fig. 12. Current and torque waveforms of the motor in generate state.

generation phase and the power of the excitation phase, which yields a generating power of 2075 W and a power generation efficiency of 87.2%.

C. Comparison with traditional SRM

To verify the superiority of the proposed salient stator tooth 12/8 structure SRM, a comparison is made with the traditional structure SRM. Except for the different tooth shape of the stator, the remaining dimensions of the traditional SRM are identical to those of the proposed SRM with the optimal structure.

The inductance characteristics of the traditional SRM are tested. When the phase A current is 10 A, the maximum inductance is 2.42 mH, the minimum inductance is 0.38 mH, and the maximum-minimum inductance ratio is 6.37, while the maximum-minimum inductance ratio of the proposed SRM under the same conditions is 8.11. Thus, the proposed SRM has a larger maximum to minimum inductance ratio under unsaturated currents.

Comparison of the performance of the two motors is given in Table 5. It can be seen that the average torque and power generation of the salient stator tooth structure SRM are significantly improved compared to the traditional SRM, which confirms the superiority of employing the proposed novel structure SRM as an energy storage machine.

Table 5: Performance comparison of two SRMs

Performance	Traditional SRM	Proposed SRM
T_{avg} (Nm)	18.339	20.419
T_r (%)	154.186	153.07
P_o (W)	1641.927	1904.440
η_g (%)	81.711	82.996

V. CONCLUSION

In this paper, a salient stator tooth 12/8 structure SRM that can realize high performance is designed for gravity energy storage. Four design evaluation indicators are proposed, which include average torque and torque ripple under energy storage conditions, as well as power generation efficiency and power generation capacity under power generation conditions. A multi-objective optimization design is then conducted, improving the performance compared to the initial design. The static electromagnetic and dynamic characteristics under energy storage stage and power generation stage are carried out. The simulation results show that the novel machine structure and optimization design method proposed in this paper are effective, which has certain reference significance for the design of energy storage machine.

ACKNOWLEDGMENT

This work was supported in part by the Guangdong Basic and Applied Basic Research Foundation under Grant 2025A1515011254, the Xuzhou Science and Technology Innovation Basic Research Project under Grant KC23021, China Postdoctoral Foundation Project under Grant 2023M733749, 2022 China-CEEC University Joint Education Program (2022200), 2023 China-CEEC University Joint Education Program (2023304).

REFERENCES

[1] F. Li, J. Xie, Y. Fan, and J. Qiu, "Potential of different forms of gravity energy storage," *Sustainable Energy Technol. Assess.*, vol. 64, pp. 1-11, Mar. 2024.

[2] W. Tong, Z. Lu, J. D. Hunt, H. Zhao, M. Han, and G. Zhao, "Energy management system for modular-gravity energy storage plant," *J. Energy Storage*, vol. 74, pp. 1-14, Oct. 2023.

[3] P. Kropotin, O. Penkov, and I. Marchuk, "On using unstabilized compressed earth blocks as suspended weights in gravity energy storages," *J. Energy Storage*, vol. 72, pp. 1-10, Aug. 2023.

[4] L. Ge, N. Du, J. Song, J. Zhang, Z. Fan, D. Zhang, and S. Song, "Advanced technology of switched reluctance machines in more electric aircraft: A review," *IEEE Trans. Power Electron.*, vol. 40, no. 1, pp. 195-216, Jan. 2025.

[5] X. Guo, S. Zeng, R. Zhong, and W. Hua, "High-precision injection current sampling scheme for direct drive low-speed position sensorless control of switched reluctance machine," *IEEE Trans. Ind. Electron.*, vol. 71, no. 11, pp. 13754-13765, Nov. 2024.

[6] H. Wang, Y. Xue, J. Du, and H. Li, "Design and evaluation of modular stator hybrid-excitation

switched reluctance motor for torque performance improvement," *IEEE Trans. Ind. Electron.*, vol. 71, no. 10, pp. 12814-12823, Oct. 2024.

[7] A. Madanimohammadi, M. Abbasian, M. Delshad, and H. Saghafi, "Electromagnetic and thermal analysis of a 6/4 induction switched reluctance machine for electric vehicle application," *Applied Computational Electromagnetics Society (ACES) Journal*, vol. 38, no. 05, pp. 361-370, May 2023.

[8] X. Sun, K. Diao, G. Lei, Y. Guo, and J. Zhu, "Study on segmented-rotor switched reluctance motors with different rotor pole numbers for BSG system of hybrid electric vehicles," *IEEE Trans. Veh. Technol.*, vol. 68, no. 6, pp. 5537-5547, June 2019.

[9] W. Ding, H. Bian, K. Song, Y. Li, and K. Li, "Enhancement of a 12/4 hybrid-excitation switched reluctance machine with both segmented-stator and -rotor," *IEEE Trans. Ind. Electron.*, vol. 68, no. 10, pp. 9229-9241, Oct. 2021.

[10] F. Yu, H. Chen, W. Yan, V. F. Pires, J. F. Martins, P. Rafajdus, A. Musolino, L. Sani, M. P. Aguirre, M. A. Saqib, M. Orabi, and X. Li, "Design and multi-objective optimization of a double-stator axial flux SRM with full-pitch winding configuration," *IEEE Trans. Transp. Electrif.*, vol. 8, no. 4, pp. 4348-4364, Dec. 2022.

[11] L. Liu, Y. Huang, M. Zhao, and Y. Ruan, "Parametric modeling and optimization of switched reluctance motor for EV," *Applied Computational Electromagnetics Society (ACES) Journal*, vol. 37, no. 09, pp. 948-958, Sep. 2022.

[12] D. Marcsa and M. Kuczmann, "Design and control for torque ripple reduction of a 3-phase switched reluctance motor," *Comput. Math. Appl.*, vol. 74, no. 1, pp. 89-95, July 2017.

[13] N. Prasad, S. Jain, and S. Gupta, "Comparative analysis of new improved force split-teeth linear switched reluctance motor for high-speed transit systems," *Sadhana-Academy Proc. Eng. Sci.*, vol. 45, no. 1, pp. 1-13, June 2020.

[14] Q. Li, W. Sun, L. Sun, and L. Li, "Rotor segment split and its optimization of axial-field dual-rotor segmented switched reluctance machine," *Energy Rep.*, vol. 6, no. S9, pp. 1144-1150, Dec. 2020.

[15] G. Guidkaya, E. D. K. Fankem, and J. Y. Effa, "A new rotor shape design of 6/2 switched reluctance motor: Comparative analysis of its chaotic behavior with other structures," *J. Electr. Eng. Technol.*, vol. 16, no. 1, pp. 309-320, Oct. 2020.

[16] H. Ma, C. Huang, X. Liu, W. Shi, and W. Liu, "The effect of a single-sided pole shoe and slot on reducing torque ripple in a switched reluctance motor," *Concurrency Comput. Pract. Exper.*, vol. 32, no. 19, p. e5810, May 2020.

[17] W. Yan, H. Chen, S. Liao, Y. Liu, and H. Cheng, "Design of a low-ripple double-modular-stator switched reluctance machine for electric vehicle applications," *IEEE Trans. Transp. Electrif.*, vol. 7, no. 3, pp. 1349-1358, Sep. 2021.

[18] P. Upadhyay and Ragavan K., "Design of two-phase 4/6 switched reluctance motor for bidirectional starting in washing machine application," *IEEE Trans. Ind. Appl.*, vol. 59, no. 2, pp. 1519-1529, Mar. 2023.

[19] K. Diao, G. Bramerdorfer, X. Sun, Z. Yang, and S. Han, "Multiobjective design optimization of a novel switched reluctance motor with unequal alternating stator yoke segments," *IEEE Trans. Transp. Electrif.*, vol. 9, no. 1, pp. 512-521, Mar. 2023.

Wenju Yan (M'19) received the B.S. degree in Electrical Engineering and Automation from the China University of Mining and Technology, Xuzhou, China, in 2013. He received the Ph.D. degree in electrical engineering from the China University of Mining and Technology, Xuzhou, China, in 2018. Since 2018, he has been with China University of Mining and Technology, where he is currently an associate professor in the School of Electrical Engineering. His current research interests include electric vehicles, electric traction, iron loss analysis, and motor design.

Xinzhu Sun received the B.S degree from of Electrical Engineering, Sichuan University, Chengdu, China, in 2023, She is currently working towards the M.S. degree in electrical engineering from the China University of Mining and Technology, Xuzhou, China. Her research interests include integrated drive systems for electric vehicles and energy storage.

Jun Xin received the B.S. degree in Electrical Engineering and Automation from the China University of Mining and Technology, Xuzhou, China, in 2023. He is currently working toward the M.S. degree in electrical engineering from the China University of Mining and Technology, Xuzhou, China. His research interests include integrated drive systems for electric vehicles and double-stator switched reluctance motors.

Hao Chen received the B.S. and Ph.D. degrees in Electrical Engineering from the Department of Automatic Control, Nanjing University of Aeronautics and Astronautics, Nanjing, China, in 1991 and 1996, respectively. In 1998, he became an Associate Professor with the School of Information and Electrical Engineering, China University of Mining and Technology, Xuzhou, China, where he has been a professor since 2001. From 2002 to 2003, he was a Visiting Professor at Kyungsung University, Busan, Korea. Since 2008, he is Adjunct Professor at the University of Western Australia, Perth, Australia. He is the author of one book and has authored more than 200 papers. His current research interests include motor control, linear launcher, electric vehicles, electric traction, servo drives, and wind power generator control. Chen was the recipient of both the Prize of Science and Technology of Chinese Youth and the Prize of the Fok Ying Tong Education Foundation for Youth Teachers in both 2004. He became the Chinese New Century National Hundred-Thousand Ten-Thousand Talents Engineering National Talent in 2007 and won the Government Especial Allowance of People's Republic of China State Department in 2006.

Yang Wang received the B.S. degree in Electrical Engineering and Automation from the Hefei University of Technology, Hefei, China, in 2023. He is currently working toward the M.S. degree in electrical engineering from the China University of Mining and Technology, Xuzhou, China. His research interests include electric machine control.

Vuong Dang Quoc received the Ph.D. degree in electrical engineering in July 2013 at the Faculty of Applied Sciences at the University of Liège in Belgium. He moved to Hanoi University of Science and Technology in September 2013, where he is currently working as a deputy director of Training Center of Electrical and Electrical Engineering, School of Electrical Engineering (SEEE), Hanoi University of Science and Technology (HUST). He became an associate professor in 2020. Vuong's research domain encompasses modeling of electromagnetic systems, electrical machines, optimization method, numerical methods and subproblem methods.

Thanh Nguyen Vu received the Ph.D. degree in 2015 from the Department of Electrical Engineering, School of Electrical Engineering, Hanoi University of Science and Technology (HUST). He is currently working as a Head of Department of Electrical Engineering, School of Electrical and Electronic Engineering, HUST. His research domain encompasses modeling of electrical machines, optimization and numerical methods.

Dynamic Evolutionary Control Strategy for Switched Reluctance Generator DC Microgrid System

Wenju Yan[1,2], Yang Wang[1], Jiangpeng Hu[1], Hao Chen[1], Ryszard Palka[3], Marcin Wardach[3], and Konrad Woronowicz[3]

[1]School of Electrical Engineering
China University of Mining and Technology, Xuzhou 221116, China
6288@cumt.edu.cn, ts23230161p31ld@cumt.edu.cn, ts22230175p31@cumt.edu.cn, hchen@cumt.edu.cn

[2]Shenzhen Research Institute
China University of Mining and Technology, Shenzhen 518057, China

[3]Department of Electrical Machines and Drives
West Pomeranian University of Technology, Sikorskiego 37, 70-313 Szczecin, Poland
ryszard.palka@zut.edu.pl, marcin.wardach@zut.edu.pl, Konrad.Woronowicz@zut.edu.pl

Abstract – This paper introduces a double-stator novel switched reluctance machine employed as a wind generator. To stabilize the fluctuating power output of an off-grid wind power storage system and maintain the bus voltage stability of the power generation system, a dynamic evolutionary control strategy utilizing closed-loop bus voltage regulation is proposed. This includes constructing a multi-objective optimization function with four parameters: power generation efficiency, output voltage, torque smoothness coefficient, and power smoothness coefficient. These parameters serve as the basis for mode selection in multi-mode operation. Furthermore, in order to further enhance the system's power generation efficiency, a real-time optimization method based on efficiency optimization for the commutation angle is designed. The integration of these two methods results in a multi-mode operation method for double-stator switched reluctance generator (DSSRG) based on efficiency optimization control. Simulation and experimental results validate the feasibility and effectiveness of the new DSSRG system and its control methods. This research holds significant importance for the application of DSSRGs in the field of power generation.

Index Terms – Efficiency optimization, Fibonacci search algorithm, mode selection, switched reluctance generator.

I. INTRODUCTION

The overconsumption of fossil energy has led to global warming, and there is an urgent need for clean energy to supplement and replace traditional fossil energy. New energy sources represented by wind power are being developed and utilized on a large scale, and wind power has the advantages of being clean and renewable, relatively low development cost and wide application prospects [1–3]. The switched reluctance generator (SRG) has a simple structure, low cost, no windings on the rotor, made of silicon steel sheet stacked and pressed, does not need permanent magnet efficiency and other characteristics, and can be based on the change of wind speed real-time change in the excitation current for maximum power tracking to improve the utilization of wind energy [4–5]. Compared with synchronous generators, SRG emits direct current (DC), has no output frequency limitation at different wind speeds, and can be used to generate power with variable speed direct drive, which has good research significance and application potential in the field of wind power generation. The SRG is fault tolerant during operation, has good temperature resistance, can still operate stably even under phase loss conditions, and is highly adaptable to harsh environments [6–7].

DC microgrids, as an emerging technology, can easily integrate renewable energy and energy storage devices. In many remote areas abundant in wind energy and other renewable resources, implementing wind-powered DC microgrid systems to achieve electricity self-sufficiency is a cost-effective approach to enhancing local living standards and improving inhabitants' quality of life [8–9].

The variable and unpredictable nature of wind energy can significantly impact the grid when renewable energy sources are widely utilized. Sudden variations in renewable energy sources can result in voltage

Submitted On: December 3, 2024
Accepted On: June 11, 2025

https://doi.org/10.13052/2025.ACES.J.400905

fluctuations, negatively affecting the power quality of the grid. Stochastic fluctuations in renewable energy sources are unavoidable. To address the power fluctuations, energy storage devices are used as energy buffers so as to maintain the power balance and overall stability of the wind turbine DC microgrid system [10]. In [11], the authors propose a model predictive control strategy for DC microgrids, where the energy storage system's state of charge is constrained to operate within a safe range. However, the implementation of model predictive control is discrete as it depends on scattered system models and cost functions. In [12], the energy storage system of electric vehicles uses an adaptive fuzzy logic control (AFLC) method. The energy storage system's power target value can be calculated by the AFLC method, which helps to keep the overall power balance of the system stable. However, a lot of computing resources are required in the proposed control strategy. In [13], adaptive neural network control technology is used to regulate the current of the energy storage system in electric vehicles. In this method, a variety of datasets are used to train the neural network control and generate an optimal current reference at a given load condition. However, its performance relies on the size of the dataset used to train the artificial neural network and can only ensure superior performance with sufficient computing resources. In [14], the extended droop control method extends traditional resistance-based droop characteristic control by incorporating emulated capacitance droop characteristic control to produce the current reference for the energy storage system. The traditional PI-based double closed-loop control for voltage and current regulation has a wide parameter range for the PI controller, and its performance is highly sensitive to parameter selection [15–17]. When the system's operating point shifts, the PI parameters often fail to adapt to the new conditions, compromising the stability of the DC microgrid system during sudden changes in wind power generation or load demand [18]. In [19], dynamic evolutionary control has been applied to the reversible converter control of a fuel cell system driving a supercapacitor, achieving better results than those obtained with the traditional PI strategy. In [20], dynamic evolutionary control improves the boost converter's transient performance and makes the system better. In [21], supercapacitor systems often use PWM control methods to adjust the operation. The PWM's advantage lies in its ability to achieve an uninterrupted and effortless transition between energy intaking and releasing operating modes. In [22], the dynamic evolution control (DEC) method has been applied to compute the pulse width ratio of a reversible DC/DC converter using prediction components and feed-forward components to turn on/off switching transistors, which has smaller bus voltage fluctuations and better control effects when there is a disturbance in the system, which is superior to the traditional PI control, but there is always some degree of discrepancy between the set value and the data in reality.

From the above control methods, PI controllers are applied to keep the DC link voltage. Incorrect selection of PI controller parameters can compromise the consistency of the DC bus voltage, making it difficult to keep the overall system stable. Under all circumstances, the DC bus voltage must remain within the defined range to enable the DC microgrid system connecting with the AC grid [23]. A method to obtain the phase current equation used to determine the optimal control variables is proposed in [24]. A novel two phase double layer switched reluctance generator (DLSRG) under static eccentricity fault is introduced and analyzed. The proposed generator consists of two magnetically independent stator and rotor layers [25].

In order to settle the problems above, a DEC method of a bus voltage based on a PI closed-loop is proposed. In the mentioned control strategy, the conventional PI closed-loop control is combined with a dynamic evolutionary control, where the bus voltage is closed-looped by the PI to get a part of the target current, and the bus voltage is controlled by the dynamic evolutionary method. This is a novel method of dealing with the problem that the parameters of the PI controller are difficult to select correctly under different working conditions and that there is a deviation between the actual voltage and the given value of the busbar in the dynamic evolutionary control method.

This paper is organized as follows. The system framework is shown in section II. Section III covers the design of both system and controller parameters. Section IV provides detailed simulation results, while section V presents the experimental results and analysis. Finally, conclusions are drawn in section VI.

II. NOVEL DC MICROGRID SYSTEM FRAMEWORK FOR WIND TURBINES

The overall framework presented in this paper is illustrated in Fig. 1. The generator adopts a 16/18/16 type double-stator switched reluctance generator (DSSRG), which has the windings of the inner stator U-type stator module connected in series with the radially symmetrical position windings to form the four phases of *A*, *B*, *C* and *D*, respectively. The windings of the outer stator U-type stator module are also connected in series with the radially symmetrical position windings to form four phases of *E*, *F*, *G* and *H*.

A, *B*, *C* and *D* are opposite to *E*, *F*, *G* and *H*, respectively. The generator rotor is an inner and outer double-sided convex pole structure, and the inner and outer adjacent rotor convex poles are staggered by 7.5

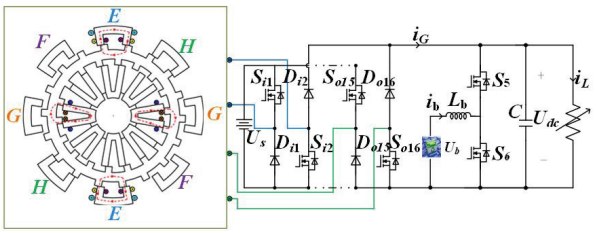

Fig. 1. A novel DSSRG power generation system.

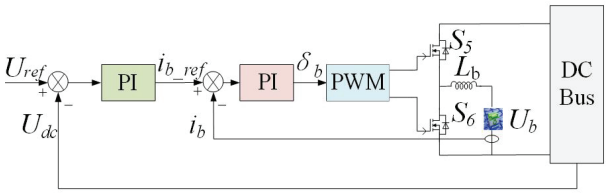

Fig. 2. Block diagram of double closed-loop control.

mechanical angles between their central axes. Different from the winding pole distribution form of DSSRG in the traditional sense, the magnetic field polarity distribution of the inner stator winding of this DSSRG follows the pattern S-N-N-S-S-S-N-S-S-N-S-S-N-S, while the polarity distribution of the outer stator winding is arranged as N-S-S-S-N-S-S-S-S-N-S-S-S-S-N. This configuration enables the DSSRG to simultaneously exhibit the characteristics of both a U-shaped magnetic circuit and a parallel magnetic circuit, which makes the overall working efficiency and power density of the generator higher.

The generator is integrated with the DC bus via an asymmetrical half-bridge power converter, and the energy storage device is linked to the bus through a reversible DC-DC converter, with variable loads connected to the bus. According to the operation of the system in reality, the switching signal of the reversible DC-DC converter is controlled to realize the bidirectional flow of energy in the energy storage device. i_G, i_b and i_L denote the generator, battery, and DC load currents, respectively, and L_b is the filter inductance parameter of the DC-DC converter integrated to the battery. C_{dc} and R_{dc} denote the total DC bus capacitance and load resistance, respectively. U_b is the battery's voltage, U_s is the DSSRG excitation supply voltage, and U_{dc} is the DC bus voltage. S_{i1} and S_{i2} are the control switches for phase A in the inner stator winding, and D_{i1} and D_{i2} are the continuity diodes for phase A in the four-phase winding of the inner stator. Similarly, S_{o9} and S_{o10} are the control switches for phase E in the four-phase winding of the outer stator, D_{o9} and D_{o10} are the continuity diodes for phase E in the four-phase winding of the outer stator, and S_5 and S_6 are the control switches for the reversible DC-DC converter.

III. CONTROL METHODS

A. Control method formulation

The block diagram of the conventional control method employed for stabilizing the DC microgrid bus voltage is presented in Fig. 2.

In this method, the deviation term between the DC bus voltage U_{dc} and the bus voltage reference value U_{ref} are sent to the outer-loop PI controller to compute the battery current reference value i_{b_ref}, then the difference between i_{b_ref} and the current sampling value i_b is sent to the inner-loop PI controller to get the pulse width ratio of the switching device, and then the switching signals of the power switching transistors of the reversible DC-DC converter are obtained through the PWM modulation to complete the double closed-loop control of the bus voltage system. The control of bus voltage double closed-loop system is completed. Dual closed-loop control requires adjusting the proportional and integral coefficients of the voltage outer loop and current inner loop respectively, and the stability of the DC bus voltage will be directly affected by the target value of the PI regulator parameters. When the operating point of the system is changed, too many PI parameters need to be adjusted which is not conducive to the stability of the system in case of large fluctuations in the generation side or load demand side of the system. In order to settle problems in the above, a DEC strategy of bus voltage based on PI closed-loop (PIDEC) is proposed.

The power balance equation for the entire wind turbine DC microgrid system in the PIDEC is:

$$P_H = P_L - P_G, \tag{1}$$

where P_H is the total power to be dissipated by the energy backup unit, P_L is the power requirement and P_G is the wind turbine power.

The DC bus voltage reflects the power equilibrium between the generation side, the load side and the energy backup system. In order to respond to DC bus voltage fluctuations and to stabilize the DC bus voltage quickly at a given value of voltage, the battery reference current is:

$$\begin{cases} U_e = U_{ref} - U_{dc} \\ i_{b\_ref} = \frac{P_H}{U_b} + i_{PI} + \beta U_e \end{cases}, \tag{2}$$

where i_{PI} is the PI compensation term current value and β is the bus voltage error term coefficient. In order to transfer the bus voltage fluctuation to the energy storage device for smoothing, β is generally taken as a value of 5 [22].

The energy storage system power P_H is separated by the battery voltage U_b to obtain a portion of the transient current reference controlled by a DC-DC converter connected to the battery. In addition, the battery reference current i_{b_ref} includes a bus voltage error term and a PI compensation term, and the battery is controlled using a DEC.

B. Battery current control

Equations (3) and (4) indicate that the battery operates in buck mode and boost mode, respectively. The current dynamics of the reversible DC-DC power converter in one cycle is:

$$\frac{di_{\mathrm{b}}(t)}{dt}=\frac{(U_{\mathrm{dc}}-U_{\mathrm{b}})}{L_{\mathrm{b}}}\delta_{\mathrm{b}}(t)-\frac{U_{\mathrm{dc}}}{L_{\mathrm{b}}}(1-\delta_{\mathrm{b}}(t)), \quad (3)$$

$$\frac{di_{\mathrm{b}}(t)}{dt}=\frac{U_{\mathrm{b}}}{L_{\mathrm{b}}}\delta_{\mathrm{b}}(t)-\frac{(U_{\mathrm{dc}}-U_{\mathrm{b}})}{L_{\mathrm{b}}}(1-\delta_{\mathrm{b}}(t)), \quad (4)$$

where $d_{\mathrm{b}}(\mathrm{t})$ is the switching device's pulse width ratio in the DC-DC power converter circuit integrated to the battery.

When the external environment changes, battery current control plays a crucial role in quickly achieving DC bus voltage stabilization. Throughout the process, the reversible DC-DC converter operates in a complementary approach, the controller design in the power-boosting mode is analyzed and can be computed from equation (4):

$$U_{\mathrm{b}}=L_b\frac{di_b(t)}{dt}+U_{\mathrm{b}}(1-\delta_{\mathrm{b}}(t)). \quad (5)$$

Equation (2) shows that the battery reference current contains the instantaneous current, the PI compensation term current and the bus voltage deviation. For better control of voltage and current, the DEC method is used. Before adopting this method, the dynamic evolution path needs to be selected, and the exponential evolution path selected here is shown in equation (6). The corresponding dynamic evolution process is shown in equation (7) :

$$U_e^*(t)=U_{e0}\exp(-mt), \quad (6)$$

$$\frac{dU_e^*(t)}{dt}+mU_e^*(t)=0, m>0, \quad (7)$$

where $\mathrm{U_e^*(t)}$ denotes the transient characteristics of the system, U_{e0} is the starting value of the system deviation voltage and m is the rate at which the deviation voltage is minimized when the system responds. To ensure that the proposed evolutionary path reduces the error voltage to zero quickly, in practice, a linear function of the dynamic characteristics of the system is given as:

$$U_e^*(t)=kU_e, k>0, \quad (8)$$

where k is a direct proportionality factor.

Combining equations (7) and (8), the new dynamic evolution process is obtained as:

$$k\frac{dU_e(t)}{dt}+mkU_e(t)=0. \quad (9)$$

Combining equations (4) and (9), we get:

$$U_b=L_b\frac{di_b(t)}{dt}+k\frac{dU_e(t)}{dt}+(mk-1)U_e(t)+U_{ref}-U_{dc}\delta_b(t) \quad (10)$$

The bidirectional DC/DC circuit switching transistor duty cycle linked to the battery is obtained from the above analysis:

$$\delta_b(t)=\frac{U_{ref}-U_b}{U_{dc}}+\frac{mk-1}{U_{dc}}U_e(t)+\frac{k}{U_{dc}}\frac{dU_e(t)}{dt}+\frac{L_b}{U_{dc}}\frac{di_b(t)}{dt}. \quad (11)$$

Control of the pulse width ratio of the switching transistor in the above equation consists of four parts. The first is the feed-forward term, which is sensitive to the change of the input voltage and helps to compensate it in time. The second is the voltage deviation ratio term, which can enhance the response speed for minimizing the voltage deviation. The next term is the derivative term of the voltage error, and the last reacts to the change of the inductance current which is also the change of the energy intaking and releasing currents of the energy storage system. In PIDEC, the coefficients of each item change with the change of output voltage, which can make the bus voltage stabilize at the given value more quickly, and the PIDEC requires fewer parameters to be adjusted and simplifies the framework of the controller compared with the traditional double closed-loop control method. The block diagram of this control method is shown in Fig. 3.

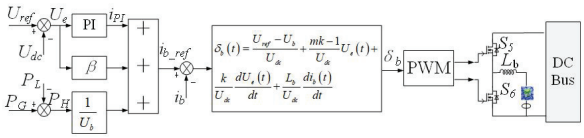

Fig. 3. Block diagram of PIDEC control.

IV. SIMULATION ANALYSIS

Under the MATLAB/Simulink simulation environment, the simulation model of the DC microgrid system of double-stator switched reluctance wind turbine is constructed as shown in Fig. 4.

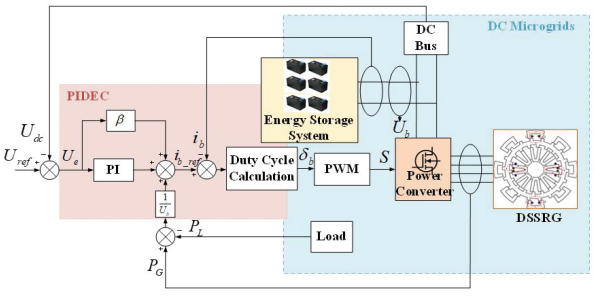

Fig. 4. Model of DC microgrid system with DSSRG.

The switch-on and switch-off angles of the fixed switched reluctance generator in the type and the simulation platform parameter settings are provided in Table 1.

To validate the effectiveness of the PIDEC, the aforementioned simulation platform is utilized to simulate and compare the traditional PI voltage-current

Table 1: Simulation platform parameters

Parameters	Value
DC bus voltage (V)	48
Rated battery voltage (V)	24
Battery capacity (Ah)	21
DC bus capacitor (F)	5e-3
Bus voltage error term gain β	5
Evolutionary coefficient m	31
Proportionality coefficient k	0.03
Switching frequency (Hz)	20000
Sampling time (s)	5×10^{-6}
Voltage proportionality coefficient k_{p1}	1.1
Voltage integration coefficient k_{i1}	80

double-closed-loop control strategy with the DEC strategy for bus voltage based on the PI closed-loop.

A. System performance at variable speeds

System simulation is carried out under a certain load. In order to simulate the change of motor speed caused by the change of wind speed during the actual operation of the wind turbine, the initial speed of the motor is set to be 900 r/min, the speed is reduced to 600 r/min in 0.7 s, and the speed is restored to 900 r/min in 1.3 s and, under the above conditions, the PIDEC control strategy and the traditional voltage double-closed-loop control strategy are adopted respectively for simulation. The simulation results are shown in Figs. 5 and 6. The simulation results show that at 0.7 s, the generator speed decreases from 900 r/min to 600 r/min due to the wind speed becoming slower, the generating power decreases

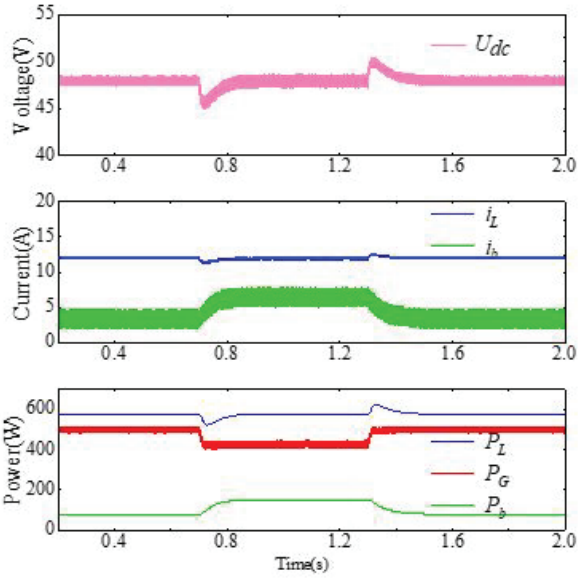

Fig. 5. Double closed-loop control strategy.

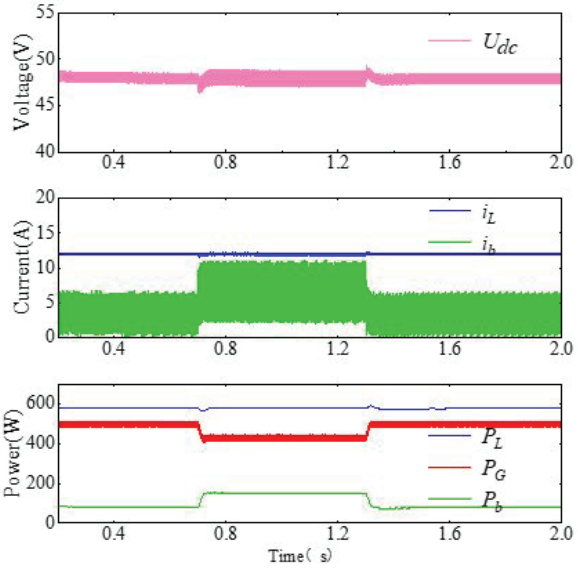

Fig. 6. PIDEC control strategy.

and R_L is 4Ω, and the load power remains constant. In this case, the power generated is less than the power consumed by the load, and the system power deficit is replenished by the releasing of the energy backup device, and the releasing current of the battery increases. At 1.3 s, the wind speed returns to 900 r/min, the turbine generating power increases, the system power difference decreases, and the battery discharge current becomes smaller. The bus voltage waveforms in Figs. 5 and 6 show that, compared with the traditional double-closed-loop control strategy, the DC bus voltage of the PIDEC has smaller bus voltage fluctuation and shorter bus voltage recovery time at the moment of perturbation, and the energy storage device has a faster current response.

B. System performance under variable load scenarios

The motor speed is set to 900 r/min, the generating power is constant, and the load is changed to simulate the change of load power during the actual operation of the system. The simulation results are shown in Figs. 7 and 8. At 0.7 s, the load $R_L = 4\Omega$ is reduced to $R_L = 3\Omega$, the load power demand increases, the generation power remains unchanged, the generation is less than the demand for electricity, and the energy releasing current of the energy storage device increases to compensate for the increased load power demand. At 1.3 s, the load reverts to 4Ω, the load power demand is reduced and the battery discharge power is subsequently reduced to meet the overall power balance of the system. The simulation results show that, at the moment of load change, the control method proposed in this paper exhibits superior dynamic characteristics and better system stability compared to the double closed-loop control.

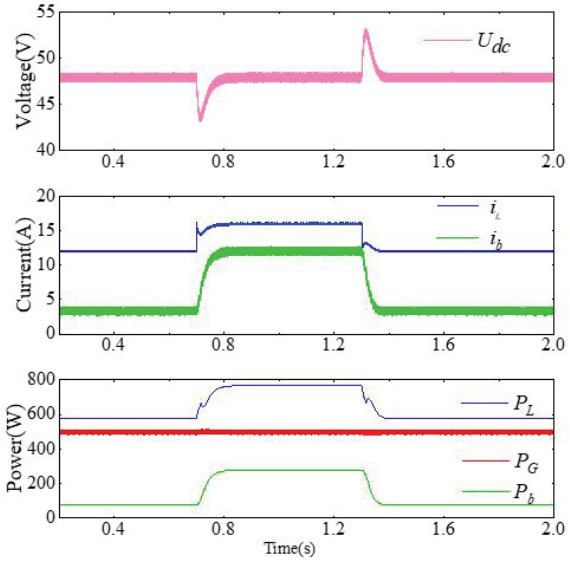

Fig. 7. Double closed-loop control strategy.

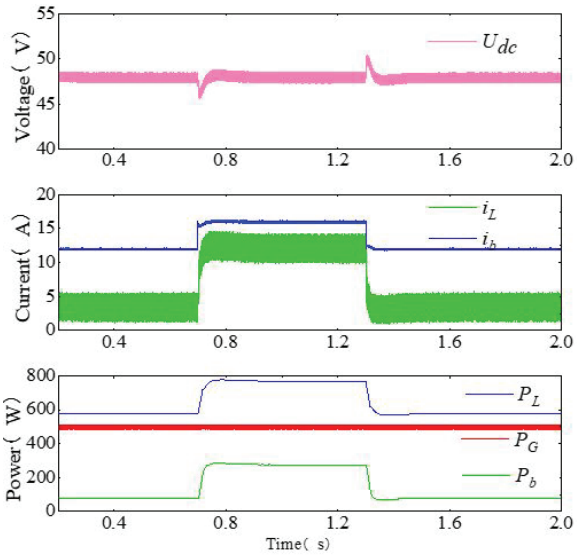

Fig. 8. PIDEC control strategy.

C. System performance under variable bus reference voltage scenarios

If we set the bus voltage reference U_{ref} to change from 48 V to 55 V, the motor speed to remain at 900 r/min, and the load R_L is kept at 4Ω, we can observe the output voltage shift. Figure 9 shows the simulation results using the conventional voltage double closed-loop control strategy when the dc bus reference voltage is varied. Fig. 10 shows the simulation results using the PIDEC control strategy when the dc bus reference voltage is varied. At 0.6 s, the bus voltage reference value

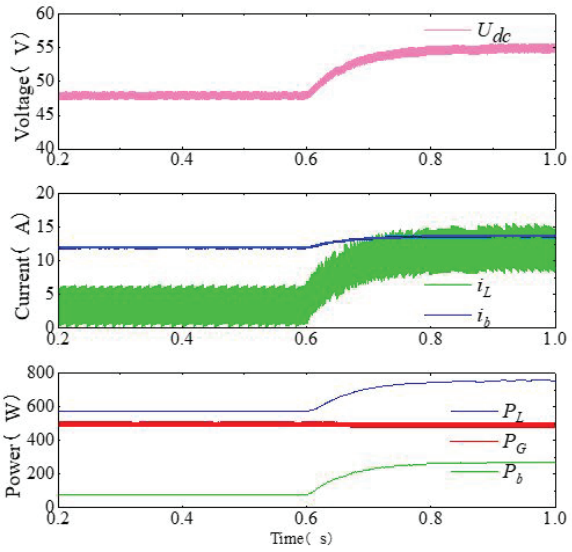

Fig. 9. Double closed-loop control strategy.

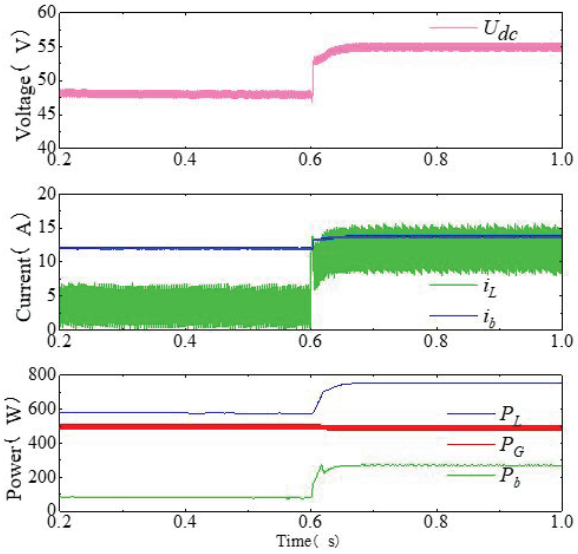

Fig. 10. PIDEC control strategy.

U_{ref} changes from 48 V to 55 V. In this case, the load current i_L increases from 12 A to 13.75 A. If the load demand increases and the power deficit of the system increases, the power required to keep the system stable is supplied by the energy storage system, and it is evident from the simulation results that the bus voltage has a much faster response under the PIDEC.

V. EXPERIMENTAL VERIFICATION

In order to verify the feasibility of the control method proposed in this paper, an experimental platform was constructed and is presented in Fig. 11. The DSSRG

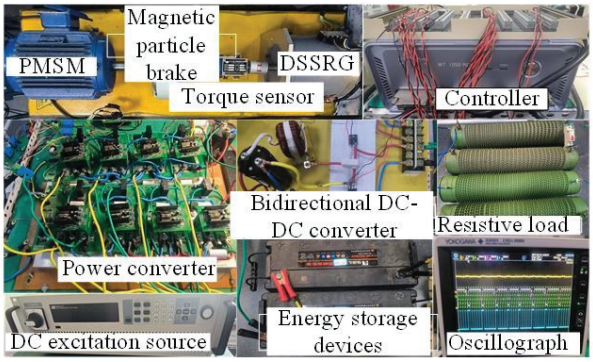

Fig. 11. Test platform.

prototype, power converter, bidirectional DC-DC converter, controller, DC excitation source, energy storage device, resistive load, permanent magnet synchronous motor (PMSM), and other parts are included in the experimental platform. The relevant parameters of the double-stator motor are shown in Table 2.

Table 2: Parameters related to DSSRG

Parameter	Value
Poles	4
Convex pole number	16/18/16
Rated voltage (V)	48
Rated power (W)	1600
Number of turns of outer stator convex pole	22
Number of turns of inner stator convex pole	17

A. Variable speed experiment

The observational results of the customary PI control method and the PIDEC for the experiment of variable speed are shown in Figs. 12 and 13, respectively.

During the process, the DC resistive load R_L is maintained at 4Ω. The motor speed is changed from 900 r/min to 600 r/min, the generating power is changed from 500 W to 440 W, and the load power is kept at about 576 W. The stability of the system is maintained by an energy

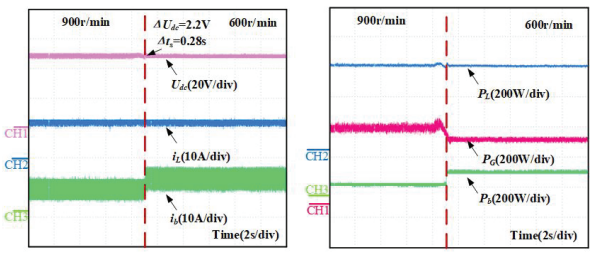

Fig. 12. Experimental results of PI control under variable speed: (a) Changes in U_{dc}, i_L and i_b and (b) changes in P_L, P_G and P_b.

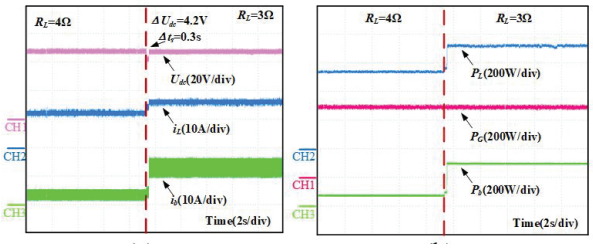

Fig. 13. Experimental results of PIDEC control at variable speed: (a) Changes in U_{dc}, i_L and i_b and (b) changes in P_L, P_G and P_b.

storage device after a change in generation power. The battery power P_b is increased from 76 W to 136 W to compensate for power instability. From the observational results, it can be seen that the DC bus voltage overshoot of the conventional control method is about 4.5% and the bus voltage recovery time Δt_s is 0.28 s. By using the PIDEC, improved regulation of the DC voltage across the link is achieved. The M_p of the PIDEC is less than 2.3% and the Δt_s is less than 0.08 s.

B. Variable load experiment

In the variable load experiment, the functionality of the customary control method is shown in Fig. 14 and the performance of the PIDEC is shown in Fig. 15. In the experiment, the load R_L is decreased from 4Ω to 3Ω, the load current i_L is increased from 12 A to 16 A accordingly, and the motor speed is kept at 900 r/min. In order to keep the DC voltage across the bus constant when the load power is stepped, the power deficit is supplemented by the energy backup device, and the battery power P_b is increased from 76 W to 268 W, with a consequent increase in the discharge current of the battery. From the experimental results, it can be observed that the DC bus voltage overshoot of the customary control method is about 8.7%, and the bus voltage recovery time Δt_s is 0.3 s. The PIDEC has M_p less than 3.2% and Δt_s less than 0.06 s. The control method achieves better DC bus voltage regulation with greater robustness.

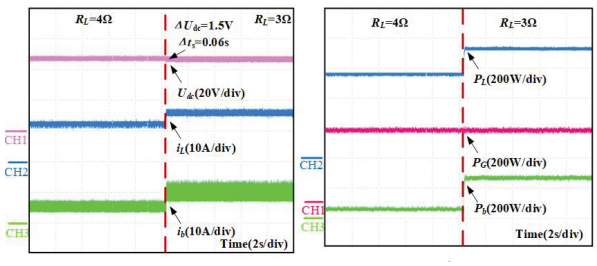

Fig. 14. Experimental results of PI control under variable load: (a) Changes in U_{dc}, i_L and i_b and (b) changes in P_L, P_G and P_b.

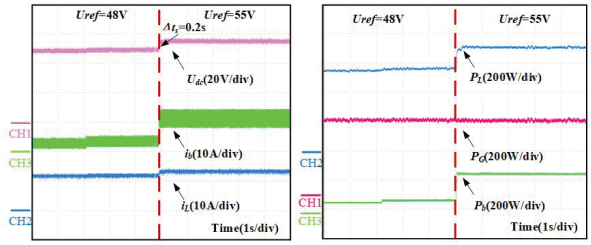

Fig. 15. Experimental results of PIDEC control under variable load: (a) Changes in U_{dc}, i_L and i_b and (b) changes in P_L, P_G and P_b.

C. Variable DC bus reference voltage experiment

The observed results at a reference change in DC bus voltage are shown in Figs. 16 and 17. The voltage at the output is changed from 48 V to 55 V. At the same time, R_L is maintained at 4Ω and the motor speed is kept at 900 r/min. It is observed that, due to the increase in bus reference voltage, the load power increases. The power required to keep the system stable is provided by the battery and the battery power P_b is increased from 76 W to 256 W to compensate for the system power fluctuation. As the DC bus voltage changes, the load current i_L increases accordingly from 12 A to 13.75 A. It can be seen that the bus voltage response time Δt is 0.2 s for the conventional control strategy, and the PIDEC is more effective at handling step changes in the reference value

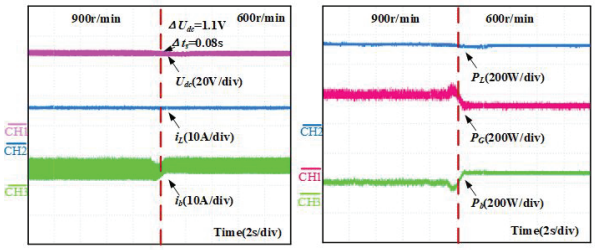

Fig. 16. Experimental results of PI control under variable bus reference voltage: (a) Changes in U_{dc}, i_L and i_b and (b) changes in P_L, P_G and P_b.

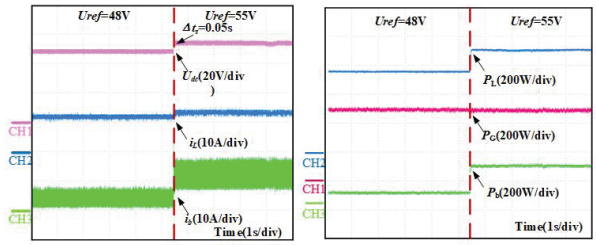

Fig. 17. Experimental results of PIDEC control under variable bus reference voltage: (a) Changes in U_{dc}, i_L and i_b and (b) changes in P_L, P_G and P_b.

of the output voltage, with a response time Δt of 0.05 s from the experimental results. The response time Δt is 0.05 s for the conventional control strategy.

D. Stability comparison

Based on the above experimental results, Table 3 compares the bus voltage overshoot M_p and the recovery time Δt_s of the PIDEC with the conventional control strategy under different experimental conditions, where M_p is calculated as:

$$M_p = \frac{\Delta U_{dc}}{U_{dc}} \times 100\%, \tag{12}$$

where ΔU_{dc} is the maximum value of the voltage deviation from the bus voltage reference.

Table 3: Comparison of bus voltage stability performance under different control strategies

Situation	Parameter	Conventional	PIDEC
Speed change	Voltage overshoot (M_p)	4.5%	2.3%
	Recovery time (Δt_s)	0.28 s	0.08 s
Load change	Voltage overshoot (M_p)	8.7%	3.2%
	Recovery time (Δt_s)	0.3 s	0.06 s
Bus voltage change	Response time (Δt)	0.2 s	0.05 s

VI. CONCLUSION

This paper focuses on the use of a new DSSRG for wind power generation and proposes a new DSSRG standalone DC microgrid system. A dynamic evolutionary control strategy based on a closed-loop bus voltage is proposed for this new DC microgrid system. The control method combines the traditional closed-loop control and DEC, which has an improvement effect on the problem of the PI controller parameters being difficult to be correctly selected under different working conditions in the traditional PI control and the problem of the actual voltage deviating from the given value of the busbar in the DEC method. The proposed method is simulated and experimentally verified under three typical working conditions, and it can be seen that the PIDEC control strategy has a smaller bus voltage overshoot and a shorter bus voltage recovery time, which makes the DC bus voltage remain at a given value and improves the power supply quality and reliability of the wind power microgrid. Due to the phenomenon of increased current ripple of the battery with PIDEC control strategy in the experiment, which will damage the battery life of the battery, a hybrid energy storage system, i.e., a storage system with

an energy-based storage original battery and a power-based storage element supercapacitor, will be established in the future to achieve the bus voltage stability and the improvement of the dynamic performance without depletion of the battery's service life.

ACKNOWLEDGMENT

This work was supported in part by the Xuzhou Science and Technology Innovation Basic Research Project under Grant KC23021, the Guangdong Basic and Applied Basic Research Foundation under Grant 2025A1515011254, China Postdoctoral Foundation Project under Grant 2023M733749, 2022 China-CEEC University Joint Education Program (2022200), 2023 China-CEEC University Joint Education Program (2023304).

REFERENCES

[1] V. Paul, D. Katherine, and B. Sukanta, "Grand challenges: Wind energy research needs for a global energy transition," *Wind Energy Science*, vol. 7, no. 6, pp. 2491-2496, 2022.

[2] A. Clifton, S. Barber, and Y. Ding, "Grand challenges in the digitalisation of wind energy," *Wind Energy Science*, vol. 8, no. 6, pp. 947-974, 2023.

[3] B. Mostafa, S. Mehdi, M. Saad, S. Alex, and H. Ben, "Small-scale wind turbine control in high-speed wind conditions: A review," *Sustainable Energy Technologies and Assessments*, vol. 60, p. 103577, Dec. 2023.

[4] N. Vahidreza, K. Shahriyar, and D. Ali, "Output power maximization and optimal symmetric free-wheeling excitation for switched reluctance generators," *IEEE Transactions on Industry Application*, vol. 49, no. 3, pp. 1031-1042, 2013.

[5] L. Liu, Y. Huang, M. Zhao, and Y. Ruan, "Parametric modeling and optimization of switched reluctance motor for EV," *Applied Computational Electromagnetics Society (ACES) Journal*, vol. 37, no. 9, pp. 948-958, 2022.

[6] C. Da-Woon, B. Sang-In, and C. Yun-Hyun, "A study on the maximum power control method of switched reluctance generator for wind turbine," *IEEE Transactions on Magnetics*, vol. 50, no. 1, p. 1, 2013.

[7] J. Mukhopadhyay, S. Choudhuri, and S. Senguota, "ANFIS based speed and current control with torque ripple minimization using hybrid SSD-SFO for switched reluctance motor," *Sustainable Energy Technologies and Assessments*, vol. 49, p. 101712, Feb. 2022.

[8] F. Nejabatkhah and Y. Li, "Overview of power management strategies of hybrid AD/DC microgrid," *IEEE Transactions on Power Electronics*, vol. 30, no. 12, pp. 7072-7089, 2015.

[9] S. Raul, F. Luis, M. G. Carlos Andres, and J. Francisco, "Dynamic evaluation of two configurations for a hybrid DFIG-based wind turbine integrating battery energy storage system," *Wind Energy*, vol. 18, no. 9, pp. 1561-1577, 2015.

[10] C. Wan, W. Qian, C. Zhao, Y. Song, and G. Yang, "Probabilistic forecasting-based sizing and control of hybrid energy storage for wind power smoothing," *IEEE Transactions on Sustainable Energy*, vol. 12, no. 4, pp. 1841-1852, 2021.

[11] S. K. Kollimalla, A. Ukil, H. B. Gooi, U. Manandhar, and N. R. Tummuru, "Optimization of charge/discharge rates of a battery using a two-stage rate-limit control," *IEEE Transactions on Sustainable Energy*, vol. 8, no. 2, pp. 516-529, Apr. 2017.

[12] H. Yin, W. Zhou, M. Li, C. Ma, and C. Zhao, "An adaptive fuzzy logic-based energy management strategy on battery/ultracapacitor hybrid electric vehicles," *IEEE Transactions on Transportation Electrification*, vol. 2, no. 3, pp. 300-311, 2016.

[13] O. Micah, M. Jorge, and D. Juan, "Ultracapacitor-based auxiliary energy system for an electric vehicle: Implementation and evaluation," *IEEE Transactions on Industrial Electronics*, vol. 54, no. 4, pp. 2147-2156, 2007.

[14] Q. Xu, X. Hu, P. Wang, J. Xiao, P. Tu, C. Wen, and M. Lee, "A decentralized dynamic power sharing strategy for hybrid energy storage system in autonomous dc microgrid," *IEEE Transactions on Industrial Electronics*, vol. 64, no. 7, pp. 5930-5941, 2017.

[15] S. Bayandy, S. Kanat, and D. Ton Duc, "High order disturbance observer-based PI-PI control system with tracking Anti-Windup technique for improvement of transient performance of PMSM," *IEEE Access*, vol. 9, pp. 66323-66334, 2021.

[16] Z. Liu, J. Nie, H. Wei, C. Lei, X. Li, and M. Lv, "Switched PI control-based MRAS for sensorless control of PMSM drives using Fuzzy-Logic-Controller," *IEEE Open Journal of Power Electronics*, vol. 3, pp. 368-381, 2022.

[17] S. K. Kollimalla, M. K. Mishra, A. Ukil, and H. B. Gooi, "DC grid voltage regulation using new HESS control strategy," *IEEE Transactions on Sustainable Energy*, vol. 8, no. 2, pp. 772-781, Apr. 2017.

[18] Y. Sun, X. Tang, X. Sun, D. Jia, Z. Cao, J. Pan, and B. Xu, "Model predictive control and improved low-pass filtering strategies based on wind power fluctuation mitigation," *Journal of Modern Power Systems and Clean Energy*, vol. 7, no. 3, pp. 512-524, 2019.

[19] S. Ahmad Saudi and Y. Abdul Halim Mohamed, "Implementation of dynamic evolution control of bidirectional DC-DC converter for interfacing ultracapacitor energy storage to fuel-cell system," *IEEE Transactions on Industrial Electronics*, vol. 57, no. 10, pp. 3468-3473, 2010.

[20] M. Pratap Ranjan and P. Anup Kumar, "A nonlinear control scheme based on dynamic evolution path theory for improved dynamic performance of boost PFC converter working on nonlinear features," *ISA Transactions*, vol. 65, pp. 254-261, 2016.

[21] K. Saichand and V. John, "PWM block method for control of an ultracapacitor-based bidirectional DC–DC backup system," *IEEE Transactions on Industry Applications*, vol. 52, no. 5, pp. 4126-4134, Sep.-Oct. 2016.

[22] M. Ujjal, B. Wang, A. Ukil, and G. Hoay Beng, "Dynamic evolution control-based power sharing method for hybrid energy storage system," *IET Power Electronics*, vol. 12, no. 2, pp. 276-283, 2019.

[23] L. Xu and D. Chen, "Control and operation of a DC microgrid with variable generation and energy storage," *IEEE Transactions on Power Delivery*, vol. 26, no. 4, pp. 2513-2522, 2011.

[24] P. Thongprasri and S. Kitturatsatcha, "Analysis of control variables to maximize output power for switched reluctance generators in single pulse mode operation," *Applied Computational Electromagnetics Society (ACES) Journal*, vol. 31, no. 10, pp. 1208-1220, 2021.

[25] E. Afjei and H. Torkaman, "Finite element analysis of switched reluctance generator under fault condition oriented towards diagnosis of eccentricity fault," *Applied Computational Electromagnetics Society (ACES) Journal*, vol. 26, no. 1, pp. 8-16, 2022.

Wenju Yan (M'19) received the B.S. degree in Electrical Engineering and Automation from the China University of Mining and Technology, Xuzhou, China, in 2013. He received the Ph.D. degree in electrical engineering from the China University of Mining and Technology, Xuzhou, China, in 2018. Since 2018, he has been with China University of Mining and Technology, where he is currently an associate professor in the School of Electrical Engineering. His current research interests include electric vehicles, electric traction, iron loss analysis, and motor design.

Yang Wang received the B.S. degree in Electrical Engineering and Automation from the Hefei University of Technology, Hefei, China, in 2023. He is currently working toward the M.S. degree in electrical engineering from the China University of Mining and Technology, Xuzhou, China. His research interest includes electric machine control.

Jiangpeng Hu received the B.S. degree in Electrical Engineering and Automation, from Anhui University of Science and Technology, Huainan, Anhui, China, in 2020. He is currently working toward the M.S. degree in electrical engineering from the China University of Mining and Technology, Xuzhou, China. His research interests include new energy wind power and hybrid energy storage technologies.

Hao Chen (SM'08) received the B.S. and Ph.D. degrees in Electrical Engineering from the Department of Automatic Control, Nanjing University of Aeronautics and Astronautics, Nanjing, China, in 1991 and 1996, respectively. In 1998, he became an Associate Professor with the School of Information and Electrical Engineering, China University of Mining and Technology, Xuzhou, China, where he has been a professor since 2001. From 2002 to 2003, he was a Visiting Professor at Kyungsung University, Busan, Korea. Since 2008, he has been an Adjunct Professor at the University of Western Australia, Perth, Australia. He is the author of one book and has authored more than 200 papers. His current research interests include motor control, linear launcher, electric vehicles, electric traction, servo drives, and wind power generator control. Chen was the recipient of both the Prize of Science and Technology of Chinese Youth and the Prize of the Fok Ying Tong Education Foundation for Youth Teachers in both 2004. He became the Chinese New Century National Hundred-Thousand Ten-Thousand Talents Engineering National Talent in 2007 and won the Government Especial Allowance of People's Republic of China State Department in 2006.

Ryszard Palka D.Sc. Ph.D. Eng. is Head of Department of Electrical Machines and Drives, West Pomeranian University of Technology, Szczecin, Poland. In 1987-2005 he was with the Institute of Electrical Machines, Traction and Drives, TU Braunschweig, Germany. Areas of research include electromagnetic field theory, numerical field calculations, optimization of electromagnetic fields, electrical machines, and high temperature superconductivity. He is the author of about 320 refereed journal articles, conference papers, technical reports, and co-author of four books. He is a member of IEEE, International Compumag Society, Polish Society of Theoretical and Applied Electrical Engineering, International Maglev Board and Committee on Electrical Engineering, Polish Academy of Sciences.

Marcin Wardach D.Sc. Ph.D. Eng. was born in Poland in 1980. He graduated and received the Ph.D. degree from the Electrical Department, Szczecin University of Technology, Szczecin, Poland, in 2006 and 2011, respectively. From 2020 until now, he has been an Associate Professor with the Faculty of Electrical Engineering, West Pomeranian University of Technology, Szczecin. His research interests include the design of electrical machines and drives especially unconventional and hybrid excited. He is the author of over 100 scientific papers and post-conference publications. He is a member of Association of Polish Electrical Engineers and Polish Society of Theoretical and Applied Electrical Engineering.

Konrad Woronowicz received the Ph.D. degree in adaptive linear induction motors (LIM) control and the D.Sc. degree in an area of Wireless Power Transfer from the West Pomeranian University of Technology, Szczecin, Poland, in 2001 and 2015, respectively. From 1995 until 2019, he was with Bombardier Transportation, Canada, involved in various transportation and research and development projects and played a key role in commercializing LIM-based mass transit systems in such locations as New York, Beijing, Vancouver, Kuala Lumpur and Seoul. Later, he partook in the development of a high power WPT (Wireless Power Transfer) system for buses and light rail vehicles. He has authored numerous patents in WPT, converter topology, converter controls, and motors. He is currently an Associate Professor with the West Pomeranian University of Technology, Department of Electrical Engineering. His current research interests include electromagnetic design for WPT, development of high-performance linear motors, resonant circuits and power conversion for energy storage.

Modeling and Analysis of Equivalent Magnetic Network Model for Novel Asymmetric Rotor Permanent Magnet-assisted Synchronous Reluctance Motor

Hao Chen[1,2,3], Ziqiang Wei[2], Xing Wang[1], Shudong Hou[3], Antonino Musolino[4], Murat Shamiyev[5], Pulatov Abror Abidovich[5], Emmanuel Karapidakis[6], Aris Dimeas[7], and Sherif Moussa[8]

[1]Shenzhen Research Institute
China University of Mining and Technology, Shenzhen 515100, China
hchen@cumt.edu.cn, 3512@cumt.edu.cn

[2]School of Electrical Engineering
China University of Mining and Technology, Xuzhou 221116, China
tb23230015p41@cumt.edu.cn

[3]Nexus Intelligent Equipment (Zhejiang) Co. Ltd.
Zhejiang, China
njdr2007@126.com

[4]Department of Energy, System, Territory and Construction Engineering (DESTEC)
University of Pisa, 56122 Pisa, Italy
antonino.musolino@unipi.it

[5]Tashkent State Technical University
Tashkent City, Republic of Uzbekistan
antonino.musolino@unipi.it, Hello_murat@mail.ru, abrorobidovich@mail.ru

[6]School of Engineering
Hellenic Mediterranean University (HMU),
Estavromenos Campus, 71004 Heraklio, Crete, Greece
karapidakis@hmu.gr

[7]Athens National University of Technology
Greece
adimeas@power.ece.ntua.gr

[8]School of Engineering
Canadian University, Sheikh Zayed Road, 117781 Dubai, UAE
smoussa@cud.ac.ae

***Abstract* –** This paper presents a novel asymmetric rotor permanent magnet-assisted synchronous reluctance motor (NAR-PMa-SynRM) designed to enhance torque output and reduce torque ripple by employing unconventional methods compared to traditional approaches where permanent magnets are embedded within magnetic barriers. In this design, tile-shaped permanent magnets are embedded along the rotor d-axis, coupled with an asymmetric magnetic barrier structure. To streamline the motor design process, a nonlinear equivalent magnetic network (EMN) model tailored to the distinctive structure of the NAR-PMa-SynRM is proposed.

Submitted On: November 30, 2024
Accepted On: September 2, 2025

https://doi.org/10.13052/2025.ACES.J.400906

However, modeling the complex magnetic barrier structure poses a significant challenge in magnetic network modeling. To address this challenge, an effective method for representing the magnetic barriers equivalently is proposed to enhance modeling accuracy. Finally, the effectiveness of the proposed equivalent barrier method and magnetic network model is validated by comparing air gap magnetic flux density results obtained from finite element and magnetic network simulations.

Index Terms – Equivalent magnetic network, finite element analysis, permanent magnet-assisted synchronous reluctance motor.

I. INTRODUCTION

In recent years, global initiatives such as "carbon neutrality" and "peak carbon emissions" have driven advancements in carbon reduction technologies, among which high-efficiency, high-power-density electric motors play a pivotal role in sectors like new energy vehicles, industrial drives, and compressors [1–3]. Rare-earth permanent magnet (PM) motors have emerged as key solutions in this context; however, their sustainability is constrained by the volatility of rare-earth supply chains and associated cost instabilities, given rare-earths' strategic resource status [4].

To mitigate reliance on rare-earth PM materials while maintaining performance and reducing costs, synchronous reluctance motors (SynRMs) have gained attention. Characterized by rotor structures free of windings and PMs, SynRMs generate torque exclusively via reluctance effects enabled by their multi-layer air gap design, offering advantages such as low manufacturing costs, temperature insensitivity, and robust transient overload capability [5–8]. Nevertheless, their inherent limitations, including low torque output and poor power factor, often restrict their applicability in high-performance scenarios.

To address these drawbacks, permanent magnet-assisted synchronous reluctance motors (PMa-SynRMs) have been developed by strategically embedding moderate amounts of PMs within the multi-layer air gap structure of SynRMs. This integration combines PM-derived electromagnetic torque with reluctance torque, achieving a balance between low cost and enhanced performance [9–11]. Notably, PMa-SynRMs exhibit exceptional power density in high-speed applications through optimized structural design, alongside improved efficiency and reduced torque ripple; attributes that make them well-suited for electric vehicle propulsion [12–14]. Extensive research has further validated their effectiveness in such applications, yielding significant technical information [15–18]. In [19], the SynRM of the rotor structure with flux barriers is proposed, and the two types of rotors are compared using 2-D finite-element analysis. The results show that the rotor structure with flux barriers is more effective in generating torque and suspension force. Reference [20] highlighted the suitability of external rotor PMa-SynRMs for hub motors in electric vehicles, successfully integrating them into the two-wheel drive systems of electric cars.

This paper introduces a novel asymmetric rotor permanent magnet-assisted synchronous reluctance motor (NAR-PMa-SynRM), which integrates embedded surface-mounted permanent magnet motor (Embedded-SPM) and SynRM technologies in a coherent manner. By employing mechanical rotation and an asymmetric rotor structure, the motor effectively harnesses both electromagnetic torque and reluctance torque. In this configuration, tile-shaped PMs are embedded on the rotor surface, akin to surface-mounted PM motors. The rotor core features an asymmetric design of magnetic barriers, where each layer of barriers can be independently designed in terms of angle and length.

The work presented in this paper is at the preliminary design stage of the NAR-PMa-SynRM. A equivalent magnetic network (EMN) model tailored to the specific structure of NAR-PMa-SynRM is proposed, alongside a simplified equivalent method during the modeling process. Results from the EMN model align closely with finite element analysis (FEA) results, validating the effectiveness of the proposed equivalent method and the accuracy of the EMN model. Based on the EMN model, an initial electromagnetic design of the motor is conducted. FEA results indicate that compared to Embedded-SPM, NAR-PMa-SynRM demonstrates superior output capability. In section II, the structure and key parameters of NAR-PMa-SynRM are presented. Section III outlines the modeling and computational methodologies of the EMN model and equivalent methods tailored specifically for NAR-PMa-SynRM. These approaches are aimed at accurately capturing the motor's electromagnetic characteristics. Validation of these methods against FEA results demonstrates their reliability and effectiveness. In section IV, the structure preliminarily designed based on the EMN model is implemented in a finite element model, where both no-load characteristics and rated output performance are analyzed. Finally, in section V, a summary of the paper is presented.

II. DESCRIPTION OF NOVEL ASYMMETRIC ROTOR PERMANENT MAGNET-ASSISTED SYNCHRONOUS RELUCTANCE MOTOR

The NAR-PMa-SynRM integrates elements from Embedded-SPM and SynRM. Unlike conventional PMa-SynRM, the NAR-PMa-SynRM adopts a configuration where tile-shaped PMs are embedded along the rotor's d-axis, and the rotor core's magnetic barriers feature an

asymmetric design. These innovations aim to enhance torque output and minimize torque ripple. Figure 1 depicts a two-dimensional cross-section of the NAR-PMa-SynRM rotor structure. Here, the radial direction with the least reluctance is identified as the d-axis, whereas the radial direction along the centerline of the magnetic barrier is termed the q-axis. A mechanical angular offset of β/P is present between the PMs and the rotor's d-axis.

The design criteria for the NAR-PMa-SynRM are outlined in Table 1, taking into consideration the power, spatial, and voltage requirements of electric vehicle drive systems. Given constraints on enclosure size and installation space, the stator core has an outer diameter of 175 mm. Moreover, the power system mandates a 380 V DC bus voltage to accommodate the machine's high-power output needs. Table 2 presents the principal parameters of the PM synchronous motor designed in accordance with these specifications. The machine features 36 slots and 4 poles, maintaining a rated current density of 10 A/mm^2 in preliminary designs. Initial design simulations using this current density suggest compliance with the requirements specified in Table 1.

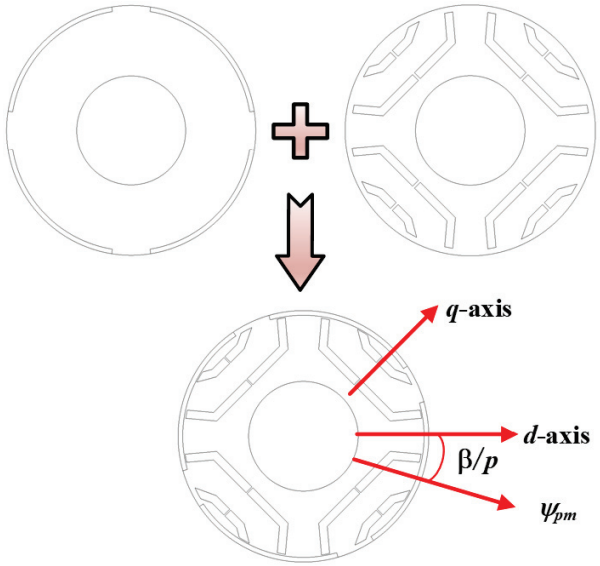

Fig. 1. Rotor structure of NAR-PMa-SynRM.

Table 1: Design requirements of the machine

Parameter	Value
Rated power (kW)	5.5
Rated speed (r/min)	3000
DC bus voltage (V)	380
Efficiency (%)	90
Outer diameter (mm)	175

Table 2: Main parameters of the NAR-PMa-SynRM

Parameter	Value
Slot/Pole number	36/4
Stator outer diameter (mm)	175
Stator inner diameter (mm)	93.5
Core length (mm)	50
Conductor diameter (mm)	0.8
Rated current density (A/mm^2)	10
Turns	16

The stator core and rotor core are assembled using stacked laminations of M350-50A silicon steel, known for its excellent electrical conductivity. NdFe35 magnets are utilized for the PM material. The stator windings employ 0.8 mm enamel-coated wire, with 16 turns per slot, utilizing a short-pitch winding configuration with a coil span of 8.

III. EQUIVALENT MAGNETIC NETWORK MODELING

Due to the motor's structural symmetry about the origin center, an EMN model of a 1-pair pole, 18-slot motor is established to reduce computational complexity and enhance computational speed. Based on the motor's flux distribution, three typical equivalent magnetic conductivities—axial, tangential, and radial—are determined. Diagrams illustrating these three typical flux directions are presented in Fig. 2, accompanied by their respective magnetic conductivity calculation formulas:

$$G_{axial} = \frac{\mu A_m}{l}, \tag{1}$$

$$G_{radial} = \frac{\mu l \theta}{\ln \frac{r_o}{r_i}}, \tag{2}$$

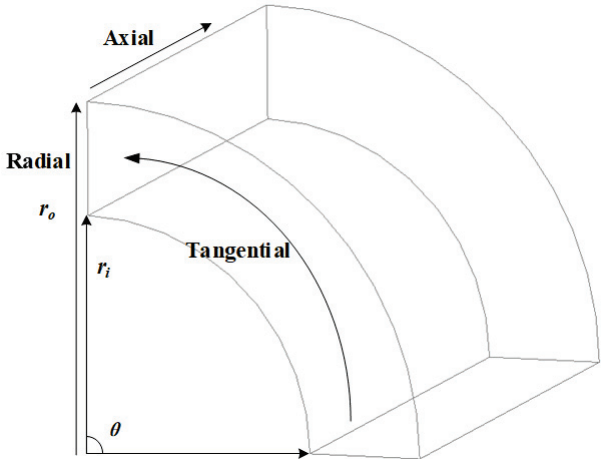

Fig. 2. Schematic diagram of typical flux directions.

$$G_{tangential} = \mu \frac{\ln \frac{r_o}{r_i}}{\theta} l, \tag{3}$$

where G_{axial} is the axial permeability, G_{radial} is the radial permeability, $G_{tangential}$ is the tangential permeability, l is the axial length of the unit, r_o is the outer diameter, r_i is the inner diameter, A_m is the area of the unit, θ is the arc of the center angle of the unit, μ is the relative permeability.

In the magnetic network method, the calculation of equivalent magnetic potential sources for magnetic field sources is divided into two parts: the armature reaction magnetic potential source generated by the current and the PM magnetic potential source generated by the PM. For the unloaded operation of a PM SynRM, only the PM provides the magnetic potential source, as the armature current is negligible (0 A) and does not contribute to the magnetic potential source. Thus, the calculation focuses solely on the equivalent magnetic potential source of the PM. Figure 3 depicts the model diagram of unit permanent magnet magnetic network.

The magnitude of the equivalent magnetic flux source of the PM and its intrinsic magnetic conductivity is expressed as follows, with the PM's intrinsic magnetic conductivity assumed to be linear:

$$\Phi_{pm} = B_r w_{pm} l_{pm}, \tag{4}$$

$$G_{pm} = \frac{\mu_0 \mu_{pm} w_{pm} l_{pm}}{h_{pm}}, \tag{5}$$

where Φ_{pm} is the PM equivalent flux source, G_{pm} is the self-permeability of a PM, B_r is the residual magnetic density of a PM, w_{pm} is the width of a PM, l_{pm} is the axial length of a PM, h_{pm} is the thickness of a PM, μ_0 is the vacuum permeability, μ_0 is relative permeability of a PM.

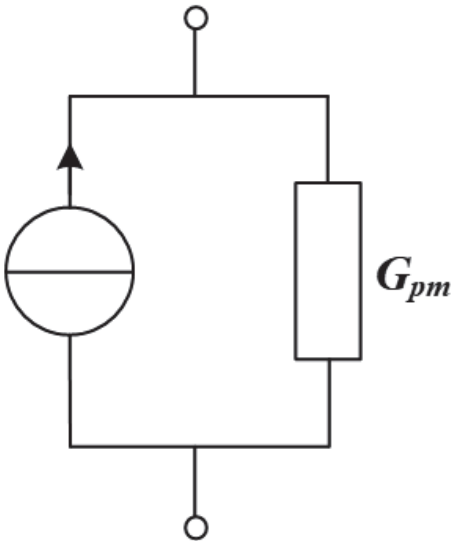

Fig. 3. Model diagram of unit permanent magnet magnetic network.

A. Magnetic barrier equivalent method

In the rotor structure of the NAR-PMa-SynRM, the magnetic barriers are dual-layered U-shaped, with slight variations in angles between the layers and between left and right sides. During magnetic network modeling, ensuring accuracy for the barriers and surrounding magnetic resistances poses challenges. Therefore, this paper proposes an effective method for barrier equivalence, significantly enhancing modeling precision, and meeting modeling requirements primarily through equations (1-3).

For simplifying the magnetic network modeling of the rotor structure, this paper equivalently models the magnetic barriers, central column, and surrounding iron core sections as sector-shaped structures. Each central column of the magnetic barriers per layer is taken as the equivalent center, transforming the same layer of magnetic barriers into sector rings around the motor's center circle. The schematic diagrams of the magnetic barriers before and after equivalence are depicted in Fig. 4. The specific calculations for equivalence are detailed as follows:

$$R_{o\_1} = \frac{R_{b\_r1} + R_{b\_r2}}{2}, \tag{6}$$

$$R_{i\_1} = R_{o\_1} - t_{b\_1}, \tag{7}$$

$$\theta 1 = \frac{180 \times 2}{\pi \cdot (R_{o\_1} + R_{i\_1})} \cdot l1, \tag{8}$$

$$l1 = (l_{b\_l} + l_{b\_r} + rib\_w1 + l_{b\_ll1} \cdot \cos(\alpha 1) + l_{b\_rr1} \cdot \cos(\alpha 2)), \tag{9}$$

$$\theta 7 = \sigma \cdot \theta 1 = \frac{rib\_w1}{l1} \cdot \theta 1, \tag{10}$$

$$R_{o\_2} = R_{i\_1} - t\_core, \tag{11}$$

$$R_{i\_2} = R_{o\_2} - t_{b\_2}, \tag{12}$$

$$\theta 2 = \frac{180 \times 2}{\pi \cdot (R_{o\_2} + R_{i\_2})} \cdot l2, \tag{13}$$

$$l2 = (l_{b\_l2} + l_{b\_r2} + rib\_w2 + l_{b\_ll2} \cdot \cos(\alpha 3) + l_{b\_rr2} \cdot \cos(\alpha 4)), \tag{14}$$

$$\theta 8 = \sigma \cdot \theta 2 = \frac{rib\_w2}{l2} \cdot \theta 2, \tag{15}$$

where R_{o_1} is the outside radius of the first layer of magnet barriers, R_{i_1} is the inside radius of the first layer of magnet barriers, R_{b_r1} is the radius of the inner side of the transverse barrier, R_{b_r2} is the radius of the outer side of the transverse barrier, t_core is the thickness between the first layer and second layer of magnet barriers, rib_w1 and rib_w2 are the widths of the first- and second-layer center columns, respectively, $\theta 1$ to $\theta 8$ are the radians of each part of the magnetic barrier.

In the research on rotor magnetic barrier equivalence, [21] focuses on multi-layer flux barriers in symmetric SynRMs, adopting a topology partition method to decompose barriers into fan-shaped subdomains and

integrating an equivalent current method to simulate saturation, though its partition process is relatively complex and primarily suited for symmetric structures. Reference [22] targets two-layered rectangular barriers in symmetric delta-type IPM motors, reconstructing them into equivalent spoke-type magnets via magnetic equivalent circuits and equivalent air-gap functions, which relies heavily on material parameter calibration. In contrast, this paper addresses dual-layer U-shaped asymmetric magnetic barriers in NAR-PMa-SynRM by equivalently transforming barriers, central columns, and surrounding iron cores into sector rings centered on the central column. This method directly preserves the original asymmetric structural features, with validation showing good consistency in back-EMF, air-gap flux density, and their harmonics with the initial model, achieving a better balance between simplicity and accuracy, especially in adapting to asymmetric structures.

The equivalent rotor structure of the NAR-PMa-SynRM, as shown in Fig. 4, can be modeled using sectorial units for the entire rotor section in magnetic network analysis. Figure 5 depicts the no-load back electromotive force (EMF) waveforms of the motor before and after equivalence at rated speed (3000 r/min). Specifically, the amplitude of the line back-EMF prior to equivalence is 158 V, while that after equivalence is 152 V, resulting in an error of only 3.8%. In terms of harmonics, the 3rd and 5th harmonics are slightly reduced, while the 7th and 9th harmonics are slightly increased. It is observed that the amplitude of the equivalent EMF decreases slightly, while maintaining good sinusoidal characteristics. Figure 6 presents the Fourier decomposition of the no-load EMF before and after equivalence, revealing a reduction in fundamental, 3rd, and 5th harmonic amplitudes after equivalence, with an increase in seventh and ninth harmonic amplitudes.

Figure 7 illustrates the air-gap flux density of the motor before and after equivalence at rated speed (3000 r/min). The waveform of air-gap flux density remains largely consistent before and after equivalence, with a

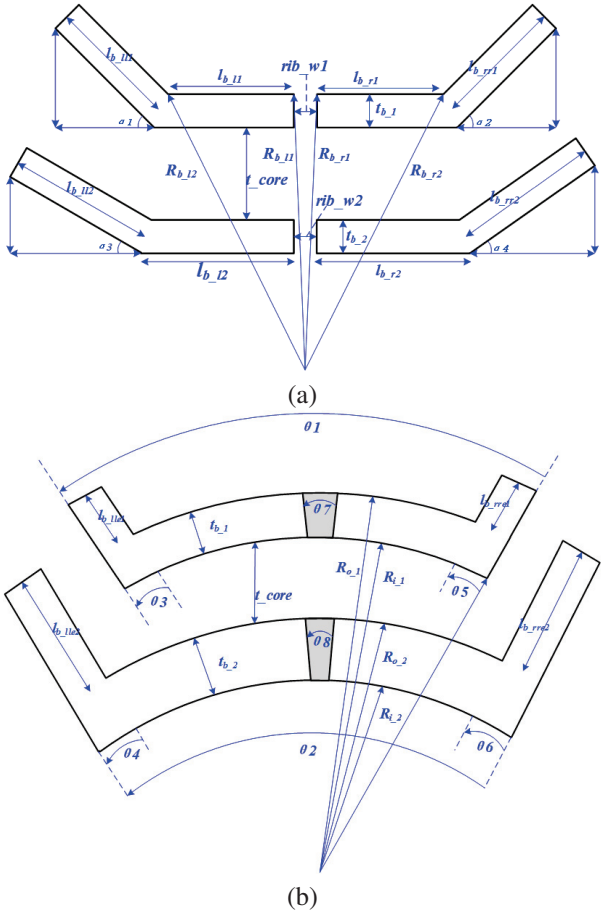

Fig. 4. Equivalent schematic of the rotor magnetic barrier: (a) before equivalence and (b) after equivalence.

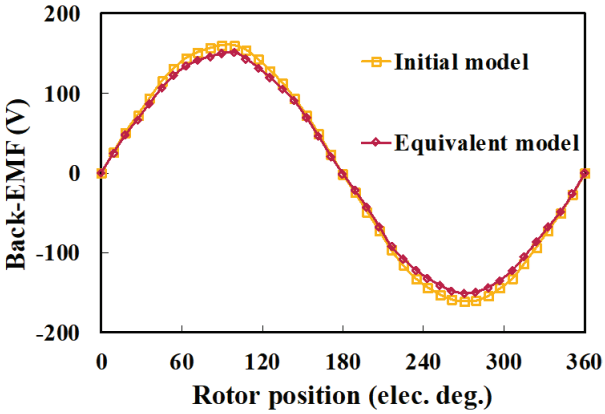

Fig. 5. Back-EMF waveforms of the motor before and after equivalence at rated speed (3000 r/min).

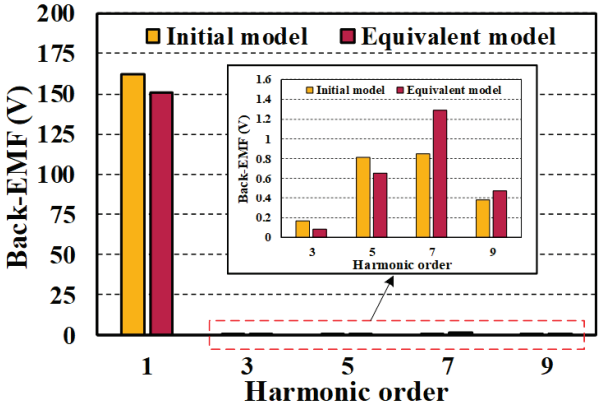

Fig. 6. Harmonic component of back-EMFs.

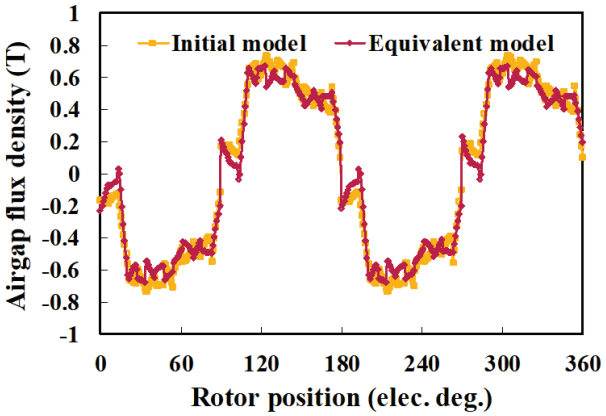

Fig. 7. Airgap flux density of the motor before and after equivalence.

slight decrease in flux density amplitude after equivalence, within acceptable error margins. Figure 8 shows the Fourier decomposition of the air-gap flux density of the motor before and after equivalence.

In terms of the harmonic distribution of the overall waveform, the equivalent model and the initial model show a high degree of consistency in harmonic trends (a decrease in low-order harmonics and an increase in high-order harmonics). Combined with the controllable attenuation degree of the fundamental wave, it further verifies the effectiveness of the simplified modeling method in preserving the core characteristics of the magnetic network.

Figure 9 presents a cross-section of the magnetic network model of NAR-PMa-SynRM. Figure 9 illustrates the magnetic circuit connections of selected magnetic network units.

It is evident that the magnetic circuit structure of the stator core is relatively straightforward, whereas that of the rotor is more intricate. The PMs are not perfectly

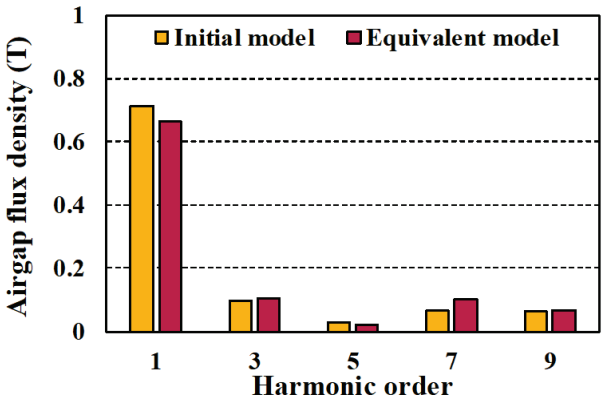

Fig. 8. Harmonic component of airgap flux density.

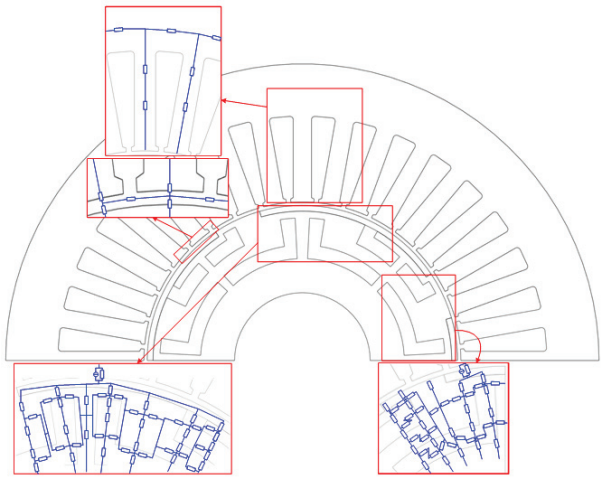

Fig. 9. Schematic representation of the cross-section of the EMN model.

aligned with the rotor d-axis, resulting in certain magnetic bridges being in close proximity to the air gap. This complex magnetic barrier structure causes significant differences in the magnetic paths of the rotor in the radial and tangential directions. The EMN model is built through three key steps, with clear boundary conditions defined for credibility:

(1) Break down continuous magnetic flux paths into distinct segments. (2) For each segment, calculate magnetic reluctance based on its length, cross-sectional area, and material permeability. PMs are treated as equivalent magnetomotive force sources. (3) Construct the network using nodes (junctions where flux paths meet) and branches (combining reluctance segments and magnetomotive force sources). The network follows basic magnetic laws: flux is conserved at nodes (incoming flux equals outgoing flux), and the total magnetomotive force in a closed loop balances the magnetic "drops" across reluctance segments.

Flux remains continuous at material interfaces (e.g., between iron cores and air gaps). Nodes within high-permeability iron cores are considered equipotential (minimal magnetic potential variation). Symmetry constraints (if the system is symmetric) simplify the network by enforcing balanced flux distribution at symmetry axes.

The principles of the EMN circuit were employed to develop a corresponding DC circuit model in Simulink for computing the two-dimensional EMN model, as illustrated in Fig. 10. During the no-load condition of the motor, an iterative method was employed to calculate the magnetic flux through each magnetic reluctance, thereby determining the operational state of the entire motor magnetic circuit. The approach involved initially assigning predefined values to each reluctance and

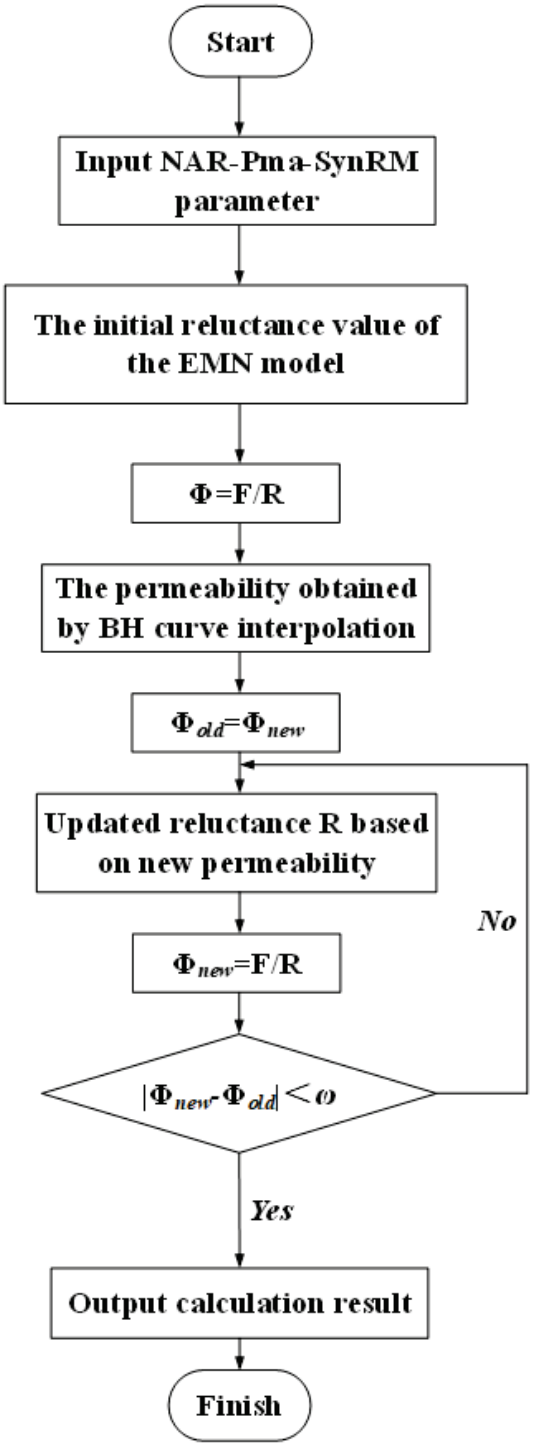

Fig. 10. Flow chart of EMN model method calculation.

subsequently allocating these values to the corresponding resistances in the Simulink EMN model. Through Simulink simulation, the flux through each reluctance was computed, and these values were returned to the MATLAB workspace as predefined flux values. Using these flux values, the magnetic induction intensity of each partition cell was calculated, followed by redefining the permeability of each unit through interpolation of the magnetization curve.

The reluctance values of each partition unit were recalculated and assigned to the corresponding resistances in the Simulink EMN model. Subsequent simulation through Simulink computed the flux through each reluctance and returned these values to the MATLAB workspace. The computed flux values were compared with the predefined values, and if the difference fell within the specified reference range, the computation met the requirements and thus concluded. Otherwise, the magnetic flux was iteratively adjusted using the Aitken acceleration convergence algorithm until the desired accuracy was achieved.

Figure 11 displays the air-gap magnetic flux density results computed by the EMN model. The amplitude of the air-gap magnetic flux density is 0.643. The initial model yielded an air-gap magnetic flux density amplitude of 0.712, while the equivalent model produced 0.664. The error in the air-gap magnetic flux density amplitude is within a reasonable range. However, due to the limited number of sampling points, the fitted curve does not perfectly coincide with the curve of the original model. A finer sampling method would yield a more accurate curve but at the expense of increased computational time. The above results prove the effectiveness of the EMN model.

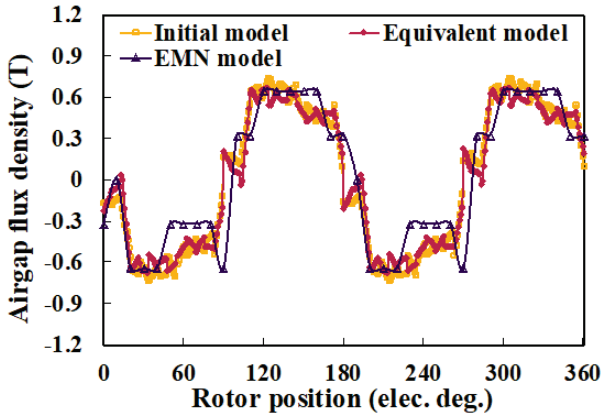

Fig. 11. Results of air gap flux density calculated by EMN model.

IV. FINITE ELEMENT ANALYSIS

Building upon the EMN model, a preliminary design of the motor's stator-rotor structure is conducted to facilitate efficient parametric iterations during the conceptual design phase. Figure 12 presents the no-load magnetic field distribution of the motor. As visualized, magnetic flux emanating from the stator teeth travels through the

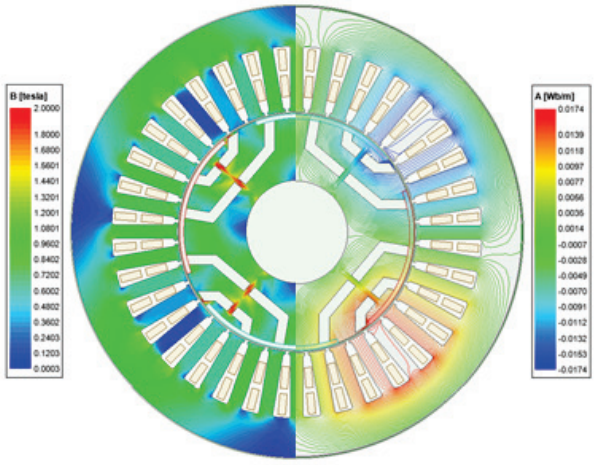

Fig. 12. No-load magnetic field distribution of the preliminarily designed NAR-PMa-SynRM.

airgap, penetrates the rotor pole shoes, and converges at the rotor magnetic bridges, where significant magnetic saturation occurs. This saturation arises due to the narrow width of the magnetic bridges, which increases local magnetic reluctance and concentrates the flux density in these regions. Given that the magnetic bridges are made of electrical steel (with a saturation flux density of approximately 1.8T), the concentrated flux easily drives these areas into saturation even under no-load conditions.

Figure 13 illustrates the open-circuit back-EMF waveforms of the Embedded-SPM and NAR-PMa-SynRM. It can be observed that both motors exhibit well-maintained sinusoidal characteristics in their EMF waveforms. The amplitude of the back-EMF in NAR-PMa-SynRM is slightly lower compared to that in Embedded-SPM, attributable to mechanical rotation of the PMs.

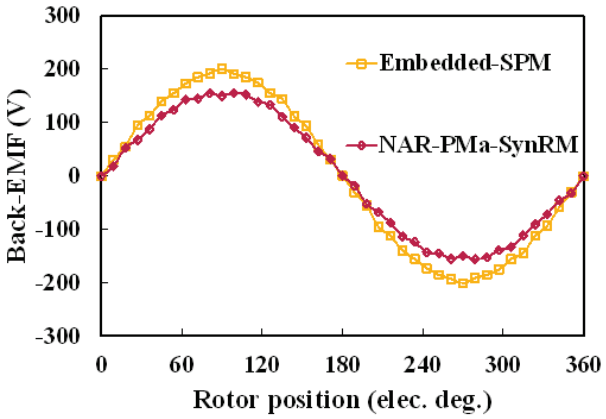

Fig. 13. No-load line back-EMF of the preliminarily designed NAR-PMa-SynRM.

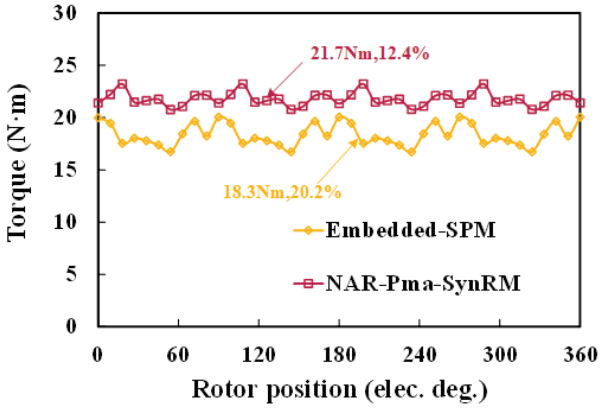

Fig. 14. Output torque of the preliminary designed NAR-PMa-SynRM is at the rated operating condition.

Figure 14 depicts the torque waveform of the motor under rated conditions. Leveraging both electromagnetic torque and reluctance torque effectively, NAR-PMa-SynRM exhibits an average torque increase of 18.6% compared to Embedded-SPM, with a reduction in torque ripple by 7.8%.

V. CONCLUSION

This paper introduces a novel asymmetric rotor permanent magnet-assisted synchronous reluctance motor (NAR-PMa-SynRM), integrating embedded surface-mounted PM technology with SynRM principles to enhance motor output performance by effectively leveraging both electromagnetic and reluctance torque. The focus of this study lies in the preliminary design phase of the motor, which includes the development of a magnetic network model tailored specifically for NAR-PMa-SynRM. To simplify the modeling process and improve the accuracy of rotor magnetic circuit equivalences, a simplified equivalent method is proposed. The computational results of the equivalent magnetic network (EMN) model align closely with finite element analysis (FEA) results, validating the effectiveness of the proposed EMN model and equivalent methods. Subsequently, based on the preliminary design outcomes derived from the EMN model, a finite element model is established. The results demonstrate that NAR-PMa-SynRM achieves an average torque increase of 18.6% compared to Embedded-SPM, with a reduction in torque ripple by 7.8%.

This study demonstrates the substantial potential of NAR-PMa-SynRM in terms of output performance. Future efforts in refining the design of NAR-PMa-SynRM will involve detailed parameterization, multi-objective optimization, and the integration of multi-physics coupling for equivalent stress and thermal management.

ACKNOWLEDGEMENT

This work was supported by the 2023 China-CEEC University Joint Education Program (2023304).

REFERENCES

[1] X. Zhou, X. Zhu, W. Wu, Z. Xiang, Y. Liu, and L. Quan, "Multi-objective optimization design of variable-saliency-ratio PM motor considering driving cycles," *IEEE Transactions on Industrial Electronics*, vol. 68, no. 8, pp. 6516-6526, Aug. 2021.

[2] A. M. El-Refaie, "Fractional-slot concentrated-windings synchronous permanent magnet machines: opportunities and challenges," *IEEE Transactions on Industrial Electronics*, vol. 57, no. 1, pp. 107-121, Jan. 2010.

[3] K. T. Chau, C. C. Chan, and C. Liu, "Overview of permanent-magnet brushless drives for electric and hybrid electric vehicles," *IEEE Transactions on Industrial Electronics*, vol. 55, no. 6, pp. 2246-2257, June 2008.

[4] S. Zheng, X. Zhu, L. Xu, Z. Xiang, L. Quan, and B. Yu, "Multi-objective optimization design of a multi-permanent-magnet motor considering magnet characteristic variation effects," *IEEE Transactions on Industrial Electronics*, vol. 69, no. 4, pp. 3428-3438, Apr. 2022.

[5] A. Vagati, "The synchronous reluctance solution: A new alternative in ac drives," in *Proc. 20th Int. Conf. Ind. Electron., Control Instrum.*, vol. 1, pp. 1-13, Sep. 1994.

[6] A. Boglietti, A. Cavagnino, M. Pastorelli, and A. Vagati, "Experimental comparison of induction and synchronous reluctance motors performance," in *Proc. 14th IAS Annu. Meet. Conf. Rec. Ind. Appl. Conf.*, vol. 1, pp. 474-479, 2005.

[7] A. T. de Almeida, F. J. T. E. Ferreira, and G. Baoming, "Beyond induction motors—Technology trends to move up efficiency," *IEEE Transactions on Industry Applications*, vol. 50, no. 3, pp. 2103-2114, May/June 2014.

[8] R. R. Moghaddam and F. Gyllensten, "Novel high-performance SynRM design method: An easy approach for a complicated rotor topology," *IEEE Transactions on Industrial Electronics*, vol. 61, no. 9, pp. 5058-5065, Sep. 2014.

[9] M. Xu, G. Liu, Q. Chen, J. Ji, and W. Zhao, "Design and optimization of a fault tolerant modular permanent magnet assisted synchronous reluctance motor with torque ripple minimization," *IEEE Trans. Ind. Electron.*, vol. 68, no. 9, pp. 8519-8530, Sep. 2021.

[10] M. Z. Islam, A. Arafat, S. S. R. Bonthu, and S. Choi, "Design of a robust five-phase ferrite-assisted synchronous reluctance motor with low demagnetization and mechanical deformation," *IEEE Trans. Energy Convers.*, vol. 34, no. 2, pp. 722-730, June 2019.

[11] S. Ciceo, F. Chauvicourt, B. Varaticeanu, J. Gyselinck, and C. Martis, "PMASynRM late design-stage rotor shape NVH optimization," in *Proc. IEEE Int. Conf. Elect. Mach.*, pp. 278-283, 2020.

[12] G. Gallicchio, M. D. Nardo, M. Palmieri, A. Marfoli, M. Degano, C. Gerada, and F. Cupertino, "High speed permanent magnet assisted synchronous reluctance machines - Part I: A general design approach," *IEEE Transactions on Energy Conversion*, vol. 37, no. 4, pp. 2556-2566, Dec. 2022.

[13] Y.-H. Jeong, K. Kim, Y.-J. Kim, B.-S. Park, and S.-Y. Jung, "Design characteristics of PMa-SynRM and performance comparison with IPMSM based on numerical analysis," in *2012 XXth International Conference on Electrical Machines*, Marseille, France, pp. 164-170, 2012.

[14] S. S. Maroufian and P. Pillay, "Design and analysis of a novel pm-assisted synchronous reluctance machine topology with AlNiCo magnets," *IEEE Transactions on Industry Applications*, vol. 55, no. 5, pp. 4733-4742, Sep.-Oct. 2019.

[15] T. Teratani, K. Kuramochi, H. Nakao, T. Tachibana, K. Yagi, and S. Abou, "Development of Toyota mild hybrid system (THS-M) with 42V power net," in *IEEE International Electric Machines and Drives Conference 2003* (*IEMDC'03*), Madison, WI, USA, vol. 1, pp. 3-10, 2003.

[16] I. Boldea, "Automobile electrification trends: A review," in *2007 International Aegean Conference on Electrical Machines and Power Electronics*, Bodrum, Turkey, pp. 369-377, 2007.

[17] L. Tutelea, A. M. Popa, and I. Boldea, "50/100 kW, 1350-7000 rpm (600 Nm peak torque, 40 kg) PM assisted reluctance synchronous machine: Optimal design with FEM validation and vector control," in *2014 International Conference on Optimization of Electrical and Electronic Equipment (OPTIM)*, Bran, Romania, pp. 276-283, 2014.

[18] M. Ferrari, N. Bianchi, and E. Fornasiero, "Analysis of rotor saturation in synchronous reluctance and pm-assisted reluctance motors," *IEEE Transactions on Industry Applications*, vol. 51, no. 1, pp. 169-177, Jan.-Feb. 2015.

[19] M. Takemoto, K. Yoshida, N. Itasaka, Y. Tanaka, A. Chiba, and T. Fukao, "Synchronous reluctance type bearingless motors with multi-flux barriers," in *2007 Power Conversion Conference*, Nagoya, Japan, pp. 1559-1564, 2007.

[20] Y. Deshpande and H. A. Toliyat, "Design of an outer rotor ferrite assisted synchronous reluctance

machine (Fa-SynRM) for electric twowheeler application," in *2014 IEEE Energy Conversion Congress and Exposition (ECCE)*, Pittsburgh, PA, USA, pp. 3147-3154, 2014.

[21] H. Zhou, X. Wang, W. Zhao, Z. Xing, and J. Liu, "Research on magnetic field prediction of synchronous reluctance motor considering structure of multilayer flux barrier and saturation of rotor core," *IEEE Transactions on Transportation Electrification*, vol. 11, no. 2, pp. 5983-5998, Apr. 2025.

[22] P. Wu and Y. Sun, "A novel analytical model for on-load performance prediction of delta-type IPM motors based on rotor simplification," *IEEE Transactions on Industrial Electronics*, vol. 71, no. 7, pp. 6841-6851, July 2024.

Hao Chen (SM'08) received the B.S. and Ph.D. degrees from the Department of Automatic Control, Nanjing University of Aeronautics and Astronautics, Nanjing, China, in 1991 and 1996, respectively. In 1998, he became an Associate Professor with the School of Information and Electrical Engineering, China University of Mining and Technology, Xuzhou, China, where he has been a Professor since 2001. From 2002 to 2003, he was a Visiting Professor at Kyungsung University, Busan, Korea. Since 2008, he has also been an Adjunct Professor at the University of Western Australia, Perth, Australia. He is the author of one book and has also authored more than 190 papers. He is the holder of 14 US Patents, 23 Australian Patents, one Danish Patent, seven Canadian Patents, three South African Patents, 10 Russian Patents, 44 Chinese Invention Patents and six Chinese Utility Model Patents. His current research interests include motor control, linear launcher, electric vehicles, electric traction, servo drives, and wind power generator control.

Chen was the recipient of both the Prize of Science and Technology of Chinese Youth and the Prize of the Fok Ying Tong Education Foundation for Youth Teachers in both 2004. He was awarded the first prize in the Science and Technology advanced of Province and Ministry once, the second prize in the Science and Technology advanced of Province and Ministry seven times, and the third prize in the Science and Technology advanced of Province and Ministry 14 times. He became the Chinese New Century Hundred-Thousand Ten-Thousand Talents Engineering National Talent in 2007 and won the Government Especial Allowance of People's Republic of China State Department since 2006.

Ziqiang Wei received the B.S. degree in electrical engineering from Changzhou Institute of Technology, Changzhou, China, in 2020, and the M.S. degree in electrical engineering from Nanjing Normal University, Nanjing, China, in 2023. He is currently pursuing a Ph.D. degree in electrical engineering at China University of Mining and Technology, Xuzhou, China. His research interests include permanent magnet-assisted synchronous reluctance motor and electric vehicle motor drive system.

Xing Wang received the B.S. degree from China University of Mining and Technology, Xuzhou Jiangsu, China, in 1996, and M.S. degree from China University of Mining and Technology, Xuzhou Jiangsu, China, in 1999. In 2007, she became an Associate Professor with China University of Mining and Technology, Xuzhou, China. She is a holder of four US Patents, nine Australian Patents, two Canadian Patents, four Russian Patents, 12 Chinese Invention Patents, three Chinese Utility Model Patents, and has authored 15 papers.

Shudong Hou founded Nanjing Enchuan New Energy Power System Co. Ltd., and in September 2022, he won the third prize in the high-level talent entrepreneurship competition in Zaozhuang, Shandong. In 2024, he founded Nexus Intelligent Equipment (Zhejiang) Co., Ltd. and serves as its chairman. He has presided over the research, development, production and sales of motor and controller systems for many years.

Antonino Musolino received his Ph.D. degree in electrical engineering from the University of Pisa, Pisa, Italy, in 1994. He is currently a Full Professor of electrical machines at the University of Pisa. He has co-authored more than 130 papers published in international journals/conferences. He holds three international patents in the field of magnetorheological devices. His current research activities are focused on linear electromagnetic devices, motor drives for electric traction, and the development of analytical and numerical

methods in electromagnetics. Musolino was involved in the organization of several international conferences, where he has served as the session chairman and an organizer, and as a member of the editorial board.

Murat Shamiyev received the B.S. and M.S. degrees from Tashkent State Technical University, Tashkent, Uzbekistan, in 1999 and 2001, respectively. He served as a Professor's Assistant at the Department of Electro-mechanics and Electrotechnology, Faculty of Energy, Tashkent State Technical University from 2001 to 2005. Following that, he held the position of Head Specialist at Azia Triol Joint Venture (Russia and Uzbekistan) from 2005 to 2007. Subsequently, he served as a Technical Director at "[illegible]" LLC from 2007 to 2010. He then took on the role of Director at Techno Energo Group LLC. Currently, he holds the position of Head Engineer at Techno Energo Group LLC.

Pulatov Abror Abidovich is head of the Department of Electrical Machinery and Electrical Technology at Tashkent State Technical University. His main monographs include "Thermal Operating Conditions of Induction Crucible Furnaces," "Instruction Manual for Electrical Equipment and Power Supply in Mining Enterprises," "Guide to Laboratory Work in Electrical Technology Fundamentals," and "Design and Operation of Electrical Technology Devices." His main research directions include the research on inductors of smelting devices, monitoring, control and regulation of asynchronous motor devices. He is a Member of the Academic Committee of the "International Joint Research Center for New Energy Electric Vehicle Technology and Equipment in Central and Eastern European Countries" of the Ministry of Science and Technology of China, member of the Academic Committee of the International Cooperation Joint Laboratory for New Energy Generation and Electric Vehicles of Jiangsu Province's Universities, and member of the "New Energy Generation and Electric Vehicles" Foreign Expert Studio in Jiangsu Province.

Emmanuel Karapidakis is a professor in the Department of Power Systems at the School of Electrical and Computer Engineering of the Mediterranean University. His area of expertise is Integrating Renewable Energy Technologies into Power Systems. He holds a degree in Electrical and Computer Engineering from the Mediterranean University (1997) and a Ph.D. in Power Systems from the same university (2003). He served as a consultant for public and private construction companies (1998-2003, Athens) and as the Director of Project Evaluation and Implementation at the intermediate management organization ANK (2003-2005, Heraklion). Since 2022, he has been the President of the Hellenic Association of Energy Storage Systems (HAESS). Karapidakis has completed numerous national and European competitive projects and has published over 60 papers in international scientific journals in his field of research. His research interests include integrating renewable energy sources (RES) into power systems, power markets, energy storage systems, electric vehicles, and energy transition.

Aris Dimeas (IEEE Member) received his B.Sc. and Ph.D. degrees in Electrical and Computer Engineering from the National Technical University of Athens. Currently, he is a professor in the Department of Electrical and Computer Engineering at the same university. He has extensive experience in power system operation, renewable energy, artificial intelligence applications in power systems, smart grids, and control software development. He is particularly skilled in the development of demand-side management control software and the design of communication interfaces between energy management systems (EMS) and supervisory control and data acquisition systems (SCADA). He has collaborated with multiple departments of PPC and the Greek Distribution Network Operator (HEDNO) in areas such as electronic meters, smart grids, and research projects. He has authored or co-authored over 80 conference papers and journal articles. His teaching responsibilities include undergraduate courses such as "Industrial Electronics," "Electrical Energy Systems," and "Power System Analysis," as well as the graduate course " Probabilistic Analysis of Power Systems."

Sherif Moussa is the Dean of the School of Engineering, Applied Science, and Technology at the Canadian University Dubai (CUD), UAE. He earned his Ph.D. in Electrical and Computer Engineering from the University of Québec at Trois-Rivières, Canada, and his M.Sc. in Electrical and Computer Engineering from the University of Waterloo, Canada. Since joining CUD in 2007, Dr. Moussa has led the School's remarkable growth, overseeing the launch and accreditation of several engineering and computing programs, including Mechatronics Engineering, Computer Science, Cybersecurity, Software Design, Power and Renewable Energy Engineering, and the MSc in Artificial Intelligence. Dr. Moussa's research interests span wireless communication, computer networks, machine learning, and digital systems design. He has published widely in international journals and conferences, serves on technical committees, and is the recipient of the 2015 CUD Research Excellence Award. He is also the founder of CUD's Robotics Club and a strong advocate for innovation and experiential learning in engineering education.

Design and Analysis of Modular Transverse Flux Dual-rotor Switched Reluctance Motor

Hemiao Liu[1], Xing Wang[2], Hao Chen[1,2,3,4,5], Jun Bao[6], Haidong Yan[6], Guanjun Wang[6], and Yassen Gorbounov[7]

[1]School of Electrical Engineering
China University of Mining and Technology, Xuzhou 221116, China
TB22230006A41@cumt.edu.cn, hchen@cumt.edu.cn

[2]International Joint Research Center of Central and Eastern European Countries on New Energy Electric Vehicle Technology and Equipment
Xuzhou 221008, China
3512@cumt.edu.cn

[3]International Cooperation Joint Laboratory of New Energy Power Generation and Electric Vehicles of Jiangsu Province Colleges and Universities
Xuzhou 221008, China

[4]Jiangsu Province Foreign Expert Workshop on New Energy Power Generation and Electric Transportation
Xuzhou 221008, China

[5]Shenzhen Research Institute
China University of Mining and Technology, Shenzhen 518057, China

[6]Wuxi Institute of Inspection, Testing and Certification
Wuxi 214101, China
jsmtc12@126.com, yhd@wxmtc.com, wgjcumt@126.com

[7]New Bulgarian University
Sofia, Bulgaria
y.gorbounov@mgu.bg

***Abstract* –** The present study proposes a novel modular transverse flux dual-rotor switched reluctance motor (MTF-DRSRM), which integrates the operational principles of switched reluctance motors (SRMs) with the structural advantages of transverse flux machines (TFMs). The motor employs H-shaped modular stator cores and segmented rotor discs with embedded pole modules, employing toroidally-wound concentrated windings for excitation. Compared to conventional SRMs, the MTF-DRSRM leverages the transverse flux configuration to enable flexible decoupling of electric and magnetic loads. This design effectively enhances torque density and operational efficiency, making it suitable for high-performance drive applications such as electric vehicles. This paper introduces the fundamental structure, operational principles, and electromagnetic design methodology of the MTF-DRSRM. Due to the three-dimensional distribution of the motor's magnetic field, 3D magnetic field computation using finite element analysis (FEA) is employed to calculate key parameters, including magnetic flux linkage and torque characteristics. The design validation is performed by comparing theoretical parameters with 3D-FEA simulation results, ensuring accuracy and reliability. This work provides a robust theoretical foundation and empirical data for further optimization and practical implementation of the proposed motor topology.

***Index Terms* –** Electromagnetic design, finite element analysis, modular structure, switched reluctance motor, transverse flux.

I. INTRODUCTION

Switched reluctance motors (SRMs) are characterized by structural simplicity, high reliability, flexible control, operational efficiency, and exceptional

Submitted On: December 24, 2024
Accepted On: May 29, 2025

https://doi.org/10.13052/2025.ACES.J.400907

suitability for high-speed and harsh-environment applications. The development potential and performance advantages of SRM-based drive systems have reignited global research interest in this technology [1–2]. However, as application scenarios grow increasingly complex and performance requirements become more stringent, conventional SRMs exhibit limitations in critical metrics such as torque density and efficiency.

The advent of the transverse flux machine (TFM) concept has ushered in a novel paradigm for motor design, offering a distinctive magnetic field distribution pattern that has the potential to enhance torque density and generate more powerful torque within a confined space [3–4]. The incorporation of a dual rotor configuration serves to enhance the motor's energy conversion mechanisms and torque generation capabilities. This is achieved by leveraging the delicate electromagnetic interaction between the inner and outer rotors and the stator, thereby ensuring an overall enhancement in the motor's performance across all domains [5].

Current research efforts have historically concentrated energies on theoretical research, structural design, and control strategy in the domain of transverse flux switched reluctance motor research. Literature [6–7] utilizes finite element analysis (FEA) and other methods to model and analyze the internal magnetic field distribution of the motor, thereby facilitating the comprehension of the magnetic field strength, direction, and change rule. This, in turn, provides a theoretical foundation for the optimization of motor design. Research findings indicate that the introduction of transverse flux alters the magnetic field distribution, thereby affecting the electromagnetic performance of the motor. Literature [8–9] established a mathematical model that can accurately describe the electromagnetic characteristics of the motor and mechanical characteristics. The equivalent magnetic circuit method was used to establish mathematical models that can be used to analyze the dynamic performance of the motor, including speed, torque, current, and other parameters of the law of change. Concurrently, a series of innovative topologies have been proposed, including double U-shaped stator cores, I-type stator core, and U-type rotor core fit, with the objective of enhancing the motor's output torque, power density, and other performance metrics. These topologies have been shown to improve magnetic circuit coupling by increasing the number of poles and phases and by increasing the rotor radius to improve the output torque. As evidenced by the existing literature [10-11], the optimization of winding form, the number of turns, wire diameter, and other relevant parameters has been shown to reduce winding loss, thereby enhancing motor efficiency and power factor. This enhancement is achieved through the implementation of various winding configurations, including centralized and distributed winding, which have been studied in depth to ascertain their impact on motor performance. In the realm of control strategies, [12–13] have been instrumental in refining conventional methodologies such as current chopper control and angular position control. These refinements have been undertaken to mitigate torque pulsation, reduce noise, and enhance the smoothness and comfort of the motor. For instance, the optimization of frequency, amplitude, and other parameters of the current chopper has been a focal point of these studies. Concurrently, [14] explores the implementation of advanced intelligent control methodologies, including fuzzy control, neural network control, and sliding mode variable structure control, in transverse flux switched reluctance motors. The objective of these investigations is twofold: first, to enhance the control accuracy, response speed, and robustness of the motors and, second, to optimize their performance in complex working conditions, thereby ensuring the fulfillment of stringent control requirements.

This paper synthesizes the advantages of axial-field and conventional radial-field switched reluctance motors and proposes a modular transverse-flux dual-rotor switched reluctance motor. The motor is distinguished by a split-block rotor fixed on both sides of the motor on their respective rotor disks and a toroidally-wound concentrated winding. The space utilization of the stator part of this novel structure motor is greater in comparison to the traditional structure SRM, while the winding end effect is diminished. The rotor shaft utilizes a non-conducting material, which shortens the magnetic circuit and reduces the inter-pole magnetic leakage. The main features of a modular transverse flux dual-rotor switched reluctance motor (MTF-DRSRM) are as follows.

(a) The motor possesses greater space for winding storage and more flexible turn design. The stator and rotor are small and have shorter magnetic paths, which improves the motor efficiency.

(b) Individual windings are wound on the iron core, with reduced electromagnetic interference, facilitated heat dissipation, and simplified maintenance and winding.

(c) The motor's design is modular and highly expandable, allowing for adjustment of the number of phases and poles to increase output torque.

II. STRUCTURE AND OPERATING PRINCIPLE OF MTF-DRSRM

This paper presents an analytical study on the design of a three-phase 12/8-pole MTF-DRSRM. As shown in Fig. 1, the stator employs a segmented configuration comprising 12 identical H-shaped laminated cores

with toroidally-wound excitation coils, where three consecutive coils constitute the three-phase (ABC) excitation system. Each modular unit integrates multiple concentrated windings wound on specially profiled stator teeth, whose geometric parameters are optimized to enhance magnetic circuit efficiency and torque density. These stator segments maintain electromagnetic independence while being circumferentially symmetrical distributed, offering advantages in manufacturability, assembly, and maintenance, as well as flexible phase configuration adaptability. The rotor adopts a dual-rotor disc topology coaxially arranged with the stator, featuring eight ferromagnetic pole segments embedded in each rotor disc through precision-machined slots. Both stator and rotor cores are fabricated using grain-oriented silicon steel laminations processed by stacked lamination techniques. This manufacturing approach significantly facilitates modular production methodologies through standardized component design.

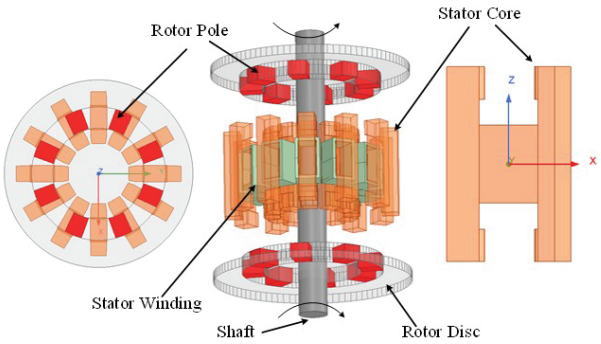

Fig. 1. Structure of three-phase 12/8-pole MTF-DRSRM.

When three-phase stator windings are electrically excited, magnetic flux is established through the stator teeth. As shown in Fig. 2, the MTF-DRSRM's magnetic circuit topology utilizes an H-shaped segmented core module in the stator, which magnetically couples with radially arranged dual rotor discs to form a closed magnetic path. At the stator-rotor unmagnetized position in Fig. 2 (a), the winding inductance reaches its minimum value. During this phase, DC pulse excitation is applied to the windings, establishing magnetic flux. Owing to the transverse flux path configuration, the magnetic flux predominantly traverses in the axial direction through stator teeth and rotor poles, inducing magnetic field distortion at rotor pole edges. This phenomenon generates reluctance torque that drives rotor rotation toward the aligned position. In the stator-rotor magnetized equilibrium position in Fig. 2 (b), the rotor poles align with the stator magnetic axis to minimize the magnetic reluctance path. Compared to conventional radial-flux switched reluctance motors (SRMs), the MTF-DRSRM

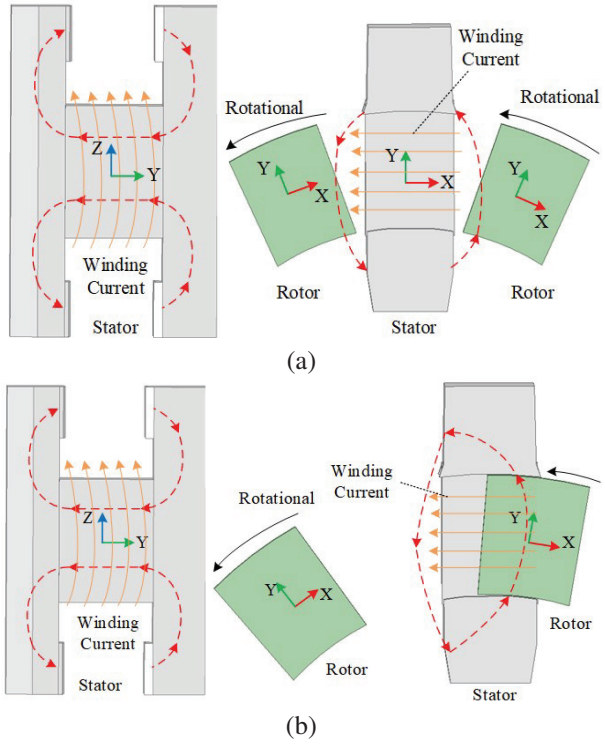

Fig. 2. Main magnetic circuit of the MTF-DRSRM: (a) stator and rotor misaligned position and (b) stator and rotor alignment position.

demonstrates significantly reduced winding overhang leakage flux, thereby improving magnetic circuit utilization efficiency. The compact axial dimension of the rotor enables high-speed operation (typically exceeding 10,000 rpm) and high specific power output. Additionally, the dual-rotor coaxial topology amplifies torque production through parallel magnetic circuit actuation, achieving torque superposition effects.

III. MAIN DIMENSIONS DESIGN OF MTF-DRSRM

The width and height of the stator teeth have a significant effect on the magnetic chain and torque of the motor. The number of turns of the stator winding determines the inductance and resistance of the winding, which in turn affects the current magnitude, torque, and efficiency of the motor. A reasonable selection of the number and angle of rotor teeth can reduce torque pulsation and improve the smoothness of motor operation. The thickness of the rotor core has been found to influence the magnetic field strength and the degree of magnetic circuit saturation of the motor. An excessively thin rotor core may lead to saturation of the magnetic circuit and reduce the performance of the motor, while an excessively thick core will increase the weight and

cost of the motor. Therefore, it is necessary to design the parameters of MTF-DRSRM. Figure 3 provides a schematic representation of the stator and rotor cores of MTF-DRSRM for dimensioning purposes.

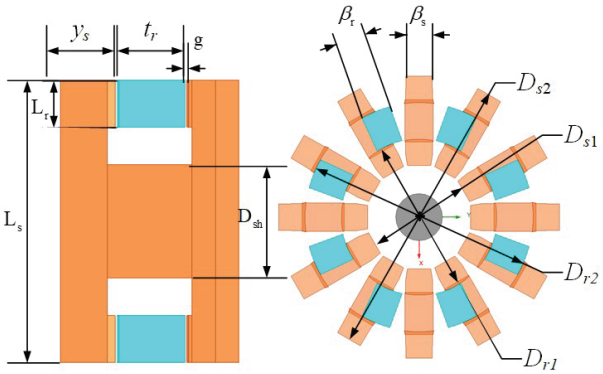

Fig. 3. Schematic illustration of stator and rotor core dimensioning for MTF-DRSRM.

According to Kirchhoff's law, the voltage equation of MTF-DRSRM for any phase can be derived:

$$u = Ri + \frac{\mathrm{d}\psi}{\mathrm{d}t} = Ri + \frac{\mathrm{d}(Li)}{\mathrm{d}t}, \tag{1}$$

where u is the terminal voltage, R is the stator resistance, i is the stator current, Ψ is the magnetic chain, L is the inductance.

During rotor-stator tooth overlap, a period of significant inductance changes where the inductive reactance dominates, the resistance R can be neglected for steady-state analysis. Equation (1) can thus be simplified to:

$$u = \frac{\mathrm{d}\psi}{\mathrm{d}t} = i\omega_m \frac{\mathrm{d}L}{\mathrm{d}\theta} = i\omega_m \frac{L_a - L_u}{\beta_s}, \tag{2}$$

where ω_m is the rotating mechanical angular velocity of the motor, L_a is the aligned position inductance, L_u is the unaligned position inductance, β_s is the stator pole arc.

Let us define k as the ratio of the inductance L_a at the aligned position to the inductance L_u at the unaligned position:

$$k = 1 - \frac{L_u}{L_a}. \tag{3}$$

Then, equation (2) can be rewritten as:

$$u = kL_a i \frac{\omega_m}{\beta_s}. \tag{4}$$

When the stator and rotor are aligned, the expression for the magnetic chain is:

$$\psi = L_a i = B_{sp} A_{sp} N_{\mathrm{ph}}, \tag{5}$$

where β_{sp} is the average magnetic density of the surface of the stator pole section at the aligned position, initially assumed to be 1.6 T. A_{sp} is the cross-sectional area of the stator pole and N_{ph} is the number of windings turns per phase of the motor.

MTF-DRSRM's adopt a double rotor structure and its stator cross-sectional area can be expressed as:

$$A_{sp} = \frac{2\pi D_{r1} L_r}{\beta_s}, \tag{6}$$

where D_{r1} is the rotor inner diameter and L_r is the rotor pole yoke thickness.

In the motor design, the rotor axial width t_r must be carefully controlled. On the one hand, t_r impacts overall motor volume; on the other, it influences coil slot fullness. Therefore, at the initial design stage, the rotor axial width is set equal to the stator axial width y_s, that is:

$$t_r = 1.4 y_s. \tag{7}$$

According to equations (4-6):

$$u = 2kB_{sp} H_s L_r N_{\mathrm{ph}} \omega_m. \tag{8}$$

Electrical load expression of the MTF-DRSRM can be written as:

$$A = \frac{2mN_{\mathrm{ph}} i}{\pi D_{s1}}, \tag{9}$$

where m is the number of phases and D_{s1} is the stator inner diameter. The initial assumed electrical load is 50000 A/m.

The load factor for switching one cycle of each phase of the winding is:

$$k_d = \frac{N_r \theta_c}{2\pi}, \tag{10}$$

where N_r is the number of rotor poles and θ_c is the opening angle of each phase.

The motor output power is:

$$P_{\mathrm{out}} = \eta m k_d u i, \tag{11}$$

where η is motor efficiency.

Substituting equations (6-8) into equation (9), the stator inner diameter D_{s1} of MTF-DRSRM is:

$$D_{s1} = \sqrt{\frac{2P_{out}}{k\eta N_r \theta_c B_s A \omega_m L_r \sin(\beta_s/2)}}. \tag{12}$$

Rotor inner diameter D_{r1} is taken as (1.8~2.5)D_{s1}.

In order to ensure that the MTF-DRSRM has a self-starting capability for forward and reverse rotation in any position, the stator-rotor pole arc needs to be satisfied:

$$\begin{cases} \beta_s + \beta_r \le 2\pi / N_r \\ \beta_s \ge \lambda \\ \beta_r \ge \beta_s \end{cases}, \tag{13}$$

where λ is the step angle $\lambda = 2\pi/(m \cdot N_r)$ and β_s is the rotor pole arc. In this paper, the rotor pole arc β_r is equal to the stator pole arc β_s.

The stator-rotor tooth width expression is:

$$\begin{cases} H_s = D_{s1} \sin\left(\frac{\beta_s}{2}\right) \\ H_r = D_{r1} \sin\left(\frac{\beta_r}{2}\right) \end{cases}. \tag{14}$$

The motor satisfies all conditions when $H_s = H_r$. The stator-rotor radial yoke thickness is chosen as:

$$\begin{cases} D_{sh} = (1.3 \sim 1.4) H_s \\ L_r = (1.3 \sim 1.4) \frac{H_s}{2} \end{cases}. \tag{15}$$

Table 1: Specific parameters of the designed prototype

Parameter	Value	Parameter	Value
Stator inner diameter D_{s1}	60 mm	Rated power P_N	4 kW
Stator outer diameter D_{s2}	220 mm	Phase number m	3
Rotor inner diameter D_{r1}	112 mm	Stator and rotor poles N_s/N_r	12/8
Rotor outer diameter D_{r2}	168 mm	Rated voltage U_N	300 V
Air gap g	0.4 mm	Rated speed n_N	1500 rpm
Stator radial yoke thickness D_{sh}	65 mm	Rotor radial yoke thickness L_r	25 mm
Stator tooth width H_s	17 mm	Rotor tooth width H_r	20 mm
Stator pole arc β_s	15 deg	Rotor pole arc β_r	15 deg
Stator axial width y_s	26 mm	Rotor axial width t_r	15 mm
Stator length L_s	135 mm	Turns of coil N_{ph}	50

The number of motor winding turns is:

$$N_{\text{ph}} = \frac{u\theta_c}{2B_{sp}H_sL_r\omega_m}. \tag{16}$$

Compared with the traditional axial motor, the MTF-DRSRM with double-rotor structure has a more centralized ring winding, higher potential, and high flexibility of winding space, which makes it suitable for designing it as a SRM with low rotational speed and high torque. The preliminary parameter design of the MTF-DRSRM can be carried out according to equations (1-15), and the motor parameters required for the load design are determined through several iterations of calculations. The specific parameters of the designed prototype are given in Table 1.

IV. 3D FINITE ELEMENT CALCULATION OF MTF-DRSRM

Electromagnetic performance of the designed MTF-DRSRM is simulated using the finite element method and, during the simulation and analysis, the effect of eddy currents in the core on the magnetic field is neglected. The core magnetic vector distributions in the stator and rotor at both aligned and unaligned positions were obtained under independent single-phase excitation, as shown in Figs. 4 and 5. In the aligned position, the average maximum magnetic density of the stator core is about 1.6 T.

Figure 6 shows the inductance characteristic curve for rotor position angles from 0° to 45° and currents from 5 A to 30 A, where 0° is the rotor inter-pole

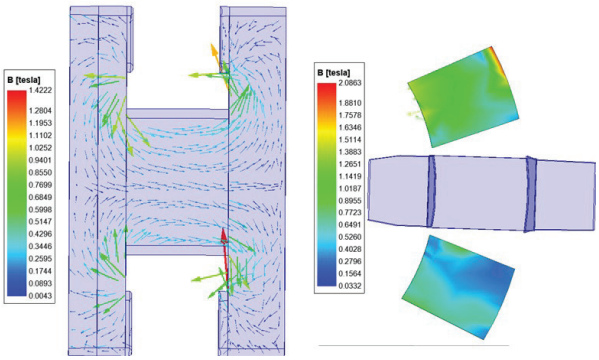

Fig. 4. Stator and rotor magnetic vector distribution under misaligned positions.

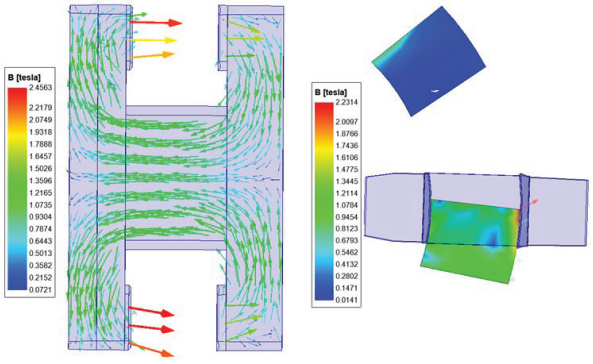

Fig. 5. Stator and rotor magnetic vector distribution under aligned positions.

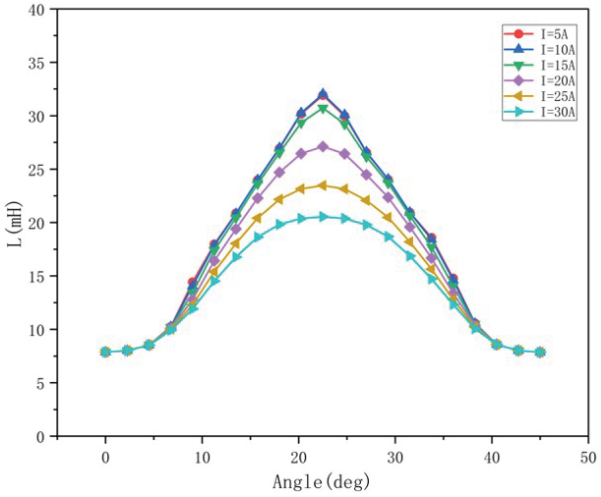

Fig. 6. Inductance characteristic curve.

centerline to the excitation pole centerline position, and 22.5° is the rotor pole centerline to the excitation pole centerline position. From Fig. 6, it can be seen that, for the three-phase 12/8-pole MTF-DRSRM, inductance increases with the increase of the rotor angle from 0° to 22.5° and decreases with the change of angle from 22.5° to 45°. The inductance period of this motor is 45° and is symmetrical about 22.5°.

Figure 7 shows the moment-angle characteristic curves for rotor position angle from 0° to 45° and current from 5 A to 30 A. In the range of rotor position angle 0° to 22.5°, $dL/d>0$, torque is positive. Torque increases with increase of current. In the range of rotor position angle 22.5° to 45°, $dL/d<0$, torque is negative, which is in line with theoretical derivation.

Figure 8 shows change of magnetic flux linked with three-phase curve for one operation cycle under angle control. When a phase of the motor conducts, the magnetic chain of the phase increases from 0. When the phase is disconnected, the magnetic chain reaches the maximum value, the winding renews the current, and the magnetic chain gradually decays to 0, and stays at 0 until the next cycle when the phase re-conducts. Figure 9 shows the three-phase rotating potential variation curve corresponding to the magnetic chain shown in Fig. 8.

The MTF-DRSRM is stabilized by angular position control (APC) to measure the dynamic performance of the motor under rated operating conditions. Figures 10, 11, and 12 show the torque, three-phase current, and inductance curves of the motor at the rated speed of 1500 r/min. Figure 10 shows the instantaneous synthetic torque waveforms measured by simulation, with the maximum torque of 32.12 N-m, the minimum torque of 13.65 N-m, the average torque of 22.6 N-m, and the torque fluctuation coefficient of about 40.86%. From Fig. 11, it can be seen that the phase current waveform and the corresponding phase potential waveform under APC control are ideal.

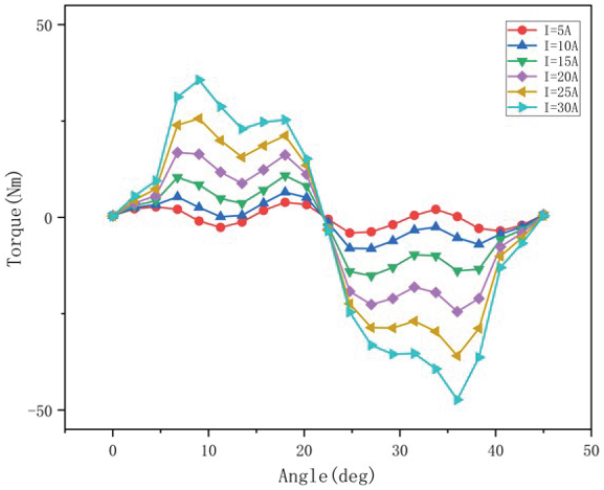

Fig. 7. Moment angle characteristic curve.

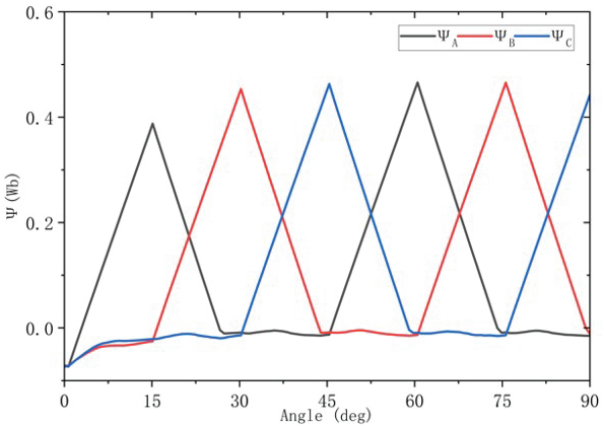

Fig. 8. Characteristic curve of magnetic chain.

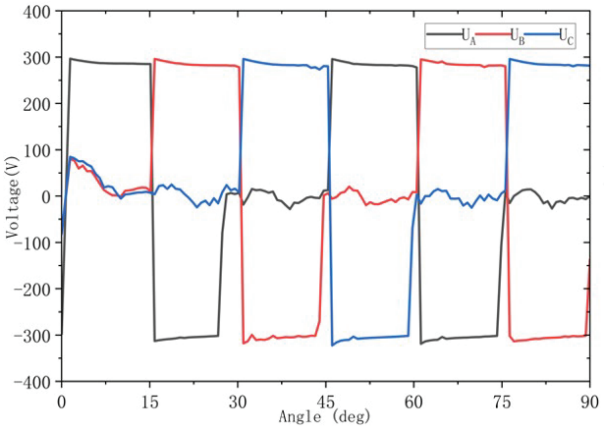

Fig. 9. Electric potential waveform.

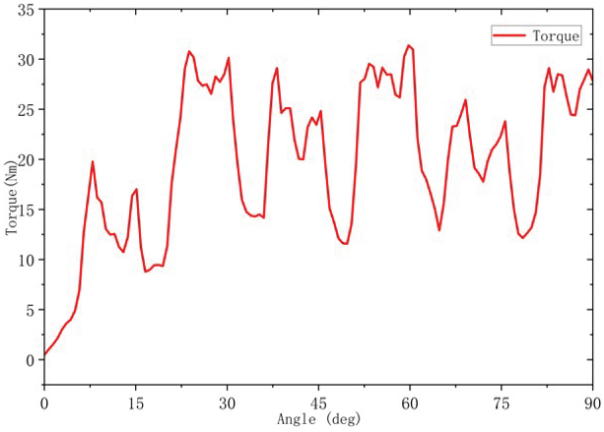

Fig. 10. Torque graph.

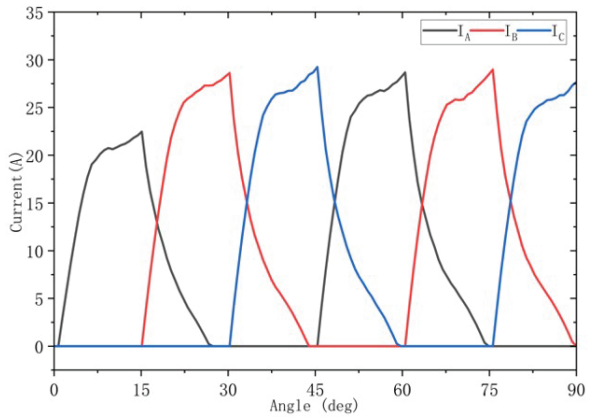

Fig. 11. Three-phase current waveforms.

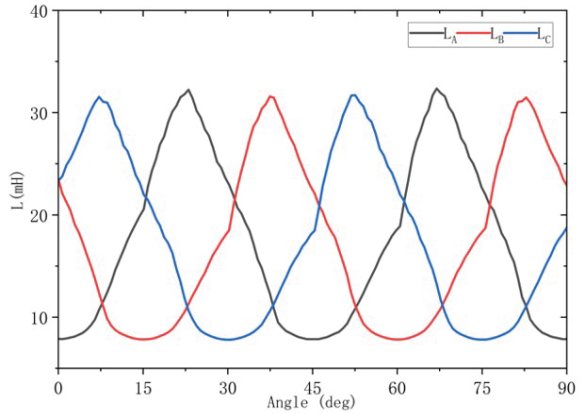

Fig. 12. Three-phase inductance waveforms.

V. CONCLUSION

This paper proposes a novel dual-rotor transverse-flux switched reluctance machine that synthetically integrates the magnetic circuit topology of transverse flux machines with modular stator-rotor construction. The motor demonstrates enhanced slot fill factor and flexible distributed winding configurations through axially aligned stator slots. Its modular assembly architecture combined with near-net shape manufacturing processes significantly reduces prototyping complexity and per-unit production costs while achieving high locked-rotor torque density characteristics that make it particularly suitable for direct-drive electric vehicle powertrains. The motor design parameters are analyzed by simulation to verify the correctness of the motor design method. The simulation shows that the MTF-DRSRM has a large output torque as well as low torque pulsation and stator copper consumption. The motor meets the initial design requirements, verifies the effectiveness of the MSRTFM design method proposed in this paper, and provides a theoretical basis for further optimization of the MSRTFM.

ACKNOWLEDGMENT

This work is supported by the Jiangsu Science and Technology Plan Special Fund (Innovation Support Plan International Science and Technology Cooperation/ Hong Kong Macao Taiwan Science and Technology Cooperation) Project (BZ2022014), and Jiangsu Provincial Market Supervision Administration Science and Technology Plan Project (KJ2025017),Shenzhen Basic Research Special (Natural Science Foundation) Key Project (JCYJ20220818100000001), 2022 China-CEEC University Joint Education Program (2022200), 2023 China-CEEC University Joint Education Program (2023304).

REFERENCES

[1] X. Sun, N. Wang, M. Yao, and G. Lei, "Position sensorless control of switched reluctance motors based on angle adjustment using nonlinear inductance and flux model," *IEEE Transactions on Industrial Electronics,* vol. 71, no. 12, pp. 15467-15477, 2024.

[2] S. Xu, H. Chen, L. Tao, P. Wang, R. Nie, and J. Si, "Development of an even-phase switched reluctance motor drive for torque performance improvement," *IEEE Transactions on Energy Conversion*, vol. 39, no. 4, pp. 2439-2452, 2024.

[3] X. Li, F. Liu, W. Jiang, H. Jin, M. Li, and Q. Wang, "Design and control of a transverse flux linear switched reluctance machine for rail transit application," *IEEE Access*, vol. 10, pp. 43175-43186, 2022.

[4] H. Chen, R. Nie, and X. Li, "A transverse-flux single-phase tubular switched reluctance linear machine with 4 poles," *IEEE Transactions on Applied Superconductivity*, vol. 31, no. 8, pp. 1-4, 2021.

[5] R. De Croo and F. De Belie, "Operating principle and characterisation of a novel contra-rotating dual-rotor switched reluctance machine," *IEEE Transactions on Industry Applications,* vol. 60, no. 5, pp. 6775-6786, 2024.

[6] N. Prasad and M. Bukya, "New transverse linear switched reluctance motor design and analysis for transit uses," *Cogent Engineering*, vol. 11, no. 1, pp. 1-8, 2024.

[7] H. Chen, R. Nie, W. Zhao, and J. Liu, "A novel three-phase tubular switched reluctance linear machine with transverse-flux path," *IEEE Transactions on Applied Superconductivity*, vol. 30, no. 4, pp. 1-6, 2020.

[8] V. Mirzaei and M. Mirsalim, "A 24/28-pole hybrid reluctance motor with U-core stator," in *2023 14th Power Electronics, Drive Systems, and Technologies Conference (PEDSTC),* pp. 1-5, 2023.

[9] M. di Benedetto, A. Lidozzi, L. Solero, F. Crescimbini, P. J. Grbović, and M. Luna, "High-performance 3-phase 5-level e-type multilevel–multicell converters for microgrids," *Energies*, vol. 14, no. 4, p. 843, 2021.

[10] H. Wang, Y. Xue, J. Du, and H. Li, "Design and evaluation of modular stator hybrid-excitation switched reluctance motor for torque performance improvement," *IEEE Transactions on Industrial Electronics,* vol. 71, no. 10, pp. 12814-12823, 2024.

[11] S. Xu, H. Zeng, X. Jiang, G. Qi, and G. Han, "Reliability evaluation of dual stator switched reluctance motor system based on enhanced reliability model," *IEEE Transactions on Industry Applications,* vol. 60, no. 6, pp. 8785-8796, 2024.

[12] M. Aydemir, "An innovative and non-intrusive Hall effect sensor-based rotor position detection system for external rotor switched reluctance motor," *Electrical Engineering*, vol. 106, no. 1, pp. 1009-1019, 2024.

[13] X. Yao, H. He, J. Wang, Q. Guan, and R. Gao, "An online torque sharing function method based on region division for reducing torque ripple and copper losses of switched reluctance motors," *IEEE Journal of Emerging and Selected Topics in Power Electronics*, vol. 12, no. 5, pp. 4825-4837, Oct. 2024.

[14] W. Libiao, K. T. Lionel, C. Ping, and Y. Lianghui, "Parameter identification of nonlinear flux-linkage model for switched reluctance motor based on chaotic diagonal recurrent neural network," *Journal of Engineering Science & Technology*, vol. 17, no. 2, pp. 157-164, 2024.

Hemiao Liu received the B.S. degree in electrical and information engineering from Beihua University, Jilin, China, in 2022. Since 2022, he has been pursuing a Ph.D. degree in electrical engineering from China University of Mining and Technology, Xuzhou. His current research interests include power electronics, electric vehicles, electric traction, wireless charging, and motor drives.

Xing Wang received the B.S. and M.S. degrees from China University of Mining and Technology, Xuzhou Jiangsu, China, in 1996. In 2007, she became an Associate Professor with China University of Mining and Technology, Xuzhou. She is a holder of four US Patents, nine Australian Patents, two Canadian Patents, four Russian Patents, 12 Chinese Invention Patents, three Chinese Utility Model Patents, and has authored 15 papers.

Hao Chen received the B.S. and Ph.D. degrees in electrical engineering from the Department of Automatic Control, Nanjing University of Aeronautics and Astronautics, Nanjing, China, in 1991 and 1996, respectively. He has been a professor at the School of Electrical and Power Engineering, China University of Mining and Technology, Xuzhou, since 2001. From 2002 to 2003, he was a Visiting Professor with Kyung sung University, Busan, South Korea. Since 2008, he has been an Adjunct Professor with the University of Western Australia, Perth, WA, Australia. He has authored one book and more than 200 articles. He holds 15 U.S. patents, 23 Australian patents, one Danish patent, seven Canadian patents, three South African patents, 10 Russian patents, 66 Chinese invention patents, and six Chinese utility model patents. His current research interests include motor control, linear launcher, electric vehicles, electric traction, servo drives, and wind power generator control.

Chen was a recipient of the Prize of Science and Technology of Chinese Youth and the Prize of the Fok Ying Tong Education Foundation for Youth Teachers in 2004. He was awarded the First Prize in the Science and Technology Advanced of Province and Ministry once, the Second Prize in the Science and Technology Advanced of Province and Ministry nine times, and the Third Prize in the Science and Technology Advanced of Province and Ministry 14 times. He became the Chinese New Century Hundred-Thousand Ten-Thousand Talents Engineering National Talent in 2007 and won the Government Especial Allowance of People's Republic of China State Department in 2006.

Jun Bao was born in August 1971. He is a Full Senior Engineer, currently serving as the director of Wuxi Institute of Inspection, Testing and Certification. His primary research areas include inspection and testing technologies for new energy vehicles, as well as metrological test technologies.

Haidong Yan was born in May 1982. He has a master's degree in System Analysis and Integration from Nanjing University of Information Science & Technology, Nanjing, China. He is a Senior Engineer currently serving as the deputy director of Wuxi Institute of Inspection, Testing and Certification. His research direction mainly focuses on electromagnetic metrology, new energy vehicle specialized metrology and testing technology.

Guanjun Wang was born in September 1986. He has a master's degree in Electronic and Communication Engineering from China University of Mining and Technology, Xuzhou, China. He is a Senior Engineer, currently serving as the Director of Electrical and Information M&R Department of Wuxi Institute of Inspection, Testing, and Certification. His research direction mainly focuses on electromagnetic metrology, new energy vehicle specialized metrology and testing technology.

Yassen Gorbounov received the B.S., M.S., and Ph.D. degrees from the Sofia University of Technology, Sofia, Republic of Bulgaria, in 2002, 2004, and 2013, respectively. Since 2017, he has been working as an Associate Professor with the Sofia University of Technology. His current research interests include power electronics and the mining industry.

Analysis of Magnetic Circuit Characteristics of Axial-radial Hybrid Flux Switched Reluctance Motor

Wenju Yan[1,2], Jun Xin[1], Hongwei Yang[1], Hao Chen[1], Ryszard Palka[3], Marcin Wardach[3], and Konrad Woronowicz[3]

[1]School of Electrical Engineering
China University of Mining and Technology, Xuzhou 221116, China
6288@cumt.edu.cn, ts23230161p31ld@cumt.edu.cn, ts22230175p31@cumt.edu.cn, hchen@cumt.edu.cn

[2]Shenzhen Research Institute
China University of Mining and Technology, Shenzhen 518057, China

[3]Department of Electrical Machines and Drives
West Pomeranian University of Technology, Sikorskiego 37, 70-313 Szczecin, Poland
ryszard.palka@zut.edu.pl, marcin.wardach@zut.edu.pl, Konrad.Woronowicz@zut.edu.pl

Abstract – In order to enhance the torque output capability of Switched Reluctance Motors (SRM), this paper proposes two types of axial-radial mixed magnetic flux SRM topological structures with wide-narrow pole and same-tooth pole by combining the respective advantages of axial and radial magnetic fluxes. Two identically shaped axial stator structures are used, distributed on both sides of the rotor, forming an axial magnetic flux path with the central rotor. Simultaneously, on the outer side of the rotor, a radial stator structure is distributed, sharing the rotor to form a radial magnetic flux path. By using equivalent magnetic circuit analysis methods analyzing the flux linkage characteristic in a special position of the two topological structures, the superior torque performance of the axial-radial mixed magnetic flux SRM topology is determined. A prototype is manufactured and experimental verification is conducted.

Index Terms – Axial-radial flux, equivalent magnetic circuit analysis, switched reluctance motor.

I. INTRODUCTION

As a rare-earth-free motor, the Switched Reluctance Motor (SRM) has the following advantages compared to other types of motors: lower cost, made solely from stacked silicon steel sheets; high reliability, with no permanent magnets in the rotor and low environmental requirements; and broad high-efficiency platform, achieving efficient operation over a wide speed range and under different load conditions. When SRM is applied to electric engineering vehicles with large inertia loads, it can fully utilize its high starting torque, low starting current, traction characteristics that allow frequent heavy-load starts, and high structural reliability to meet the various driving conditions of electric engineering vehicles. However, due to its inherent structure, the large torque ripple and low torque density greatly limit the application and promotion of SRM in the field of electric dump trucks for engineering vehicles.

In order to enhance the competitiveness of SRM in the field of new energy vehicles, many studies often focus on improving motor topology structures, such as segmented stator or rotor structure, double stator structure, hybrid excitation structure, and axial flux structure. To facilitate a more intuitive understanding of the existing SRM topology structures, Table 1 summarizes the classification and corresponding characteristics of the main SRM topology structures.

Currently, there is limited study on hybrid magnetic flux in SRM. An axial-radial magnetic flux switch reluctance wheel edge drive motor is proposed in [19]. The magnetic circuit characteristics are analyzed by using the axial magnetic conductivity compensation coefficient analytical method, and the inductance and torque characteristics are studied. A new hybrid magnetic circuit switch reluctance generator is introduced in [20], and the feasibility of this method was verified through experimental results from a prototype.

In other motor fields, there is relatively more research on hybrid magnetic flux. An axial-radial magnetic flux high-temperature superconducting permanent magnet synchronous motor is proposed in [21] and, based on the study of the rotor structure and working principle, its mathematical model and magnetic field were analyzed. A type of axial and radial hybrid magnetic flux permanent magnet motor using concentrated

Submitted On: December 3, 2024
Accepted On: May 29, 2025

https://doi.org/10.13052/2025.ACES.J.400908

Table 1: Summary of novel topologies for SRM

Category	Structure	Ref.	Characteristics
Segment rotor or stator	Segment rotor	[1, 2]	Short flux path, High output torque
	Segment stator	[3, 4]	Short flux path, Easy maintenance, High reliability
Double stator	Traditional double stator	[5, 6]	High power and torque density, Low torque ripple
	Double stator with segment rotor	[7–9]	Low saturation, Flux cancellation
	Double stator with segment stator	[10]	Magnetic field decoupling, Low torque ripple
Hybrid excitation	PM in the stator slot	[11, 12]	High average torque, Low copper loss, High power density
	PM at other position	[13]	High output power, Low cogging torque
Axial flux	Axial flux with segment rotor or stator	[14–16]	Short flux path, High torque/power density
	Axial flux with hybrid excitation	[17]	High power density and efficiency, Demagnetization risk
	Axial flux with new materials	[18]	Improve motor torque performance, Cost increase

windings is proposed in [22]. By combining additional cores with concentrated windings, it has the advantage of high-power density. Reference [23] proposed a new type of hybrid hysteresis motor that combines radial and axial magnetic flux rotors, overcoming the disadvantage of poor output torque and efficiency in traditional hysteresis motors. Reference [24] proposed a novel permanent magnet motor that can switch between axial magnetic flux and radial magnetic flux as needed by using coordinate transformation theory. A brushless hybrid excitation motor with radial-axial direction is proposed in [25], which effectively expands the speed range and improves torque output capability. In order to better reflect the magnetic circuit characteristics of the proposed motors, the authors used a three-dimensional finite element analysis method to analyze the polarity distribution of magnetic flux density under different magnetic potentials.

In order to effectively alleviate the end-winding effect, a hybrid flux motor with end-windings is proposed in [26]. The performance of the motor is analyzed by using analytical calculations and three-dimensional finite element models. By optimizing the tooth size of L-stator and the appropriate tilt of magnet shape, maximum average torque output, low torque ripple and cogging torque are realized

This paper proposes two different stator structures for the Axial-Radial Flux SRM (ARFSRM), namely the Wide-Narrow Poles ARFSRM (WNP-ARFSRM) and the Equal-Width Poles ARFSRM (EWP-ARFSRM). In section II the topological structures of WNP-ARFSRM and EWP-ARFSRM are introduced. Then, by establishing equivalent magnetic circuit models for both motors, the electromagnetic characteristics of the motors are analyzed in section III. Prototypes are manufactured and experimental verification is conducted in section IV. This paper is concluded with section V.

II. STRUCTURE OF ARFSRM

As shown in Fig. 1, the topology of a three-phase 12/10/12 WNP-ARFSRM includes the radial magnetic flux part which consists of rotor core, radial stator core, and radial stator armature winding. Unlike traditional SRM structures, the WNP-ARFSRM adds an axial magnetic flux part, including two axial stator cores, rotor core, and axial stator armature winding. The structure of the left and right axial stators is identical, with wide stator poles alternating along the circumferential direction with narrow stator poles. The armature winding exclusively encircles the wide poles of the axial stator, referred to as excitation poles. Conversely, the narrower poles of the axial stator merely facilitate the magnetic flux path, termed auxiliary poles. To ensure that the axial stator meets the slot fill rate under different radius combinations, the stator tooth pole adopts a parallel slot structure. Similarly, the radial stator also uses an excitation pole and auxiliary pole structure. The axial stator and radial stator share a rotor structure, with the rotor part adopting a block structure. Independent rotor blocks are evenly placed in a non-magnetic rotor sleeve along the circumferential direction. The rotor sleeve is made of epoxy resin material, which has a magnetic isolation function to reduce eddy current losses and reduce overall motor weight.

The axial stator winding connection is shown in Fig. 2 (a). Let us take phase A as an example. On one side of the axial stator, A1 and A2 coils are opposite each other in the horizontal plane and along the circumferential direction are connected in series, and A3 and A4 coils are opposite each other on the other side of the axial stator and connected in series to form the armature winding of the axial stator. On one side of the axial stator, the winding polarity distribution is N-N-N-S-S-S, and on the other side of the axial stator, the winding polarity distribution is S-S-S-N-N-N. Figure 2 (b) shows

the radial stator winding connection. If we take phase A as an example, in the radial stator, A5 and A6 coils in relative positions are connected in series to form the armature winding of the radial stator.

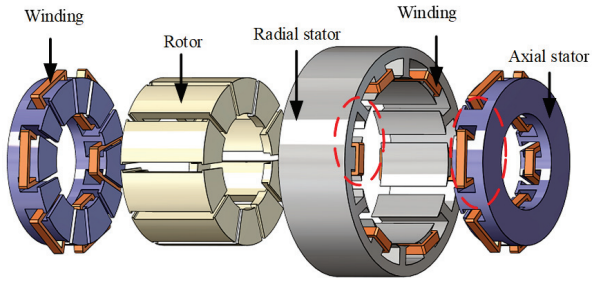

Fig. 1. Schematic of the WNP-ARFSRM structure.

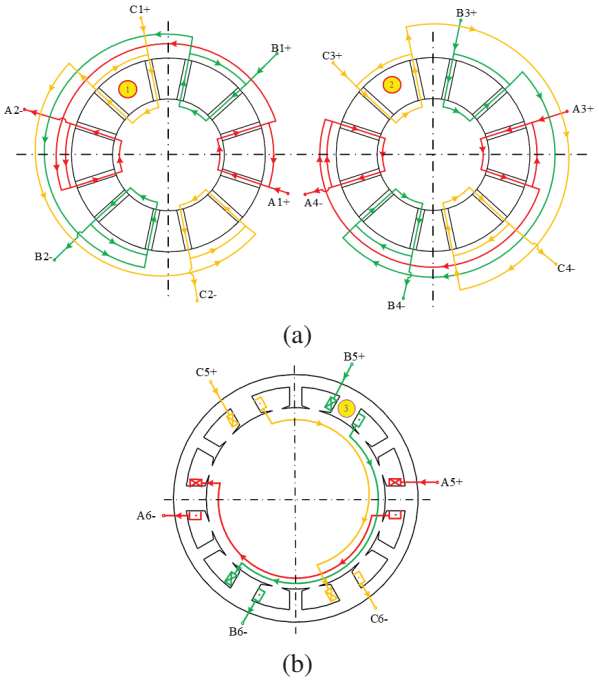

Fig. 2. WNP-ARFSRM winding connection diagram: (a) axial stator and (b) radial stator.

Figure 3 presents the topology of a three-phase 12/10/12 EWP-ARFSRM. The axial stator adopts a parallel slot structure. The rotor structure is identical to that of the WNP-ARFSRM. The stator part is similar to the traditional SRM, with coils wound in each slot of both the axial and radial stators. Coils in adjacent slots form the same phase, thereby creating axial and radial magnetic flux paths with the segmented rotor. The two motors proposed in this paper both adopt a centralized winding structure, which has the advantage of minimizing the impact of end effects on the motor, reducing the heat generated during operation and reducing the weight and cost of the motor.

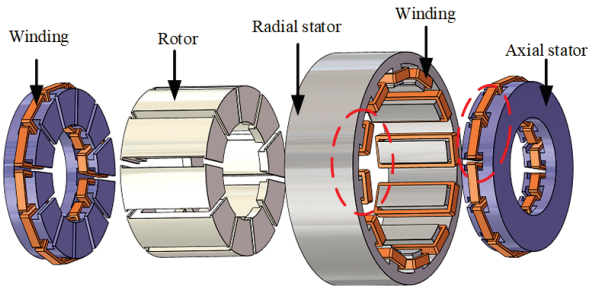

Fig. 3. Schematic of the EWP-ARFSRM structure.

The axial stator winding connection method is presented in Fig. 4 (a). Let us take phase A as an example. On one side of the axial stator, the four coils A1, A2, A3, and A4 that are opposite each other in the horizontal plane around the axis are connected in series with each other. They are also connected in series with the coils A5, A6, A7, and A8 that are opposite to them on the other side of the axial stator. If we take phase A as an example again, the radial stator winding connection method is shown in Fig. 4 (b). The coils A9 and A10 are connected in series with coils A11 and A12 that are opposite to them in position.

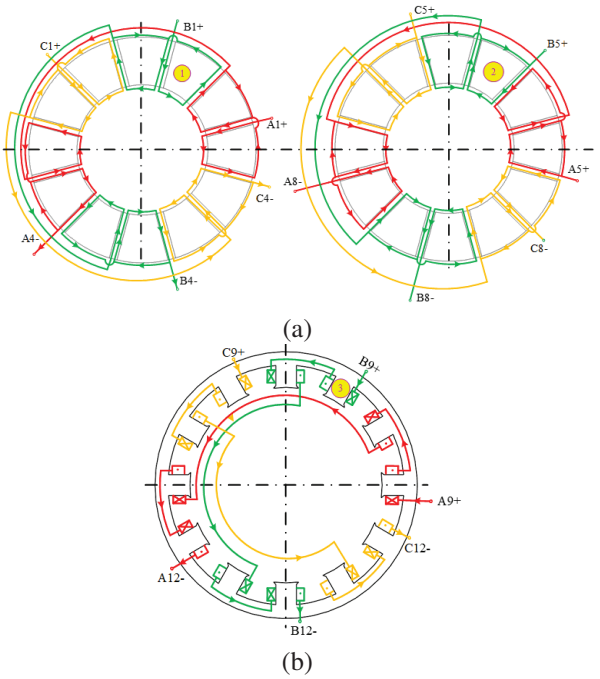

Fig. 4. EWP-ARFSRM winding connection diagram (a) axial stator and (b) radial stator.

III. ARFSRM EQUIVALENT MAGNETIC CIRCUIT ANALYSIS

A. Magnetic circuit analysis

Like traditional SRM, the electromagnetic characteristics of ARFSRM also exhibit strong non-linearity and typically operate in a high saturation state. To verify the theoretical concept proposed in this paper for ARFSRM, this section will analyze the equivalent magnetic circuit models of two machines. The equivalent magnetic circuit model of WNP-ARFSRM is shown in Fig. 5, where the mutual inductance and leakage impedance of the winding are ignored. Due to the axial symmetry of the ARFSRM structure, Figures 5 and 7 illustrate only the upper half of the motor for clarity. The lower half shares identical magnetic paths and reluctances, allowing the full magnetic circuit to be represented by doubling the flux values in the depicted half-model.

In Fig. 5, F_{re} and F_{ae} represent the magnetomotive force generated by excitation of the radial stator winding and the axial stator winding, respectively. ϕ_{re} and ϕ_{ae} are the magnetic fluxes produced by the radial stator winding and the axial stator winding, respectively. R_{ag} is the magnetic resistance of the axial magnetic air gap, R_{asp} is the magnetic resistance of the axial stator pole, R_{asy} is the magnetic resistance of the axial stator yoke, R_{rg} is the magnetic resistance of the radial magnetic air gap, R_{rsp} is the magnetic resistance of the radial stator pole, R_{rsy} is the magnetic resistance of the radial stator yoke and R_r is the segmented rotor magnetic resistance.

When the rotor is in asymmetric positions, the equivalent network undergoes topological adaptation through the introduction of a leakage reluctance branch R_{leak} and a cross-coupling reluctance branch R_{cross}. The leakage branch quantifies the flux leakage caused by partial misalignment between stator and rotor poles, with its value increasing significantly as the rotor angle deviates. The cross-coupling branch captures the magnetic interaction between adjacent phase windings, dynamically updated via FEM-predicted mutual inductance coefficients.

In order to facilitate formulation of the magnetic circuit equations for WNP-ARFSRM, further simplification is made on the equivalent magnetic circuit, as shown in Fig. 6. R_{as1} represents the sum of R_{ag1} and R_{asp1}; R_{as2} represents the sum of R_{ag2}, R_{asp2}, and R_{asy1}; and R_{as3} represents the sum of R_{ag3}, R_{asp3}, and R_{asy2}. The radial reluctance equivalent is similar to the axial equivalent and will not be further elaborated.

Based on Fig. 6, the basic magnetic circuit equation can be written as:

$$\begin{cases} F_{ae} = \phi_{ae}R_{as1} + \frac{1}{2}\phi_{ae}R_{as2} + \frac{1}{2}(\phi_{ae} + \phi_{re})R_r \\ F_{re} = \phi_{re}R_{rs1} + \frac{1}{2}\phi_{re}R_{rs2} + \frac{1}{2}(\phi_{ae} + \phi_{re})R_r \end{cases}. \quad (1)$$

The derivation is:

$$\begin{cases} F_{ae} = \phi_{ae}\left(R_{as1} + \frac{1}{2}R_{as2} + \frac{1}{2}R_r\right) + \frac{1}{2}\phi_{re}R_r \\ F_{re} = \frac{1}{2}\phi_{ae}R_r + \phi_{re}\left(R_{rs1} + \frac{1}{2}R_{rs2} + \frac{1}{2}R_r\right) \end{cases}. \quad (2)$$

$$\begin{cases} A = R_{as1} + \frac{1}{2}R_{as2} + \frac{1}{2}R_r \\ D = R_{rs1} + \frac{1}{2}R_{rs2} + \frac{1}{2}R_r \end{cases}. \quad (3)$$

The calculation formulas for radial and axial mag-

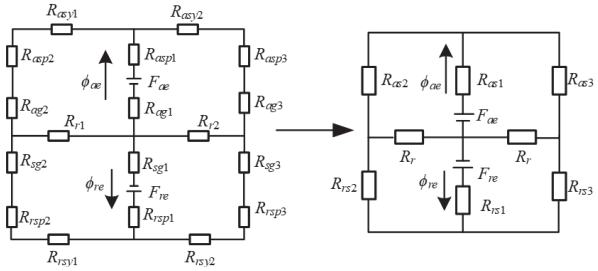

Fig. 6. Simplified magnetic circuit of the WNP-ARFSRM.

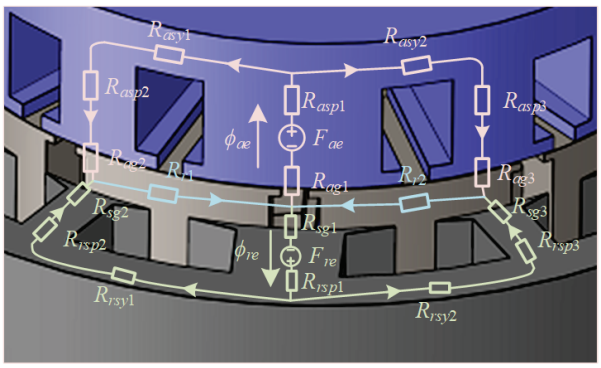

Fig. 5. Equivalent magnetic circuit of the WNP-ARFSRM.

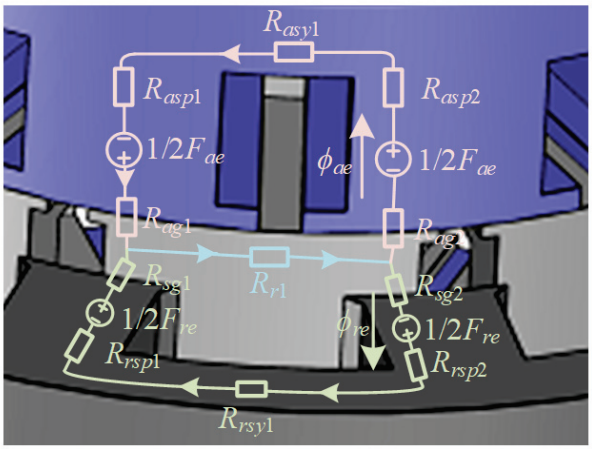

Fig. 7. Equivalent magnetic circuit of the EWP-ARFSRM.

netic flux are:

$$\begin{cases} \phi_{ae} = \frac{DF_{ae} - \frac{1}{2}R_r F_{re}}{AD - \frac{1}{4}R_r^2} \\ \phi_{re} = \frac{AF_{re} - \frac{1}{2}R_r F_{ae}}{AD - \frac{1}{4}R_r^2} \end{cases}. \tag{4}$$

The equivalent magnetic circuit model of EWP-ARFSRM is shown in Fig. 7, while the simplified equivalent magnetic circuit is shown in Fig. 8. Here, R_{as} represents the sum of $R_{ag}1$, $R_{ag}2$, $R_{asp}1$, $R_{asp}2$, and $R_{asy}1$, and R_{rs} represents the sum of $R_{sg}1$, $R_{sg}2$, $R_{rsp}1$, $R_{rsp}2$, and $R_{rsy}1$. According to Fig. 8, the basic magnetic circuit equation of EWP-ARFSRM can be written as:

$$\begin{cases} F_{ae} = \phi_{ae} R_{as} + (\phi_{ae} + \phi_{re}) R_r \\ F_{re} = \phi_{re} R_{rs} + (\phi_{ae} + \phi_{re}) R_r \end{cases}. \tag{5}$$

The derivation is:

$$\begin{cases} F_{ae} = \phi_{ae} (R_{as} + R_r) + \phi_{re} R_r \\ F_{re} = \phi_{ae} R_r + \phi_{re} (R_{rs} + R_r) \end{cases}. \tag{6}$$

The calculation formulas for radial and axial magnetic flux are:

$$\begin{cases} \phi_{ae} = \frac{(R_{rs} + R_r) F_{ae} - R_r F_{re}}{R_r (R_{as} + R_{rs}) + R_{as} R_{rs}} \\ \phi_{re} = \frac{(R_{as} + R_r) F_{re} - R_r F_{ae}}{R_r (R_{as} + R_{rs}) + R_{as} R_{rs}} \end{cases}. \tag{7}$$

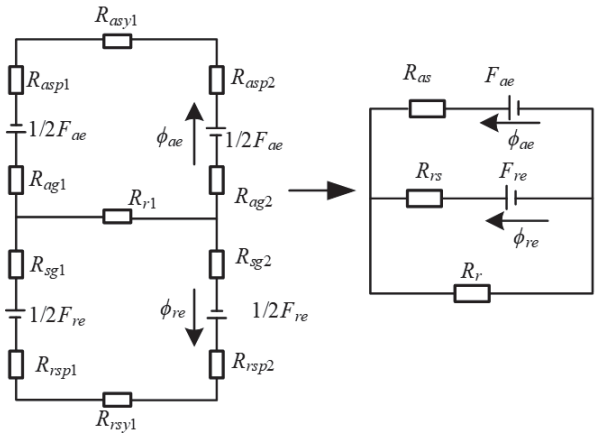

Fig. 8. Simplified magnetic circuit of the EWP-ARFSRM.

The magnetic reluctances in equations (1-7) are functions of rotor position θ. Their values are dynamically updated in practice based on two approaches: piecewise linearization of the core material's nonlinear B-H curve for iterative permeability calculations, and interpolation of precomputed finite element data to account for geometric variations in pole overlap. The empirical formulas for the axial airgap reluctance $R_{\_ag}$ and radial airgap reluctance $R_{\_rg}$ as functions of angular position are:

$$\begin{cases} R_{ag}(\theta) = \frac{g_a}{\mu_0 A_a(\theta)} \\ A_a(\theta) = \frac{\beta_s \beta_r(\theta)}{2} (r_o^2 - r_i^2) \\ \beta_r(\theta) = \beta_r - \left| \theta mod \frac{2\pi}{N_r} - \theta_0 \right| \end{cases}, \tag{8}$$

where A_a represents the effective overlap area between stator and rotor poles (unit: m^2), β_s represents the stator pole arc angle (unit: rad), β_r represents the effective rotor overlap arc angle, N_r represents the number of rotor poles, θ_0 represents the reference angle at the aligned position, r_o, r_i represents the outer and inner radii of the airgap region, g_a represents the axial airgap length, and μ_0 represents the permeability of free space.

B. Magnetic circuit solution

Construction of the equivalent magnetic circuit model is based on establishment of the magnetic flux tube. The size of the magnetic resistance can be determined by the magnetic flux tube theorem. The two end faces of the magnetic flux tube are two magnetic equipotential surfaces, and their magnetic potentials are different. Each magnetic field line vertically passes through its cross-section in the magnetic flux tube, as shown in Fig. 9.

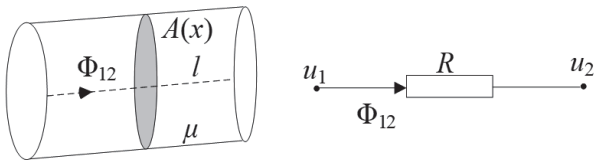

Fig. 9. Magnetic flux tube and its equivalent reluctance.

The equivalent magnetic resistance R in Fig. 9 can be calculated as:

$$R = \frac{u_1 - u_2}{\Phi_{12}} = \int_0^l \frac{dx}{u(x) \cdot A(x)}. \tag{9}$$

Based on the computational method presented in [27], the magnetic flux curves of the motor in both aligned and unaligned positions can be calculated. To reduce errors caused by the magnetic saturation effect of silicon steel sheets, this paper employs the Gauss-Seidel iteration method to solve the nonlinear problems in the equivalent magnetic circuit, with specific procedures referring to [28]. The WNP-ARFSRM and EWP-ARFSRM obtained through iterative calculations are shown in Figs. 10 and 11, respectively. In the proposed ARFSRM design, the axial stator, radial stator, and rotor components all utilize 50DW470 silicon steel sheets as the core material. The magnetization (B-H) curve of this material is shown in Fig. 12.

At the unaligned position, the magnetic flux linkage of WNP-ARFSRM is approximately equal to that

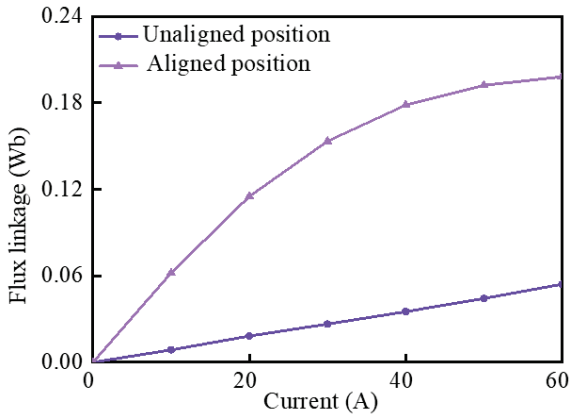

Fig. 10. Flux linkage curves by MEC at the unaligned and aligned position of WNP-ARFSRM.

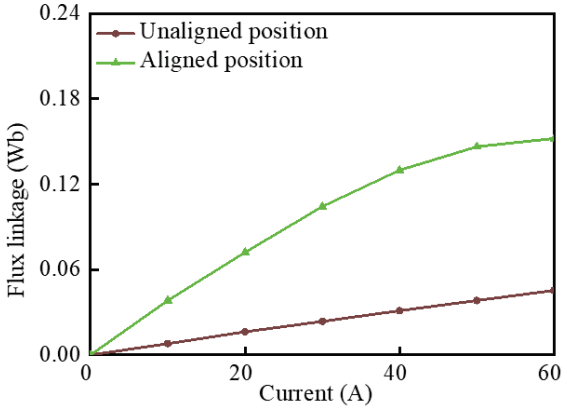

Fig. 11. Flux linkage curves by MEC at the unaligned and aligned position of EWP-ARFSRM.

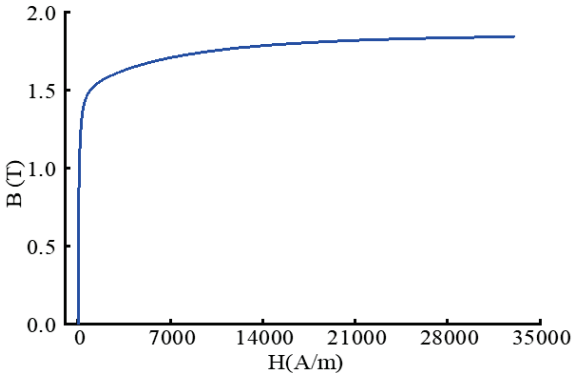

Fig. 12. Magnetization (B-H) curve of 50DW470 material.

of EWP-ARFSRM. At the aligned position, with the increase in current, the magnetic flux linkage of WNP-ARFSRM is greater than that of EWP-ARFSRM, which indicates that the maximum-to-minimum inductance ratio of WNP-ARFSRM is larger than that of EWP-ARFSRM and thus has a higher energy conversion ratio.

The electromagnetic torque of the machine is a function of position θ and phase current i. To solve the electromagnetic torque, a fixed current i is needed. Then, the partial derivative of the magnetic co-energy W' with respect to the position θ is solved. The expression is:

$$W' = \int_0^i \psi(\theta, i)\, di \,|_{\theta=const}. \tag{10}$$

The magnetic co-energy is then used to calculate the electromagnetic torque:

$$T(\theta, i) = \frac{\partial W'(\theta, i)}{\partial \theta} \,|_{i=const}. \tag{11}$$

According to equations (10) and (11), the average torque of the two machines over half a rotor cycle can be calculated, as shown in Fig. 13. As can be seen from Fig. 13, the average static torque value of WNP-ARFSRM is higher than that of EWP-ARFSRM, indicating that, under the condition of generating the same torque, WNP-ARFSRM requires less current.

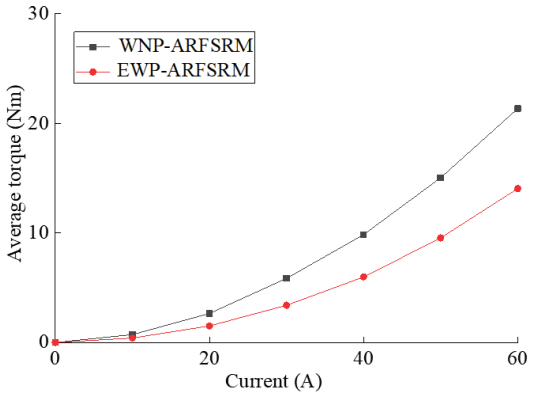

Fig. 13. Comparison of average static torque of the two motors.

C. Results analysis

Based on the analysis of the motor magnetic circuit, the following conclusions can be drawn.

(a) In the WNP-ARFSRM, due to the adoption of a single-tooth winding structure in both radial and axial directions, narrow poles do not wind the windings but only provide circuits. Therefore, the main magnetic flux is generated by the wide poles with concentrated windings. Both axial and radial directions adopt a wide-narrow pole method, so the equivalent magnetic circuit models for both axial and radial directions are basically consistent, reducing the complexity of deriving formulas.

(b) Since the EWP-ARFSRM is powered simultaneously by adjacent coils forming one phase, the magnetic flux path only passes through the two adjacent

stator poles. Compared with WNP-ARFSRM, the equivalent magnetic circuit analysis is simpler and more convenient.

(c) At the unaligned position of the motor, the magnetic flux generated axially cancels out with the radial direction, thereby improving the maximum to minimum inductance ratio of the motor. At the aligned position of the motor, the magnetic flux generated axially overlaps with the radial direction, thereby increasing the output torque of the motor. Moreover, at the aligned position, the flux linkage of WNP-ARFSRM is greater than that of EWP-ARFSRM.

(d) The average static mean torque value of WNP-ARFSRM is higher than that of EWP-ARFSRM.

IV. EXPERIMENT

To verify the correctness of the equivalent magnetic circuit analysis method proposed in this paper, a three-phase 12/10/12 pole WNP-ARFSRM prototype was designed and manufactured. A corresponding motor experimental platform was set up to test the static characteristics of the motor. Figure 13 presents the assembly diagram of the WNP-ARFSRM prototype. Figure 15 shows the actual images of the motor's radial stator, axial stator, and rotor.

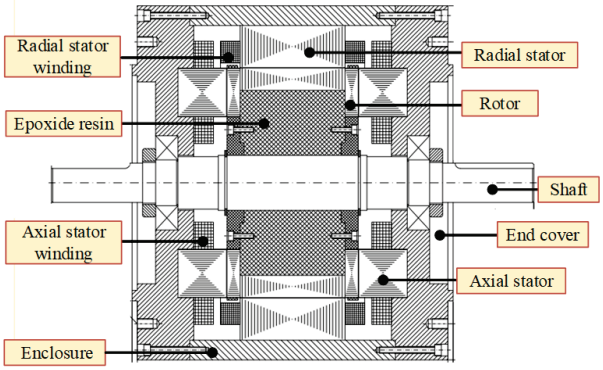

Fig. 14. Assembly schematic of the WNP-ARFSRM prototype.

In order to accurately obtain the magnetic linkage characteristics of the prototype, this paper adopts the indirect method for magnetic linkage measurement. The specific steps are as follows:

(a) At the beginning of the experiment, the initial position of the rotor of the calibration motor is found. Taking phase A as an example, the unaligned and aligned positions of the motor are found using an inductance meter and a rotary encoder, and the rotor is clamped with a magnetic powder brake to ensure that the motor is fixed at these two special positions.

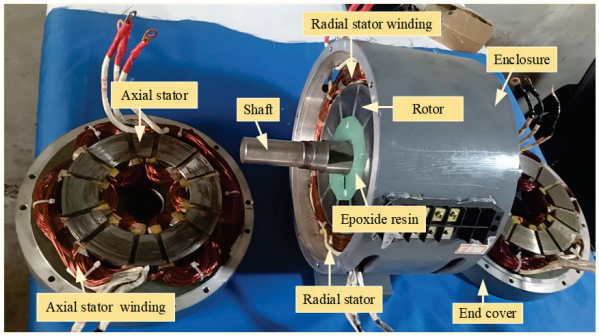

Fig. 15. Photo of WNP-ARFSRM prototype.

(b) Apply a 48 V voltage to the phase A winding and detect the changes in phase current and phase voltage through current and voltage sensors. When the winding current reaches 60 A, turn off the switch tube to stop excitation, and record the waveforms of current and voltage changes using an oscilloscope.

(c) Using the measured phase voltage and phase current waveforms at unaligned and aligned positions, the characteristics of the phase winding magnetic linkage are derived based on the magnetic linkage calculation formula. The specific calculation formula is as follows:

$$\psi(i)|_{\theta=c} = \psi(0) + \int_0^{t_i} (u - Ri)dt \qquad (12)$$

where ψ,i, and u represent the phase flux linkage, phase current, and phase voltage of the winding, respectively. R is the resistance value of the phase winding and $\psi(0)$ is the magnetic linkage value at the initial moment, typically taken as $\psi(0) = 0$.

Figure 16 presents comparison curves of magnetization between experimental measurements and equivalent magnetic circuit calculations for the WNP-ARFSRM

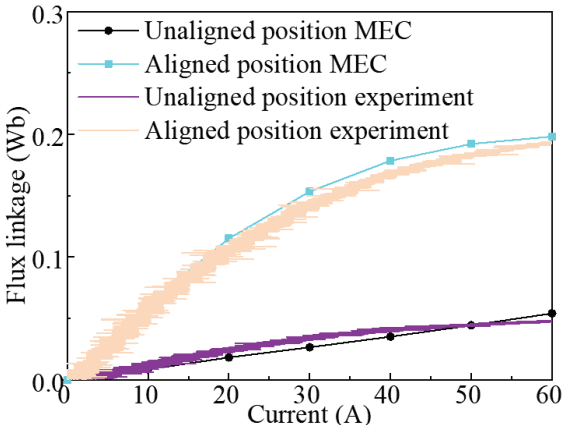

Fig. 16. Simulation and measured results of flux linkage.

prototype. As can be seen from Fig. 16, at the unaligned position, the measured flux linkage values are essentially consistent with the results of equivalent magnetic circuit calculations. At the aligned position, due to motor saturation and manufacturing assembly errors, the flux linkage values obtained from equivalent magnetic circuit calculations are slightly larger than the actual measured values.

V. CONCLUSION

Based on the structural characteristics of axial and radial SRMs, this paper proposes WNP-ARFSRM and EWP-ARFSRM. The electromagnetic characteristics of the two motors are analyzed using the equivalent magnetic circuit method. The following conclusions can be drawn.

(a) The radial stator and axial stator share the rotor structure, which is distributed around the rotor block. The rotor block adopts a U-shaped structure and is fixed in a non-magnetic rotor sleeve. Due to the use of segmented rotor structure and concentrated winding, the radial and axial magnetic flux paths of the two motors are shorter, improving the operating efficiency of the motor.

(b) By analyzing the magnetic flux paths of WNP-ARFSRM and EWP-ARFSRM at unaligned positions, it was found that the magnetic flux generated by the radial stator cancels out with the magnetic flux produced by the axial stator at the rotor, resulting in a larger maximum to minimum inductance ratio. By analyzing the equivalent magnetic circuit at aligned positions, it was found that the magnetic fluxes generated by the radial and axial stators overlap. The total torque of the motor is the sum of the torques generated by the radial and axial electric excitation.

(c) By calculating the magnetic flux of the motor in both aligned and unaligned positions, the average torque of the motor over half a cycle was obtained. The results indicate that the torque output capability of WNP-ARFSRM is stronger than that of EWP-ARFSRM.

ACKNOWLEDGMENT

This work was supported in part by the Xuzhou Science and Technology Innovation Basic Research Project under Grant KC23021, the Guangdong Basic and Applied Basic Research Foundation under Grant 2025A1515011254, China Postdoctoral Foundation Project under Grant 2023M733749, 2022 China-CEEC University Joint Education Program (2022200), 2023 China-CEEC University Joint Education Program (2023304).

REFERENCES

[1] Z. Xu, D.-H. Lee, and J.-W. Ahn, "Design and operation characteristics of a novel switched reluctance motor with a segmental rotor," *IEEE Transactions on Industry Applications*, vol. 52, no. 3, pp. 2564-2572, May-June 2016.

[2] X. Sun, K. Diao, G. Lei, Y. Guo, and J. Zhu, "Study on segmented-rotor switched reluctance motors with different rotor pole numbers for BSG system of hybrid electric vehicles," *IEEE Transactions on Vehicular Technology*, vol. 68, no. 6, pp. 5537-5547, June 2019.

[3] H. Eskandari and M. Mirsalim, "An improved 9/12 two-phase E-core switched reluctance machine," *IEEE Transactions on Energy Conversion*, vol. 28, no. 4, pp. 951-958, Dec. 2013.

[4] L. Szabo and M. Ruba, "Segmental stator switched reluctance machine for safety-critical applications," *IEEE Transactions on Industry Applications*, vol. 48, no. 6, pp. 2223-2229, Nov.-Dec. 2012.

[5] M. Asgar and E. Afjei, "Radial force reduction in a new flat-type double-stator switched reluctance motor," *IEEE Transactions on Energy Conversion*, vol. 31, no. 1, pp. 141-149, Mar. 2016.

[6] C. H. T. Lee, K. T. Chau, C. Liu, T. W. Ching, and F. Li, "Mechanical offset for torque ripple reduction for magnetless double-stator doubly salient machine," *IEEE Transactions on Magnetics*, vol. 50, no. 11, pp. 1-4, Nov. 2014.

[7] Q. Sun, J. Wu, C. Gan, C. Shi, and J. Guo, "DSSRM design with multiple pole arcs optimization for high torque and low torque ripple applications," *IEEE Access*, vol. 6, pp. 27166-27175, 2018.

[8] N. Arbab, W. Wang, C. Lin, J. Hearron, and B. Fahimi, "Thermal modeling and analysis of a double-stator switched reluctance motor," *IEEE Transactions on Energy Conversion*, vol. 30, no. 3, pp. 1209-1217, Sep. 2015.

[9] L. Maharjan, E. Bostanci, S. Wang, E. Cosoroaba, W. Cai, and F. Yi, "Comprehensive report on design and development of a 100-kW DSSRM," *IEEE Transactions on Transportation Electrification*, vol. 4, no. 4, pp. 835-856, Dec. 2018.

[10] W. Yan, H. Chen, S. Liao, Y. Liu, and H. Cheng, "Design of a low-ripple double-modular-stator switched reluctance machine for electric vehicle applications," *IEEE Transactions on Transportation Electrification*, vol. 7, no. 3, pp. 1349-1358, Sep. 2021.

[11] W. Ding, H. Bian, K. Song, Y. Li, and K. Li, "Enhancement of a 12/4 hybrid-excitation switched reluctance machine with both segmented-stator and -rotor," *IEEE Transactions on Industrial Electronics*, vol. 68, no. 10, pp. 9229-9241, Oct. 2021.

[12] S. Ullah, S. P. McDonald, R. Martin, M. Benarous, and G. J. Atkinson, "A permanent magnet assist, segmented rotor, switched reluctance drive for fault tolerant aerospace applications," *IEEE Transactions on Industry Applications*, vol. 55, no. 1, pp. 298-305, Jan.-Feb. 2019.

[13] E. F. Farahani, M. A. J. Kondelaji, and M. Mirsalim, "An innovative hybrid-excited multi-tooth switched reluctance motor for torque enhancement," *IEEE Transactions on Industrial Electronics*, vol. 68, no. 2, pp. 982-992, Feb. 2021.

[14] A. Labak and N. C. Kar, "Designing and prototyping a novel five-phase pancake-shaped axial-flux SRM for electric vehicle application through dynamic FEA incorporating flux-tube modeling," *IEEE Transactions on Industry Applications*, vol. 49, no. 3, pp. 1276-1288, May-June 2013.

[15] V. S. De Castro Teixeira, T. A. D. S. Barros, A. B. Moreira, and E. R. Filho, "Methodology for the electromagnetic design of the axial-flux C-core switched reluctance generator," *IEEE Access*, vol. 6, pp. 65463-65473, 2018.

[16] F. Yu, H. Chen, W. Yan, V. F. Pires, J. F. A. Martins, and P. Rafajdus, "Design and multiobjective optimization of a double-stator axial flux SRM with full-pitch winding configuration," *IEEE Transactions on Transportation Electrification*, vol. 8, no. 4, pp. 4348-4364, Dec. 2022.

[17] J.-H. Oh, J.-H. Lee, S.-I. Kang, K.-S. Shin, and B.-I. Kwon, "Analysis of a novel transverse flux type permanent magnet reluctance generator," *IEEE Transactions on Magnetics*, vol. 50, no. 2, pp. 809-812, Feb. 2014.

[18] J. Ma, J. Li, H. Fang, Z. Li, Z. Liang, and Z. Fu, "Optimal design of an axial-flux switched reluctance motor with grain-oriented electrical steel," *IEEE Transactions on Industry Applications*, vol. 53, no. 6, pp. 5327-5337, Nov.-Dec. 2017.

[19] C. Yang, H. Cao, and S. Xing, "Analytical calculation of magnetic circuit at key positions of axial-radial flux switched reluctance rim driven motor," in *24th International Conference on Electrical Machines and Systems (ICEMS)*, Gyeongju, Republic of Korea, pp. 2573-2578, 2021.

[20] X. D. Xue, K. W. E. Cheng, Y. J. Bao, P. L. Leung, and N. Cheung, "Switched reluctance generators with hybrid magnetic paths for wind power generation," *IEEE Transactions on Magnetics*, vol. 48, no. 11, pp. 3863-3866, Nov. 2012.

[21] H. Qiu, S. Zhang, W. Li, and C. Yang, "Improvement of ferromagnetic bridge structure of axial–radial flux type permanent magnet synchronous machine," *IEEE Transactions on Industry Applications,* vol. 56, no. 4, pp. 3498-3505, July-Aug. 2020.

[22] J. M. Seo, J. Ro, S.-H. Rhyu, I.-S. Jung, and H.-K. Jung, "Novel hybrid radial and axial flux permanent-magnet machine using integrated windings for high-power density," *IEEE Transactions on Magnetics*, vol. 51, no. 3, pp. 1-4, Mar. 2015.

[23] R. Nasiri-Zarandi, M. Mirsalim, and A. Tenconi, "A novel hybrid hysteresis motor with combined radial and axial flux rotors," *IEEE Transactions on Industrial Electronics*, vol. 63, no. 3, pp. 1684-1693, Mar. 2016.

[24] B. Guo, F. Peng, Z. D. Khedda, F. Dubas, and Y. Huang, "Equivalent transformation between axial- and radial-flux permanent-magnet machines," *IEEE Transactions on Transportation Electrification*, vol. 9, no. 2, pp. 3085-3094, June 2023.

[25] X. Wang, Y. Fan, Q. Chen, and Z. Wu, "Magnetic circuit feature investigation of a radial–axial brushless hybrid excitation machine for electric vehicles," *IEEE Transactions on Transportation Electrification*, vol. 9, no. 1, pp. 382-393, Mar. 2023.

[26] B. Shi, X. Huang, J. Li, H. Zhang, H. Zhao, and X. Zhang, "Novel end-winding hybrid flux machine," *IEEE Access*, vol. 11, pp. 133781-133791, 2023.

[27] H. Chen and W. Yan, "Flux characteristics analysis of a double-sided switched reluctance linear machine under the asymmetric air gap," *IEEE Transactions on Industrial Electronics*, vol. 65, no. 12, pp. 9843-9852, Dec. 2018.

[28] H. Chen, X. Liu, and W. Yan, "Three-dimensional magnetic equivalent circuit research of double-sided switched reluctance linear machine," *IEEE Transactions on Applied Superconductivity*, vol. 30, no. 4, pp. 1-8, June 2020.

Wenju Yan (M'19) received the B.S. degree in Electrical Engineering and Automation from the China University of Mining and Technology, Xuzhou, China, in 2013. He received the Ph.D. degree in electrical engineering from the China University of Mining and Technology, in 2018. Since 2018, he has been with China University of Mining and Technology, where he is currently an associate professor in the School of Electrical Engineering. His current research interests include electric vehicles, electric traction, iron loss analysis and motor design.

Jun Xin received the B.S. degree in Electrical Engineering and Automation from the China University of Mining and Technology, Xuzhou, China, in 2023. He is currently working toward the M.S. degree in electrical engineering from the China University of Mining and Technology. His research interests include integrated drive systems for electric vehicles and double-stator switched reluctance motors.

Hongwei Yang received the B.S. degree in Electrical Engineering and Automation from the School of Mechanical and Electrical Engineering and Automation, Nanhang Jincheng College, Nanjing, China, in 2022. He is currently working toward the M.S. degree in electrical engineering with the China University of Mining and Technology, Xuzhou, China. His research interest includes electric machine design and double-stator switched reluctance motor.

Hao Chen (SM'08) received the B.S. and Ph.D. degrees in Electrical Engineering from the Department of Automatic Control, Nanjing University of Aeronautics and Astronautics, Nanjing, China, in 1991 and 1996, respectively. In 1998, he became an Associate Professor with the School of Information and Electrical Engineering, China University of Mining and Technology, Xuzhou, China, where he has been a professor since 2001. From 2002 to 2003, he was a Visiting Professor at Kyungsung University, Busan, Korea. Since 2008, he has been an Adjunct Professor at the University of Western Australia, Perth, Australia. He is the author of one book and has authored more than 200 papers. His current research interests include motor control, linear launcher, electric vehicles, electric traction, servo drives and wind power generator control. Chen was the recipient of both the Prize of Science and Technology of Chinese Youth and the Prize of the Fok Ying Tong Education Foundation for Youth Teachers in 2004. He became the Chinese New Century Hundred-Thousand-Ten Thousand Talents Engineering National Talent in 2007 and won the Government Especial Allowance of People's Republic of China State Department in 2006.

Ryszard Palka D.Sc. Ph.D. Eng. is Head of Department of Electrical Machines and Drives, West Pomeranian University of Technology, Szczecin, Poland. In 1987-2005, he was with the Institute of Electrical Machines, Traction and Drives, TU Braunschweig, Germany. Areas of research include electromagnetic field theory, numerical field calculations, optimization of electromagnetic fields, electrical machines and high-temperature superconductivity. He is the author of over 320 refereed journal articles, conference papers, and technical reports, and co-author of four books. He is a member of IEEE, International Compumag Society, Polish Society of Theoretical and Applied Electrical Engineering, International Maglev Board and Committee on Electrical Engineering and Polish Academy of Sciences.

Marcin Wardach D.Sc. Ph.D. Eng. was born in Poland in 1980. He graduated and received the Ph.D. degree from the Electrical Department, Szczecin University of Technology, Szczecin, Poland, in 2006 and 2011, respectively. From 2020 until now, he is an Associate Professor with the Faculty of Electrical Engineering, West Pomeranian University of Technology, Szczecin. His research interests include the design of electrical machines and drives especially unconventional and hybrid excited. He is the author of over 100 scientific papers and post-conference publications. He is a member of the Association of Polish Electrical Engineers and Polish Society of Theoretical and Applied Electrical Engineering.

Konrad Woronowicz received a Ph.D. degree in adaptive linear induction motors (LIM) control and a D.Sc. degree in an area of Wireless Power Transfer (WPT) from the West Pomeranian University of Technology, Szczecin, Poland, in 2001 and 2015, respectively. From 1995 until 2019, he was with Bombardier Transportation, Canada, involved in various transportation and research and development projects and played a key role in commercializing LIM-based mass transit systems in such locations as New York, Beijing, Vancouver,

Kuala Lumpur and Seoul. Later, he partook in the development of a high power WPT system for buses and light rail vehicles. He has authored numerous patents in WPT, converter topology, converter controls, and motors. He is currently an Associate Professor with the West Pomeranian University of Technology, Department of Electrical Engineering. His current research interests include electromagnetic design for WPT, development of high-performance linear motors, resonant circuits and power conversion for energy storage.

Electromagnetic Characteristics Comparative Investigation of Five-phase Wide-and-Narrow Stator Poles Axial Flux Switched Reluctance Motors with Different Rotor Poles Number

Fengyuan Yu[1], Xing Wang[2], Hao Chen[1,2,3], Wenju Yan[1], Hongwei Yang[1], Popov Stanislav Olegovich[4], Bodrenkov Evgenii Alexandrovich[4], Nurkhat Zhakiyev[5], and Yassen Gorbounov[6]

[1]School of Electrical Engineering
China University of Mining and Technology, Xuzhou 221116, China
fyyu@cumt.edu.cn, hchen@cumt.edu.cn, yanwenju09@126.com, ts22230175p31@cumt.edu.cn

[2]International Joint Research Center of Central and Eastern European Countries on New Energy Electric Vehicle Technology and Equipment
Xuzhou 221008, China
3512@cumt.edu.cn

[3]Shenzhen Research Institute
China University of Mining and Technology
Shenzhen 518057, China

[4]Institute of Energy
Peter the Great Saint-Petersburg Polytechnic University
195251 Saint Petersburg, Russia
popovso@spbstu.ru, bodrenkovea@spbstu.ru

[5]Department of Science and Innovation
Astana IT University, Astana, Kazakhstan
nurkhat.zhakiyev@astanait.edu.kz

[6]Department of Informatics
New Bulgarian University, Sofia 1618, Bulgaria
y.gorbounov@mgu.bg

Abstract – Axial flux switched reluctance motors (AFSRMs) offer advantages such as a large air-gap surface area, compact structure, and high torque density. This paper proposes a novel five-phase AFSRM structure featuring wide-and-narrow stator poles (NWS-AFSRM) and presents a comparative study of the electromagnetic characteristics of the five-phase NWS-AFSRM with varying rotor pole numbers. Firstly, while maintaining a constant stator pole count, four feasible rotor pole configurations are determined: 20/12, 20/14, 20/16, and 20/18-poles. Subsequently, based on these four pole combinations, their corresponding phase excitation sequences are investigated. Using the finite element analysis (FEA) method, both static and dynamic electromagnetic characteristics are evaluated to analyze the influence of rotor pole number on the motor's electromagnetic performance.

Index Terms – Axial flux switched reluctance motor, electromagnetic performance, finite element analysis, phase excitation sequence.

I. INTRODUCTION

The switched reluctance motor (SRM) has the advantages of robust structure, low manufacturing cost, high fault tolerance and high DC-link voltage utilization. Hence, SRM has been applied in electric vehicles, aerospace, and mining industry equipment [1, 2]. Depending on the direction of the main flux path of the air gap with respect to the direction of the rotation axis, SRM could be classified into radial flux SRM (RFSRM), transverse flux SRM (TFSRM) and axial flux SRM (AFSRM) structures [3–5]. The torque output capacity of RFSRM is affected by its axial length, making it unsuitable for applications where axial mounting space

Submitted On: December 25, 2024
Accepted On: September 8, 2025

https://doi.org/10.13052/2025.ACES.J.400909

is limited. In contrast, the AFSRM has a higher torque density and is more advantageous in low speed and high torque operating conditions.

In recent years, AFSRM has been investigated from the perspective of novel motor structure and parameter optimization. Reference [6] presented a 6/4-pole single stator single rotor AFSRM structure with doubly salient stator-rotor poles. The electromagnetic performance was evaluated using the finite element analysis (FEA) method, and the results showed that the AFSRM obtained a stronger torque output capability than the conventional RFSRM. However, the long flux path constituted by the doubly salient structure results in the motor's torque output capability not being fully exploited. References [7–9] proposed the short magnetic path by combining the single-tooth winding and the segmented rotor structure on the SRM, thus improving the torque output capability of the motor.

References [10, 12] compare the static and dynamic performance of SRMs with different flux paths. In [13–18], SRM structures combining axial and short flux paths are proposed, demonstrating their ability for torque performance improvement. However, all of the above structures use a three-phase structure. Compared with the three-phase SRM drive system, the multiphase SRM drive system has the following advantages: (1) single-phase drive voltage is reduced so that low power level switching devices can be used, reducing the requirement for inverter capacity per phase; (2) multiphase motor torque frequency is increased and the torque pulsation is reduced; (3) fault tolerance and reliability of multiphase motors are improved, providing a higher degree of freedom for applications requiring high reliability; (4) more controllable resources.

In this paper, characteristics of the five-phase wide-and-narrow stator poles (NWS)-AFSRM are investigated, and the influence of rotor poles numbers on motor performance is analyzed. The paper is organized as follows. In section II, the NWS-AFSRM structure is presented and the phase excitation sequence of four five-phase NWS-AFSRM is investigated. In section III, the FEA model of the four NWS-AFSRM is developed and the static electromagnetic performance is analyzed. Section IV investigates the dynamic electromagnetic performance of four motors and analyses the impact of phase conduction sequence on the dynamic torque output capacity. Section V concludes this paper.

II. FIVE-PHASE WIDE-AND-NARROW STATOR POLES AFSRM

Figure 1 illustrates the three-phase double stator NWS-AFSRM structure. The NWS-AFSRM has double stator and single rotor configuration with two identical stator discs set axially on either side of the segmented inner rotor. The main flux path flows along the axial direction of the motor, and there is a plane-type air gap between two stator discs and one segmented rotor disc. Its stator features alternately arranged wide-and-narrow poles, with concentrated windings wound solely on the wide poles, while the narrow poles remain unwound. In references [9, 10], this winding configuration is referred to as a single-tooth winding or a single-layer conventional winding configuration.

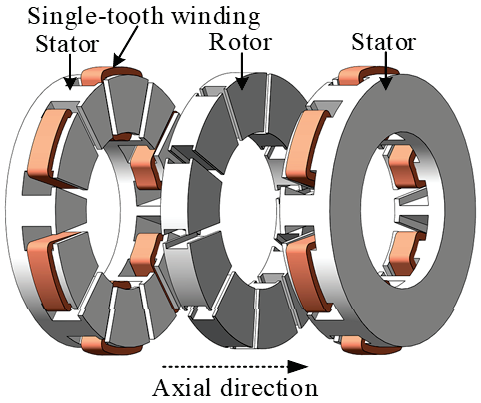

Fig. 1. Three-phase double stator wide-and-narrow stator poles AFSRM structure.

The number of stator and rotor poles has a significant influence on the motor performance. The possible combination of stator and rotor poles for the NWS-AFSRM is:

$$\begin{cases} LCM(N_s/2, N_r) = N_{ph}N_r \\ N_s = mN_{sd} = 2mN_{ph} \\ N_r = mN_{rd},\ m \geq 2 \\ N_{sd} > N_{rd} \end{cases}, \quad (1)$$

where LCM means the least common multiple, N_s, N_r, and N_{ph} represent the number of stator poles, rotor poles, and motor phases, N_{sd} and N_{rd} denote the number of poles of the stator and rotor of the unit motor.

Based on equation (1), the feasible stator/rotor pole combinations for three-phase, four-phase, and five-phase NWS-AFSRMs are readily obtained, as summarized in Table 1.

According to Table 1, the feasible stator/rotor pole number combinations for three-phase NWS-AFSRMs are identified as 12/8 and 12/10, while potential combinations for four-phase NWS-AFSRMs are 16/10

Table 1: Stator and rotor poles selection for NWS-AFSRM with different phase number

Phase Number	N_{sd}	N_{rd}
3	6	4, 5
4	8	5, 7
5	10	6, 7, 8, 9

and 16/14. Additionally, possible stator/rotor pole numbers for five-phase NWS-AFSRMs include 20/12, 20/14, 20/16, and 20/18.

Based on the principle of minimum reluctance, the phase excitation sequence for both the three-phase 12/8 and 12/10 NWS-AFSRMs is ABC. Similarly, the sequence for the four-phase 16/10 and 16/14 NWS-AFSRMs is ABCD. It can be observed that for both three-phase and four-phase NWS-AFSRMs, variations in rotor pole number do not result in new excitation sequences and the next conducting phase is always adjacent to the previous one.

However, for five-phase NWS-AFSRMs, differences in rotor pole number lead to the emergence of distinct excitation sequences. Figure 2 illustrates schematic diagrams of the phase excitation sequences for four five-phase NWS-AFSRMs with differing rotor pole numbers. As depicted in Fig. 2, the phase excitation sequence for the 20/12 five-phase NWS-AFSRM is ABCDE. For the 20/14, 20/16, and 20/18 machines, the excitation sequences are ADBEC, ACEBD, and AEDCB, respectively. It should be noted that for 20/12 and 20/18 motors, the next conducting phase is always adjacent to the preceding phase. Conversely, for 20/14 and 20/16 motors, the next conducting phase is non-adjacent to the preceding phase.

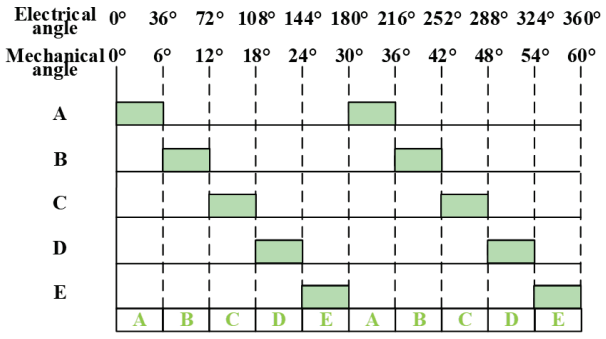

(a)

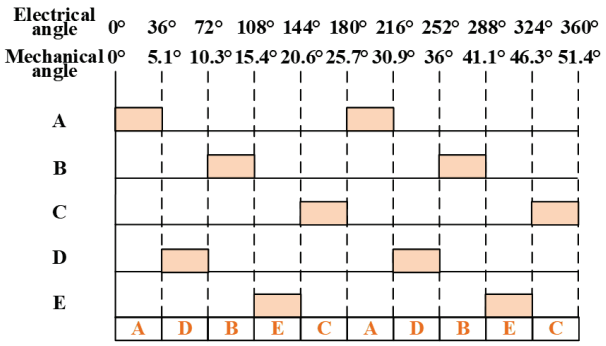

(b)

Fig. 2. *Continued.*

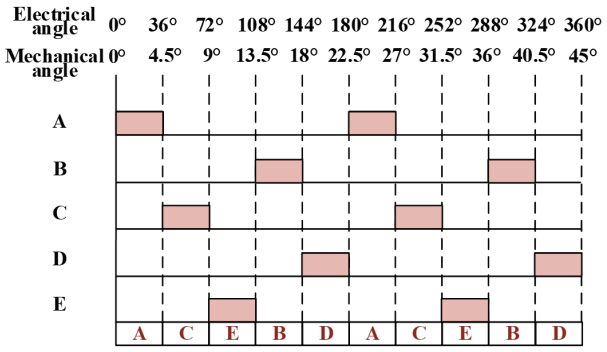

(c)

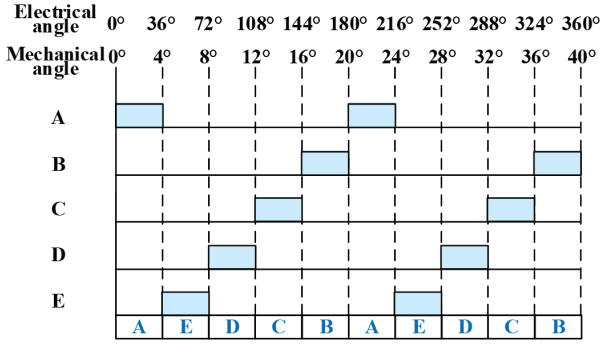

(d)

Fig. 2. Excitation phase sequence of the four five-phase NWS-AFSRMs: (a) 20/12, (b) 20/14, (c) 20/16, and (d) 20/18.

Furthermore, as a multiphase motor, the five-phase NWS-AFSRM offers advantages over conventional three-phase motors, such as lower overall cost of the drive system, reduced torque ripple, and enhanced reliability. Therefore, this paper focuses on the five-phase NWS-AFSRM to investigate the influence of rotor pole number and phase excitation sequence on its electromagnetic characteristics.

III. STATIC PERFORMANCE ANALYSIS

The main parameters of the five-phase NWS-AFSRM with four different rotor poles number are listed in Table 2. In order to achieve a fair comparison, these motors have the same dimensions externally, such as the same stator-rotor inner diameter, stator-rotor outer diameter, air gap length, axial length, and winding parameters.

Based on the parameters of the four motors in Table 2, their 3D finite element models were built in Altair flux software, as shown in Fig. 3.

A. Magnetic density characteristics

The magnetic density distribution map can reflect the magnetic saturation level of the motor's stator and rotor cores. By applying an excitation current of 30 A to phase-C individually, the results of the magnetic density distribution of these four motors in the rotor aligned

Table 2: Parameters of the five-phase NWS-AFSRM

Motor Parameters	Items	20/12	20/14	20/16	20/18
Rated voltage	V	96	96	96	96
Rated speed	r/min	600	600	600	600
Outer diameter	mm	175	175	175	175
Inner diameter	mm	101	101	101	101
Stator yoke length	mm	7.5	7.5	7.5	7.5
Stator pole length	mm	32	32	32	32
Stator slot width	mm	10	10	10	10
Rotor pole length	mm	17	17	17	17
Rotor slot width	mm	19	15	14	11.5
Air-gap length	mm	0.4	0.4	0.4	0.4
Winding coil turns per slot	/	50	50	50	50
Axial length	mm	96.8	96.8	96.8	96.8

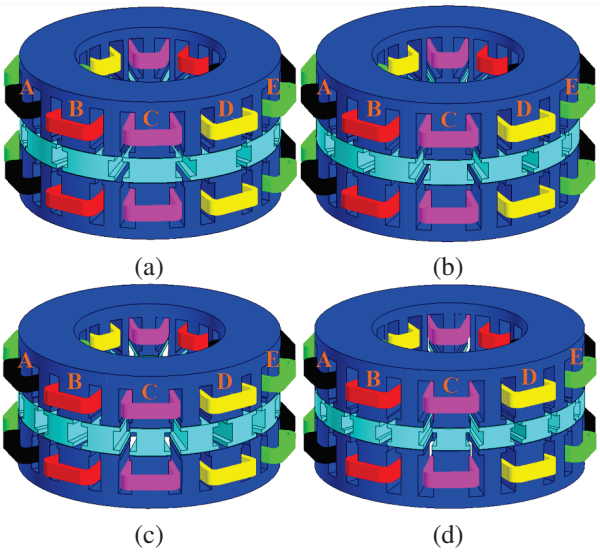

Fig. 3. Finite element models of four five-phase NWS-AFSSRMs with different rotor poles number: (a) 20/12, (b) 20/14, (c) 20/16, and (d) 20/18.

position and the unaligned position are obtained, as illustrated in Figs. 4 and 5.

From Fig. 4, it can be observed that in the completely unaligned position, the magnetic flux density of the rotor segment core is small, and magnetic saturation occurs only at the rotor pole shoes. Meanwhile, there is little difference in the manifestation of magnetic density

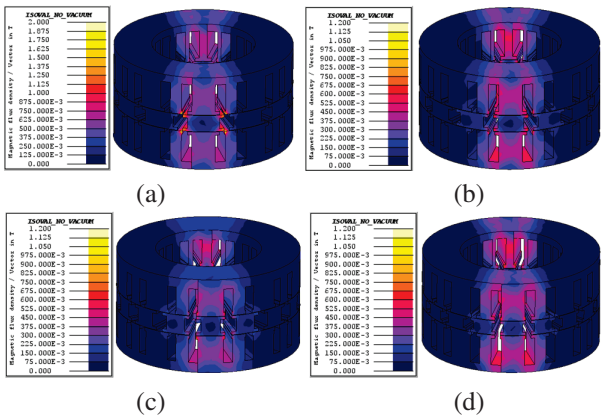

Fig. 4. Magnetic density maps of the four five-phase NWS-AFSSRMs at the rotor unaligned position: (a) 20/12, (b) 20/14, (c) 20/16, and (d) 20/18.

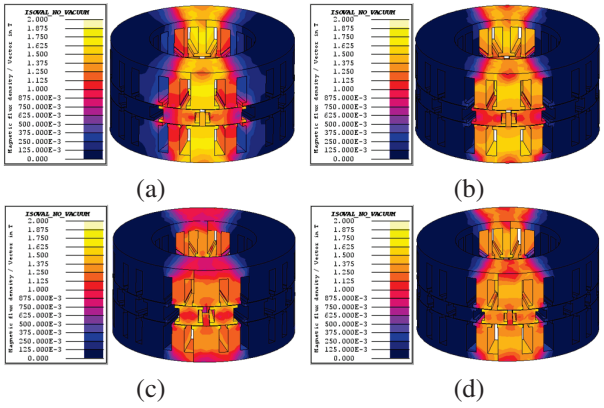

Fig. 5. Magnetic density maps of the four five-phase NWS-AFSSRMs at the rotor aligned position: (a) 20/12, (b) 20/14, (c) 20/16, and (d) 20/18.

among the four motors, only slightly varying numerically. As found in Fig. 5, the magnetic flux density is uniformly distributed in the stator yoke, stator wide pole, stator narrow pole, and rotor block. Similar to the phenomenon in the unaligned position, the magneto-density clouds of the four motors in the aligned position are only slightly different in terms of the magneto-density intensity.

B. Inductance and torque characteristics

The inductance-angle-current and torque-angle-current characteristics can reflect the torque output capability of the NWS-AFSRM. Therefore, the phase self-inductance and static torque characteristics of four five-phase NWS-AFSRMs at different current levels (30 A and 60 A) are shown in Figs. 6 and 7.

Root mean square values of static torque at different current levels (30 A, 45 A, 60 A, 75 A) are listed in Table 3. As observed, as the number of rotor poles increases,

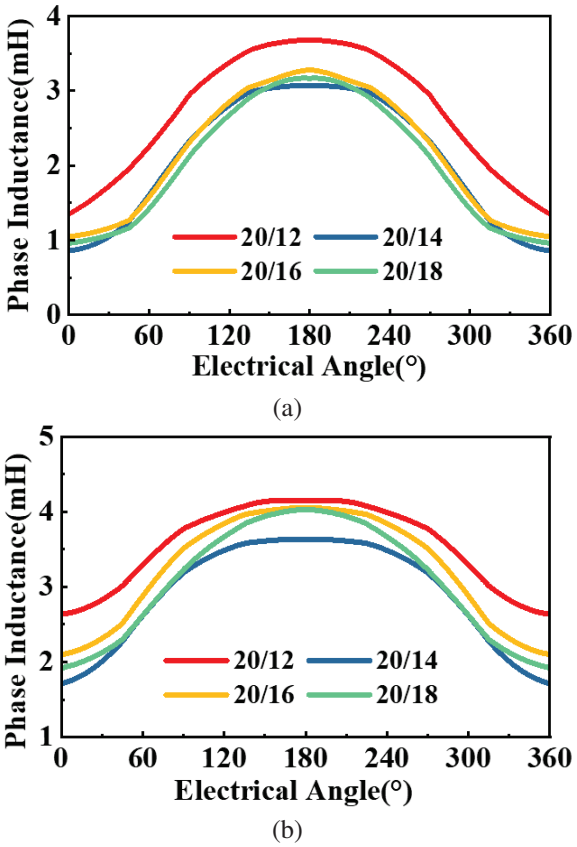

Fig. 6. Phase self-inductance of the four five-phase NWS-AFSRMs at different excitation currents: (a) 30 A and (b) 60 A.

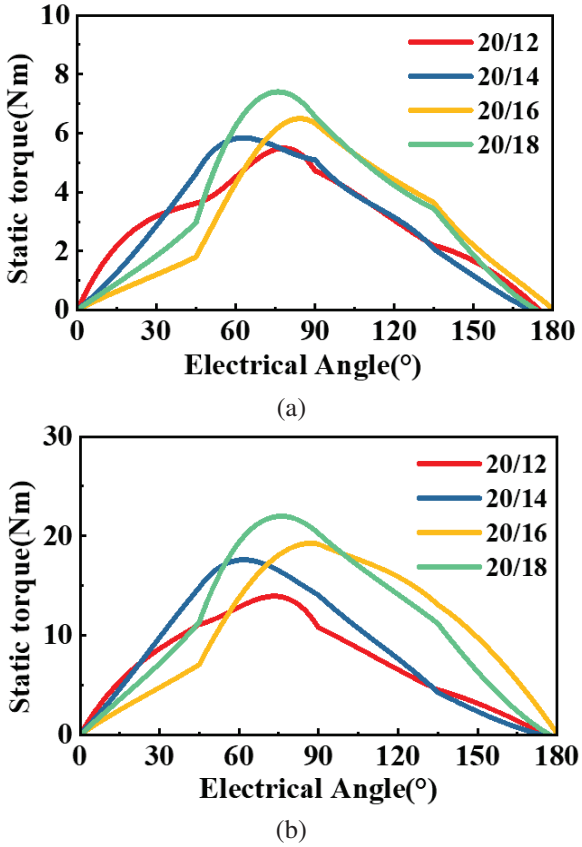

Fig. 7. Static torque of the four five-phase NWS-AFSRMs at different excitation currents: (a) 30 A and (b) 60 A.

Table 3: Root mean square value of static torque for the four motors

Excitation Current	20/12	20/14	20/16	20/18
30 A	3.417	3.539	3.713	4.257
45 A	6.332	7.177	8.033	8.954
60 A	8.702	10.527	12.414	13.275
75 A	10.741	12.748	14.902	16.635

the root mean square of the static torque increases as well in different excitation current. It can be noted that the step angle decreases with increasing N_r as compared to motors with low rotor pole numbers. This leads to a decrease in the relative stator pole arc angle per revolution for the same multiphase conduction cycle. This means that more slot area is available for the excitation winding without reducing the maximum multiphase conduction cycle. Therefore, increasing the number of rotor poles can increase the static torque capacity of the motor.

IV. DYNAMIC PERFORMANCE ANALYSIS

In order to further analyze the dynamic performance of the motor, dynamic simulation models are established. It should be noted that the asymmetrical half-bridge converter circuit is employed for the power converter module, as depicted in Fig. 8.

Figure 9 shows the dynamic torque waveforms of the four motors under the single pulse control method. The rotational speeds are set at 600 r/min and 1000 r/min. In order to ensure the fairness of the comparison, the turn-on and turn-off angles of the four motors are uniformly set at 0 and 36 electrical angles.

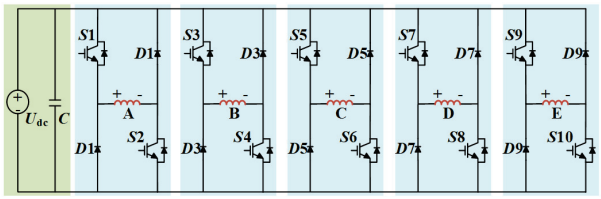

Fig. 8. Five-phase asymmetric half-bridge power converter.

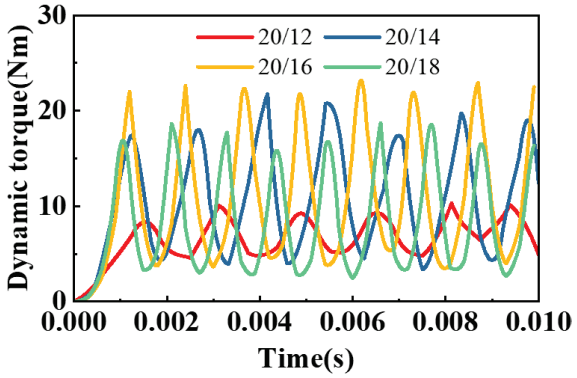

(a)

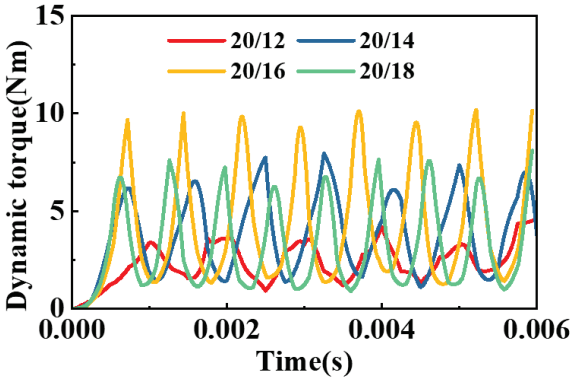

(b)

Fig. 9. Dynamic torque of the four five-phase NWS-AFSRMs at different speeds: (a) 600 r/min and (b) 1000 r/min.

From the results of Fig. 9 and Table 4, it is analyzed that the dynamic torque of the motor at the same number of ampere-turns is not increasing as the number of rotor poles increases. Among these four motors, the motor with the highest dynamic torque is 20/16 which is not the same as the static torque results.

The mutual inductance characteristics of the four motors are further analyzed in this paper. In NWS-AFSRM, mutual inductance refers to the ability of a current change in one phase winding to induce an effect in another phase winding. Generally, a lower mutual inductance value between phases corresponds to reduced interference between the respective windings [19-20]. Results of the mutual inductance of the four motors analyzed by FEA are presented in Fig. 10. Note that L_{AB}, L_{AC}, L_{AD}, and L_{AE} denote the mutual inductance values measured in windings B, C, D, and E, respectively, when current is applied to phase winding A.

As observed in Fig. 10, when excitation current is applied to phase A, the mutual inductances L_{AB} and L_{AE} are significant for all four motors, whereas L_{AC} and L_{AD} remain negligible. This phenomenon can be attributed to the structural characteristics of the NWS-AFSRM. Specifically, phase A shares auxiliary stator poles with both phase B and phase E. Consequently, excitation of phase A inevitably influences phases B and E to some degree. In contrast, the C-phase winding is separated from the A-phase winding by the B-phase winding and,

Table 4: Dynamic torque for the four motors

Speed		20/12	20/14	20/16	20/18
600 r/min	T_{min}	4.538	3.396	3.163	2.449
	T_{max}	10.318	21.960	22.715	19.449
	T_{avg}	7.133	11.108	11.151	8.482
1000 r/min	T_{min}	0.940	1.136	1.163	0.914
	T_{max}	4.636	8.024	10.133	8.049
	T_{avg}	2.582	3.997	4.365	3.274

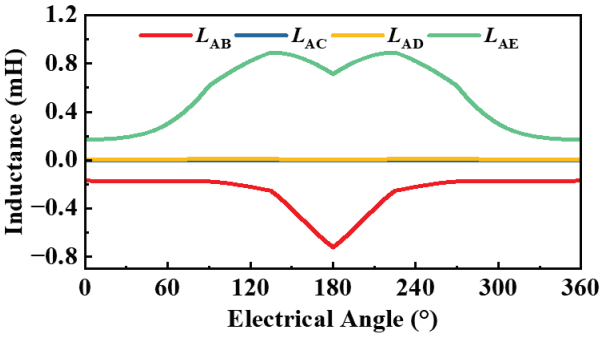

(a)

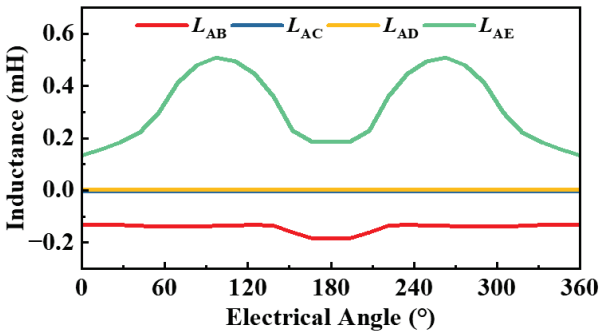

(b)

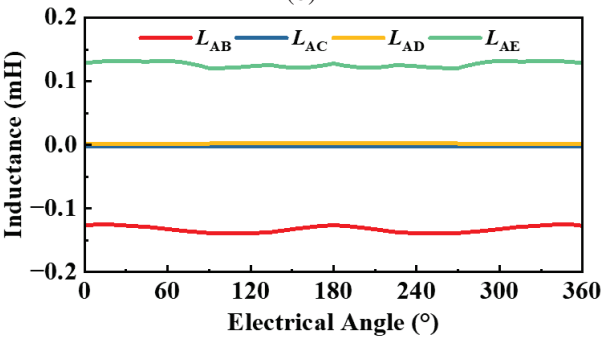

(c)

Fig. 10. *Continued.*

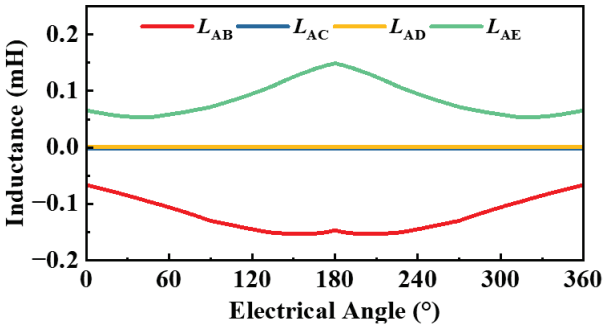

(d)

Fig. 10. Comparison of mutual inductance for the four five-phase NWS-AFSRMs: (a) 20/12, (b) 20/14, (c) 20/16, and (d) 20/18.

similarly, the D-phase winding is separated from the A-phase winding by the E-phase winding. As a result, excitation of phase A has minimal effect on phases C and D. These observations are corroborated by the magnetic flux density distributions presented in Figs. 4 and 5.

As established in section II, the 20/12-pole and 20/18-pole NWS-AFSRMs exhibit ABCDE and AEDCB phase excitation sequences, respectively, where each subsequently energized phase is spatially adjacent to its predecessor. Due to the mutual coupling between adjacent phases, this configuration induces torque decay in the outgoing phase during commutation. Conversely, the ADBEC and ACEBD sequences of the 20/14-pole and 20/16-pole NWS-AFSRMs feature non-adjacent phase transitions, effectively avoiding inter-phase torque decay. In summary, among the four five-phase NWS-AFSRM configurations, the limited dynamic torque capability of the 20/12-pole and 20/18-pole machines is attributed to their significant mutual inductances L_{AB} and L_{AE}. These substantial mutual inductances adversely affect the dynamic torque performance. Conversely, the superior dynamic torque capability of the 20/14-pole and 20/16-pole configurations stems from their negligible mutual inductances L_{AC} and L_{AD}. This minimal mutual coupling enables them to maximize their inherent dynamic torque potential.

V. CONCLUSION

In this paper, the three-dimensional FEA approach is employed to investigate the influence of rotor poles number and phase commutation sequence on the electromagnetic performance of five-phase NWS-AFSRM. It was found that the static and dynamic electromagnetic torque of the four machines exhibited distinct characteristics, and potential underlying causes for this phenomenon were analyzed. Key findings are summarized as follows.

(1) Phase excitation sequence varies with the rotor pole number. The sequences for the 20/12, 20/14, 20/16, and 20/18-pole configurations are ABCDE, ADBEC, ACEBD, and AEDCB, respectively.

(2) Static torque under identical ampere-turn excitation increases monotonically with increasing rotor pole number. The static torque values, ranked from lowest to highest, correspond to the 20/12, 20/14, 20/16, and 20/18-pole machines.

(3) In contrast, dynamic torque does not exhibit a monotonic increase with rotor pole number. The dynamic torque values, ranked from lowest to highest, correspond to the 20/12, 20/18, 20/14, and 20/16-pole machines.

(4) Owing to the single-tooth wound structure and short flux path characteristics of the NWS-AFSRM, flux generated during the excitation of one phase adversely affects adjacent phases but minimally impacts non-adjacent phases. This phenomenon is identified as the primary reason for the superior dynamic torque of the 20/14-pole and 20/16-pole five-phase NWS-AFSRMs compared to the 20/12-pole and 20/18-pole counterparts.

Therefore, by designing appropriate combinations of stator slot number and rotor pole number in multi-phase NWS-AFSRMs, the detrimental effects of mutual inductance between adjacent phases on motor performance can be mitigated. This provides a novel perspective for enhancing the performance of five-phase and higher-phase-count machines.

Note that the conclusions drawn in this study are based on the results of three-dimensional FEA. While this method represents a well-established standard in the electromagnetic design and analysis of electric machines, it is acknowledged that physical prototyping and experimental validation remain essential. Accordingly, future work will involve fabricating a prototype and establishing a test platform to experimentally verify the FEA results presented herein.

ACKNOWLEDGMENT

This work is supported by the National Natural Science Foundation of China International (regional) cooperation and exchange projects NSFC-RSF (W2412064), the Shenzhen Collaborative Innovation Special Plan International Cooperation Research Project (GJHZ20220913144400001), the General Research Project of Shenzhen Science and Technology Plan (JCYJ20220818100000001), the Jiangsu Funding Program for Excellent Postdoctoral Talent (2024ZB008), the China Postdoctoral Science Foundation (2024M763541), the 2022 China-CEEC University Joint Education Program (2022200), and the 2023

China-CEEC University Joint Education Program (2023304).

REFERENCES

[1] L. Ge, N. Du, J. Song, J. Zhang, Z. Fan, D. Zhang, and S. Song, "Advanced technology of switched reluctance machines in more electric aircraft: A review," *IEEE Trans. Power Electron*., vol. 40, no. 1, pp. 195-216, Jan. 2025.

[2] K. Diao, G. Bramerdorfer, X. Sun, Z. Yang, and S. Han, "Multiobjective design optimization of a novel switched reluctance motor with unequal alternating stator yoke segments," *IEEE Trans. Transp. Electrif.*, vol. 9, no. 1, pp. 512-521, Mar. 2023.

[3] H. Torkaman, A. Ghaheri, and A. Keyhani, "Axial flux switched reluctance machines: A comprehensive review of design and topologies," *IET Electr. Power Appl.*, vol. 13, no. 3, pp. 310-321, Mar. 2019.

[4] M. Belhadi, G. Krebs, C. Marchand, et al., "Evaluation of axial SRM for electric vehicle application," *Electr. Power Syst. Res.*, vol. 148, pp. 155-161, July 2017.

[5] J. Ma, J. Li, H. Fang, Z. Li, Z. Liang, Z. Fu, L. Xiao, and R. Qu, "Optimal design of an axial-flux switched reluctance motor with grain-oriented electrical steel," *IEEE Trans. Ind. Appl*., vol. 53, no. 6, pp. 5327-5337, Nov.-Dec. 2017.

[6] H. Arihara and K. Akatsu, "Basic properties of an axial-type switched reluctance motor," *IEEE Trans. Ind. Appl.*, vol. 49, no. 1, pp. 59-65, Jan.-Feb. 2013.

[7] Z. Xu, D.-H. Lee, and J.-W. Ahn, "Design and operation characteristics of a novel switched reluctance motor with a segmental rotor," *IEEE Trans. Ind. Appl.*, vol. 52, no. 3, pp. 2564-2572, May-June 2016.

[8] X. Sun, K. Diao, G. Lei, Y. Guo, and J. Zhu, "Study on segmented-rotor switched reluctance motors with different rotor pole numbers for BSG system of hybrid electric vehicles," *IEEE Trans. Veh. Technol.*, vol. 68, no. 6, pp. 5537-5547, June 2019.

[9] B. C. Mecrow, E. A. El-Kharashi, J. W. Finch, and A. G. Jack, " Segmental rotor switched reluctance motors with single-tooth windings," *IEE Proc.-Electr. Power Appl.*, vol. 150, no. 5, Sep. 2003.

[10] X. Y. Ma, G. J. Li, G. W. Jewell, and Z. Q. Zhu, "Recent development of reluctance machines with different winding configurations, excitation methods, and machine structures," *CES Transactions on Electrical Machines and Systems (TEMS)*, vol. 2, no. 1, pp. 82-92, Mar. 2018.

[11] T. Husain, W. Uddin, and Y. Sozer, "Performance comparison of short-pitched and fully pitched switched reluctance machines over wide speed operations," *IEEE Trans. Ind. Appl.*, vol. 54, no. 5, pp. 4278-4287, Sep.-Oct. 2018.

[12] E. Cosoroaba, E. Bostanci, Y. Li, et al., "Comparison of winding configurations in double-stator switched reluctance machines," *IET Electr. Power Appl.*, vol. 11, no. 8, pp. 1407-1415, Sep. 2017.

[13] A. Labak and N. C. Kar, "Designing and prototyping a novel five-phase pancake-shaped axial-flux SRM for electric vehicle application through dynamic FEA incorporating flux-tube modeling," *IEEE Trans. Ind. Appl.*, vol. 49, no. 3, pp. 1276-1288, May-June 2013.

[14] R. Madhavan and B. G. Fernandes, "Axial flux segmented SRM with a higher number of rotor segments for electric vehicles," *IEEE Trans. Energy Convers.*, vol. 28, no. 1, pp. 203-213, Mar. 2013.

[15] R. Madhavan and B. G. Fernandes, "Performance improvement in the axial flux-segmented rotor-switched reluctance motor," *IEEE Trans. Energy Convers.*, vol. 29, no. 3, pp. 641-651, Sep. 2014.

[16] W. Sun, Q. Li, L. Sun, L. Zhu, and L. Li, "Electromagnetic analysis on novel rotor-segmented axial-field SRM based on dynamic magnetic equivalent circuit," *IEEE Trans. Magn.*, vol. 55, no. 6, pp. 1-5, June 2019.

[17] W. Sun, Q. Li, L. Sun, and L. Li, "Development and investigation of novel axial-field dual-rotor segmented switched reluctance machine," *IEEE Trans. Transp. Electrif.*, vol. 7, no. 2, pp. 754-765, June 2021.

[18] F. Yu, H. Chen, W. Yan, V. Pires, J. Martins, P. Rafajdus, A. Musolino, L. Sani, M. Aguirre, M. Saqib, M. Orabi, and X. Li, "Design and multi-objective optimization of a double-stator axial flux SRM with full-pitch winding configuration," *IEEE Trans. Transp. Electrif*., vol. 8, no. 4, pp. 4348-4364, Dec. 2022.

[19] E. S. Sanches and J. A. Santisteban, "Mutual inductances effect on the torque of an axial magnetic flux switched reluctance motor," *IEEE Latin America Trans.*, vol. 13, no. 7, pp. 2239-2244, July 2015.

[20] J. Ye, B. Bilgin, and A. Emadi, "Elimination of mutual flux effect on rotor position estimation of switched reluctance motor drives," *IEEE Trans. Power Electron.*, vol. 30, no. 3, pp. 1499-1512, Mar. 2015.

Fengyuan Yu received the Ph.D. degree from the School of Electrical Engineering, China University of Mining and Technology, Xuzhou, China, in 2023. Since 2023, he has been a Post-Doctoral Researcher with the China University of Mining and Technology. His research interests include switched reluctance drive, special motor design, power converters, and motor control.

Xing Wang received the B.S. and M.S. degrees from China University of Mining and Technology, Xuzhou, China, in 1996 and 1999, respectively. Her research interests include switched reluctance drive, electric vehicle, electric traction, wind power generator, power converters, and motor control.

Hao Chen received his B.S. and Ph.D. degrees from the Department of Automatic Control, Nanjing University of Aeronautics and Astronautics, Nanjing, China, in 1991 and 1996, respectively. Since 1996, he has been with China University of Mining and Technology, where he is currently a Full Professor with the School of Electrical Engineering. His research interests include motor control, linear launcher, electric vehicles, electric traction, servo drives, and wind power generator control.

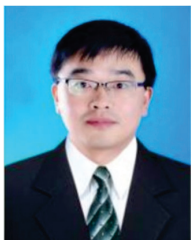

Wenju Yan received the B.S. and Ph.D. degrees from the China University of Mining and Technology, Xuzhou, China, in 2013 and 2018, respectively. Since 2018, he has been with China University of Mining and Technology, where he is currently an Associate Professor with the School of Electrical Engineering. His research interests include electric vehicles, electric traction, iron loss analysis, and motor design.

Hongwei Yang is pursuing his master's degree in electrical engineering at China University of Mining and Technology, Xuzhou, China. His current research interests include electric vehicles, electric traction, and special motor design.

Popov Stanislav Olegovich received the M.S. degree from in the field of electric power plants and automation of power systems in 2008, and the PhD degree of Technical Sciences associate professor Institute of Energy, working from 2008 to the present in SPBSTU.

Bodrenkov Evgenii Alexandrovich received the B.S. and M.S. degrees from Federal State Budgetary Educational Institution of Higher Education, Amur State University, and the Ph.D. degrees from Federal State Autonomous Educational Institution of Higher Education, Peter the Great St. Petersburg Polytechnic University.

Nurkhat Zhakiyev is a senior researcher and associate professor with a Ph.D. in the field of physics and currently serves as the head of the Department of Science and Innovation at the Astana University of Information Technology, Kazakhstan. He has nearly a decade of research experience in computational modeling of energy systems and physical processes, with a focus on data science in energy and environmental economics and climate change mitigation analysis. He started his career in 2007 as a junior researcher at West Kazakhstan State University, then rose through the ranks in various higher education institutions and research institutes in Astana, where he gained extensive experience in research and project management. He has worked as a principal researcher or co-researcher on projects

funded by the Ministry of Science and Higher Education of Kazakhstan, the Royal Academy of Engineering, the British Council and other institutions in various fields such as low carbon development, greenhouse gas emission forecasting, energy efficiency solutions and more.

Yassen Gorbounov received his B.S., M.S., and Ph.D. degrees from the Sofia University of Technology, Sofia, Republic of Bulgaria, in 2002, 2004, and 2013, respectively. Since 2017, he has been working as an Associate Professor at the Sofia University of Technology. His current research interests include power electronics and the mining industry.

Research on Electromagnetic Characteristics for an Outer Rotor Doubly Salient Permanent Magnet Reluctance Generator in Direct-drive Vertical Axis Fans

Zhe Zhou, Yifei Gao, Kuan Zhang, Ge Qi, and Shuai Xu

School of Electrical and Information Engineering
Zhengzhou University, Zhengzhou, Henan, 450001, China

Abstract – To enhance the operation efficiency of generators in variable wind conditions, this paper proposes an outer rotor doubly salient permanent magnet reluctance generator(ORDS-PMRG). First, the operation principles of ORDS-PMRG are presented. Then, the magnetic modulation effect of the multi-tooth structure on generator air-gap flux density is analyzed. Next, the operation modes of the proposed generator are analyzed and can be flexibly switched by changing the winding connection methods. Meanwhile, the electromagnetic characteristic analysis is developed based on the finite element model. The results indicate that the proposed ORDS-PMRG has more operation modes and higher power density compared to traditional doubly salient permanent magnet reluctance generators.

Index Terms – Electromagnetic characteristic, multi-mode operation, outer rotor, permanent magnet reluctance generator.

I. INTRODUCTION

A. Vertical axis wind turbine

As a clean energy source, wind power has emerged as a key focus area in renewable energy development. In the field of distributed generation, vertical-axis wind turbine (VAWT) has many advantages over horizontal-axis wind turbine (HAWT). Notable advantages include its ability to harness wind energy across full speed ranges, simplified installation procedures, and reduced mechanical complexity [1]. The direct-drive VAWT further reduces the transmission structure. The power generation efficiency and reliability of the system have been further improved [2].

In terms of generators, medium and large direct-drive VAWTs mostly use permanent magnet synchronous generators [3], electrically excited synchronous generators, and switched reluctance generators [4]. There are also some generators with hybrid excitation, such as induction reluctance motor [5] and permanent magnet assisted reluctance synchronous motor [6]. However, these generators are subject to problems such as large volume, high maintenance costs, and large vibrations. It is difficult to apply in small direct drive VAWT.

In terms of fan speed regulation, VAWT still needs to pitch the blades to adjust the speed [7]. If the mechanical devices required for fan speed regulation can be reduced, the reliability and power generation efficiency of the power generation system will be further improved, and the cost will be reduced.

B. Permanent magnet reluctance generator

In recent years, permanent magnet vernier generators (PMVG) have been widely adopted because of their large torque and low speed [8, 9]. It is also widely used in the field of direct-drive wind turbines [10, 11].This structure of the generator brings new inspiration to the doubly salient permanent magnet reluctance generators. The tangentially excited PMVG has the characteristics of high mechanical strength and strong excitation ability, which has received further attention [12]. However, in recent years, scholars have gradually noticed that although its power density is relatively large, there is still room for improvement [13]. Several methods are proposed to improve its power density, such as increasing the magnetic bridge to improve the no-load back EMF. Reference[14] investigated a structural design for enhancing power density in generators. By adding two connecting bridges at the stator ends, this configuration effectively increases power generation by over 15%. Reference[15] proposes an innovative asymmetric cross-section rotor design (featuring 45° skewed salient poles) for high-speed surface permanent magnet motors, achieving phase synchronization between reluctance torque and magnetic torque for the first time. The breakthrough enhances torque density by 20%.

However, the previous studies have not considered the matching relationship between the generator and wind speed under direct-drive conditions. It is difficult to achieve optimal matching between rotational speed and wind speed with a single operating mode. This paper aims to develop a multi-mode operating generator capable of switching the motor's operating mode according to different wind speeds.

Submitted On: December 2, 2024
Accepted On: March 31, 2025

https://doi.org/10.13052/2025.ACES.J.400910

C. Multi-mode operation

References [16, 17] mentioned some multi-mode operation strategies to control the generator power by changing the connection mode of the winding. However, scholars focus on the constant voltage control of the generator at different speeds. For wind power generation, this will lead to a decrease in power generation efficiency and wind energy utilization [18]. However, its proposed multi-mode operation principle gives the generator the potential for active speed regulation. However, traditional multi-mode operation motors have all adopted a dual-stator structure. This increases the mechanical complexity of the wind power generation system and elevates the probability of system failures. For VAWTs, however, low maintenance costs are one of their key advantages.

D. Contributions

Based on the above content, this paper designs an outer rotor doubly salient permanent magnet reluctance generator (ORDS-PMRG) with multi-mode capability for small direct-drive VAWT. Specifically, it can be summarized as

1. The dual-stator structure of the traditional multi-mode generator is simplified by combining the multi-tooth structure with the multi-mode operation. Reduce the production cost.
2. Electromagnetic analysis based on finite element is carried out. It is proved that the ORDS-PMRG has higher power density and torque density. And the effectiveness of multi-mode operation demonstrates good engineering value.

In this paper, section IIintroduces the structure and operating principles of generators. Section III analyzes the principles of multi-mode operation. In the section IV, the finite element simulation of ORDS-PMRG is carried out. Section V is the summary of the full paper.

II. ORDS-PMRG STRUCTURE AND WORKING PRINCIPLE

A. Structure of ORDS-PMRG

An ORDS-PMG is proposed in this paper, as shown in Fig.1. Compared with the traditional structure, ORDS-PMRG is characterized by its multi-tooth structure which can form multiple sets of windings. It can improve the performance of the generator, which will be described in detail in part C of this section.

The ORDS-PMRG is designed for VAWT and adopts an outer rotor structure that can be directly connected to the blades. There is a magnetic bridge outside the rotor permanent magnet to connect a magnetic pole of the rotor. This structure has been proven to improve the performance of the tangentially excited PMG. The

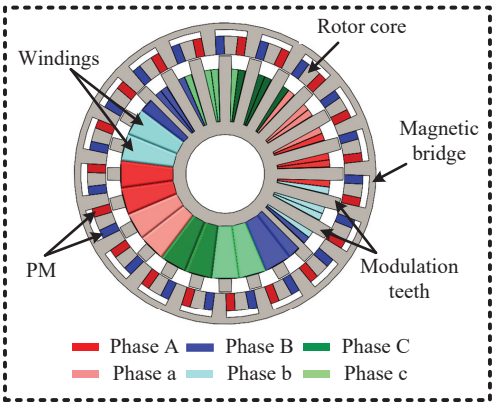

Fig. 1. Structure of proposed ORDS-PMRG.

24-slot structure improves the diversity of winding connections. It is convenient to realize the multi-mode operation of the generator.

The above-mentioned structural design not only simplifies the mechanical complexity of traditional dual-stator multi-mode generators, but also lays the foundation for subsequent multi-mode operation through the flexibility of the combination of the multi-tooth structure and the windings. The next section will further analyze how this structure achieves the low-speed high-torque operating characteristics, in combination with the principle of magnetic field modulation.

B. Principle of ORDS-PMRG

ORDS-PMRG follows the principle of magnetic field modulation [19]. The rotor magnetic field is modulated by the modulation teeth. The greatest advantage of the PMRG is its ability to achieve low-speed, high-torque operation. Because of the effect of the modulation teeth, the air gap flux density of the generator produces a specific number of harmonics. Its modulation effect can be derived by the following formula:

$$\begin{cases} B_{agr} = \sum_{m=1,3,5}^{+\infty} b_{rm}(c_r, r)\, cos\left[mp_r(\theta - \omega_r t + \alpha_{0m})\right] \\ \Lambda = a_0(c_{stt}) + \sum_{n=1,2}^{+\infty} a_n(c_{stt})\, cos\left[nN_{st}(\theta + \beta_{0m})\right] \end{cases}, \tag{1}$$

where B_{agr} denotes the waveform of the magnetic field excited by the excitation source, which is a square wave with zero DC component in ORDS-PMRG. The parameter Λ quantifies the modulation effect induced by the modulation teeth, which is a square wave with a certain DC component. Additionally, c_r is the pole arc coefficient of the rotor, p_r is the number of permanent magnet poles, ω_r is the rotation speed of the rotor, a_{0m} is the angle between the rotor and the magnetic pole axis, and b_{rm} is the Fourier coefficient. c_{stt} is the stator tooth arc coefficient, N_{st} is the number of stator teeth, β_{0m} is the deviation angle of the stator from the center of the slot, a_0 and a_n are Fourier coefficients.

Considering only the case where $m=1$ and $n=1$, by multiplying the two equations in equation (1) and then performing trigonometric transformations, the approximate expression of air gap flux density can be obtained:

$$\begin{aligned}
&B_{agr\Lambda} = B_{agr}^{m=1} \times \Lambda^{n=1} \\
&= a_0 b_{r1} \cos\left[p_r(\theta - \omega_r t + \alpha_0)\right] \\
&+ a_1 b_{r1} \cos\left(m p_r(\theta - \omega_r t + \alpha_{0m})\right) \cos\left(n N_{st}(\theta + \beta_{om})\right) \\
&= a_0 b_{r1} \cos\left[p_r(\theta - \omega_r t + \alpha_0)\right] \\
&+ \frac{a_1 b_{r1}}{2} \\
&\cos\left[(p_r + N_{st})\left(\theta - \frac{p_r \omega_r}{p_r + N_{st}} t + p_r \alpha_{01} + N_{st} \beta_{01}\right)\right] \\
&+ \frac{a_1 b_{r1}}{2} \\
&\cos\left[(p_r - N_{st})\left(\theta - \frac{p_r \omega_r}{p_r - N_{st}} t + p_r \alpha_{01} + N_{st} \beta_{01}\right)\right]
\end{aligned} . \quad (2)$$

The following can be obtained:

$$p_a = |p_r - N_{st}| . \quad (3)$$

The variable p_a represents the number of pole pairs in the generator, which also corresponds to the effective harmonic order of the air gap magnetic field. The next step is to obtain the ratio between the electromagnetic speed and the mechanical speed of the ORDS-PMRG:

$$\omega_{smf} = \frac{p_r}{p_r - p_a} \omega_r = G_r \omega_r, \quad (4)$$

where ω_{smf} is the angular velocity of the effective harmonic, while ω_r refers to the angular velocity of the rotor. Finally, G_r symbolizes the variable gear ratio. From equation (1) to equation (4), the working principle of PMRG with low speed and high torque can be obtained.

Based on the above-mentioned magnetic field modulation principle, the ORDS-PMRG can output high torque at low speeds, meeting the requirements of direct-drive vertical-axis wind turbines. However, a single operating mode is difficult to adapt to the dynamic changes of wind speed, so it is necessary to combine a multi-mode operation strategy.

III. MULTI-MODE OPERATION

A. ORDS-PMRG with multi-mode operation

For the ORDS-PMRG mentioned in this paper, 24 modulation teeth can form a dual three-phase winding. The combination method is shown in Fig.1. Among them, A B C forms one set of three-phase windings, and a b c forms another set of three-phase windings. Similar to the above, A B C windings and a b c windings are distinguished by color. The two sets of windings are combined to produce different operation modes.

As mentioned above, the previous multi-mode generator needs to be realized by double stators. However, ORDS-PMRG has multiple stator teeth, it can be formed by the combination of different teeth. The method shown in Fig.1 is a double three-phase winding with a 30° phase difference.

B. Principles of multi-mode operation

Reference [20] proposes a dual-stator generator that can achieve multi-mode operation. The principle is to adjust the output voltage by connecting the windings on the two misalignment stators. By changing the connection method of the inner and outer windings, a series of EMFs can be generated. As shown in Fig.2, the winding link diagram and EMF vector diagram of the four modes are given. The EMF generated by different operating modes can be approximately obtained by the following formula:

$$E_{mi} = 2E_g \cos\left(\frac{\theta_i}{2}\right), \quad (5)$$

where θ_i represents the electrical angle between windings, E_g represents the phase no-load back EMF amplitude. Affected by the winding connection mode and the stator angle.

When the winding link mode is switched, the voltage on the generator load will change. At the same time, the output power of the generator will change. This will affect the speed and torque of the VAWT input to the generator.

At the same time, the multi-mode operation generators often adopt the double stator structure. Because the realization of multi-mode operation requires a certain electrical angle difference between the dual three-phase

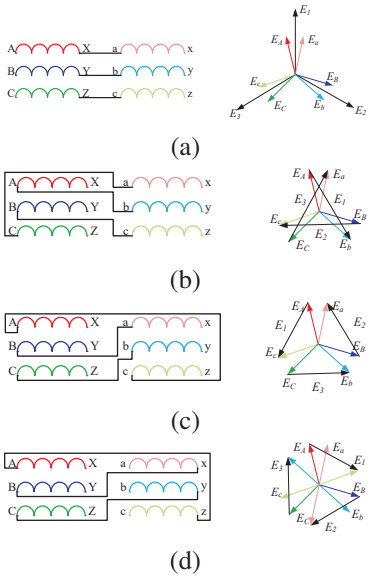

Fig. 2. Multi-mode operation schematic: (a) series connection of phase A and phase a, (b) reverse series connection of phase A and phase b, (c) series connection of phase A and phase c, and (d) reverse series connection of phase A and phase c.

windings, this makes the manufacture of such generators more difficult and costly. For ORDS-PMRG, a dual three-phase winding with a certain electrical angle difference can be realized without the dual-stator structure.

To verify the effectiveness of ORDS-PMRG and its multi-mode operation, the finite element software is used to simulate it. Key design parameters of the generator are shown in Table 1.

Table 1: Key design parameters of ORDS-PMRG

Parameters	Value
Rated power/kW	0.75
Rated speed/rpm	158
PM poles pairs	19
Teeth number	24
Poles pairs	5
Frequency/Hz	50
Operation modes	4
Stack thickness/mm	95
Stator tooth width/mm	7
Modulation tooth width/mm	6
Stator yoke thickness/mm	10
PM length/mm	14.5
PM width/degree	3
Magnetic bridge/mm	5
Stator outer diameter/mm	90
ORDS-PMRG outer diameter/mm	230
Winding turns	60
Length of air gap/mm	0.5

IV. FEA VERIFICATION AND COMPARISON

The finite element simulation of the generator was carried out using Altair Flux software. The 2D finite element models of ORDS-PMRG is established.

A. No-load characteristic

For convenience, the four operating modes of the generator are referred to as M1, M2, M3, and M4 respectively.

Figure 3 shows a comparative analysis of the magnetic density cloud images and magnetic force lines for uneven teeth and even teeth at the same moment. When the magnetic flux in a tooth reaches its maximum, there is a notable difference in the magnetic flux size in another tooth of the same group. The synchronization rate of the magnetic flux between the two teeth in each group is higher for uneven teeth. This results in a larger amplitude of EMF generated by a set of windings under the uneven teeth structure. Consequently, the no-load back EMF of the generator is also increased.

Figure 4 shows the no-load back EMF of the generator. It can be seen that the amplitude and phase of the no-load back EMF are different under different operating

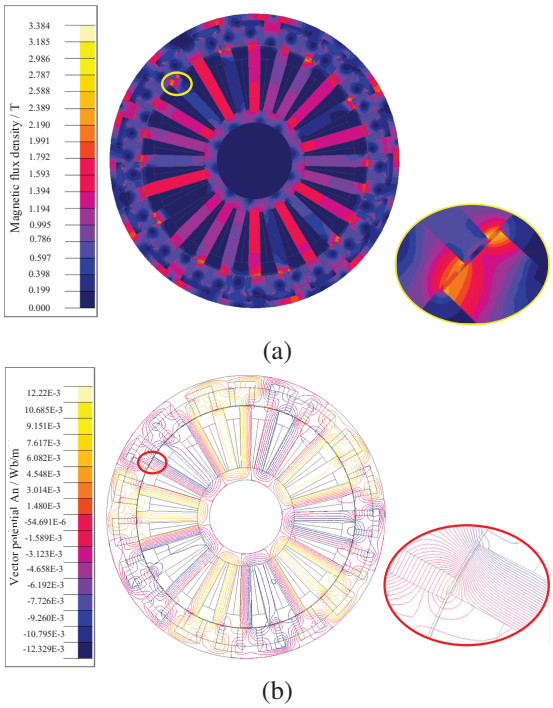

Fig. 3. (a) ORDS-PMRG magnetic density cloud and (b) ORDS-PMRG magnetic lines.

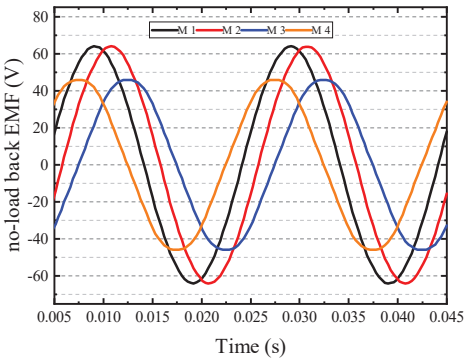

Fig. 4. No-load back EMF of ORDS-PMRG.

modes. The no-load back electromotive forces (EMF) of ORDS-PMRG are measured as follows: M1 = 65.93 V, M2 = 65.91 V, M3 = 46.44 V, M4 = 46.42 V.

In reality, there is a certain difference between the EMF value obtained by simulation and the value calculated by equation (5). This issue arises closely associated with the actual EMF waveform generated by the ORDS-PMRG. Owing to the influence of permanent magnets, partial magnetic saturation occurs on the stator teeth of the ORDS-PMRG, a phenomenon that is also evident in Fig.3 (a). As a result, the EMF waveform deviates from a purely sinusoidal shape. This phenomenon warrants enhancement in future work.

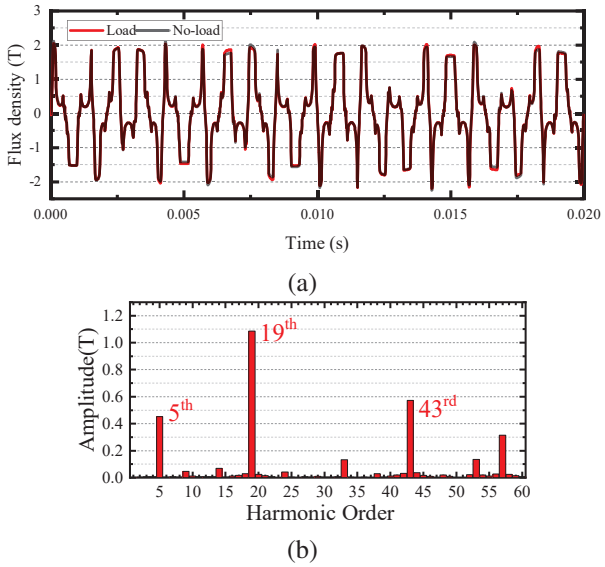

Fig. 5. Air gap magnetic density comparison: (a) Air gap magnetic density waveform and (b) Harmonic analysis.

Table 2: Performance characteristics of ORDS-PMRG

Performance	M1	M2	M3	M4
Average torque (N.m)	47.0	47.0	27.6	27.6
Torque ripple	1.55%	1.63%	3.6%	3.3%
Rated power (kW)	0.75	0.75	0.45	0.45
Total loss (W)	70.5	70.6	41.0	40.9
Efficiency	90.93%	90.92%	91.03%	91.06%

Figure 5 shows a comparison of air gap magnetic density. An FFT analysis on Fig.5 (a) yields Fig.5 (b). Based on the operating principle of PMVG, the 5th, 19th, and 43th harmonics are the main no-load back EMF sources of the generator.

B. Load comparison

Figures 6 and 7 demonstrate the torque and load voltage characteristics across operational modes. While the ORDS-PMRG shows superior torque stability in M1 and M2 with less than 3% ripple variation, this multi-tooth configuration introduces minor trade-offs. The 24-19 stator-rotor poles architecture fundamentally suppresses cumulative pulsations through phase-misaligned dual salient-pole units, as mechanistically validated in [21].

Table 2 shows the performance of ORDS-PMR. Although the absolute value of torque ripple is large, the increase in average torque results is relatively small in its ratio. Furthermore, this structure does not introduce additional losses, maintaining the generator efficiency at a higher level.

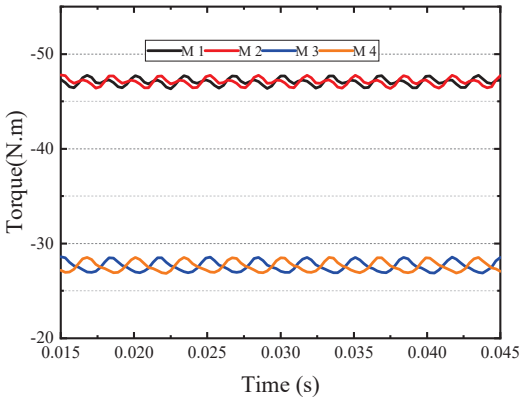

Fig. 6. The generator input torque in four operation modes.

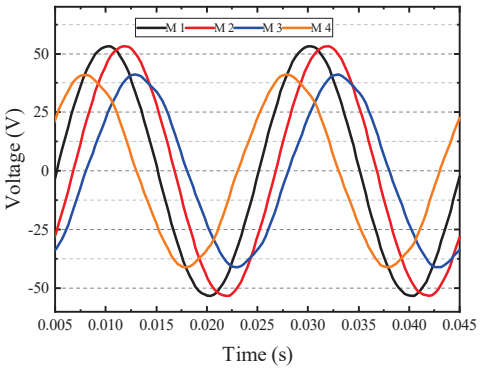

Fig. 7. The generator output voltage in four operation modes.

V. CONCLUSION

This paper proposes an ORDS-PMRG for small direct-drive vertical-axis wind turbines, featuring multi-mode operational capability. The design integrates a multi-tooth structure with adaptive operating modes, validated through finite element simulations demonstrating its structural efficacy and operational flexibility. Future directions include:

1. Enhancing power density via modulated tooth topologies and advanced magnetic materials.
2. Implementing model predictive control for real-time mode switching to optimize wind energy harvesting.

These advancements will establish theoretical foundations for next generation switched reluctance and hybrid-excitation motor designs.

ACKNOWLEDGMENT

This project is supported by Natural Science Foundation of Henan Province 252300421316 and he National Natural Science Foundation of China under Grant 52107215.

REFERENCES

[1] S. Roga, S. Bardhan, Y. Kumar, and S. K. Dubey, "Recent technology and challenges of wind energy generation: A review," *Sustainable Energy Technologies and Assessments*, vol. 52, no. C, p. 102239, Aug. 2022.

[2] E. Taherian-Fard, R. Sahebi, T. Niknam, A. Izadian, and M. Shasadeghi, "Wind turbine drivetrain technologies," *IEEE Transactions on Industry Applications*, vol. 56, no. 2, pp. 1729-1741, Mar. 2020.

[3] M. Zhao, X. Wang, L. Liu, X. Tu, and Q. Yang, "Optimization of PMSM for EV based on vibration and noise suppression," *Applied Computational Electromagnetics Society (ACES) Journal*, pp. 64-80, Jan. 2024.

[4] L. Liu, Y. Huang, M. Zhao, and Y. Ruan, "Parametric modeling and optimization of switched reluctance motor for EV," *Applied Computational Electromagnetics Society (ACES) Journal*, pp. 948-958, Sep. 2022.

[5] M. Joodi, M. Abbasian, and M. Delshad, "Introducing a 12/10 induction switched reluctance machine (ISRM) for electric powertrains," *Applied Computational Electromagnetics Society (ACES) Journal*, pp. 452-460, May 2024.

[6] X. Deng, R. Li, L. Hao, A. Zhang, and J. Zhou, "Design and finite element analysis of a novel permanent magnet assisted reluctance synchronous motor," *Applied Computational Electromagnetics Society (ACES) Journal*, vol. 35, no. 9, pp. 1012-1021, Nov. 2020.

[7] D. Ma, "Research on real-time pitch system of H-type vertical axis wind turbine," master's thesis, China University of Petroleum (East China), 2021.

[8] H. Lin, Y. Zhang, H. Yang, S. Fang, and Y. Huang, "Overview and recent developments of permanent magnet vernier machines," *Proceedings of the CSEE*, vol. 36, no. 18, pp. 5021-5034+5127, 2016.

[9] X. Li, M. Cheng, G. Zou, and X. Li, "Principle and analysis of a new flux-concentrating field-modulated permanent-magnet wind power generator," *Transactions of China Electrotechnical Society*, vol. 29, no. 11, pp. 1-9, 2014.

[10] A. Jafarian-Fini, M. Barghamadi, A. Hajiamiri-Damavandi, and M. Ardebili, "Optimization of an axial flux permanent magnet vernier generator for wind power generation," in *2023 3rd International Conference on Electrical Machines and Drives (ICEMD)*, pp. 1-6, Dec. 2023.

[11] P. Sharma and S. Sashidhar, "Permanent magnet vernier generator with surface ferrite magnets for a direct-drive wind generator," in *2022 International Conference on Electrical Machines (ICEM)*, pp. 328-333, Sep. 2022.

[12] S. Alshibani, R. Dutta, and V. G. Agelidis, "Optimization of a MW halbach PMSG for wind turbine applications," in *2016 XXII International Conference on Electrical Machines (ICEM)*, pp. 1963-1969, Sep. 2016.

[13] J. Mushenya and A. Khan, "Comparative analysis of outer-rotor flux-modulated permanent magnet generator topologies," in 2020 IEEE Energy Conversion Congress and Exposition (ECCE), Detroit, MI, USA, pp. 1161-1166, 2020.

[14] Y. Zhang, D. Li, P. Yan, X. Ren, R. Qu, and J. Ma, "A high torque density claw-pole permanent-magnets vernier machine," *IEEE Journal of Emerging and Selected Topics in Power Electronics*, vol. 10, no. 2, pp. 1756-1765, Apr. 2022.

[15] K. Yamaguchi, T. Yamamoto, N. Omura, and T. Jikumaru, "Torque enhancement of surface permanent magnet motors utilizing reluctance torque for high-speed motors with bonded magnets," in *2022 International Power Electronics Conference (IPEC-Himeji 2022- ECCE Asia)*, pp. 678-684, May 2022.

[16] M.-F. Hsieh, F.-S. Hsu, and D. G. Dorrell, "Winding changeover permanent-magnet generators for renewable energy applications," *IEEE Transactions on Magnetics*, vol. 48, no. 11, pp. 4168-4171, Nov. 2012.

[17] J. Yu, C. Liu, and H. Zhao, "Design and multimode operation of double-stator toroidal-winding PM vernier machine for wind-photovoltaic hybrid generation system," *IEEE Transactions on Magnetics*, vol. 55, no. 7, pp. 1-7, 2019.

[18] L. Li, J. Yang, Z. Feng, F. Zou, Q. Bao, Y. Li, and J. Zhao, "Robust control of wind power system with direct-driven PMSG based on effective wind speed estimation," *Smart Power*, vol. 51, no. 8, pp. 82-88, 2023.

[19] X. Li, K. T. Chau, and M. Cheng, "Analysis, design and experimental verification of a field-modulated permanent-magnet machine for direct-drive wind turbines," *IET Electric Power Applications*, vol. 9, no. 2, pp. 150-159, Feb. 2015.

[20] B. Sun, "Design and optimization of 20kW direct drive vertical axis switched reluctance generator," master's thesis, School of Electrical Engineering, University of Science and Technology, 2019.

[21] D. Yan, Z. Chen, Z. Wang, H. Wang, T. Shi, and C. Xia, "The torque ripple reduction in PMAREL machine using time-space harmonics analysis of air-gap flux density," *IEEE Transactions on Industrial Electronics*, vol. 69, no. 3, pp. 2390-2401, Mar. 2022.

Zhe Zhou received B.E. degree in electrical engineering in 2023 from Henan University of Science and Technology, Henan, China. He is currently pursuing a M.S. degree in electrical engineering at Zhengzhou University. His research interests include permanent magnet generator design.

Yifei Gao received B.S. degree in electrical engineering in 2024 from Henan University of Technology, Henan, China. He is currently pursuing a M.S. degree in electrical engineering at Zhengzhou University. His research interests include fault tolerant control of dual three-phase permanent magnet synchronous motor.

Kuan Zhang received the B.E. degree from China University Mining and Technology, Xuzhou, China, in 2014. She is currently a Ph.D. student at the School of Control Science and Engineering, Zhengzhou University. Her current research interest is multi-motor control.

Ge Qi received the master's degree in electrical engineering from Harbin Institute of Technology, Harbin, China, in 2004, and the Ph.D. degree in electrical engineering from Huazhong University of Science and Technology, Wuhan, China, in 2010. Currently, she is a lecturer at Zhengzhou University of China. Her main research interests are design and control of special motors.

Shuai Xu (Member, IEEE) received the B.S. degree in electrical engineering and automation and the Ph.D. degree in electrical engineering from the China University of Mining and Technology, Xuzhou, China, in 2014 and 2019. Since 2021, he has been an Associate Professor at Zhengzhou University. His current research interests include motor design and control.

Research on Switched Reluctance Motor Power Converters in Multi-port Low-carbon Building Microgrid System

Cheng Liu[1,2], Yu Zhao[1,4], Qing Wang[1], Xiaofeng Wan[1], and Lei Cao[3]

[1]School of Information Engineering
Nanchang University, Nanchang 330031, China
liucheng08@ncu.edu.cn, wangq@ncu.edu.cn, xfwan@ncu.edu.cn

[2]School of Advanced Manufacturing
Nanchang University, Nanchang 330031, China

[3]Architecture and Design College
Nanchang University, Nanchang 330031, China
caolei@ncu.edu.cn

[4]State Grid Zhejiang Electric Power Co. Ltd.
Daishan County Power Supply Company, Daishan 316229, China
2235272392@qq.com4

Abstract – This paper presents research on a dual-source three-level power converter for a switched reluctance motor (SRM) in a multi-port low-carbon building microgrid system. A front-end circuit is added to the proposed power converter based on the conventional asymmetric half-bridge power converter (AHBPC) for power flow control. It can achieve a three-level power supply by using solar photovoltaic (PV) cells and lead-acid batteries which can be replaced with other power supply modules as needed without affecting system functionality. Three working modes can be achieved according to actual applications by a simple strategy. With the proposed converter, system efficiency and dynamic response can be improved. Working modes of the proposed solution are explained and current paths in the proposed converter are analyzed in detail. Finally, experimental results on a four-phase 8/6 SRM platform are given to confirm the effectiveness of the proposed solution.

Index Terms – Asymmetric half-bridge power converter, dual-source three-level power converter, power flow control, switched reluctance motor.

I. INTRODUCTION

In recent years, the global climate change problem has become increasingly serious, and low-carbon environmental protection has become a global consensus. In this context, the low-carbon transformation of building construction becomes particularly important. Figure 1 shows a multi-port microgrid system of a low-carbon building. In this model, a switched reluctance motor (SRM) can drive the loads through photovoltaic (PV) and battery hybrid or separate power supply, such as elevator lifting and water pumping. Furthermore, the power supply modes can be applied to various electrical appliances and charging electric vehicles. The excess electric energy generated by PV power generation and gravity potential energy generated by elevator lifting can be recovered through an energy storage system. In [1], a general power distribution system of buildings, namely, PVs, energy storage, direct current, and flexibility (PEDF) is proposed to provide an effective solution from the demand side. As the core component of the low-carbon building microgrid drive system, drive motor performance can affect operation of the microgrid system directly. Switched reluctance machines have been studied for many years and have become one of the most promising candidates in renewable-energy-related industries such as wind power systems, gas energy recovery systems, electric vehicles and wave energy systems [2–5].

The power converter, as the core part of the SRM drive system, plays a decisive role in the performance of the entire motor system. The conventional power converter is mainly based on an asymmetric half-bridge (AHB) structure, with the most significant advantages of simple structure, flexible control strategy, independent phase to phase, and good fault tolerance performance. However, there are also some drawbacks, such as the impact of a single power supply on the safety of SRM systems; the excitation speed and demagnetization speed are relatively slow, which affects system

Submitted On: December 30, 2024
Accepted On: May 29, 2025
https://doi.org/10.13052/2025.ACES.J.400911

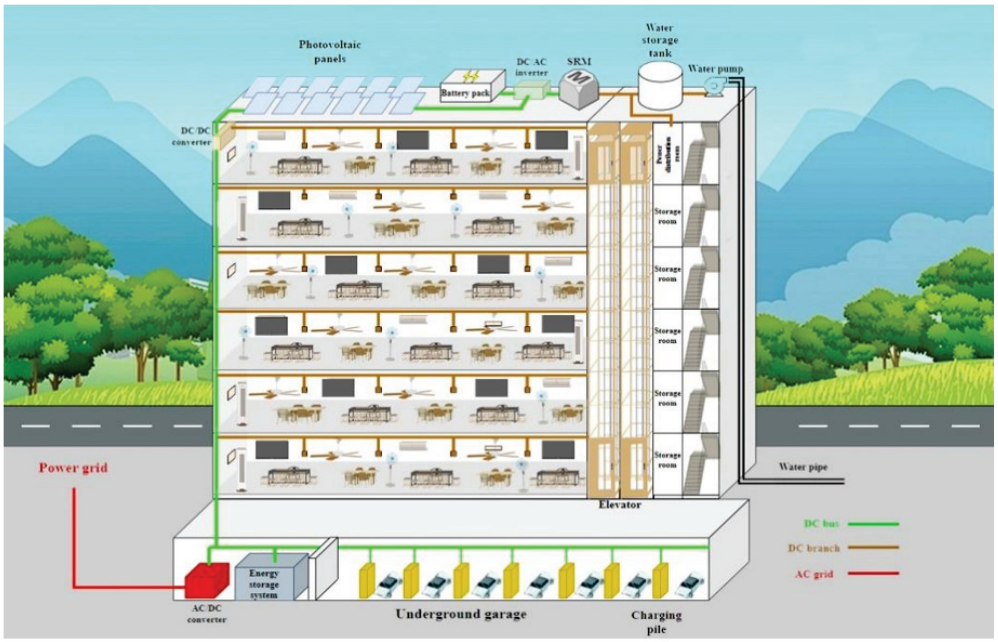

Fig. 1. A multi-port microgrid system of a low-carbon building.

efficiency; and the lack of energy feedback methods will limit the utilization rate of energy. In order to solve the above problems, new power converter topology is a hot topic in the field of SRM. In [6], a power converter is proposed for excitation and freewheeling functions by means of auxiliary windings and capacitors, which can control one phase through a MOSFET. In [7], a power converter topology is given for achieving structure simplification through reusing the MOSFETs on each phase winding. It can achieve a reduction of the number of power MOSFETs, reducing component losses and improving the performance of the SRM system. However, this kind of power converter will make the phase windings no longer independent of each other, and the reused power MOSFETs will take on the function of controlling the commutation of polyphase windings. If the reused power MOSFETs fail to control, it will seriously affect the normal operation of SRM and reduce the fault tolerance performance of the motor system.

To achieve high-speed excitation, a method of increasing the excitation voltage of SRM by adding a boost-type DC-DC converter is studied in [8]. To achieve high voltage excitation and demagnetization, a power converter topology is presented in [9]. Although the two different power converters proposed in [8] and [9] can both improve the system operating voltage, their power supply level cannot be changed flexibly according to actual operating requirements, which still has certain limitations.

As recognized, system efficiency and dynamic performance are two hot topics for SRM. For instance, some multilevel converter topologies are presented in [10–15]. In [10], a method of hybrid operation of two asymmetric half-bridge power converters (AHBPCs) is employed to achieve multilevel power supply; in [11–13], the modular designs for batteries are studied; in [14], a topology for power converter is presented by adding diode and power MOSFET to each phase; and in [15], a method of designing three excitation and freewheeling circuits for three power sources is presented. However, with the increasing complexity or cost of the system, the practicality of the system will decrease. Additionally, some fault tolerant control strategies are studied in [16–18].

In this paper, a dual-source three-level power converter topology for SRM is studied. According to the proposed topology, the operating principle, control method, and implementation of fast excitation and demagnetization functions during the operation are introduced. Then, a comparison of system efficiency and torque ripple of the proposed power converter and the conventional AHBPC is given. To validate the performance of the proposed power converter, simulation results and experimental results are given in sections III and IV, respectively. The paper is concluded in section V.

II. Topology and operational modes

A. Proposed topology

Figure 2 shows conventional AHBPC topology. Whether in excitation or demagnetization state, the

voltage on the winding is the power supply voltage. This will result in a relatively slow excitation and demagnetization process during high-speed motor operation, affecting the performance of the SRM system and reducing system efficiency.

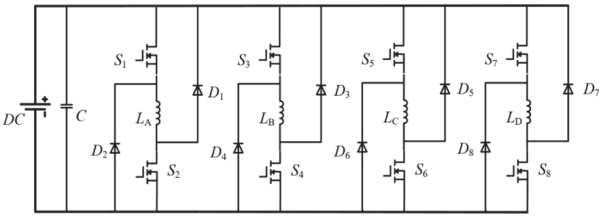

Fig. 2. Topology of conventional asymmetric half-bridge power converter.

In the proposed topology of AHBPC, which is shown in Fig. 3, a front-end circuit is added to the conventional AHBPC. The front-end circuit consists of a PV cell (U_P=12 V) and a battery (U_E=12 V), a capacitor, two diodes (D_{q2} and D_{q3}) and two MOSFETs. Diodes D_{q1} and D_{q4} are internal diodes in S_{q1} and S_{q2}, respectively. There are three operation modes in the system according to the proposed converter: PV cell independent power supply, battery independent power supply and dual-source hybrid power supply. To achieve switching between the three power supply modes, the choice of system voltage will be controlled by the two MOSFETs (S_{q1} and S_{q2}) in the front-end circuit. Three levels of output based on the two power supplies can be achieved. To improve the stability of the power supply, a capacitor is added to the front-end circuit. It can also serve as a connecting element of the energy feedback path for the freewheeling current simultaneously.

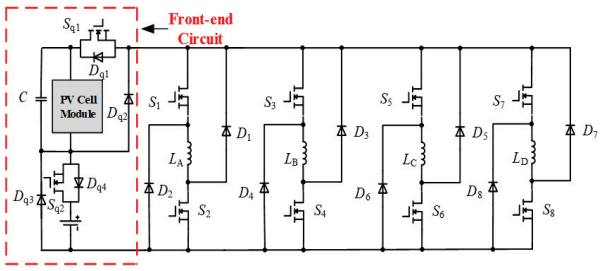

Fig. 3. Topology of proposed power converter.

B. Analysis of working modes

During each operation cycle of the motor, each phase winding undergoes three working states: excitation state, freewheeling (demagnetization) state, and zero-voltage freewheeling state. As mentioned, the three power supply modes for the proposed power converter can be switched by controlling S_{q1} and S_{q2} of the front-end circuit. Then, the level conversion will be achieved and the excitation and demagnetization process can be optimized.

As can be seen in Fig. 3, the topology of the proposed power converter is composed of three energy terminals: PV cell, battery, and SRM. The power converter is the bridge that connects the three terminals to each other. Figure 4 shows the three operation modes of the proposed power converter.

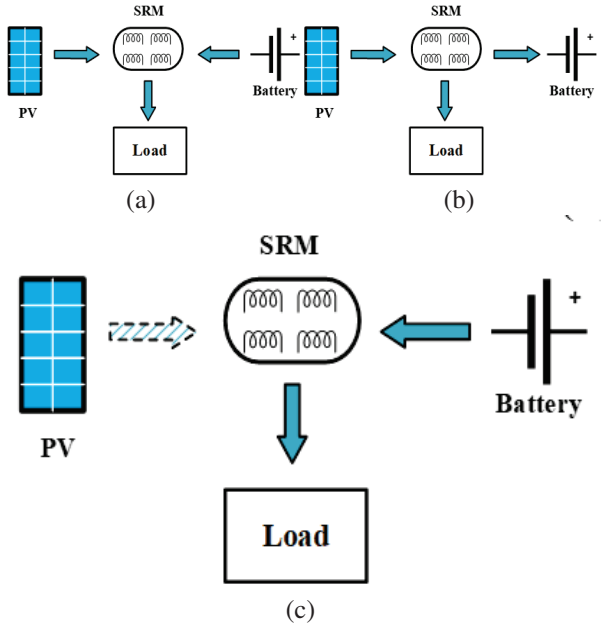

Fig. 4. Three operation modes of the proposed power converter: (a) mode 1, (b) mode 2, and (c) mode 3.

To switch between the operation modes, the corresponding MOSTETs (S_{q1} and S_{q2}) actions are shown in Table 1. In mode 1, the PV cell and battery are both power sources for the SRM system. In mode 2, the PV cell is the power source and the battery is idle. In mode 3, the battery is the power source and the PV cell is idle.

Table 1: S_{q1} and S_{q2} actions under different modes

Mode	S_{q1} and S_{q2}
1. Dual-source hybrid power supply	S_{q1} and S_{q2} turn-on
2. Photovoltaic cell power supply	S_{q1} turn-on; S_{q2} turn-off
3. Battery power supply	S_{q1} turn-off; S_{q2} turn-on

Taking phase A as an example, Fig. 5 shows the three working states in mode 1. The current paths are

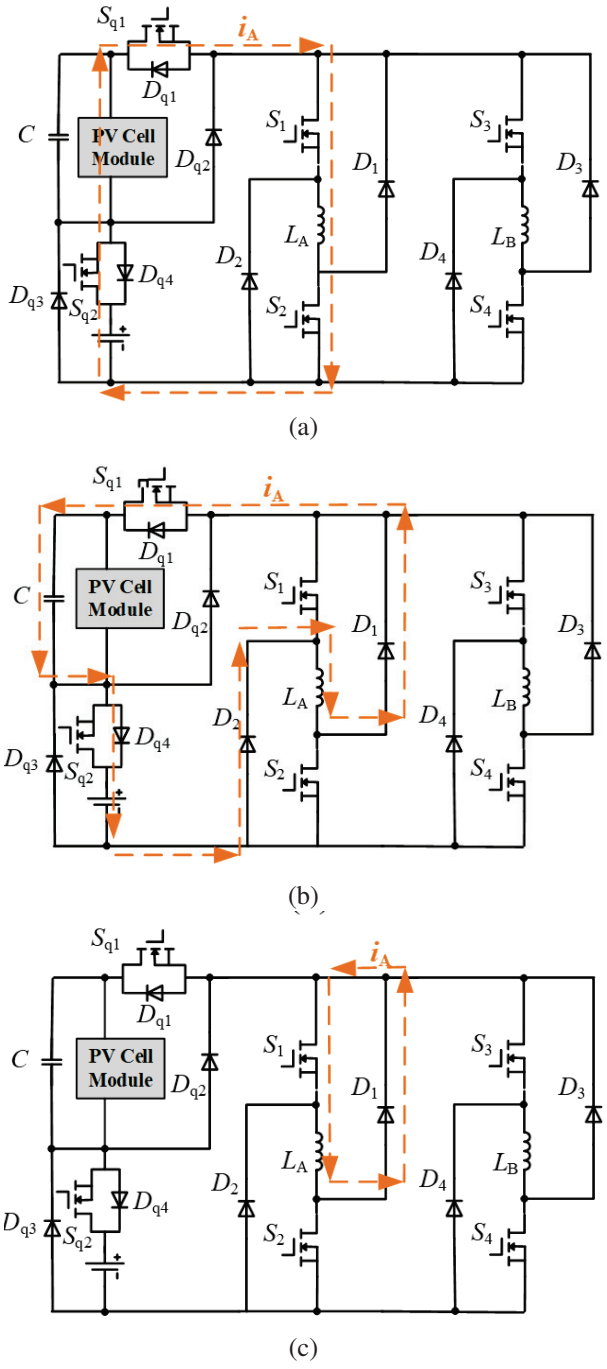

Fig. 5. Working states at mode 1: (a) winding excitation state, (b) freewheeling state, and (c) zero-voltage freewheeling state.

shown as the dashed line in Fig. 5. As shown in Fig. 5 (a), the voltage drops of phase A can be expressed as:

$$\begin{cases} U_A = U_P + U_E - 4 \times U_S \\ U_S = I_s \times R_{on} \end{cases}, \quad (1)$$

where U_A, U_P, U_E, U_S, I_s, i_A and R_{on} stand for voltage of phase A, voltage of PV cell, voltage of battery, voltage drop of each MOSFET, the transient current flowing through each MOSFET, the current of phase A and on-state resistance of each MOSFET, respectively. In this case, since L_A is the only load in the loop, the current I_s is equal to i_A, i.e. I_s=i_A.

As can be seen in Fig. 5 (b), when the excitation process ends, S_1 and S_2 will be turned off. Phase A enters the demagnetization mode, and the power converter starts working in a freewheeling state. The voltage drops of phase A can be expressed as:

$$\begin{cases} U_{DC} = U_C + U_E + 2 \times U_D \\ U_D = U_O + I_D \times R_Z \\ U_A = -U_{DC} + 2 \times U_D = -(U_C + U_E) \end{cases}, \quad (2)$$

where U_{DC} and U_C stand for bus voltage and capacitor voltage drop; U_D stands for the voltage drop of each diode on the current flow path; U_O, I_D and R_Z stand for the turn-on voltage of each diode, the transient current flowing through each diode and dynamic resistance of each diode, respectively.

As shown in Fig. 5 (c), when A-phase winding enters zero-voltage freewheeling state, the freewheeling voltage of phase A is 0 V, i.e. U_A=0.

In mode 1, the excitation voltage and demagnetization voltage of the SRM are maintained at a constant power supply voltage. Therefore, the motor cannot perform high-level excitation and high-level demagnetization.

Figure 6 shows the excitation state of mode 2 and mode 3. The A-phase winding is energized by PV cell and battery through different diodes.

According to the proposed power converter, the freewheeling current flow path is the same in mode 2 and mode 3. Therefore, the following analysis of the freewheeling current is carried out in the mode of battery independent power supply (mode 3). In actual operation, the freewheeling current of each phase winding may overlap with other phases. Thus, it is not possible to simply discuss the freewheeling current or excitation situation of a single phase. Taking phase A and phase B as examples, the following five cases are analyzed.

Figure 7 (a) shows the current flow path in case 1. In the first case, phase A enters freewheeling state while phase B is in zero-voltage freewheeling state. Capacitor C and battery will be charged by phase A. The phase A voltage drop and phase B voltage drop can be expressed as:

$$\begin{cases} U_{DC} = U_C + U_E + 2 \times U_D \\ U_A = -U_{DC} + 2 \times U_D = -(U_C + U_E) \\ U_B = 0 \end{cases}, \quad (3)$$

where U_B stands for the voltage drop of phase B.

In case 2, phase A enters excitation state, while phase B is in the freewheeling state. If i_B>i_A, where i_B stands for the current of phase B, the energy on

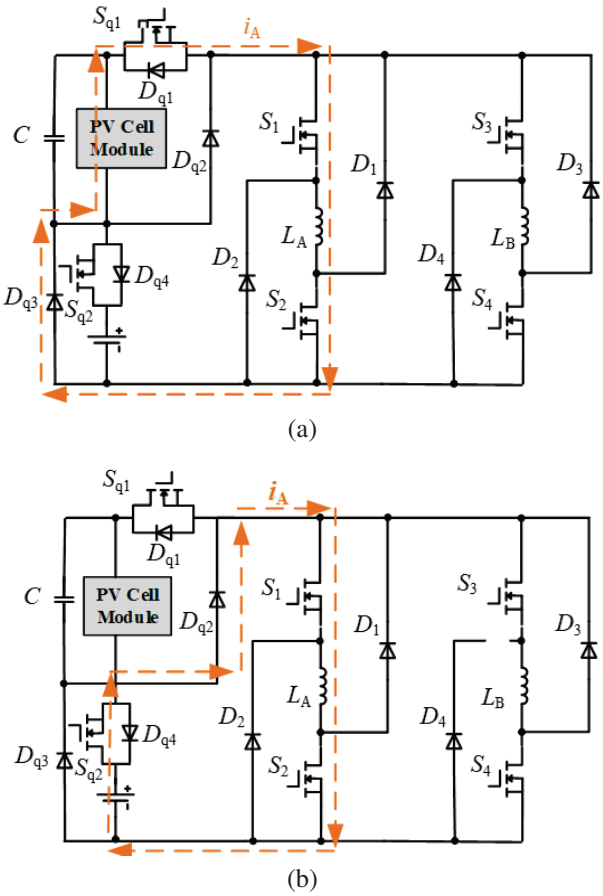

Fig. 6. Excitation state in modes 2 and 3: (a) under photovoltaic cell power supply and (b) under battery power supply.

B-phase winding is not only for charging the capacitor C and battery, but also providing energy for phase A. The current flow path can be seen in Fig. 7 (b). The voltage

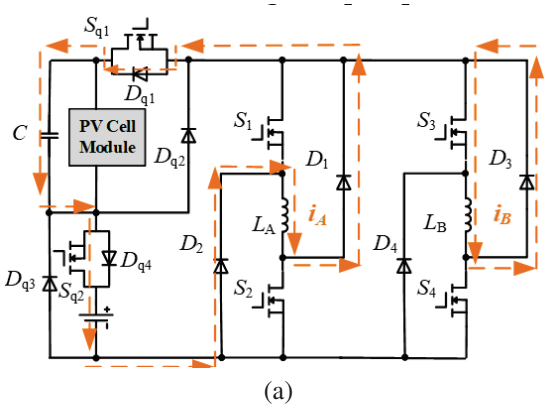

Fig. 7. *Continued.*

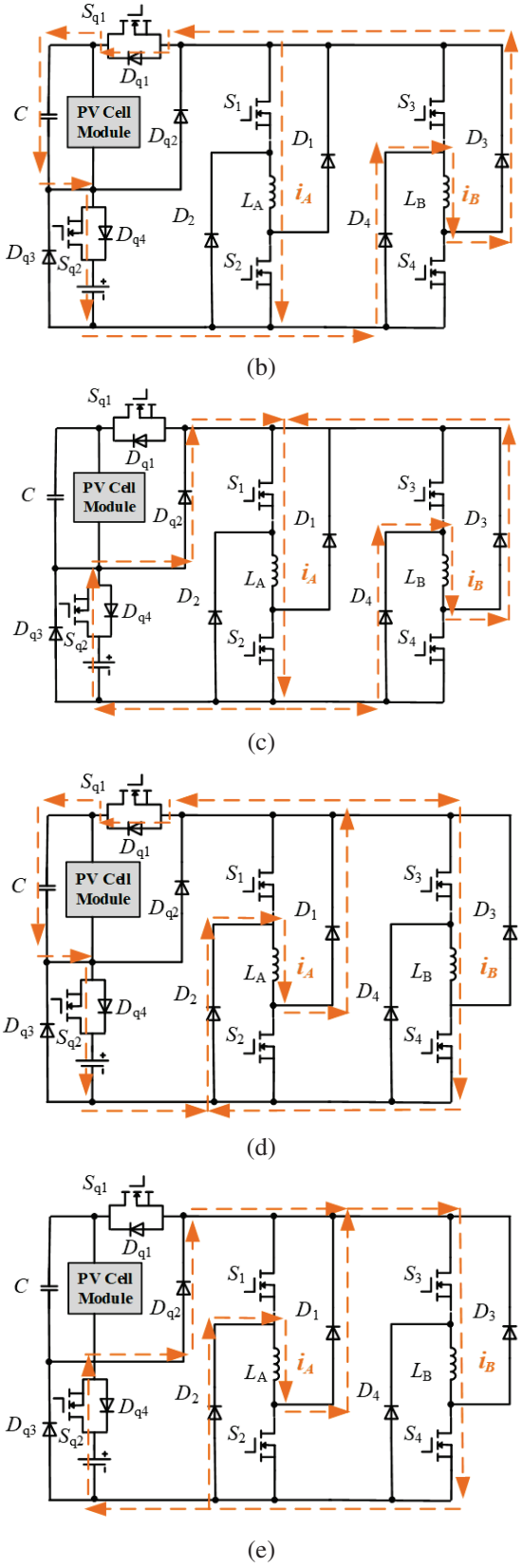

Fig. 7. Five cases in freewheeling state in mode 3: (a) case 1, (b) case 2, (c) case 3, (d) case 4, and (e) case 5.

drop of phases A and B can be expressed as:

$$\begin{cases} U_{DC} = U_C + U_E + 2 \times U_D \\ U_A = U_{DC} - 2 \times i_A \times R_{on} \\ U_B = -U_{DC} + 2 \times U_D = -(U_C + U_E) \end{cases} . \quad (4)$$

In case 3, phases A and B are in the same state as in case 2, but i_B is less than i_A ($i_B < i_A$). At this time, the voltage drops of phase A and phase B can be expressed as:

$$\begin{cases} U_{DC} = U_E - I_s \times R_{on} - U_D \\ U_A = U_{DC} - 2 \times i_A \times R_{on} \\ U_B = -U_{DC} + 2 \times U_D \end{cases} . \quad (5)$$

The current flow path is shown in Fig. 7 (c), and the excitation voltage of phase A is no longer determined by phase B.

In case 4, phase A enters freewheeling state, while phase B is in the excitation state. If $i_A > i_B$, the A-phase winding feeds back electrical energy to the capacitor C and the battery, while providing excitation current to the B-phase winding. The current flow path is shown in Fig. 7 (d). The voltage drop of phase A and B can be expressed as:

$$\begin{cases} U_{DC} = U_C + U_E + 2 \times U_D \\ U_A = -U_{DC} + 2 \times U_D = -(U_C + U_E) \\ U_B = U_{DC} - 2 \times i_B \times R_{on} \end{cases} . \quad (6)$$

In case 5, phase A and phase B are in the same state as in case 4. However, contrary to case 4, if $i_A < i_B$, A-phase winding no longer provides excitation current to B-phase winding. The current flow path can be seen in Fig. 7 (e). At this time, the voltage drop of phase A and B can be expressed as:

$$\begin{cases} U_{DC} = U_E - I_s \times R_{on} - U_D \\ U_A = -U_{DC} + 2 \times U_D \\ U_B = U_{DC} - 2 \times i_B \times R_{on} \end{cases} . \quad (7)$$

Through the analysis of mode 3, it is clear that both the voltage of the A-phase and B-phase winding in case 1, case 2 and case 4 can meet the requirements of high-level demagnetization and high-level excitation.

III. SIMULATION ANALYSIS

A. Phase voltage and current analysis

In order to verify the feasibility of the proposed power converter, the performance comparison is studied in MATLAB/Simulink between conventional AHBPC and proposed power converter for proof-of-concept.

In simulation, the rotor speed is set as 600 r/min, the turn-on angle is set as 5°, the turn-off angle is set as 20°, and the output voltage of both the battery and PV cell is 12 V. Taking phase A as an example, Fig. 8 shows the voltage and current waveform of conventional AHBPC and proposed power converter in excitation state and demagnetization state. At this time, the conventional AHBPC is powered by battery, while the proposed power converter is powered by PV cell.

As shown in Fig. 8 (a), in the excitation state, the excitation voltage of the A-phase winding is stable at

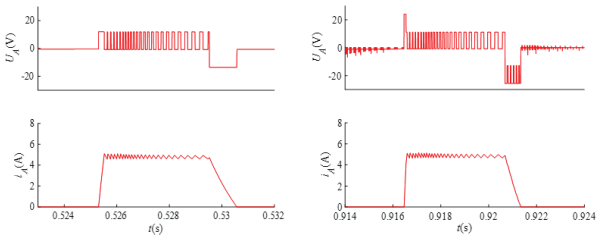

(a) (b)

Fig. 8. Comparison of voltage and current waveform between conventional AHBPC and proposed power converter in excitation state and demagnetization state when rotor speed is 600 r/min in mode 2: (a) with conventional AHBPC and (b) with proposed power converter.

12 V. In the demagnetization state, the demagnetization voltage of the A-phase winding is stable at -12 V. The constant excitation voltage and demagnetization voltage result in a longer excitation and demagnetization process of the winding, and this will slow the increase and decrease of current, which limits the performance of the SRM system. In Fig. 8 (b), when S_{q1} and S_{q2} are switched on, the excitation voltage of the phase-A winding is the sum of the voltages of the PV cell and the battery, which is 24 V, enabling fast excitation of the SRM system. After the high-level excitation is over, the excitation voltage of proposed power converter drops to 12 V until the end of the excitation process. There are two demagnetization voltages in demagnetization state, which are -12 V and -24 V. Under the -24 V demagnetization voltage, fast demagnetization can be achieved. In the fast excitation and demagnetization states, the possibility of negative torque generation can be reduced and the performance of the SRM system can be improved.

Taking phase A as an example, Figs. 9–12 show the comparison of voltage and current waveform between

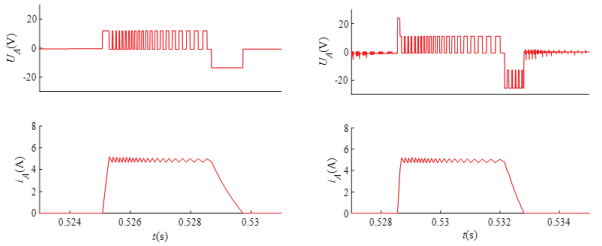

(a) (b)

Fig. 9. Comparison of voltage and current waveform between conventional AHBPC and the proposed power converter in excitation state and demagnetization state when rotor speed is 700 r/min in mode 3: (a) with conventional AHBPC and (b) with proposed power converter.

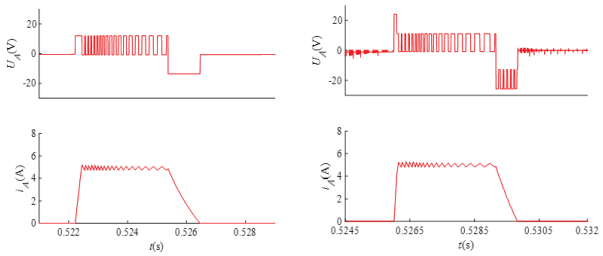

(a) (b)

Fig. 10. Comparison of voltage and current waveform between conventional AHBPC and proposed power converter in excitation state and demagnetization state when rotor speed is 800 r/min in mode 3: (a) with conventional AHBPC and (b) with proposed power converter.

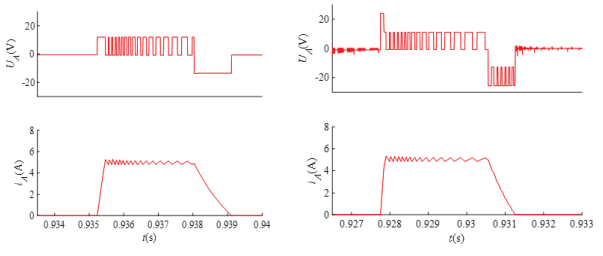

(a) (b)

Fig. 11. Comparison of voltage and current waveform between conventional AHBPC and proposed power converter in excitation state and demagnetization state when rotor speed is 900 r/min in mode 3: (a) with AHBPC and (b) with proposed power converter.

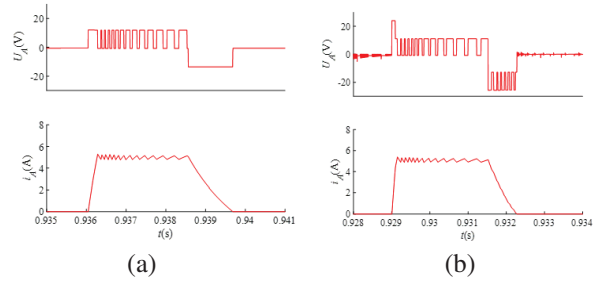

(a) (b)

Fig. 12. Comparison of voltage and current waveform between conventional AHBPC and proposed power converter in excitation state and demagnetization state when rotor speed is 1000 r/min in mode 3: (a) with conventional AHBPC and (b) with proposed power converter.

conventional AHBPC and the proposed power converter in battery-independent power supply mode under different rotor speed where the turn-on angle and the turn-off angle are set as 5° and 20°, respectively.

As shown in Figs. 9–12, when the motor operates at higher speeds, conventional AHBPCs are limited by constant excitation voltage and demagnetization voltage, and SRMs are increasingly affected by the speed of phase current rise and fall, making it difficult to further improve the system performance under high rotor speed conditions. During the process of continuously increasing the rotor speed from 700 r/min to 1000 r/min, the SRMs system with proposed power converter powered by a 12 V battery can still achieve high-level excitation and demagnetization. Compared with conventional AHBPC, the performance of the SRM system can be improved more effectively with the proposed power converter at high rotor speeds.

Figure 13 shows a comparison of the phase current rise and fall velocity in the SRM system in the case of using conventional AHBPC and proposed power converter at different rotor speeds. In Fig. 13, v_p and v_m stand for the phase current rise velocity when the phase-A excitation current reaches the upper limit of the chopping current for the first time and the phase demagnetization current fall velocity after chopping, respectively. As can be seen from Figs. 13 (a) and (b), when using the proposed power converter, v_p and v_m are both greater at different motor speeds than when using conventional AHBPC. In other words, the system performance can be improved because the excitation and demagnetization processes can be completed in a shorter time with proposed power converter.

B. Motor torque and efficiency analysis

Figure 14 shows the torque waveform with proposed power converter powered by a 12 V PV cell and a 12 V battery. The rotor speed is set as 600 r/min, the turn-on angle is set as 5°, the turn-off angle is set as 25°, and

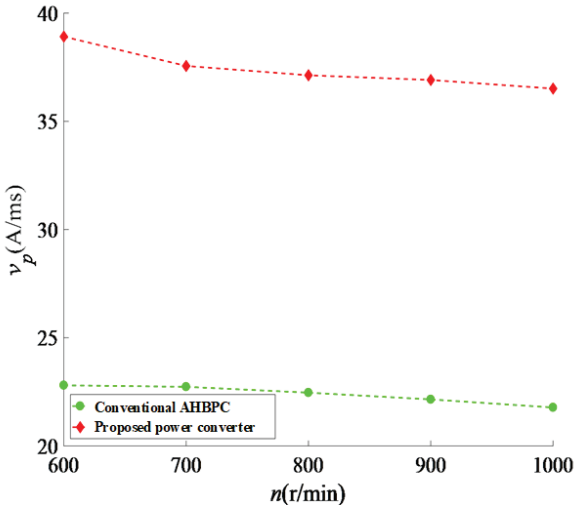

(a)

Fig. 13. *Continued.*

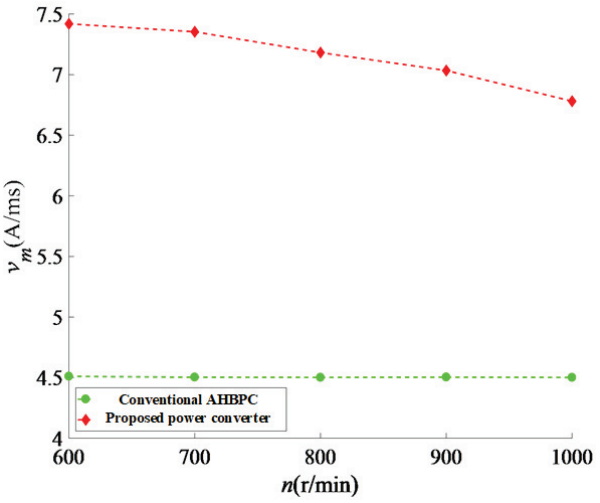

(b)

Fig. 13. Comparison of the phase current rise and fall velocity in the SRM system when using conventional AHBPC (green dash line) and proposed power converter (red dash line): (a) comparison of v_p with two different power converters and (b) comparison of v_m with two different power converters.

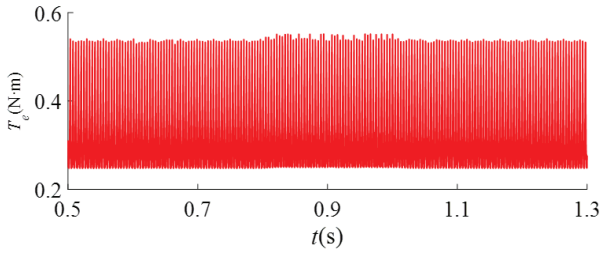

Fig. 14. Torque waveform with proposed power converter when rotor speed is 600 r/min.

the load torque is set as 0.3 N·m. At the beginning of the start-up process, the system is powered by the battery independently, and it is switched to PV cell independent power supply at t = 0.6 s. At t = 0.8 s, it is switched to hybrid power supply of PV cell and battery. At t = 1 s, it is switched back to battery independent power supply. As can be seen from Fig. 14, the output torques generated in independent battery and PV cell power supply modes are basically the same, both slightly lower than the output torque in the dual-source hybrid power supply mode. Switching between the three power supply modes will not affect system performance. At the moment, when the power supply level is switched between low and high levels, the torque can basically remain stable, allowing the SRM system to run smoothly.

Figure 15 shows the comparison of system torque ripple at different rotor speeds in the case of using conventional AHBPC and proposed power converter, where the proposed power converter is powered by the battery independently. In Fig. 15, the torque ripple coefficient K can be expressed as

$$K = \frac{T_{\max} - T_{\min}}{T_{\text{avg}}}, \tag{8}$$

where $T_{\max}$, $T_{\min}$ and T_{avg} stand for maximum torque value, minimum torque value and average torque value, respectively.

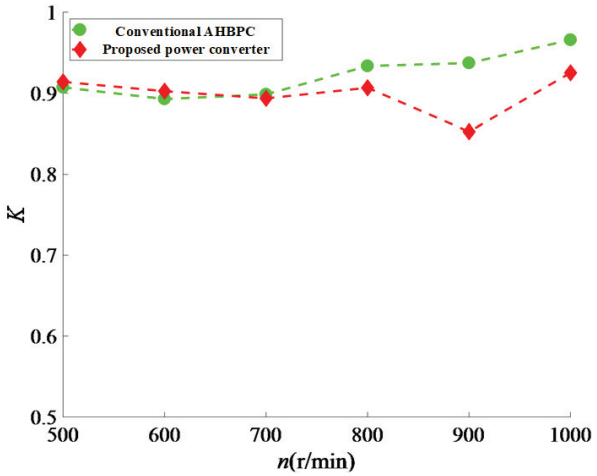

Fig. 15. Comparison of system torque ripple when using conventional AHBPC and proposed power converter.

In Fig. 15, the torque ripple curve with conventional AHBPC is shown as a green dash line, while the torque ripple curve with proposed power converter is shown as a red dash line. When the rotor speed is between 500 r/min and 600 r/min, the torque ripple coefficient using the proposed power converter is slightly larger than that using the conventional AHBPC. However, as the speed increases from 700 r/min to 1000 r/min, the torque ripple coefficient using the proposed power converter becomes lower, and reaches its lowest at the speed of 900 r/min. Thus, in high-speed operation, the system torque ripple can be reduced by using proposed power converter, which is more conducive to the stable operation of the system.

Figure 16 shows a comparison of system efficiency in the case of using conventional AHBPC and the proposed power converter, where the proposed power converter is powered by a battery independently. The battery and PV cell of proposed power converter are both 12 V. The turn-on angle is set as 5°, the turn-off angle is set as 25°, and the load torque is set as 0.3 N·m.

Table 2: Key components of the experimental platform

Component	Parameters	Value	Parameters	Value
SRM	Phase number	4	Core length (mm)	82.6
	Stator/Rotor	8/6	Stator/rotor arc angle (deg)	21/23
	Rotor outer diameter (mm)	69	Base speed (r/min)	600
	Rotor inner diameter (mm)	33	Rated output power (W)	500
	Stator outer diameter (mm)	121	Phase resistance (Ω)	0.05
	Stator inner diameter (mm)	75	Stray resistance (Ω)	0.07
Converter	MOSFET	IRFP4668	Diodes	D75E60
Power supply	PV cell	12 V	Battery	12 V, 65 Ah

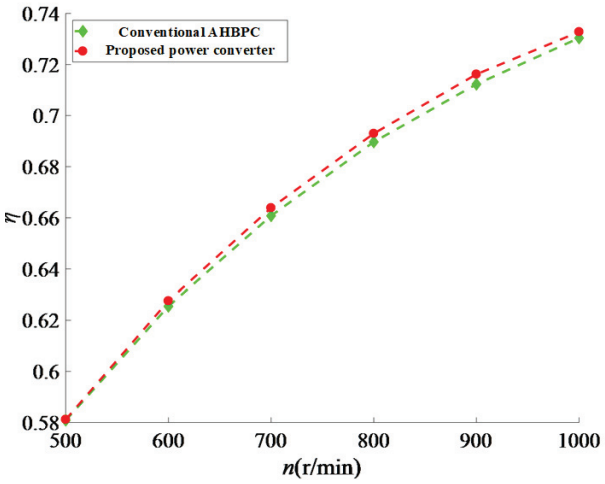

Fig. 16. Comparison of system efficiency when using a conventional AHBPC and the proposed power converter.

The system efficiency curve with conventional AHBPC is shown as a green dash line, while the system efficiency curve with proposed power converter is shown as a red dash line in Fig. 16. As can be seen from Fig. 16, the system efficiency using the proposed power converter is higher than that using conventional AHBPC. Therefore, compared with the conventional AHBPC, the proposed power converter can reduce energy consumption to a greater extent, which is conducive to cost saving and environmental protection.

IV. EXPERIMENTAL VERIFICATION

To verify the feasibility of the proposed solution, a four-phase 8/6 SRM system with proposed power converter is employed for proof-of-concept. A photograph of our experimental platform is shown in Fig. 17. Key components of the experimental platform are listed in Table 2. Key sensors are listed in Table 3.

Figure 18 shows the experimental results comparison of the voltage and current waveforms of the A-phase winding in the SRM system in the case of using conventional AHBPC and the proposed power converter. In the experiment, the rotor speed is set as 600 r/min; the turn-on angle is set as 5°, and the turn-off angle is set as 20°. The conventional AHBPC is powered by a battery, while the proposed power converter is powered by a PV cell.

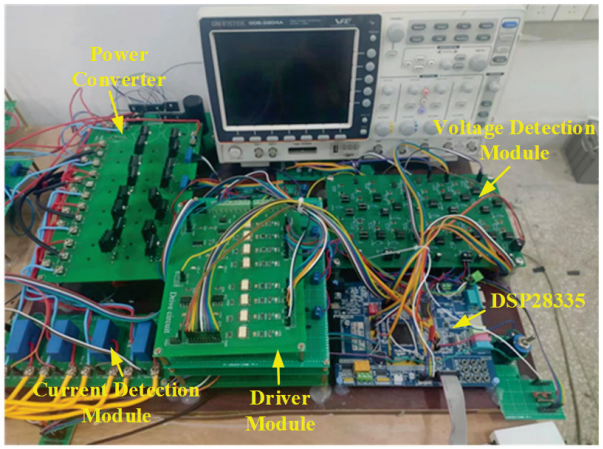

(a)

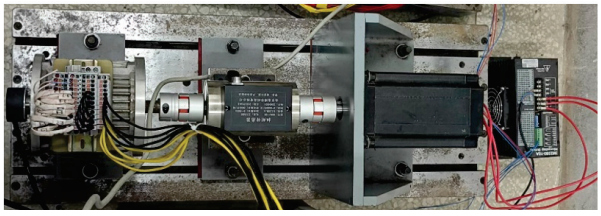

(b)

Fig. 17. Photograph of the experimental platform: (a) experimental platform of SRM system and (b) 8/6 SRM.

Table 3: Key sensors of the SRM system

Sensor	Type
DSP	TMS320F28335
Core of the drive circuit	TLP250
Current sensors	LA55P
Position sensor	GK152 (resolution 7.5°)
Voltage sensors	AD7895

As shown in Fig. 18, the excitation voltage and demagnetization voltage of the A-phase winding with the

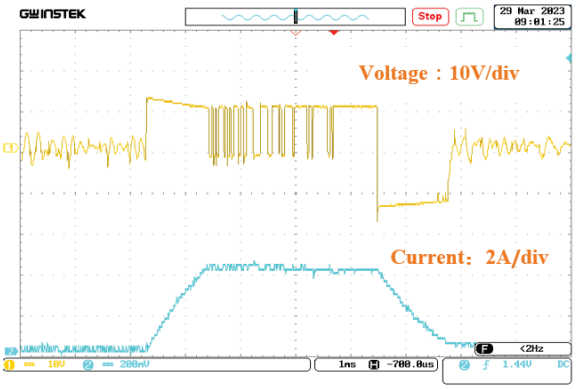

(a)

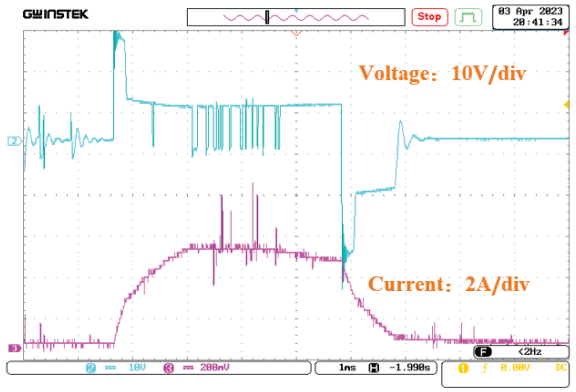

(b)

Fig. 18. Comparison of experimental results: (a) voltage and current waveform with conventional AHBPC and (b) voltage and current waveform with proposed power converter.

conventional AHBPC are both the 12 V power supply voltage, which makes the excitation and demagnetization processes relatively slow and may cause negative torque and other problems, which is not conducive to the stable operation of the SRM system. By comparison, the excitation voltage and demagnetization voltage of the A-phase winding with the proposed power converter can reach up to 24 V, which can shorten the excitation and demagnetization processes.

In order to compare the performance of the SRM system at higher speeds when using two power converters in this paper, the initial 600 r/min was gradually increased to 1000 r/min in the experiment, while other parameters remained unchanged. Figures 19–22 show the experimental results comparison of voltage and current waveforms of the A-phase winding in the SRM system at higher speeds when both the conventional AHBPC and the proposed power converter are powered by battery independently.

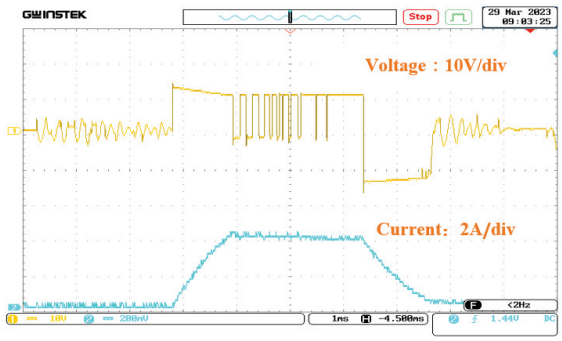

(a)

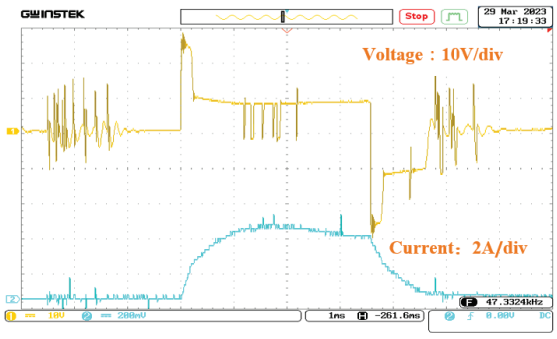

(b)

Fig. 19. Experimental results comparison with two power converters when rotor speed is 700 r/min: (a) voltage and current waveform with conventional AHBPC and (b) voltage and current waveform with proposed power converter.

It can be seen from Figs.19–22, at higher speeds, fast excitation and demagnetization can still be achieved with the proposed power converter. Even though the excitation and demagnetization velocities of the winding phase current gradually decrease due to the increase in rotor speed, high-level excitation and demagnetization greatly quicken the excitation and demagnetization processes. The performance improvement of the SRM system using

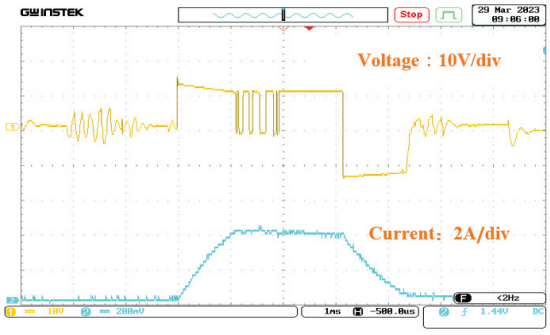

(a)

Fig. 20. *Continued.*

(b)

Fig. 20. Experimental results comparison with two power converters when rotor speed is 800 r/min: (a) voltage and current waveform with conventional AHBPC and (b) voltage and current waveform with proposed power converter.

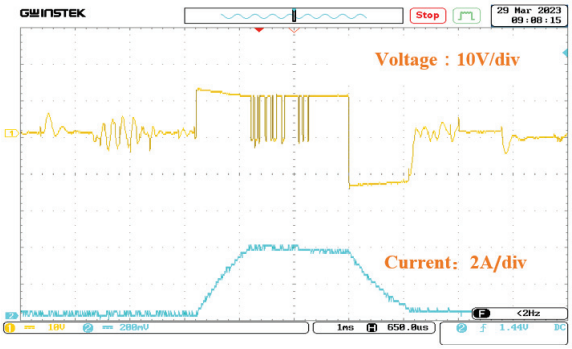

(a)

(b)

Fig. 21. Experimental results comparison with two power converters when rotor speed is 900 r/min: (a) voltage and current waveform with conventional AHBPC and (b) voltage and current waveform with proposed power converter.

the proposed power converter is more significant at high rotor speeds.

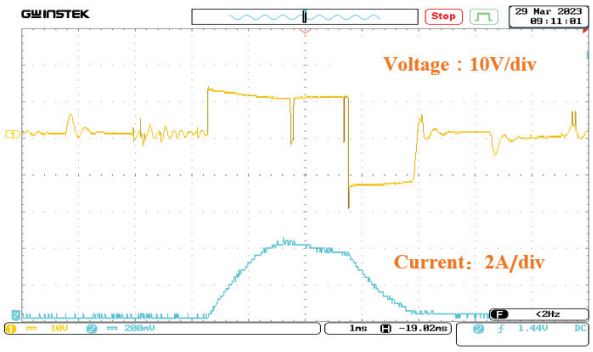

(a)

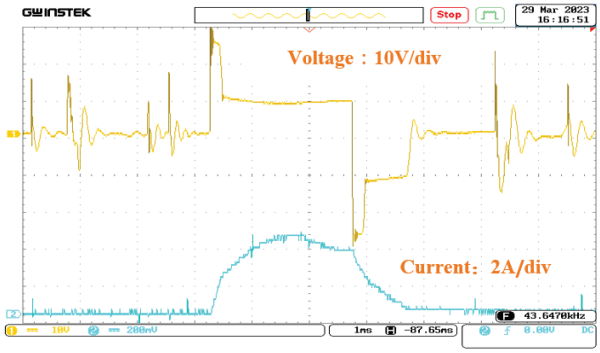

(b)

Fig. 22. Experimental results comparison with two power converters when rotor speed is 1000 r/min: (a) voltage and current waveform with conventional AHBPC and (b) voltage and current waveform with proposed power converter.

V. CONCLUSION

In this paper, a dual-source three-level power converter is proposed to be applied in a multi-port low-carbon building microgrid system. The front-end circuit of the proposed power converter is designed for switching between three power supply modes. Owing to the front-end circuit, the proposed power converter can achieve excitation and demagnetization at high levels, accelerate the excitation and demagnetization speed, and improve the efficiency of the SRM system. Although the excitation and demagnetization processes in dual-source power supply mode (mode 1) are similar to those of the conventional AHBPC, the system performance is improved in the other two working modes, which is verified in both simulation and experimental results.

ACKNOWLEDGMENT

This work was funded in part by National Natural Science Foundation of China under Grant 51967013 and in part by Natural Science Foundation of Jiangxi Province under Grant 20212BAB214061.

REFERENCES

[1] X. Liu, X. Liu, Y. Jiang, T. Zhang, and B. Hao, "Photovoltaics and energy storage integrated flexible direct current distribution systems of buildings: Definition, technology review, and application," *CSEE Journal of Power and Energy Systems*, vol. 9, no. 3, pp. 829-845, May 2023.

[2] H. Shin and K. Lee, "Optimal design of a 1-kW switched reluctance generator for wind power systems using a genetic algorithm," *IET Electric Power Applications*, vol. 10, no. 8, pp. 807-817, Sep. 2016.

[3] X. Xue, K. Cheng, J. Lin, Z. Zhang, K. Luk, T. Ng, and N. Cheung, "Optimal control method of motoring operation for SRM drives in electric vehicles," *IEEE Trans. Veh. Technol.*, vol. 59, no. 3, pp. 1191-1204, Mar. 2010.

[4] M. Michon, S. Calverley, and K. Atallah, "Operating strategies of switched reluctance machines for exhaust gas energy recovery systems," *IEEE Trans. Ind. Appl.*, vol. 48, no. 5, pp. 1478-1486, Sep./Oct. 2012.

[5] H. Chen and J. J. Gu, "Implementation of three-phase switched reluctance machine system for motors and generators," *IEEE/ASME Transactions on Mechatronics*, vol. 15, no. 3, pp. 421-432, June 2010.

[6] R. Krishnan, S.-Y. Park, and K. Ha, "Theory and operation of a four-quadrant switched reluctance motor drive with a single controllable switch-the lowest cost four-quadrant brushless motor drive," *IEEE Transactions on Industry Applications*, vol. 41, no. 4, pp. 1047-1055, July-Aug. 2005.

[7] J. Ye, B. Bilgin, and A. Emadi, "Comparative evaluation of power converters for 6/4 and 6/10 switched reluctance machines," in *IEEE Transportation Electrification Conference and Expo (ITEC)*, pp. 1-6, 2012.

[8] H.-C. Chang and C.-M. Liaw, "Development of a compact switched-reluctance motor drive for EV propulsion with voltage-boosting and PFC charging capabilities," *IEEE Transactions on Vehicular Technology*, vol. 58, no. 7, pp. 3198-3215, Sep. 2009.

[9] D.-H. Lee and J.-W. Ahn, "A novel four-level converter and instantaneous switching angle detector for high speed SRM drive," *IEEE Transactions on Power Electronics*, vol. 22, no. 5, pp. 2034-2041, Sep. 2007.

[10] K. Miyane and K. Akatsu, "High voltage driving method by using low voltage inverters for SRM," in *2015 IEEE International Electric Machines & Drives Conference (IEMDC)*, Coeur d'Alene, ID, USA, pp. 335-339, 2015.

[11] C. Gan, Q. Sun, J. Wu, W. Kong, C. Shi, and Y. Hu, "MMC-based SRM drives with decentralized battery energy storage system for hybrid electric vehicles," *IEEE Transactions on Power Electronics*, vol. 34, no. 3, pp. 2608-2621, Mar. 2019.

[12] P. Palanivel and S. S. Dash, "Multicarrier pulse width modulation methods based three phase cascaded multilevel inverter including over modulation and low modulation indices," in *TENCON 2009 - 2009 IEEE Region 10 Conference*, Singapore, 2009.

[13] R. S. Alishah, K. Bertilsson, F. Blaabjerg, M. A. J. Sathik, and A. Y. Rezaee, "New grid-connected multilevel boost converter topology with inherent capacitors voltage balancing using model predictive controller," in *2020 22nd European Conference on Power Electronics and Applications (EPE'20 ECCE Europe)*, Lyon, France, pp. 1-7, 2020.

[14] J. Borecki and B. Orlik, "Novel, multilevel converter topology for fault-tolerant operation of switched reluctance machines," in *2017 11th IEEE International Conference on Compatibility, Power Electronics and Power Engineering (CPE-POWERENG)*, Cadiz, Spain, pp. 375-380, 2017.

[15] V. F. Pires, D. Foito, A. J. Pires, A. Cordeiro, and J. F. Martins, "An 8/6 SRM drive with a multilevel topology based on a cross-switched configuration," in *2020 IEEE 14th International Conference on Compatibility, Power Electronics and Power Engineering (CPE-POWERENG)*, Setubal, Portugal, pp. 63-68, 2020.

[16] P. Azer, J. Ye, and A. Emadi, "Advanced fault-tolerant control strategy for switched reluctance motor drives," in *2018 IEEE Transportation Electrification Conference and Expo (ITEC)*, Long Beach, CA, USA, pp. 20-25, 2018.

[17] V. Fernão Pires, A. Cordeiro, D. Foito, A. J. Pires, J. Martins, and H. Chen, "A multilevel fault-tolerant power converter for a switched reluctance machine drive," *IEEE Access*, vol. 8, pp. 21917-21931, 2020.

[18] A. Cordeiro, V. F. Pires, A. J. Pires, J. F. Martins, and H. Chen, "Fault-tolerant voltage-source-inverters for switched reluctance motor drives," in *2019 IEEE 13th International Conference on Compatibility, Power Electronics and Power Engineering (CPE-POWERENG)*, Sonderborg, Denmark, pp. 1-6, 2019.

Cheng Liu received the B.S. degree in measurement control technology and instrument from Harbin Engineering University, Heilongjiang, China, in 2003, and the M.S. degree in information technology from University of Abertay Dundee (now Abertay University), Dundee, Scotland, in 2006, and is currently working toward the Ph.D. degree at the School of Information Engineering, Nanchang University, Nanchang, China. He is a Lecturer with the School of Advanced Manufacturing, Nanchang University, Nanchang, China. His research interests include renewable energy generations, micro-grids, motor control and multi-agent.

Yu Zhao received the B.S. degree in electrical engineering and automation from Shandong University of Science and Technology, Shandong, China, in 2019, and the M.S. degree in Electrical Engineering from Nanchang University, Nanchang, China, in 2023. He is currently working as a member in the power supply service team at Daishan County Power Supply Company of State Grid Zhejiang Electric Power Co. Ltd., Daishan, China. His research interests include switched reluctance motors and its control.

Qing Wang received the B.S. degree in automation from Northeastern University, Shenyang, China, in 2011, and the Ph.D. degree in electrical engineering from China University of Mining and Technology, Xuzhou, China, in 2017. In 2018, he became a Lecturer with the School of Information Engineering, Nanchang University, Nanchang, China, where he has been an Associate Professor since 2023. His research interests include electric vehicles, electrical motor drives, renewable energy generations, and micro-grids.

Xiaofeng Wan received the B.S. degree in automation from Zhejiang University, Hangzhou, China, in 1994. She became a Lecturer with the School of Information Engineering, Nanchang University, Nanchang, China, where she has been a Professor since 2006. Her research interests include electric vehicles, renewable energy generations, and micro-grids.

Lei Cao received the B.S. degree in law from Nanchang University, Nanchang, China, in 2010. He is currently working at the Architecture Experimental Center of the Architecture and Design College at Nanchang University, Nanchang, China, with the title of Experimental Engineer. His research interests include building electricity and complex system modeling.

Electromagnetic Characteristics Analysis of a Symmetrical-Stator Axial Flux Dual-Mechanical-ports Switched Reluctance Motor

Fengyuan Yu[1], Xing Wang[2], Hao Chen[1,2,3*], Wenju Yan[1], Jianfei Pan[4], Popov Stanislav Olegovich[5], Bodrenkov Evgenii Alexandrovich[5], Nurkhat Zhakiyev[6], and Yassen Gorbounov[7]

[1]School of Electrical Engineering
China University of Mining and Technology, Xuzhou 221116, China
fyyu@cumt.edu.cn, yanwenju09@126.com
*Corresponding author: hchen@cumt.edu.cn

[2]International Joint Research Center of Central and Eastern European Countries on New Energy Electric Vehicle Technology and Equipment
Xuzhou 221008, China
3512@cumt.edu.cn

[3]Shenzhen Research Institute
China University of Mining and Technology, Shenzhen 518057, China

[4]School of Electromechanical and Control Engineering
Shenzhen University, Shenzhen 518054, China
pan_jian_fei@163.com

[5]Institute of Energy
Peter the Great Saint-Petersburg Polytechnic University
Saint Peters burg 195251, Russia
popovso@spbstu.ru, bodrenkovea@spbstu.ru

[6]Department of Science and Innovation
Astana IT University, Astana, Kazakhstan
nurkhat.zhakiyev@astanait.edu.kz

[7]Department of Informatics
New Bulgarian University, Sofia 1618, Bulgaria
y.gorbounov@mgu.bg

Abstract **–**Dual-mechanical-ports motors, as a new motor type, have two mechanical ports that can operate independently or simultaneously. It has good application prospects in new energy generation and hybrid power systems with the advantages of compact structure and high integration. In this paper, a novel symmetrical-stator axial flux dual-mechanical-ports switched reluctance motor is proposed. The number of stator poles is 16, and the poles of the two rotors are 14 and 10, respectively. The three-dimensional finite element analysis model is built in Altair Flux software. The electromagnetic performance such as magnetic density, flux linkage, static torque, and decoupling characteristics are analyzed adopting the finite element analysis method. The results proved the effectiveness of the new motor structure.

Index Terms **–** Coupling characteristics, dual-mechanical-ports, electromagnetic performance, finite element analysis, switched reluctance motor.

I. INTRODUCTION

With the development of electrified transportation, new energy generation, and other emerging fields, the demand for dual-mechanical-ports motor systems is increasing and becoming a hot research direction [1–2]. For example, for hybrid vehicles, the drive system not only needs to realize the electromechanical energy conversion between the engine, the power battery, and the wheels, but also needs to regulate the energy between them to ensure that the engine operates in the optimal efficiency region. The Prius hybrid car produced

Submitted On: December 29, 2024
Accepted On: June 11, 2025

https://doi.org/10.13052/2025.ACES.J.400912

by Toyota adopts a planetary gear-based drive system. This system enables power transmission and distribution between the engine, battery, and wheels in the hybrid system. However, the many mechanical components lead to reduced reliability of the whole system. In recent years, the two-mechanical-ports motor system has been proposed to achieve the same functionality of a planetary gear-based hybrid system with the advantages of good compactness, high integration, and synergistic output of multiple ports [3–4].

Different types of dual-mechanical-port motors such as permanent magnet synchronous, brushless DC, doubly fed, and magnetic field modulated motors have been investigated [5–9]. Switched reluctance motors, due to the absence of windings and permanent magnets in the rotor, have the advantages of robust construction and high fault tolerance. Few studies related to switched reluctance motors with dual-mechanical-ports have been reported. References [10–11] proposed a radial flux dual rotor switched reluctance motor structure. However, the outer rotor needs to be designed as a cup structure, which is not stable enough for operation. In addition, the radial flux motor cannot avoid the common drawbacks such as low utilization of space and low aspect ratio.

The axial flux motor structure has the flux direction perpendicular to the direction of rotation and the torque output capability is not affected by the axial length, which has the advantages of high torque density and short axial length. Reference [12] investigated a dual rotor axial flux switched reluctance motor and obtained high torque density. However, its two rotors are connected and jointly output mechanical power through one shaft. References [13–14] studied counter-rotating dual-rotor motors and analyzed their magnetic coupling characteristics.

A symmetrical-stator axial flux dual-mechanical-port switched reluctance motor (AFDMP-SRM) is proposed in this paper. The paper is arranged as follows. Motor topology is presented in section II. In section III, the finite element model of the motor is developed and the electromagnetic performance of two mechanical ports operating independently is analyzed. The electromagnetic performance of two mechanical ports operating simultaneously is analyzed in Section IV. Section V concludes the paper.

II. MOTOR STRUCTURE

The structure of a symmetrical-stator AFDMP-SRM is given in Fig. 1. The motor has a single stator and double rotor structure with two outer rotors set on either side of a single inner stator. Note that the single stator is a symmetrical structure with alternating wide and narrow tooth poles on both sides, and the stator poles share a common stator yoke. There are 16 stator poles on each side of the stator, divided into 8 wide poles and 8 narrow poles. The AFDMP-SRM is a dual four-phase motor. Both sets of windings are of a single-tooth winding structure, with windings 1 and 2 wound on the wide poles on both sides of the stator, and no winding on the narrow pole of the stator. Note that winding 1 contains four phases ABCD and winding 2 contains four phases EFGH. The pole number of Rotor1 and Rotor2 are 14 and 10, respectively. This provides the possibility that the two mechanical ports could have different rated speeds.

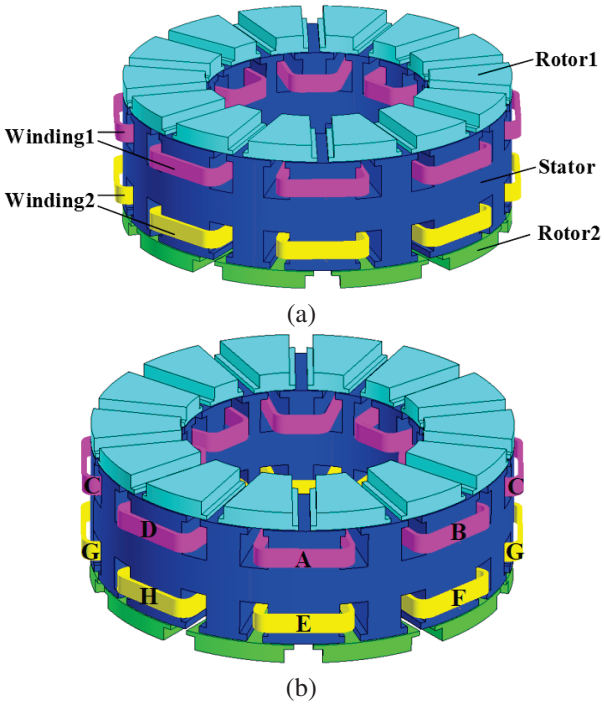

Fig. 1. Diagram of the symmetrical-stator AFDMP-SRM structure: (a) overall view and (b) winding structure.

As can be observed, the AFDMP-SRM does not employ the traditional solution of separating the two sides of the stator with a non-magnetic ring to avoid magnetic coupling of the two sets of windings. The motor is a combination of two single-stator, single-rotor motors by means of a shared stator yoke, which avoids the increase of the axial dimensions.

III. ELECTROMAGNETIC PERFORMANCE ANALYSIS OF TWO MECHANICAL PORTS OPERATING INDEPENDENTLY

To analyze the electromagnetic characteristics of the AFDMP-SRM, its three-dimensional analytical model is developed in finite element software Altair Flux. The B-H curve for 50DW470 material is illustrated in Fig. 2.

Firstly, the magnetic density characteristics of the motor are analyzed. Applying separate excitation currents to phase-A of winding 1 and phase-E of winding 2,

Table 1: Parameters of the symmetrical-stator AFDMP-SRM

Motor Parameter	Item	Value
Stator poles number	/	16
Rotor1 poles number	/	10
Rotor2 poles number	/	14
Stator/rotor outer diameter	mm	175
Stator/rotor inner diameter	mm	101
Stator yoke thickness	mm	16
Stator poles length	mm	15
Stator pole shoes length	mm	3
Stator slot width	mm	12
Rotor1 pole length	mm	6
Rotor2 pole length	mm	6
Rotor1 pole shoes length	mm	2
Rotor2 pole shoes length	mm	2
Air-gap length	mm	0.5
Winding coil turns per pole	/	50

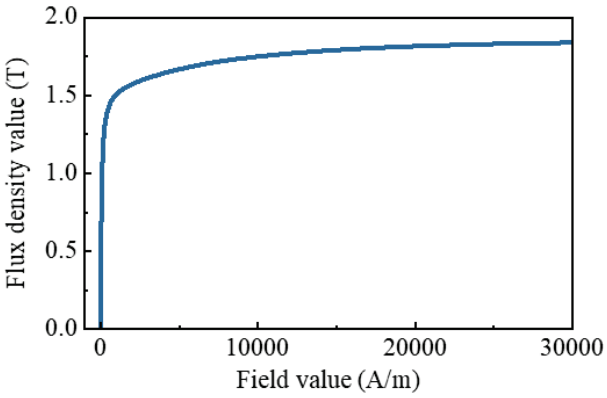

Fig. 2. B-H curve of material 50DW470.

the magnetic density cloud maps are presented in Figs. 3 and 4. From Fig. 3, it can be seen that when a 30 A current is applied to phase-A, mechanical port 1 forms a shorter flux path due to the wide and narrow stator poles, the segmented-rotor, and the single-tooth winding structure. In the Rotor1 aligned position, the magnetic density is more uniformly distributed in the stator yoke, the stator poles on the mechanical port side, and the Rotor1. In addition, the magnetic density has almost no value at phase-E stator pole and Rotor2.

Similarly, as can be seen in Fig. 4, at the Rotor2 aligned position, the magnetic density is more uniformly distributed in the stator yoke, the phase-E stator poles, and the Rotor2. Magnetic density has almost no value at phase-A stator poles and Rotor1.

Further, the static electromagnetic torque and flux linkage characteristics with the two mechanical ports of the AFDMP-SRM are analyzed. The electromagnetic

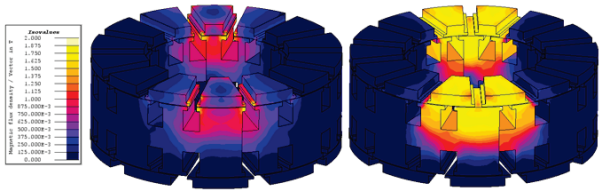

Fig. 3. Magnetic density maps when phase-A is excited alone: (a) Rotor1 unalignment position and (b) Rotor1 alignment position.

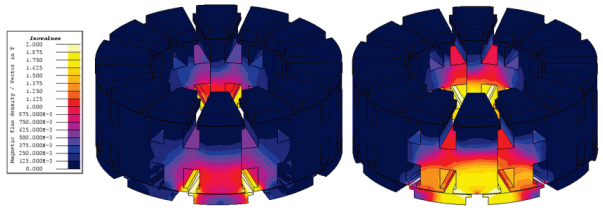

Fig. 4. Magnetic density maps when phase-E is excited alone: (a) Rotor2 unalignment position and (b) Rotor2 alignment position.

torque of Rotor1 for half rotor cycle is obtained by applying an excitation current to the phase-A alone, as shown in Fig. 5 (a). Figure 5 (b) presents the electromagnetic torque of the Rotor2 when the current is applied to the phase-E alone. It should be noted that the horizontal axis of Figs. 5 (a) and (b) ranges from half rotor cycle, from the respective rotor unaligned position to the aligned position. They have the same electrical angle of 180°, although the mechanical angle is different. For Rotor1, the mechanical angle of half rotor cycle is 360/10/2. The mechanical angle of half rotor cycle is 360/14/2 for Rotor2.

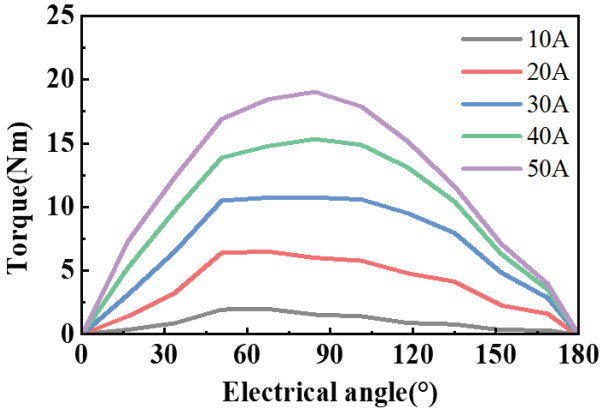

(a)

Fig. 5. *Continued.*

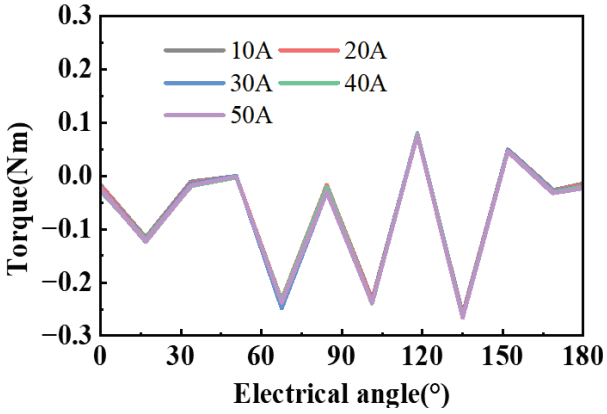

(b)

Fig. 5. Static torque of two mechanical ports of AFDMP-SRM: (a) Rotor1 and (b) Rotor2.

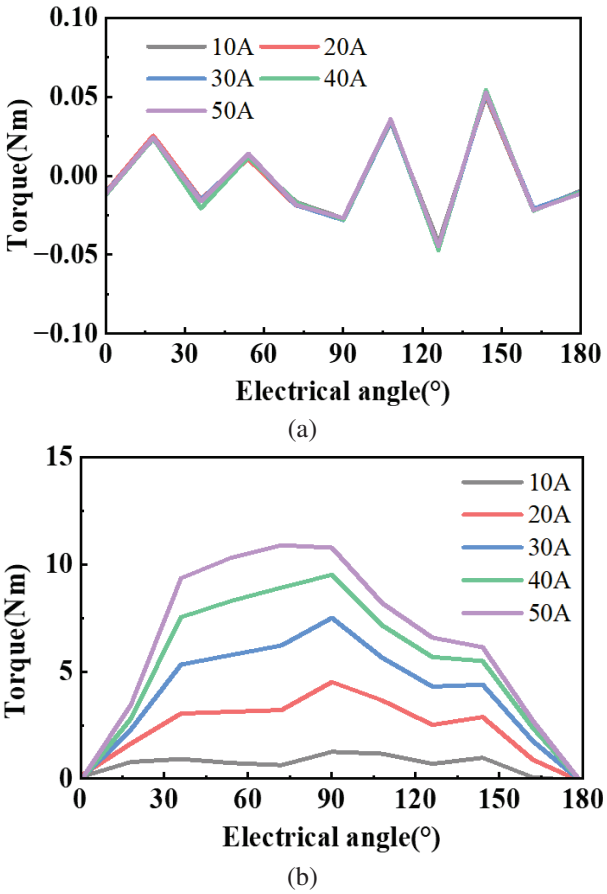

(a)

(b)

Fig. 6. Static torque of two mechanical ports of AFDMP-SRM: (a) Rotor1 and (b) Rotor2.

As can be seen, the torque output capability of mechanical port 1 with a 16/10 poles configuration is higher than that of mechanical port 2 with a 16/14 poles configuration. Moreover, when the current is applied to the winding 1 alone, the Rotor1 outputs electromagnetic torque. The electromagnetic torque of the Rotor2 is quite small, not exceeding -0.3 Nm at 50 A. When the current is applied to the winding 2 alone, the Rotor2 outputs electromagnetic torque. The electromagnetic torque of the Rotor1 is small, not more than 0.1 Nm at 50 A. Therefore, by applying separate currents to the two sets of windings, a lesser effect on the other mechanical port could be detected. It is demonstrated that the electromagnetic coupling of the AFDMP-SRM to the other is not significant when the two mechanical ports are operated separately.

Figure 7 shows the flux linkage waveforms of phase-A and phase-E when currents ranging from 0 A to 50 A are applied at the fully unaligned and aligned positions. It can be observed that the area enclosed by the magnetization curve of phase-E is smaller than that of phase-A. This indicates that, under the same magnetomotive force, the electromagnetic torque output capability of mechanical port 1 is greater than that of mechanical port 2.

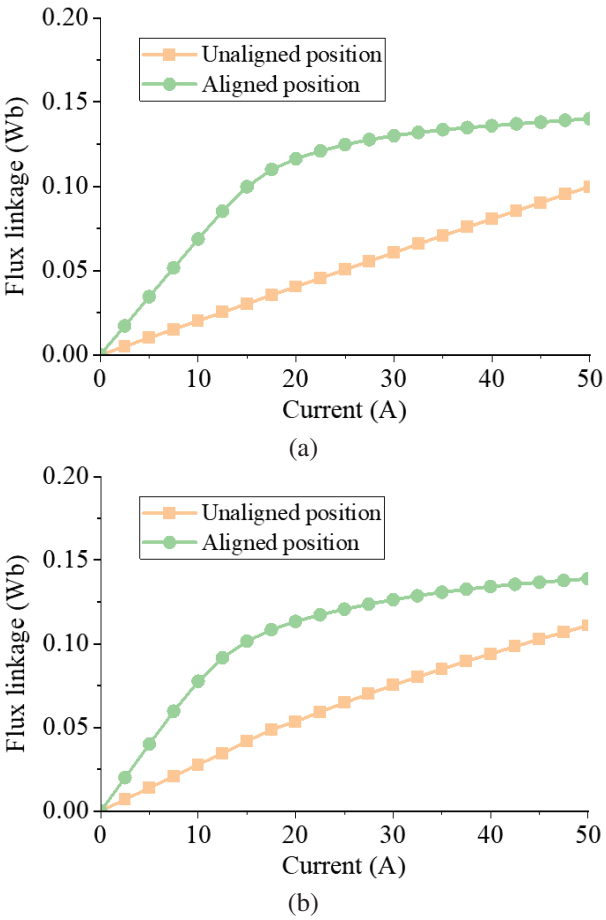

(a)

(b)

Fig. 7. Flux linkage of two sets of winding of AFDMP-SRM: (a) flux linkage of phase-A and (b) flux linkage of phase-E.

IV. ELECTROMAGNETIC PERFORMANCE ANALYSIS OF TWO MECHANICAL PORTS OPERATING SIMULTANEOUSLY

Unlike the single-mechanical-port motor, the dual-mechanical-port motor can operate their two mechanical ports independently or simultaneously. In section III, the magnetic flux density characteristics of the motor during independent operation of the two mechanical ports are investigated. The magnetic flux density characteristics when both ports are operating simultaneously also need to be examined.

When exciting the coils of phase-A with winding 1 and phase-E with winding 2 simultaneously, the magnetic flux density characteristics of two rotors, with Rotor1 and Rotor2 in the unaligned position and the aligned position, are shown in Fig. 8.

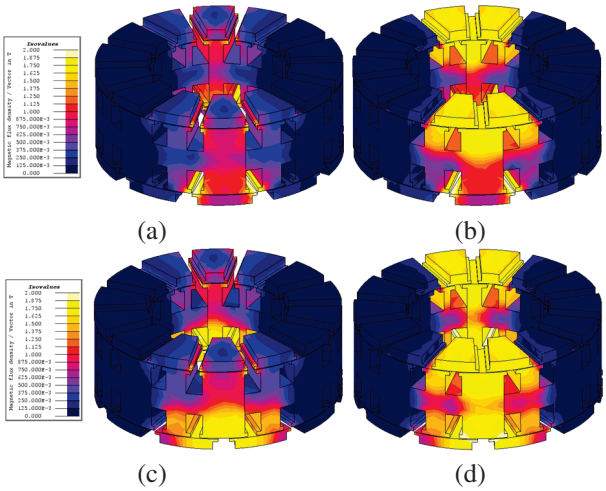

Fig. 8. Magnetic density maps when phase-A and phase-E are excited simultaneously: (a) Rotor1 unalignment position and Rotor2 unalignment position, (b) Rotor1 alignment position and Rotor2 unalignment position, (c) Rotor1 unalignment position and Rotor2 unalignment position, and (d) Rotor1 alignment position and Rotor2 unalignment position.

By examining Figs. 3 and 4, it could be observed that when Rotor1 or Rotor2 operates independently, the impact on the magnetic flux density of the other port is minimal. However, from Fig. 8, it is difficult to directly observe the mutual influence between the two mechanical ports. To quantitatively analyze the magnetic coupling characteristics between the two mechanical ports, the magnetic flux linkage and inductance characteristics are further investigated.

It should be noted that the self-inductance coefficient is defined as the rate of change of the total flux linkage through that winding to the phase current, for a given rotor position angle and phase current [15–16].

$$L_{\mathrm{ph}}(\theta, i) = \frac{d\psi_{\mathrm{ph}}(\theta, i)}{di}, \tag{1}$$

where $\psi_{\mathrm{ph}}(\theta, i)$ denotes the flux linkage of the phase winding. θ and i are the rotor position angle and phase current, respectively.

From Fig. 9, it can be observed that, as the applied current of the winding on the other side increases from 0 A to 50 A, the flux linkage of phase-A at both the fully unaligned position and the aligned position slightly increases. The inductance characteristics shown in Fig. 10 also confirm that the phase inductance increases throughout the entire rotor cycle.

Table 2 lists the maximum and minimum inductance values of the phase-A winding when the current of the phase-E winding varies. Similarly, Table 3 presents the maximum and minimum inductance values of the phase-E winding when the current of the phase-A winding varies. It can be found that, at low current levels, the difference between the maximum and minimum induc-

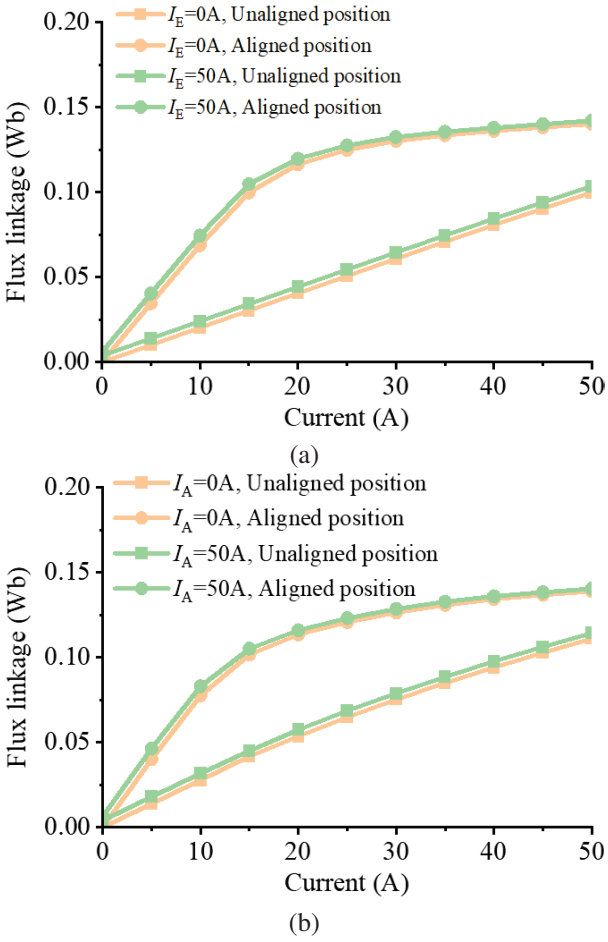

Fig. 9. Flux linkage of two mechanical ports of AFDMP-SRM: (a) Rotor1 and (b) Rotor2.

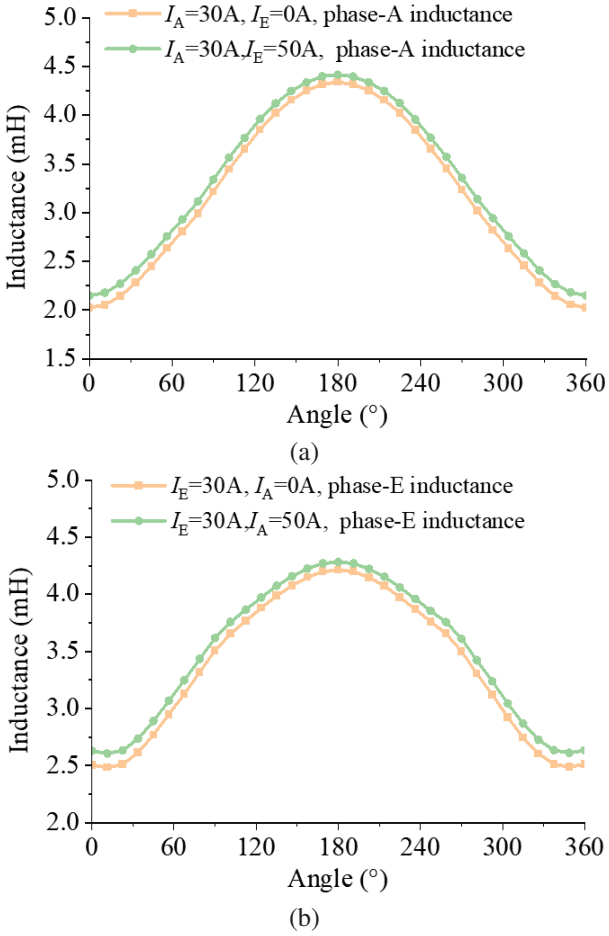

Fig. 10. Inductance of two mechanical ports of AFDMP-SRM: (a) Rotor1 and (b) Rotor2.

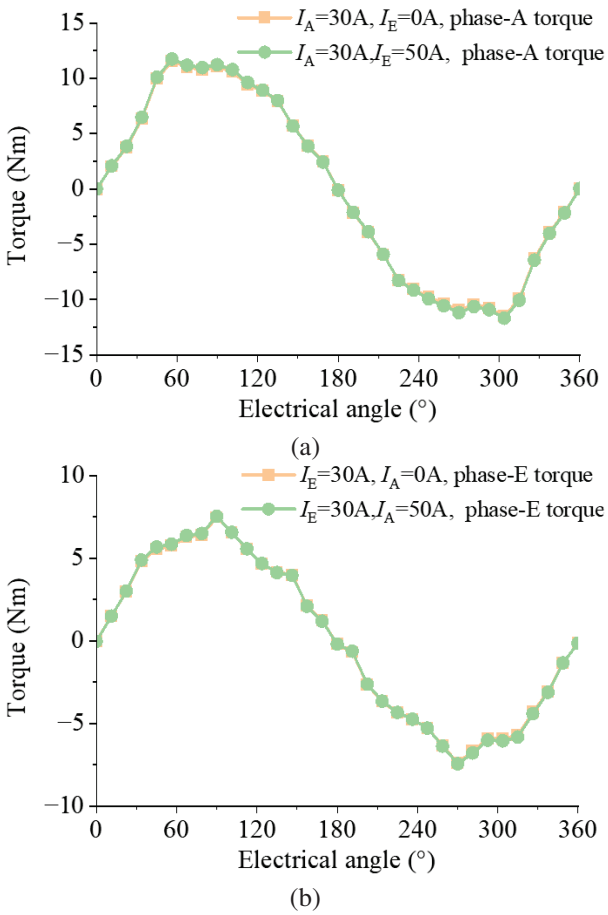

Fig. 11. Static torque of two mechanical ports of AFDMP-SRM: (a) Rotor1 and (b) Rotor2.

tance values is relatively large. However, as the current increases, the difference in inductance values decreases, which could be attributed to the electromagnetic saturation effect.

The maximum and minimum inductances refer to the peak and trough values of inductance observed over one rotor electrical cycle at a fixed current level. Generally, the maximum inductance L_{max} corresponds to the inductance at the rotor aligned position, while the minimum inductance L_{min} corresponds to the inductance at the rotor unaligned position.

From Tables 4 and 5, it could be observed that the differences and ratios between the maximum and minimum inductance values exhibit less variation compared to the variation in their absolute values.

Furthermore, Fig. 11 presents a comparison of the electromagnetic torque for Rotor1 and Rotor2 before and after applying current to the other side. It can be seen that the change in torque is not significant.

Table 2: Influence of phase-E current on inductance of phase-A

	$L_{\min}$		$L_{\max}$	
	$I_E = 0$ A	$I_E = 50$ A	$I_E = 0$ A	$I_E = 50$ A
$I_A = 10$ A	2.026	2.406	6.871	7.452
$I_A = 20$ A	2.026	2.216	5.817	5.981
$I_A = 30$ A	2.024	2.151	4.336	4.413
$I_A = 40$ A	2.016	2.108	3.399	3.446
$I_A = 50$ A	1.999	2.071	2.804	2.841

Table 3: Influence of phase-A current on inductance of phase-E

	$L_{\min}$		$L_{\max}$	
	$I_A = 0$ A	$I_A = 50$ A	$I_A = 0$ A	$I_A = 50$ A
$I_E = 10$ A	2.789	3.177	7.755	8.300
$I_E = 20$ A	2.678	2.869	5.667	5.799
$I_E = 30$ A	2.507	2.629	4.212	4.283
$I_E = 40$ A	2.351	2.440	3.355	3.397
$I_E = 50$ A	2.219	2.286	2.778	2.808

Table 4: Influence of phase-E current on inductance difference and inductance variation rate of phase-A

	L_{max}-L_{min}		L_{max}/L_{min}	
	$I_E = 0$ A	$I_E = 50$ A	$I_E = 0$ A	$I_E = 50$ A
$I_A = 10$ A	3.391	3.098	4.844	5.046
$I_A = 20$ A	2.871	2.699	3.791	3.765
$I_A = 30$ A	2.142	2.052	2.311	2.262
$I_A = 40$ A	1.686	1.634	1.384	1.338
$I_A = 50$ A	1.403	1.372	0.806	0.771

Table 5: Influence of phase-A current on inductance difference and inductance variation rate of phase-E

	L_{max}-L_{min}		L_{max}/L_{min}	
	$I_A = 0$ A	$I_A = 50$ A	$I_A = 0$ A	$I_A = 50$ A
$I_E = 10$ A	2.781	2.612	4.966	5.123
$I_E = 20$ A	2.116	2.022	2.989	2.930
$I_E = 30$ A	1.680	1.629	1.706	1.654
$I_E = 40$ A	1.427	1.392	1.005	0.957
$I_E = 50$ A	1.252	1.229	0.559	0.523

V. CONCLUSION

This paper proposes a novel 10/16/14 symmetrical-stator axial flux dual-mechanical-ports switched reluctance motor. The three-dimensions finite element model is established in Altair Flux. The electromagnetic performance of two mechanical ports operating independently and simultaneously is both investigated. The torque output capability of mechanical port 1 with a 16/10 poles configuration is higher than that of mechanical port 2 with a 16/14 poles configuration under the same magnetomotive force. When the two mechanical ports operate independently, their magnetic coupling effects are minimal. When the two mechanical ports operate simultaneously, the magnetic flux linkage and inductance values are affected. However, the impact on torque is negligible. Future work will focus on analyzing the influence of stator yoke thickness on magnetic coupling characteristics.

ACKNOWLEDGMENT

This work is supported by the National Natural Science Foundation of China International (regional) cooperation and exchange projects NSFC-RSF (W2412064), the Shenzhen Collaborative Innovation Special Plan International Cooperation Research Project (GJHZ20220913144400001), the General Research Project of Shenzhen Science and Technology Plan (JCYJ20220818100000001), the Jiangsu Funding Program for Excellent Postdoctoral Talent (2024ZB008), the China Postdoctoral Science Foundation (2024M763541), the 2022 China-CEEC University Joint Education Program (2022200), and the 2023 China-CEEC University Joint Education Program (2023304).

REFERENCES

[1] Z. Zhao, P. Tang, and H. Li, "Generation, screening, and optimization of powertrain configurations for power-split hybrid electric vehicle: A comprehensive overview," *IEEE Transactions on Transportation Electrification*, vol. 8, no. 1, pp. 325-344, Mar. 2022.

[2] X. Han, W. Kong, R. Qu, D. Li, T. Zou, and X. Ren, "Flexible energy conversion control strategy for brushless dual-mechanical-port dual-electrical-port machine in hybrid vehicles," *IEEE Transactions on Power Electronics*, vol. 34, no. 4, pp. 3910-3920, Apr. 2019.

[3] W. Ullah, F. Khan, U. B. Akuru, S. Hussain, M. Yousuf, and S. Akbar, "A novel dual electrical and dual mechanical wound field flux switching generator for co-rotating and counter-rotating wind turbine applications," *IEEE Transactions on Industry Applications*, vol. 60, no. 1, pp. 184-195, Jan.-Feb. 2024.

[4] M. Jiang and S. Niu, "Overview of dual-mechanical-port machines in transportation electrification," *IEEE Transactions on Transportation Electrification*, vol. 10, no. 3, pp. 4959-4977, Sep. 2024.

[5] M. Jiang, S. Niu, and C. C. Chan, "A high-order-harmonic compound-rotor based brushless doubly-fed machine for variable speed constant frequency wind power generation," *IEEE Journal of Emerging and Selected Topics in Power Electronics*, vol. 13, no. 2, pp. 1492-1502, Apr. 2025.

[6] R. Huang, Z. Dong, Z. Song, and C. Liu, "A novel counter-rotating AFPM machine based on magnetic-field modulation for underwater propulsion system," *IEEE Transactions on Industrial Electronics*, vol. 71, no. 3, pp. 2167-2176, Mar. 2024.

[7] T. Yang, K. T. Chau, T. W. Ching, Z. Xue, and H. Zhao, "Design and analysis of double-rotor flux-reversal PM magnetic differential motor with suppressed rotor coupling," *IEEE Transactions on Transportation Electrification*, vol. 10, no. 3, pp. 5506-5519, Sep. 2024.

[8] C. Tong, J. Lang, J. Bai, P. Zheng, and D. Ma, "Deadbeat-direct torque and flux control of a brushless axial-flux magnetic-geared double-rotor machine for power-splitting HEVs," *IEEE Transactions on Industrial Electronics*, vol. 70, no. 9, pp. 8734-8745, Sep. 2023.

[9] H. Chen, A. M. EL-Refaie, Y. Zuo, S. Cai, L. Cao, and C. H. T. Lee, "Comparative study and design optimization of a dual-mechanical-port electric machine for hybrid electric vehicle applications," *IEEE Transactions on Vehicular Technology*, vol. 71, no. 8, pp. 8341-8353, Aug. 2022.

[10] Y. Yang, N. Schofield, and A. Emadi, "Double-rotor switched reluctance machine (DRSRM)," *IEEE Transactions on Energy Conversion*, vol. 30, no. 2, pp. 671-680, June 2015.

[11] T. Guo, N. Schofield, and A. Emadi, "Double segmented rotor switched reluctance machine with shared stator back-iron for magnetic flux passage," *IEEE Transactions on Energy Conversion*, vol. 31, no. 4, pp. 1278-1286, Dec. 2016.

[12] R. Madhavan and B. G. Fernandes, "Performance improvement in the axial flux-segmented rotor-switched reluctance motor," *IEEE Transactions on Energy Conversion*, vol. 29, no. 3, pp. 641-651, Sep. 2014.

[13] R. De Croo and F. De Belie, "Operating principle and characterisation of a novel contra-rotating dual-rotor switched reluctance machine," *IEEE Transactions on Industry Applications*, vol. 60, no. 5, pp. 6775-6786, Sep.-Oct. 2024.

[14] R. Huang, B. Zhang, Y. Liu, and C. Liu, "Investigation of magnetic isolation in a double-side asynchronous rotor-AFPM machine based on harmonic analysis," *IEEE Transactions on Industrial Electronics*, vol. 72, no. 1, pp. 240-250, Jan. 2025.

[15] M. Zhang, N. Ali, and Q. Gao, "Winding inductance and performance prediction of a switched reluctance motor with an exterior-rotor considering the magnetic saturation," *CES Transactions on Electrical Machines and Systems*, vol. 5, no. 3, pp. 212-223, Sep. 2021.

[16] X. Guo, S. Zeng, R. Zhong, and W. Hua, "Automatic offline measurement of full-cycle unsaturated inductance for low-speed rotor position estimation in switched reluctance machines," *IEEE Journal of Emerging and Selected Topics in Power Electronics*, vol. 12, no. 1, pp. 849-861, Feb. 2024.

Fengyuan Yu received the Ph.D. degree from the School of Electrical Engineering, China University of Mining and Technology, Xuzhou, China, in 2023. Since 2023, he has been a Post-Doctoral Researcher with the China University of Mining and Technology. His research interests include switched reluctance drive, special motor design, power converters, and motor control.

Xing Wang received the B.S. and M.S. degrees from China University of Mining and Technology, Xuzhou, China, in 1996 and 1999, respectively. Her research interests include switched reluctance drive, electric vehicle, electric traction, wind power generator, power converters, and motor control.

Hao Chen received his B.S. and Ph.D. degrees from the Department of Automatic Control, Nanjing University of Aeronautics and Astronautics, Nanjing, China, in 1991 and 1996, respectively. In 1998, he became an Associate Professor with the School of Information and Electrical Engineering, China University of Mining and Technology, Xuzhou, where he has been a Professor since 2001. From 2002 to 2003, he was a Visiting Professor at Kyungsung University, Busan, Korea. Since 2008, he has also been an Adjunct Professor at the University of Western Australia, Perth, Australia. He is the author of one book and has also authored more than 190 papers. He is the holder of 14 US Patents, 23 Australian Patents, one Danish Patent, seven Canadian Patents, three South African Patents, 10 Russian Patents, 44 Chinese Invention Patents and six Chinese Utility Model Patents. His current research interests include motor control, linear launcher, electric vehicles, electric traction, servo drives, and wind power generator control.

Chen was the recipient of both the Prize of Science and Technology of Chinese Youth and the Prize of the Fok Ying Tong Education Foundation for Youth Teachers in both 2004. He was awarded the first prize in the Science and Technology advanced of Province and Ministry once, the second prize in the Science and Technology advanced of Province and Ministry seven times, and the third prize in the Science and Technology advanced of Province and Ministry 14 times. He became the Chinese New Century Hundred-Thousand Ten-Thousand Talents Engineering National Talent in 2007 and won the Government Especial Allowance of People's Republic of China State Department in 2006.

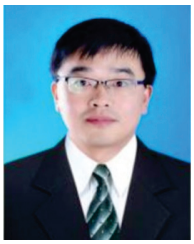

Wenju Yan received the B.S. and Ph.D. degrees from the China University of Mining and Technology, Xuzhou, China, in 2013 and 2018, respectively. Since 2018, he has been with China University of Mining and Technology, where he is currently an Associate Professor with the School of Electrical Engineering. His research interests include electric vehicles, electric traction, iron loss analysis, and motor design.

Jianfei Pan graduated from Department of Electrical Engineering of Hong Kong Polytechnic University in Hong Kong for the Ph.D. degree in 2006. Currently he is working in College of Mechatronics and Control Engineering, Shenzhen University. His main research interests are wireless power transfer, electric machine design and control.

Popov Stanislav Olegovich received the M.S. degree from in the field of electric power plants and automation of power systems in 2008, and the PhD degree of Technical Sciences associate professor Institute of Energy, working from 2008 to the present in SPBSTU.

Bodrenkov Evgenii Alexandrovich received the B.S. and M.S. degree from Federal State Budgetary Educational Institution of Higher Education, Amur State University, Russia, and the Ph.D. degree from the Federal State Autonomous Educational Institution of Higher Education, Peter the Great St. Petersburg Polytechnic University.

Nurkhat Zhakiyev is a senior researcher and associate professor with a Ph.D. in the field of physics and currently serves as the head of the Department of Science and Innovation at the Astana University of Information Technology, Kazakhstan. He has nearly a decade of research experience in computational modeling of energy systems and physical processes, with a focus on data science in energy and environmental economics and climate change mitigation analysis. He started his career in 2007 as a junior researcher at West Kazakhstan State University, then rose through the ranks in various higher education institutions and research institutes in Astana, where he gained extensive experience in research and project management. He has worked as a principal researcher or co-researcher on projects funded by the Ministry of Science and Higher Education of Kazakhstan, the Royal Academy of Engineering, the British Council and other institutions in various fields such as low carbon development, greenhouse gas emission forecasting, energy efficiency solutions and more.

Yassen Gorbounov received his B.S., M.S., and Ph.D. degrees from the Sofia University of Technology, Sofia, Republic of Bulgaria, in 2002, 2004, and 2013, respectively. Since 2017, he has been working as an Associate Professor at the Sofia University of Technology. His current research interests include power electronics and the mining industry.

Sensorless Position Estimation with Virtual Inductance Vector for Switched Reluctance Machines Considering Asymmetrical Phase Inductance

Kai Liu[1], Zongwen Jiang[2], Qing Wang[3*], and Jiangtao Hu[3]

[1]School of Electrical Engineering
Changzhou Vocational Institute of Mechatronic Technology, Changzhou 213164, China
czimtlk@163.com

[2]Zoomlion Agriculture Machinery Co. Ltd.
Wuhu 052165, China
1428363576@qq.com

[3]School of Information Engineering
Nanchang University, Nanchang 330031, China
406100230026@email.ncu.edu.cn
*Corresponding author: wangq@ncu.edu.cn

Abstract – This paper proposes an online sensorless rotor position estimation technique for switched reluctance motors, by which the real-time rotor position is estimated by detecting the virtual inductance vector of the machine. With the proposed technique, rotor position can be estimated accurately, even if the inductance of each phase is asymmetrical. It is achieved by first detecting real-time voltage and real-time current of each phase winding, according to which flux-linkage and inductance of each phase can be thus calculated. With the calculated inductance of each phase, a coordinate system can be established for rotor position estimation. However, since the position estimation accuracy will be reduced by asymmetrical phase inductance, a conversion rule is proposed to convert actual phase inductance to virtual inductance, by which the symmetry of phase inductance can be corrected. Then, according to virtual inductance, a new coordinate system is established for rotor position estimation. In the new coordinate system, position estimation shows high accuracy under both normal condition and asymmetric inductance condition. To conclude, simulation and experimental results are given to verify the effectiveness of the proposed sensorless position estimation technique.

Index Terms – Asymmetry inductance, phase inductance estimation, sensorless position estimation, switched reluctance machine, virtual inductance vector.

I. INTRODUCTION

In recent years, switched reluctance machines (SRMs) have been attracting attention in aerospace [1–2], electric vehicles [3–6], and wind power generation [7–9] because of its simple and robust structure, low manufacturing cost, and flexible operation. However, due to the natural tendency, position sensors are required in conventional SRM systems for accurate commutation and rotor speed detection. However, the additional position sensor will not only increase manufacturing cost but also increases the potential failure rate of the system. In order to overcome such problems, sensorless position estimation techniques are required for SRM control, especially in some specific applications [10].

A variety of sensorless position estimation methods have been proposed in published papers. For example, neural network methods, fuzzy logic methods, and artificial intelligence algorithms show good estimation accuracy in [11–12]. However, those methods need premeasured data, which not only makes the estimation process complicated but also requires extra memory space for data storage. In order to simplify the estimation process, some key characteristics of SRM are employed for sensorless control. For example, in [13–14], flux-linkage is obtained and compared with the threshold to detect particular angle. In [15–16], current and inductance gradient are obtained for position estimation. In [17], a hybrid sensorless control algorithm is proposed to determine the phase commutation point based on the characteristics of overlap position. However, the accuracy of the estimated position by the above methods would be influenced by many factors in actual systems, such as voltage drop on power devices, phase resistance, and rotor speed.

In order to improve the accuracy of the estimated rotor position, techniques which contain compensation methods can be found in published papers. In [18], an improved sensorless control strategy is proposed,

Submitted On: December 30, 2024
Accepted On: March 31, 2025
https://doi.org/10.13052/2025.ACES.J.400913

in which the effect of both resistive voltages drop and back-EMF are considered. In [19], the phase inductance waveform is assumed to be a sine wave and the rotor position at standstill is obtained by computing the angle of space vector of inductance. However, the proposed method is only discussed under starting operation. In [20], by measuring the full-cycle inductance of each phase, the corresponding sensorless control scheme is implemented, which possesses good potential for extending the sensorless operating range for SRM. According to the analysis of rotor position estimation methods under inductance asymmetric conditions in [20], an inductance asymmetric will affect the estimation accuracy of the proposed method, and the proposed method can be implemented only when the degree of asymmetry is low.

According to published papers, most existing sensorless position estimation strategies are designed for the ideal SRM prototype (i.e. inductance of each phase is symmetric). However, due to reasons such as machining errors, measure errors, and inter turn short-circuit fault, the estimated inductance of each phase might be asymmetric, which eradicates the accuracy of position estimation. The inductance asymmetric would be more common for SRM applied in harsh environments. Thus, it is necessary to design a sensorless position estimation technique for SRM, which is suitable for full-speed range and shows good tolerance under inductance asymmetric conditions.

In this paper, we present a novel sensorless position estimation for SRM, which shows the following primary contributions: the proposed method relies on the inherent inductance characteristic in SRM, premeasured data is not required for position estimation; during the estimation process, actual inductance is converted into virtual inductance, by which real-time rotor position can be accurately estimated even if the inductance is asymmetric; the proposed method can be generalized to any SRMs with n phases.

The rest of this paper is organized as follows. In section II, the basic theory of position estimation with inductance vector coordinate is introduced for SRM. In section III, position estimation accuracy is analyzed under asymmetric inductance, and virtual inductance is proposed for SRM position estimation. In sections IV and V, simulation results and experimental results are given to verify the proposed method. Discussion and conclusions are given in section V.

II. POSITION ESTIMATION WITH INDUCTANCE VECTOR COORDINATE

A. Principles of inductance vector in SRM

Figure 1 shows the typical inductance waveform in a four-phase 8/6 SRM, in which the aligned position is

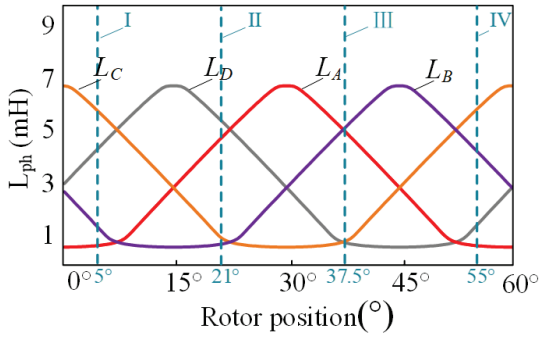

Fig. 1. Typical inductance profile for a four-phase 8/6 SRM.

defined as 30° and the unaligned position is defined as 0°. For an ideal SRM, phase inductances are periodic and symmetric with each other.

According to the symmetry between each phase inductance, a rectangular coordinate can be established. To take $\theta = 15°$ as an example, the relationships between the concerned four phase windings are illustrated as $L_A \sim L_D$ in Fig. 2. As shown in the figure, L_A, L_B, L_C, and L_D are represented by four vectors that differ by 90°. The modulus of each vector represents the actual corresponding phase inductance. According to the principle of vector summation, a rotating vector, which is marked as L_θ in Fig. 2, can be obtained by synthesizing all inductance vectors. The rotation trajectory of synthesized inductance vector, L_θ, is marked as a black dotted line in Fig. 2.

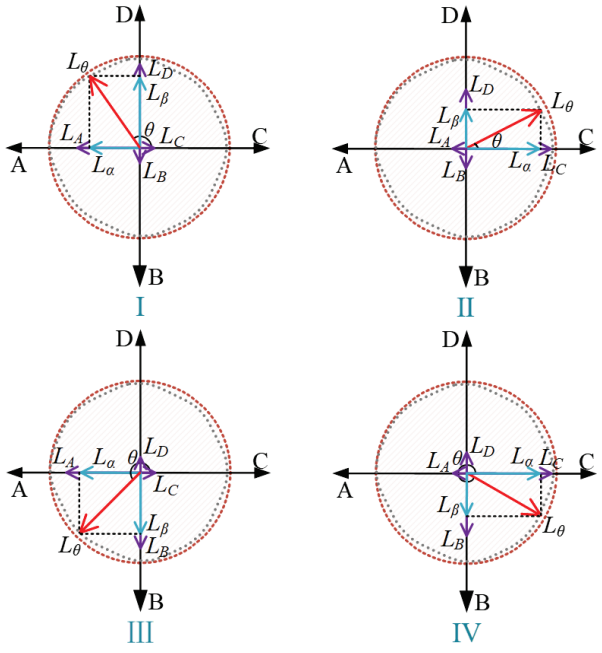

Fig. 2. Inductance vector coordinate system in SRM.

The relationship between synthesized inductance and four phase inductance vectors can be expressed as:

$$\begin{cases} L_\alpha = L_C - L_A \\ L_\beta = L_D - L_B \\ L_\theta = L_\alpha / \cos\theta = L_\beta / \sin\theta \end{cases}. \quad (1)$$

The x-axis inductance component, L_α, and the y-axis inductance component, L_β, can be calculated by:

$$\begin{cases} L_\alpha = L_\theta \sin\theta \\ L_\beta = L_\theta \cos\theta \end{cases}. \quad (2)$$

A standard circle trajectory, the radius of which equals to the difference between maximum phase inductance and minimum phase inductance, can be expressed as:

$$\begin{cases} x = r\sin\theta \\ y = r\cos\theta \end{cases}. \quad (3)$$

The circle trajectory is marked as a dotted orange line in Fig. 2. For steady operation, the trajectory of the synthesized inductance vector is closed to the trajectory of a standard cycle. Combing equations (1), (2), and (3), the trajectory of standard cycle and synthesized inductance vector are marked as a dotted gray line and a blue line in Fig. 3. Considering the magnetic saturation in SRM, the concerned two trajectories will not be perfectly matched but show good consistency.

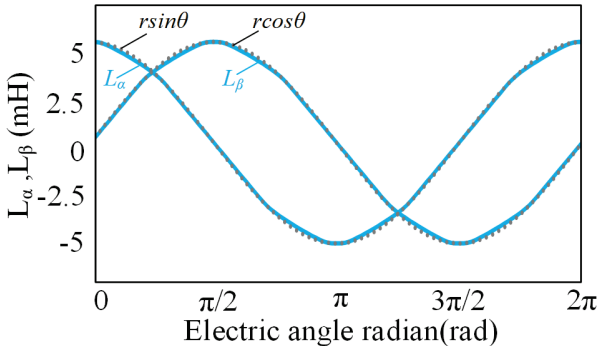

Fig. 3. Schematic of the x-axis component and y-axis component of synthesized inductance vector.

Combing the geometrical relationship in Fig. 2 with equation (1), the electric angle of synthesized inductance vector, θ_{arc}, can be expressed as:

$$\begin{cases} \theta_{arc} = \arctan\left(\frac{|L_\beta|}{|L_\alpha|}\right) & (0 < L_\alpha, 0 < L_\beta) \\ \theta_{arc} = \arctan\left(\frac{|L_\alpha|}{|L_\beta|}\right) + \frac{\pi}{2} & (0 > L_\alpha, 0 < L_\beta) \\ \theta_{arc} = \arctan\left(\frac{|L_\beta|}{|L_\alpha|}\right) + \pi & (0 > L_\alpha, 0 > L_\beta) \\ \theta_{arc} = \arctan\left(\frac{|L_\alpha|}{|L_\beta|}\right) + \frac{3\pi}{2} & (0 < L_\alpha, 0 > L_\beta) \end{cases}. \quad (4)$$

Then, the real-time rotor position of SRM can be thus obtained by:

$$\theta_r = \frac{180}{\pi}\frac{\theta_{arc}}{N_r}. \quad (5)$$

According to equations (4) and (5), the real-time rotor position of SRM can be obtained by detecting the electric angle of the synthesized inductance vector in the coordinate system.

B. Full period inductance estimation

In order to obtain inductance vectors, the inductance of each phase should be obtained for the full period. When SRM is driven by a traditional asymmetric half-bridge power converter, phase voltage can be expressed as:

$$\begin{cases} U_k = U_{DC} - i_k(R_k + 2R_{on\_state}) & \text{excitation mode} \\ U_k = -(R_k + R_{on\_state})i_k - U_{diode} & \text{zero-voltage mode} \\ U_k = -U_{DC} - i_k R_k - 2U_{diode} & \text{demagnetizing mode} \end{cases} \quad (6)$$

Flux-linkage at moment t can be calculated by:

$$\varphi_k = \int_{t_0}^{t} U_k(t)dt + \varphi_k(t_0). \quad (7)$$

When a digital processer is employed for SRM control, the flux-linkage in the nth sampling cycle can be obtained by:

$$\varphi_k(n) = \varphi_k(n-1) + U_k T_{ad}. \quad (8)$$

Since the digital processer shows high sampling frequency, rotor position can be assumed as constant between neighboring sampling cycles. Taking magnetic saturation into consideration, the inductance of each phase winding can be obtained by the digital controller as:

$$L_k(n)|_{\theta=\text{constant}} = \frac{\varphi_k(n) - \varphi_k(n-1)}{i_k(n) - i_k(n-1)}. \quad (9)$$

C. Rotor position estimation with asymmetry inductance

The inductance of each phase winding might be asymmetric because of machining accuracy or winding fault in the machine. In this condition, the asymmetry inductance brings large errors between estimated rotor position and actual rotor position.

Figure 4 shows the condition when the inductance of phase D is larger than the inductance of the other three phases. This might be caused by machining accuracy. In Fig. 4, θ''_{arc} represents estimated electrical angle estimated by increased phase inductance L''_k. Accordingly, the inductance at y-axis component will be changed from a dotted line to a solid line in Fig. 4 (a).

Since L_D is increased, we can obtain $L_\beta'' > L_\beta$ in Section I and II and $L_\beta'' < L_\beta$ in Section III and IV, as shown in Fig. 4 (b). Take Section I as an example. Since L_D is increased, the ideal electrical angle θ_{arc} and estimated electrical angle θ''_{arc} can be expressed as:

$$\theta_{arc} = \arctan\left(\frac{|L_\beta|}{|L_\alpha|}\right) \theta''_{arc} = \arctan\left(\frac{|L''_\beta|}{|L_\alpha|}\right). \quad (10)$$

It is clear that $\theta_{arc} < \theta''_{arc}$ and the estimated electrical angle is ahead of the ideal electrical angle. Thus, an

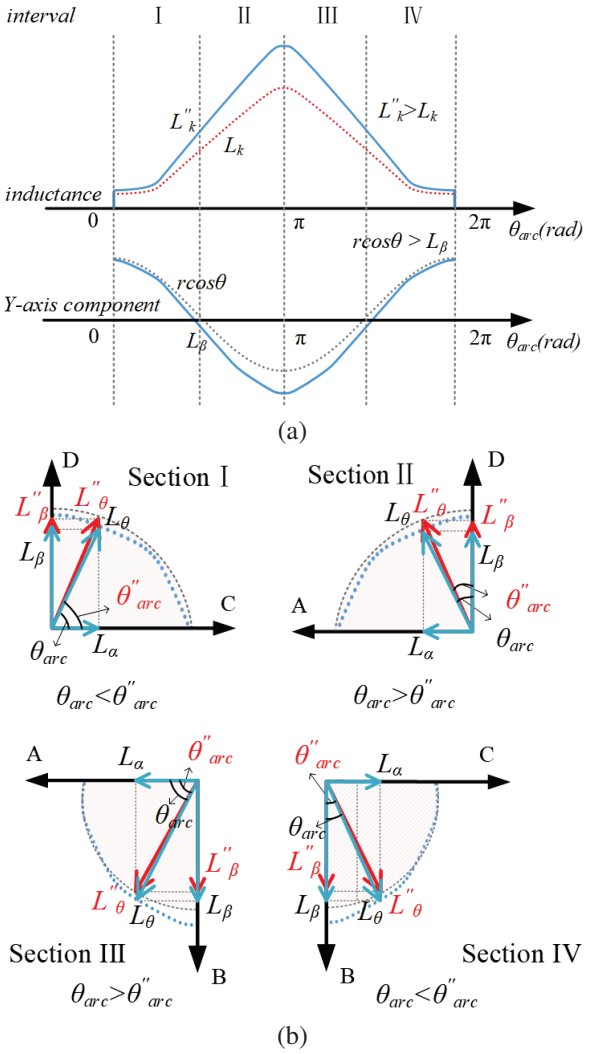

Fig. 4. Inductance vector under asymmetry inductance (L_D>$L_A = L_B = L_C$): (a) schematic of one phase inductance increase and (b) corresponding estimated error.

error would be obtained by equation (5) during the rotor position estimation process. A similar error can be also obtained when the inductance of phase D is smaller than the inductance of the other three phases.

Figures 5 (a) and (b) show the change of L_α and L_β when the inductance of phase D is increased and decreased, respectively. When L_D is increased, the trajectory of L_β would be changed from a dotted line to a solid line in Fig. 5 (a). When L_D is decreased, the trajectory of L_β would be changed from a dotted line to a solid line in Fig. 5 (b). Accordingly, the trajectory of the synthetic inductance vector of the two conditions can be expressed as dotted black lines in Figs. 5 (c) and (d). Obviously, the trajectory of the estimated synthetic inductance vector is deviated from the ideal trajectory, which brings significant rotor position estimation error.

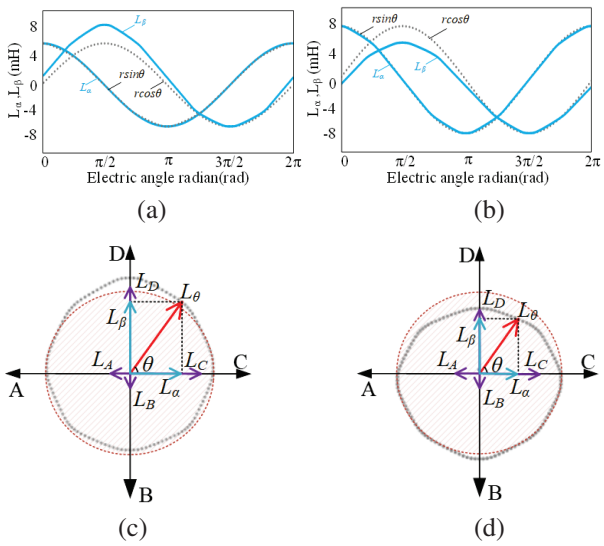

Fig. 5. Trajectory of the synthetic inductance vector under nonideal phase D inductance: (a) L_D is increased, (b) L_D is decreased, (c) L_D is increased, and (d) L_D is decreased.

For some more serious conditions, more than one phase inductance is nonideal in the machine. For example, L_D>L_A>$L_B = L_C$ and $L_B = L_C$>$L_D = L_A$. Figure 6 shows the estimated trajectory of key parameters during the rotor position process under these two conditions. It is clear that the accuracy of rotor position estimation will be further decreased

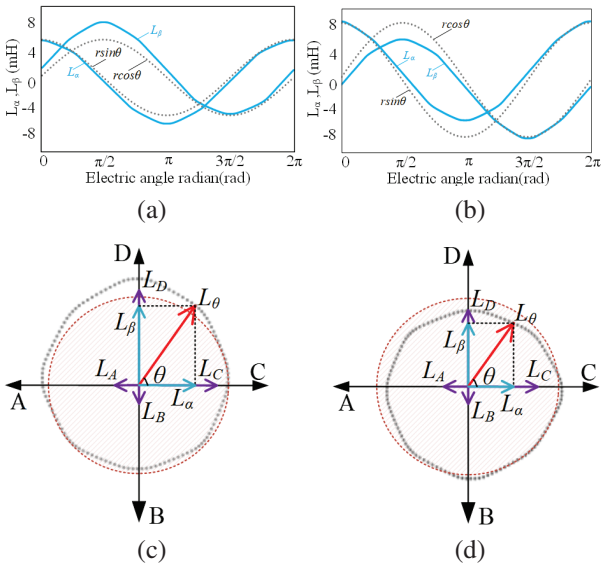

Fig. 6. Trajectory of synthetic inductance vector when more than one phase inductance is nonideal: (a) L_D>L_A>$L_B = L_C$, (b) $L_B = L_C$>$L_D = L_A$, (c) L_D>L_A>$L_B = L_C$, and (d) $L_B = L_C$>$L_D = L_A$.

D. Proposed rotor position estimation method with virtual inductance vector

Normally, if magnetic saturation is not considered, the trend of inductance change is approximately trapezoidal. As shown in Fig. 7, when the inductance of the motor is asymmetric, the inductance of the asymmetric phase still maintains a good trapezoidal law. The inductance of the other phases remains stable. Therefore, the symmetry between the inductances of each phase can be finally restored by analyzing and correcting the inductances of each phase separately.

According to the inductance characteristics of SRM, inductance can be divided into four intervals. As shown in Fig. 7, the inductance in the rising interval and falling interval are symmetrical to each other and have a good linear relationship with the rotor position. The inductance of the inductance minimum interval and maximum interval change less with the rotor position. In Fig. 7, assuming single-phase inductance is larger than others as an example, the solid blue line indicates the actual inductance of the deviated phase, the dashed gray line indicates the actual inductance of the non-deviated phase, and the dashed red line indicates the ideal inductance of the deviated phase. The asymmetry of inductance is mainly reflected in:

(i) Rotor misalignment interval: the minimum value of inductance of each winding is different, and the minimum value of the deviation phase is larger compared to the other winding.

(ii) Inductance increased interval and inductance decreased interval: the rising slope and falling slope of each winding are different, and the rising slope of the deviation phase is larger than the other winding.

(iii) Alignment interval: the maximum inductance has a deviation and the inductance of the deviation phase is larger than other phases in the alignment interval.

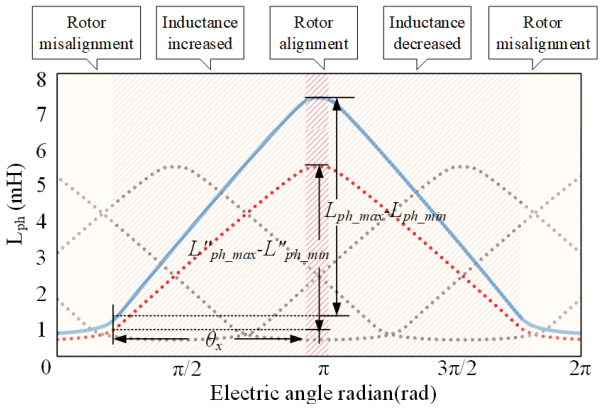

Fig. 7. SRM inductor ladder.

To reduce the error of the estimated position restored by estimated inductance directly under conditions of inductance asymmetry, a strategy was proposed to convert the estimated inductance in this paper, the structure of which is shown in Fig. 8. The estimated inductance is converted into a virtual inductance, and then we use the virtual inductance to construct a Cartesian coordinate system to restore the rotor position. The principle of inductance conversion is as follows:

Before the inductance deviates, the inductance curve is shown as the dotted line in Fig. 7. At this time, the slope of the inductance increased interval and inductance decreased interval can be expressed as:

$$K''_n = \pm(L''_{ph\_\max} - L''_{ph\_\min})/\theta_x. \tag{11}$$

After the inductance deviation, the maximum inductance, the minimum inductance, and the slope of inductance are changed. As shown in Fig. 9, the slope of the inductance increased interval and inductance decreased interval can be expressed as:

$$K_n = \pm(L_{ph\_\max} - L_{ph\_\min})/\theta_x, \tag{12}$$

where K''_n is the slope of actual inductance, K_n is the slope of ideal inductance, L''_{ph_max} is the maximum value of the actual inductance, L''_{ph_min} is the minimum value of the actual inductance, L_{ph_max} is the maximum value of the ideal inductance, L_{ph_min} is the minimum value of the ideal inductance, and θ_x is the mechanical angle spanned by the rising or decreasing interval.

From the above analysis, the inductance in different intervals can be expressed as:

$$\begin{cases} L_{ph} = L_{ph\_\min} & (\theta_{\min\_0} < \theta < \theta_{\min\_1}) \\ L_{ph} = K_n(\theta - \theta_{\min\_1}) + L_{ph\_\min} & (\theta_{\min\_1} < \theta < \theta_{\max\_0}) \\ L_{ph} = K_n(\theta_{\max\_0} - \theta_{\min\_1}) + L_{ph\_\min} & (\theta_{\max\_0} < \theta < \theta_{\max\_1}) \\ L_{ph} = K_n(60 - \theta_{\min\_1} - \theta) + L_{ph\_\min} & (\theta_{\max\_1} < \theta < \theta_{\min\_0}) \end{cases}, \tag{13}$$

where θ_{min_0} and θ_{max_0} are the rotor angle at the start position of the inductance minimum interval and the inductance maximum interval, respectively. θ_{min_1} and θ_{max_1} are the rotor angle at the end position of the inductance minimum interval and the inductance maximum interval, respectively.

As shown in equation (13), it can be seen that inductance asymmetry is mainly affected by maximum inductance and the slope of the inductance. Therefore, the minimum value of the estimated inductance of each winding can be first converted by:

$$L'_{ph\_0} = L_{ph} - L_{ph\_\min}. \tag{14}$$

Secondly, the slope of the estimated inductance in the linear region for each winding can be converted by:

$$L'_{ph\_1} = L_{ph\_0}/K_n. \tag{15}$$

According to equations (14) and (15), the total expression for inductive conversion can be expressed as:

$$L'_{ph} = \left(L_{ph} - L_{ph\_\min}\right)/K_n, \tag{16}$$

where L'_{ph_0}, L'_{ph_1}, and L'_{ph} are inductance after step 1, inductance after step 2, and the virtual inductance converted by estimated inductance.

The block diagram of the system for the virtual inductance calculation is shown in Fig. 8. The curve of virtual inductance is shown in Fig. 9. When the coordinate system is constructed with the virtual inductance vector, the trends of the x-axis component and y-axis component of the synthesized inductance vector are shown in Fig. 10. Among them, the solid blue line indicates the component before conversion, the solid red line indicates the component after conversion, and the dashed line indicates the component of the standard circle vector at different radii. The trajectory of the virtual synthesized inductance vector is shown in Fig. 11. The dashed red line indicates the motion trajectory of the virtual synthesized inductance vector shown as L'_θ, and the dashed orange line indicates the trajectory of the standard circle.

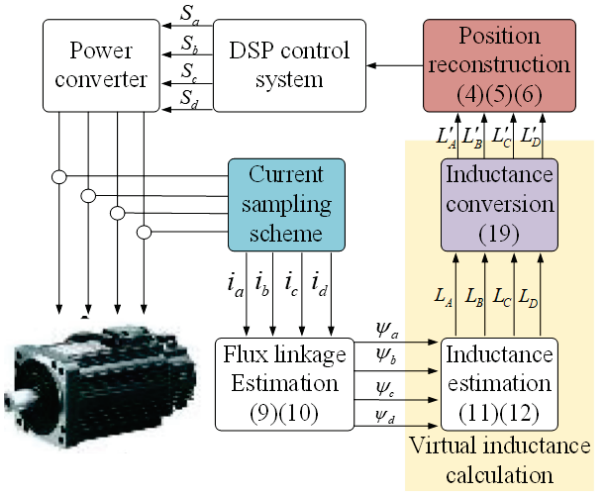

Fig. 8. Block diagram of the virtual inductance calculation.

In Fig. 9, it can be seen that the virtual inductance of each winding converted by estimated inductance has a good symmetry between the windings. The amplitude of the virtual inductance of each phase varies within 0∼1 mH. At the same time, the virtual inductance retains the original inductance characteristics. In Figs. 10 and 11, it can be seen that the components of the virtual synthesized inductance vector have a high degree of coincidence with the components of the standard circle vector. The motion trajectory of the virtual synthesized inductor vector is coincident with the trajectory of the standard circle. At this time, the error of estimated position restoration by using the virtual synthesized inductor vector will be reduced effectively.

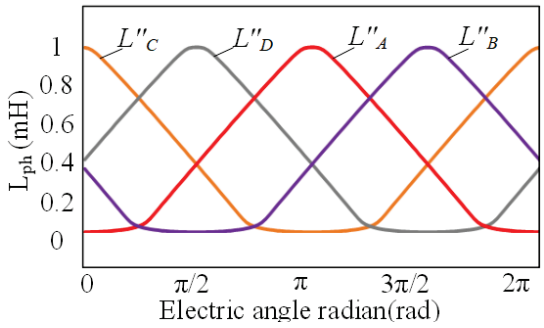

Fig. 9. Virtual inductance curves under asymmetric conditions.

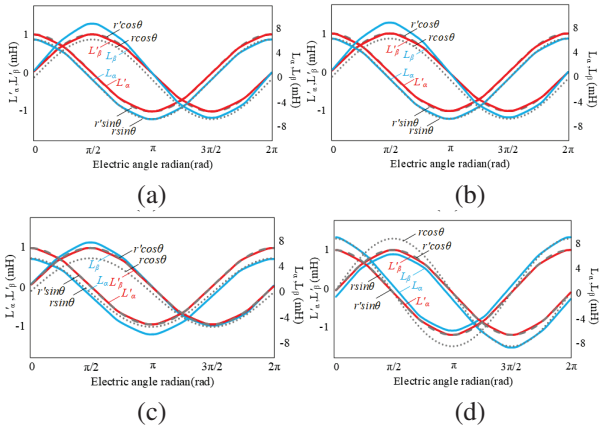

Fig. 10. Trends of L_α and L_β before and after asymmetric conversion of inductance: (a) single-phase inductance is larger, (b) single-phase inductance is smaller, (c) multi-phase inductance is larger, and (d) multi-phase inductance is smaller.

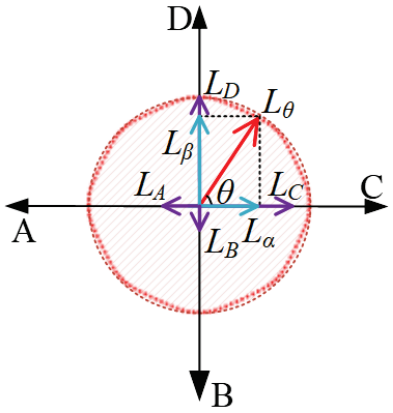

Fig. 11. Vector coordinate system before and after inductance conversion.

III. SIMULATION ANALYSIS

To verify the correctness of the theory, a simulation of four-phase 8/6 SRM was built on MATLAB/Simulink.

To verify the feasibility of the method by using the inductance vector to estimate the rotor position, we simulate the process of rotor position estimation based on estimated inductance under the condition of inductance symmetry. The turn-on angle is set to 3°, and the turn-off angle to 27°. The small current hysteresis bandwidth is 0.5∼1.5 A. The normal chopper current hysteresis bandwidth is 2.75∼3.25 A. The result is shown in Fig. 12.

In Fig. 12, it can be seen that, in the normal conduction interval, normal chopping is carried out in the winding. In the non-conduction interval, small current hysteresis chopping is carried out in the winding. The current in the winding is kept continuous in the full cycle. When the switching tube is on, the voltage is positive and the magnetic linkage rises. When the switching tube is off, the voltage is reversed and the magnetic linkage decreases. The magnetic linkage of the winding can be obtained by integrating the voltage of the winding in real time. The error between the estimated inductance and the actual inductance is small. The error between the estimated rotor position and the actual rotor position is within $\pm 1^{\circ}$.

To verify the effectiveness of the inductance correction strategy proposed in this paper under inductance asymmetry conditions, we simulate the position estimation process based on estimated inductance vectors and virtual inductance vectors, respectively. The simulation conditions are kept the same as above.

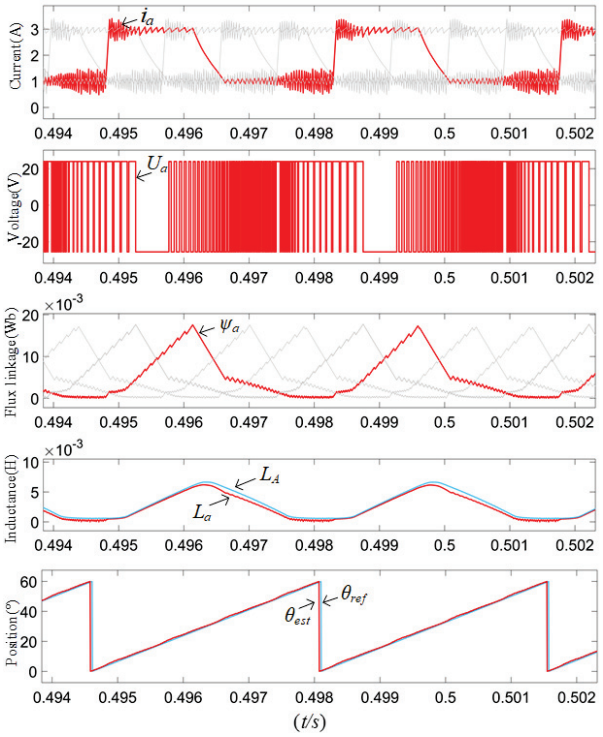

Fig. 12. Schematic simulation of position reconstruction based on estimated inductance.

First, let us take the D-phase as the deviation phase to simulate the single-phase inductance asymmetry of the motor. In Fig. 13, i_a, i_b, i_c, i_d are the phase currents; ψ_a, ψ_b, ψ_c, ψ_d are the magnetic linkage; L_A, L_B, L_C, L_D are the inductance of the windings; L'_A, L'_B, L'_C, L'_D are the virtual inductance of the windings; θ_{est} and θ_{ref} are the estimated rotor position and reference rotor position, respectively; θ_{err} is the error of estimated position before inductive correction; θ'_{err} is the error of estimated position after inductive correction.

In Fig. 13, it can be seen that under the condition of single-phase inductance asymmetry, it is still applicable to restore the rotor position by estimating inductance directly. Due to the obvious asymmetry between the estimated inductance of the deviated phase and the estimated inductance of the other phase, the error of the estimated position is increased compared with that under the condition of symmetry of inductance. As is shown in the left part of Fig. 13 (a), before correcting the inductance, the actual inductance of the deviated phase in increased interval and decreased interval is larger than its ideal inductance, which leads to the y-axis component of the synthesized inductance being smaller. Therefore, there is a significant error in the estimated position. At this time, the maximum error reaches 3°. After correcting the inductance, as is shown in the right part of Fig. 13 (a), the virtual inductance of each phase has good symme-

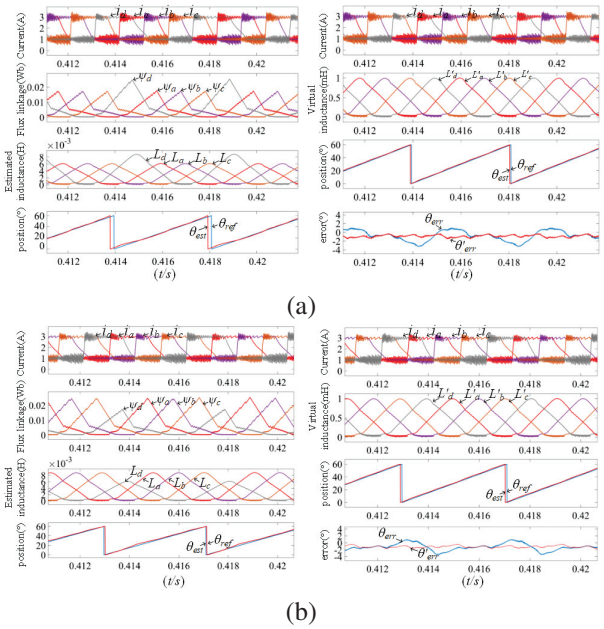

Fig. 13. Schematic simulation of single-phase inductive asymmetry: (a) single-phase inductance is larger and (b) single-phase inductance is smaller.

try. The maximum error and fluctuation are reduced. The error is within ±1.5°. Under the condition that D-phase inductance is smaller, as shown in Fig. 13 (b), the actual inductance of the deviating phases in increased interval and decreased interval are smaller than the ideal inductance, which leads to the y-axis component of the synthesized inductance vector being larger than other. Maximum error reaches 3°, but maximum error and fluctuation are reduced after inductance correction. The error is within ±1.5°.

We then take the A and D phases as the deviation phases to simulate the multi-phase inductance asymmetry of the motor. The simulation results are shown in Fig. 14.

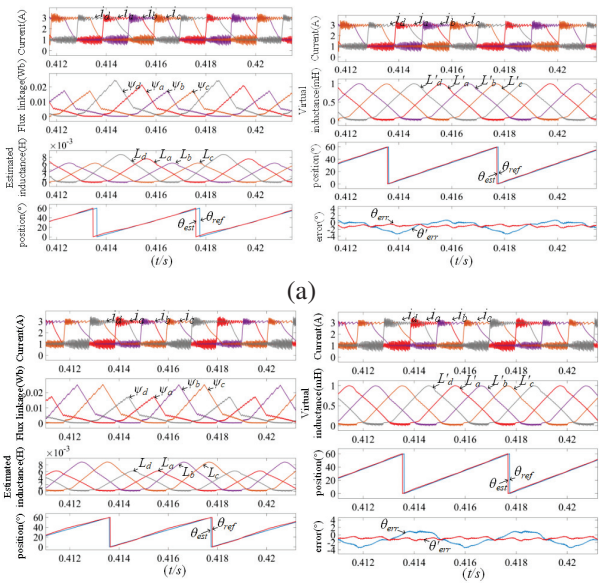

(a)

(b)

Fig. 14. Schematic simulation of multi-phase inductive asymmetry condition: (a) multi-phase inductance is larger and (b) multi-phase inductance is smaller.

In Fig. 14, it is clear that under the condition of multiphase inductance asymmetry, the error of the estimated position is very obvious. As shown in Fig. 14 (a), the inductance of the A-phase and D-phase are deviated, and the deviation of the D-phase is more obvious. The results of the estimated position in different intervals all have a large error before inductance conversion. In Fig. 14 (b), the inductance of A-phase and D-phase has the same degree of deviation. The results of the estimated position in different intervals also have a large error before inductance conversion. After correcting the inductances, the maximum error and fluctuation are reduced. The error is within ±1.5°.

IV. EXPERIMENTAL ANALYSIS

In order to validate the feasibility of the strategy, some experiments were carried out on a four-phase 8/6 structure SRM. A photograph of the experimental platform is shown in Fig. 15. The parameters of the motor are listed in Table 1.

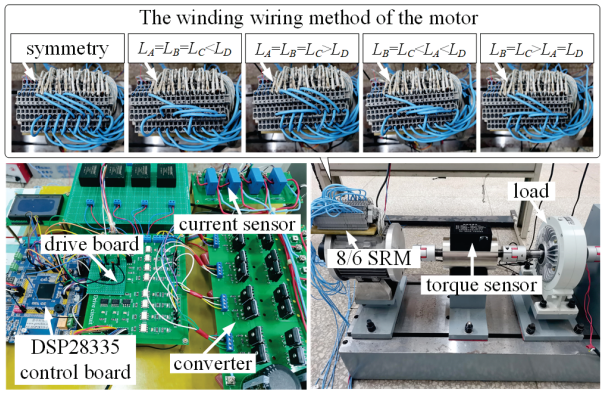

Fig. 15. Experimental platform.

Table 1: Parameters of the sample machine

Parameters	Value
Pitch of stator tooth (mm)	11.6
Pitch of rotor tooth (mm)	12.8
Rated voltage (V)	24
Rated power (W)	200
Rated speed (r/min)	2000
Number of stators	8
Number of rotors	6
Number of turns per pole	35

First, in order to verify the validity of the sensorless position estimation strategy based on estimated inductance, an experiment was conducted under the condition of the symmetrical inductance of the four-phase windings of an 8/6 SRM. Figure 16 shows the result at 1600 r/min.

In Fig. 16, it can be seen that the current is chopped normally in the conduction interval. A small current is injected in the non-conduction interval. The current is continuous in the full cycle. The magnetic linkage is obtained by voltage. The inductance obtained by the magnetic linkage and the current can be continuous in the full cycle, and it shows good mapping with the rotor position. Under the condition of symmetrical inductance, the rotor position can be estimated directly by estimated inductance. The error between the estimated position and the actual position is small. The error is within 2.8°.

We can now verify the effectiveness of virtual inductance in terms of decreasing the error of estimated

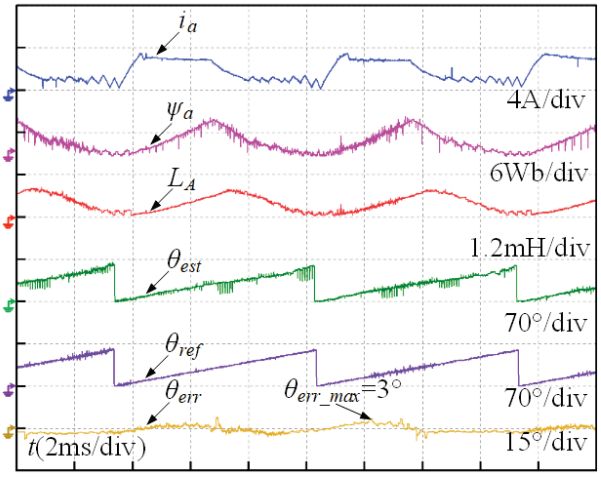

Fig. 16. Position estimation based on estimated inductance.

position in the case of inductance asymmetry. First, take the D-phase as the deviation phase and change the winding wiring (the number of turns in each pole of the D-phase is 35 turns, with the total number of turns being 70 turns, and each pole of the remaining phases of the windings is reduced to 30 turns, with the total number of turns being 60 turns). The motor speed is set to 1600 r/min, the turn-on angle is 3°, the turn-off angle is 27°, the small current hysteresis bandwidth is 0.5∼1.5 A, and the normal chopper current hysteresis bandwidth is 2.75∼3.25 A. The results are given in Fig. 17.

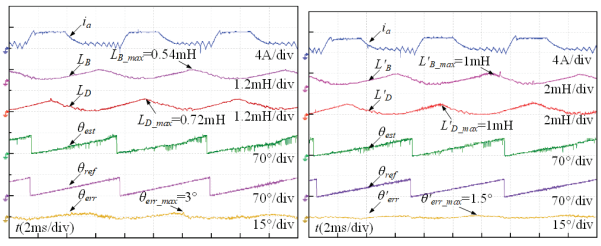

(a) (b)

Fig. 17. Position estimate experiment under the condition of single-phase inductance is larger: (a) before and (b) after.

Figure 17 (a) shows that the rotor position can be estimated directly through the estimated inductance. There is an obvious asymmetry between the inductance of the deviation phase and the inductance of the normal phase. The maximum inductance of the deviation phase is 0.72 mH, and the maximum inductance of the remaining phases is 0.54 mH. The error of estimated position increases significantly compared with that under the inductance symmetry condition. The maximum error is about 3°. Figure 17 (b) shows that the maximum value of the virtual inductance is 1 mH, and the maximum error of the estimated position is reduced to 1.5° after inductance correction. Using virtual inductance vectors to reduce the error of estimated position is effective.

We then changed the winding writing so that the inductance of the D-phase is smaller than the other phases (each pole of the D-phase is 30 turns, with a total of 60 turns, and each pole of the remaining phases is 35 turns, with a total of 70 turns) and the other operating parameters remained. The results of the experiment are given in Fig. 18.

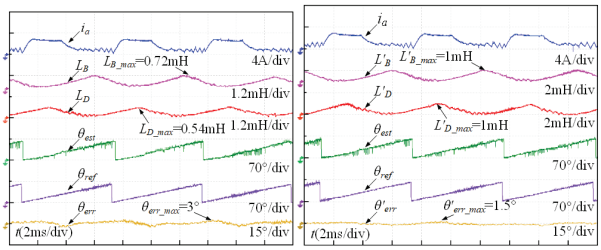

(a) (b)

Fig. 18. Position estimate experiment under the condition of single-phase inductance being smaller: (a) before and (b) after.

Figure 18 (a) shows that the maximum inductance of the deviating phase is 0.54 mH, and the maximum inductance of the remaining phases is 0.72 mH under the condition of single-phase inductance being smaller than others. The maximum error is 3°. Figure 18 (b) shows that the maximum value of the virtual inductance of each winding is 1 mH after inductance correction. The maximum error is similarly reduced to 1.5°.

In order to further verify the effectiveness of the strategy in the case of multiphase inductance asymmetry, the experiment was conducted under the condition of multiphase inductance asymmetry by taking A-phase and D-phase as the deviation phases and changing the winding wiring. (One of the poles of the A-phase is 35 turns, another pole is 30 turns, and the total number is 65 turns. Each pole of the D-phase is 35 turns, the total number is 70 turns. Each pole of the rest of the phase is 30 turns, the total number is 60 turns.) Other operating parameters remained the same. The results are given in Fig. 19.

In Fig. 19 (a), it can be seen that the maximum inductance of the deviated A-phase and deviated D-phase is 0.64 mH and 0.72 mH, respectively, and the maximum inductance of the rest phases is 0.54 mH. The symmetry between the inductances is reduced. The maximum error of the estimated position is about 2.7°. In Fig. 19 (b), it can be seen that the symmetry between the inductances of each phase is improved after the

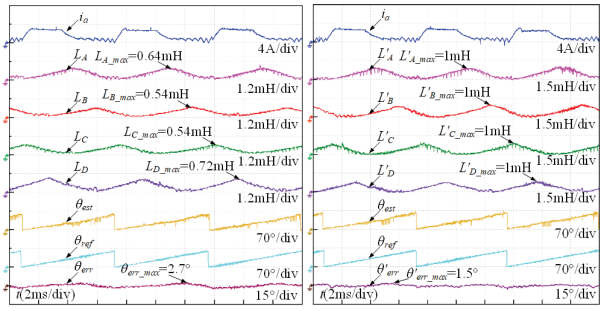

(a) (b)

Fig. 19. Position estimate experiment under the condition of multi-phase inductance being larger: (a) before and (b) after.

inductance correction, and the maximum error of the estimated position is reduced to 1.5°.

We then changed the winding wiring so that the inductance of the A-phase and D-phase decreased at the same time (each pole of the A-phase and D-phase is 30 turns, the total number is 60 turns; each pole of the rest of the phases is 35 turns, the total number is 70 turns). Other operating parameters remained the same. The results are given in Fig. 20.

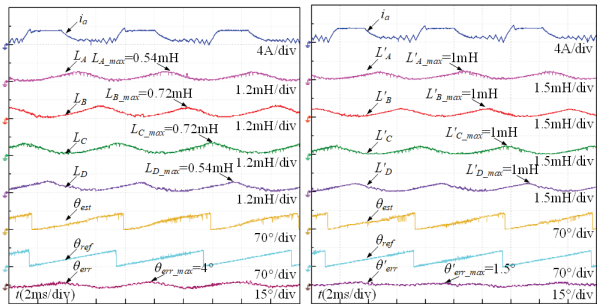

(a) (b)

Fig. 20. Position estimate experiment under the condition of multi-phase inductance being smaller: (a) before and (b) after.

In Fig. 20 (a), it can be seen that the maximum inductance of the deviated A-phase and deviated D-phase is 0.54 mH, and the maximum inductance of the remaining phases is 0.72 mH. The symmetry between the inductances of the phases is low. The maximum error between the estimated position and the actual position is about 4°. Figure 20 (b) shows that the symmetry between the inductances of each phase is improved after the inductance correction. The maximum error of the estimated position is 1.5°.

It can be concluded from the above experiments, under the condition of inductive asymmetry, there is an obvious difference in the inductance amplitude between the normal phase and the deviation phase. The symmetry between the phase inductances is low. After correction of the estimated inductances, the amplitude of the virtual inductance is between 0 mH and 1 mH. There is good symmetry between the virtual inductances of each phase. Under the condition of inductance asymmetry, the error of the estimated position restored by estimated inductance directly is relatively large. Maximum error and fluctuation are reduced after inductance correction. The experiments verified the effectiveness of the inductance correction strategy proposed in this paper.

V. CONCLUSION

This paper focuses on sensorless position estimation under conditions of inductance asymmetry and proposes a position estimation method based on virtual inductance vectors. The research results show that:

(i) The proposed strategy is not limited by the motor structure and parameters, and can be used for SRM with other phases or parameters.

(ii) The proposed strategy uses the full-cycle inductance estimated in real time as an indirect basis for position estimation, which is not limited by the speed range of the motor, and it is suitable for sensorless position estimation over a wide speed range.

(iii) A strategy for inductance conversion under asymmetric inductance conditions is proposed in this article. The error of the estimated position is effectively reduced by using the virtual inductance to restore the rotor position under asymmetric inductance conditions.

ACKNOWLEDGEMENT

This work was supported by the Qing Lan Project (2024-2) and Jiangsu Province Universities' Basic Science (Natural Science) Research Major Project (24KJA510001).

REFERENCES

[1] S. Ullah, S. P. McDonald, R. Martin, M. Benarous, and G. J. Atkinson, "A permanent magnet assist, segmented rotor, switched reluctance drive for fault-tolerant aerospace applications," *IEEE Trans. Ind. Appl*, vol. 55, no. 1, pp. 298-305, Jan./Feb. 2019.

[2] J. Borg Bartolo, M. Degano, J. Espina, and C. Gerada, "Design and initial testing of a high-speed 45-kW switched reluctance drive for aerospace application," *IEEE Trans. Ind. Electron,* vol. 64, no. 2, pp. 988-997, Feb. 2017.

[3] X. Sun, K. Diao, G. Lei, Y. Guo, and J. Zhu, "Study on segmented-rotor switched reluctance

motors with different rotor pole numbers for BSG system of hybrid electric vehicles," *IEEE Trans. Veh. Technol,* vol. 68, no. 6, pp. 5537-5547, June 2019.

[4] W. Yan, H. Chen, S. Liao, Y. Liu, and H. Cheng, "Design of a low-ripple double-modular-stator switched reluctance machine for electric vehicle applications," *IEEE Transactions on Transportation Electrification,* vol. 7, no. 3, pp. 1349-1358, Sep. 2021.

[5] C. Gan, Q. Sun, J. Wu, W. Kong, C. Shi, and Y. Hu, "MMC-based SRM drives with decentralized battery energy storage system for hybrid electric vehicles," *IEEE Trans. Power Electron.,* vol. 34, no. 3, pp. 2608-2621, Mar. 2019.

[6] F. Yi and W. Cai, "Modeling, control, and seamless transition of the bidirectional battery-driven switched reluctance motor/generator drive based on integrated multiport power converter for electric vehicle applications," *IEEE Trans. Power Electron.,* vol. 31, no. 10, pp. 7099-7111, Oct. 2016.

[7] E. Bostanci, M. Moallem, A. Parsapour, and B. Fahimi, "Opportunities and challenges of switched reluctance motor drives for electric propulsion: A comparative study," *IEEE Trans. Transp. Electric.,* vol. 3, no. 1, pp. 58-75, Mar. 2017.

[8] N. Yan, X. Cao, and Z. Deng, "Direct torque control for switched reluctance motor to obtain high torque-ampere ratio," *IEEE Trans. Ind. Electron.,* vol. 66, no. 7, pp. 5144-5152, July 2019.

[9] Z. Yu, C. Gan, Y. Chen, and R. Qu, "DC-biased sinusoidal current excited switched reluctance motor drives based on flux modulation principle," *IEEE Trans. Power Electron.,* vol. 35, no. 10, pp. 10614-10628, Oct. 2020.

[10] D. Zhou, H. Chen, X. Wang, V. F. Pires, and J. Martins, "Synthetic sensorless control scheme for full-speed range of switched reluctance machine drives with fault-tolerant capability," *IEEE Transactions on Transportation Electrification,* vol. 8, no. 4, pp. 4456-4469, Dec. 2022.

[11] A. D. Cheok and N. Ertugrul, "High robustness and reliability of fuzzy logic-based position estimation for sensorless switched reluctance motor drives," *IEEE Trans. Power Electron.,* vol. 15, no. 2, pp. 319-334, Mar. 2000.

[12] Y. Cai, Y. Wang, H. Xu, S. Sun, C. Wang, and L. Sun, "Research on rotor position model for switched reluctance motor using neural network," *IEEE/ASME Trans. Mechatronics,* vol. 23, no. 6, pp. 2762-2773, Dec. 2018.

[13] W. Ding and K. Song, "Position sensorless control of switched reluctance motors using reference and virtual flux linkage with the one-phase current sensor in medium and high speed," *IEEE Trans. Ind. Electron.,* vol. 67, no. 4, pp. 2595-2606, Apr. 2020.

[14] Y. Liang and H. Chen, "Circuit-based flux linkage measurement method with the automated resistance correction for SRM sensorless position control," *IET Electr. Power Appl.,* vol. 12, no. 9, pp. 1396-1406, Nov. 2018.

[15] C. J. Bateman, B. C. Mecrow, A. C. Clothier, P. P. Acarnley, and N. D. Tuftnell, "Sensorless operation of an ultra-high-speed switched reluctance machine," *IEEE Trans. Ind. Appl.,* vol. 46, no. 6, pp. 2329-2337, Nov./Dec. 2010.

[16] J. Cai, Z. Liu, and Y. Zeng, "Aligned position estimation-based fault-tolerant sensorless control strategy for SRM drives," *IEEE Trans. Power Electron.,* vol. 34, no. 8, pp. 7754-7762, Aug. 2019.

[17] Jie Shao and Zhiquan Deng, "Sensorless control of switched reluctance motor based on current waveform detection," *Electric Power Components & Systems,* vol. 49, no. 13-14, pp. 1-10, 2022.

[18] T. Bamba, A. Komatsuzaki, and I. Miki, "Estimation of rotor position for switched reluctance motor at standstill," in *Proc. Power Convers. Conf.*, pp. 259-263, 2007.

[19] J. Kim and R. Kim, "Online sensorless position estimation for switched reluctance motors using characteristics of overlap position based on inductance profile," *IET Electr. Power Appl.,* vol. 13, no. 4, pp. 456-462, Apr. 2019.

[20] J. Cai and Z. Deng, "Sensorless control of switched reluctance motor based on phase inductance vectors," *IEEE Transactions on Power Electronics,* vol. 27, no. 7, pp. 3410-3423, July 2012.

Kai Liu received the B.S. degree in electrical engineering and automation and M.S. degree in electrical engineering from China University of Mining and Technology, in June 2011 and June 2014, respectively. From September 2014 to May 2017, Liu worked as a teaching assistant at Changzhou Vocational Institute of Mechatronic Technology, and from June 2017 to present, as lecturer and professional leader at Changzhou Vocational Institute of Mechatronic Technology. His main interests include switched reluctance machines, machine vision, robotic application.

Zongwen Jiang received the M.S degree in Nanchang University. His research focuses on motors and their control, and he currently works at Zoomlion Agriculture Machinery Co. Ltd. He is engaged in the research of electrical systems for dryers.

Qing Wang received the B.S. degree in automation from Northeastern University, Shenyang, China, in 2011, and the Ph.D. degree in electrical engineering from China University of Mining and Technology, Xuzhou, China, in 2017. In 2018, he was a Lecturer with the School of Information Engineering, Nanchang University, Nanchang, China, where he has been an Associate Professor since 2023. His research interests include electric vehicles, electrical motor drives, renewable energy generations, and micro-grids.

Jiangtao Hu received the B.S. degree in electrical engineering from Jiangxi University of Science and Technology, Ganzhou, China, in 2023. He is currently working toward the M.S. degree at the School of Information Engineering, Nanchang University, Nanchang, China. His research interests include power electronics and motor control.

Influence of Pole Pitch Ratio on Performance of Segmented-stator Tubular Flux Switching Permanent Magnet Linear Generator

Rui Nie, Hao Zhang, Yifei Jia, Guozhen Zhang, Zhongwen Li, Jikai Si, and Jing Liang

School of Electrical and Information Engineering
Zhengzhou University, Zhengzhou 450001, China
nierui@zzu.edu.cn, zhanghao0405@gs.zzu.edu.cn, jiayifei2023@gs.zzu.edu.cn,
zhanggz18312@126.com, lzw@zzu.edu.cn, sijikai@zzu.edu.cn, liangjing@zzu.edu.cn

Abstract **–** Tubular Flux-Switching Permanent Magnet Linear Generator (TFSPMLG) has high winding utilization and no radial force, which is one of the most competitive generators in direct-drive wave energy conversion system. In this paper, a Segmented-Stator TFSPMLG (SS-TFSPMLG) is proposed to solve the problems of large detent force and three-phase unbalance of TFSPMLG, and the influence of different pole pitch ratios on performance is researched for judging a proper topology for the SS-TFSPMLG. First, its topology and operation mechanism are analyzed to prove the feasibility of the generator. Second, the structural parameters of 12-slot SS-TFSPMLG with four different pole pitch ratios are calculated, and the corresponding winding arrangement is determined. The electromagnetic performances of the SS-TFSPMLG with four different pole pitch ratios are simulated and compared, including static characteristics and output characteristics. Finally, the SS-TFSPMLG topology suitable for wave power generation is determined, which lays an important foundation for the follow-up study of SS-TFSPMLG.

Index Terms **–** Detent force, electromagnetic design, performance analysis, pole pitch ratio, segmented-stator, tubular flux-switching permanent magnet linear generator.

I. INTRODUCTION

With the development of social economy and the aggravation of the energy crisis, the exploration and utilization of renewable energy has attracted more and more attention [1]. China has a extensive sea area and abundant marine energy. Among them, wave energy has large reserves, high energy density and good predictability, and has broad development and application prospects [2]. Compared with other forms of wave power generation systems [3, 4], the direct-drive wave power generation system has no intermediate energy conversion device, which simplifies the system structure and improves the operating efficiency. It has been widely used in the development and utilization of wave energy [5, 6]. In direct-drive wave power generation, linear generators with high power density, high operating efficiency and low detent force have always been our research goals.

Recently, the research on linear generators for the wave energy conversion system mainly focuses on permanent magnet synchronous linear generators, flux-switching permanent magnet linear generators and switched reluctance linear generators. Among them, the Flux-Switching Permanent Magnet Linear Generator (FSPMLG) with simple structure, high robustness and strong thermal stability significantly improves the reliability of the wave energy conversion system. The permanent magnet and armature coils of the FSPMLG are installed on the stator, and the mover is only composed of iron core, which avoids the irreversible demagnetization of the permanent magnet and mechanical damage. At the same time, it has high force density and efficiency [7], which combine the structural merits of a switched reluctance generator [8, 9] and the performance features of a permanent magnet synchronous linear generator. It is considered to be one of the most promising generators for wave energy conversion systems [10].

Reference [11] proposed a quadrilateral FSPMLG for wave energy collection. The generator is composed of four FSPMLGs, and its unilateral FSPMLG is shown in Fig. 1. Each phase of the stator has two U-shaped iron cores. Permanent magnets are embedded between the two U-shaped iron cores. The coils are wound in the corresponding iron core slots. The stators of each phase

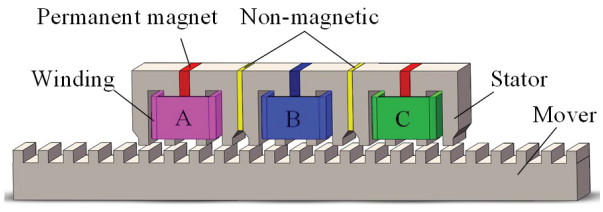

Fig. 1. Configuration of the FSPMLG.

Submitted On: December 31, 2024
Accepted On: May 29, 2025

https://doi.org/10.13052/2025.ACES.J.400914

are separated by non-magnetic materials, and the mover is composed only of iron cores. The proposed FSPMLG has the advantages of simple structure, excellent voltage waveform, small cogging effect and high efficiency, which is suitable for the application of wave energy conversion.

To reduce the weight of the mover and broaden the application of FSPMLG, [12] proposed a split translator secondary stator FSPMLG. The stator is divided into main stator and supporting stator. The main stator is located outside the mover, which is the same as the traditional flux switching generator. The supporting stator composed of iron core is located inside the mover, which is used to improve the flux linkage of the main stator. The cogging force and force ripples are minimized by proper cascading of main and supporting stators to avoid mechanical design complexity. Benefiting from the lighter weight and higher peak speed of the mover, more power can be generated and efficiency is higher.

However, the generators in [11, 12] are all composed of a mover and a different number of single-sided stators with end windings, which increases the amount of copper used. The copper consumption of the generator reduces power generation efficiency and increases temperature rise, which has an adverse effect on the performance of the generator. Tubular linear generators of different structures are proposed in [13, 14]. The tubular structure does not have end windings, which increases the winding utilization rate and eliminates the transverse edge effect. Moreover, the tubular structure is symmetrical and does not have radial suction. By combining the advantages of a Tubular Linear generator and a Flux-Switching generator, [7, 15] proposed the Tubular Flux-Switching Permanent Magnet Linear Generator (TFSPMLG). This type of generator not only has no end windings but also has high thrust density and efficiency. Furthermore, the double convex structure has a concentrated magnetic effect which can provide higher power.

Nevertheless, this kind of cylindrical flux switching generator has the problem of high detent force caused by the end effect of the linear generator [16–18]. Excessive detent force will lead to increased vibration, noise and poor accuracy of the generator. Moreover, it can be seen from the TFSPMLG winding layout that there are side-end phases and intermediate phases in the generator winding, which leads to instability of the three-phase parameters, which in turn affects the output performance of the generator [19, 20]. Therefore, it is necessary to reduce the detent force and weaken the influence of three-phase parameter imbalance on TFSPMLG.

The relationship between different pole pitch ratios and electromagnetic performance of a high temperature superconducting flux switching linear motor is studied in [21]. By comparing the advantages and disadvantages of different pole pitch ratios, the structural parameters of the switched flux linear motor which is most suitable for urban rail transit are obtained. In this paper, the relationship between polar distance ratio and SS-TFSPMLG is also studied in order to find a more suitable structural parameter for direct-drive wave power generation.

Targeting the problems existing in the TFSPMLG, this paper innovatively proposes a SS-TFSPMLG structure. The main contents of this paper are as follows. Firstly, the basic topology and working principle of SS-TFSPMLG are described, and the winding layout design is explained in detail. Secondly, the influence of mover tooth width and end tooth width on the detent force of the generator is analyzed to determine the optimal auxiliary tooth width and mover tooth width. Finally, the static characteristics and output characteristics of four SS-TFSPMLGs with different pole pitch ratios are compared and analyzed to select different structural topologies to deal with different application scenarios.

II. THE SS-TFSPML GENERATOR

A traditional 12-slot 14-pole (12s/14p) TFSPMLG topology is shown in Fig. 2. It uses a short stator and a long mover structure. Both the permanent magnet and the armature winding are located in the stator. The permanent magnet is magnetized along the axial direction and clamped between the stator U-shaped cores. The armature winding is different from the rotating generator and the flat linear generator, and the annular structure is wound in the stator slot. In addition, the structure adds two auxiliary teeth to the stator end to weaken the influence of the end effect.

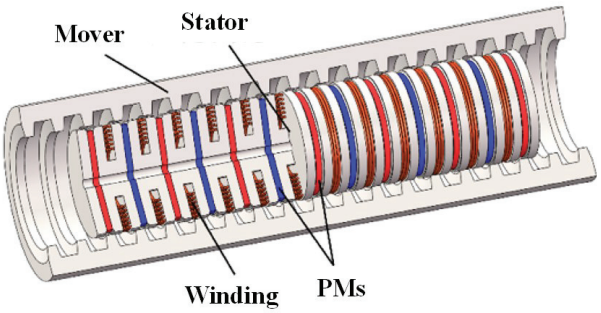

Fig. 2. Configuration of the TFSPMLG.

A. Topology of the SS-TFSPMLG

To weaken the detent force and balance the interphase characteristics, a Segmented-Stator Tubular Flux-Switching Permanent Magnet Linear (SS-TFSPML) Generator with 12 stator slots is proposed, as shown in Fig. 3. Different from the conventional TFSPML machines, the stator of the SS-TFSPMLG is split into three segments and each segment incorporates permanent magnets (PMs), windings and stator core. There is a

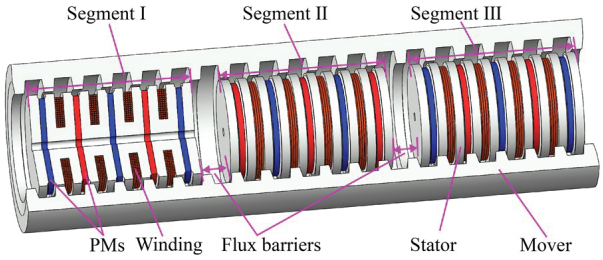

Fig. 3. Configuration of the SS-TFSPMLG.

flux barrier between adjacent segmented-stators. Thereinto, PMs with opposite magnetization are sandwiched between dumbbell-shaped iron core, which are wound by toroidal-shaped coils. The mover consists only of iron core.

B. Design procession

The structure of 12s/14p SS-TFSPMLG in axial and radial (RZ) coordinate is shown in Fig. 4 and the dimensions are shown in Fig. 5.

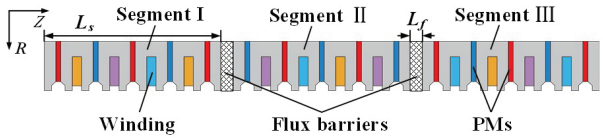

Fig. 4. Structure of 12s/14p SS-TFSPMLG in RZ coordinate.

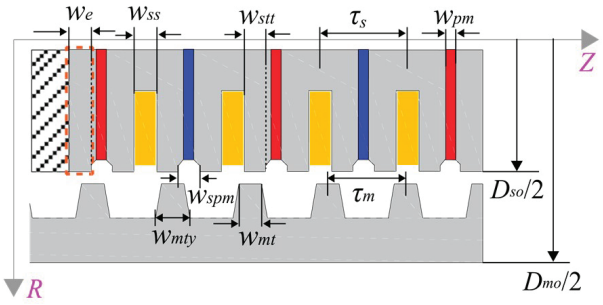

Fig. 5. Dimensions of 12s/14p SS-TFSPMLG in RZ coordinate.

Evolved from TFSPMLG, SS-TFSPMLG only needs to change the stator and winding layout; electromagnetic parameters such as PM thickness and slot width are the same as TFSPMLG.

Assuming that the segments of the stator do not affect each other [22], the detent force of the whole generator is the sum of the detent forces of three segments. In order to minimize the detent force of the whole generator, the phase difference of the detent force among three segments should be 120°. As has been shown in [23], the detent force fluctuates periodically with one pole pitch, so the distance between the segments should meet

$$L_s + L_f = \frac{3k \pm 1}{3}\tau_{\mathrm{m}}. \tag{1}$$

L_s and L_f are the axial length of the segment and the flux barrier, respectively, τ_m is the polar distance of the mover and k is an arbitrary positive integer.

For linear generators, the pole pitch ratio of the generator has a great influence on the performance of the generator. In this paper, the SS-TFSPMLG with primary/secondary slot/pole combinations τ_s/τ_m of 10/12, 11/12, 13/12 and 14/12 are comparatively analyzed.

C. Windings configuration

Different from a permanent magnet synchronous linear generator, whose pole distance of two mover corresponds to an electric cycle, one mover pole distance of the FSPMLG corresponds to an electric cycle. According to equation (1), the phase difference of SS-TFSPMLG between the unit stators is 120°. Therefore, the end slots of each stator segment correspond to different phases, and the six end parts belong to three-phase respectively, so that the number of coils at the end of each phase is the same and the three-phase windings are symmetrical in space. Due to the symmetry of the winding, the end effect is balanced with each other, which reduces the influence of the end effect and reduces the detent force. It is worth noting that in order to weaken the influence between the stator segments, the magnetization directions of the permanent magnets on both sides of the flux barrier are opposite, which leads to a three-phase difference. To balance the above difference, the coil winding direction of the unit stator II is opposite to that of the unit stators I and III. At this point, the topology of a three-phase SS-TFSPMLG is obtained, which effectively solves the problem of large detent force and three-phase unbalance of TFSPMLG.

Taking the 12s/14p SS-TFSPMLG shown in Fig. 4 as an example, the axial length L_s of the unit stator is $49\tau_m/9$ mm. According to equation (1), the length L_f of the flux barrier is selected as $11\tau_m/9$ mm (k=7). Compared with TFSPMLG, since the flux barrier occupies a certain electrical angle, there is a phase difference between the coils of the unit stator. Therefore, it is necessary to redetermine the connection sequence of the winding coils in each unit stator to obtain the maximum electrical potential.

According to the calculation method of the slot pitch angle of the SS-TFSPMLG structure proposed in [24] and the calculation method of the phase difference between the unit stators in equation (2), the slot potential vector star diagrams of SS-TFSPMLG with pole

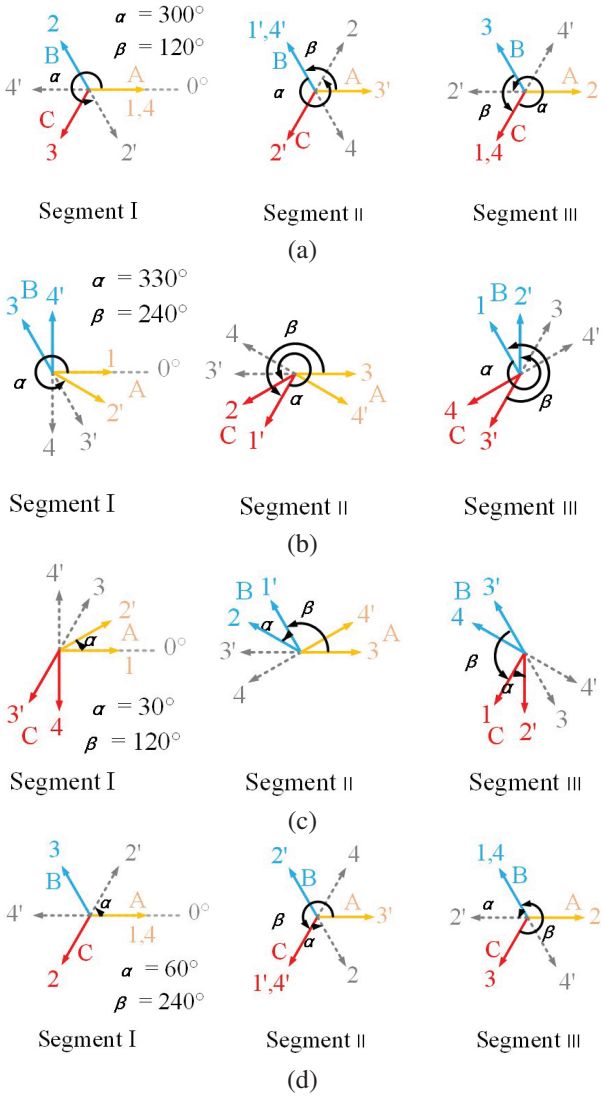

Fig. 6. Star diagram of slot voltage vector of SS-TFSPMLG with pole-to-pitch ratio of (a) 10/12, (b) 11/12, (c) 13/12 and (d) 14/12.

pitch ratios of 10/12, 11/12, 13/12 and 14/12 are shown in Fig. 6.

$$\beta = \frac{L_s + L_f}{\tau_m} \times 360. \tag{2}$$

β is the phase difference between the unit stators.

It can be seen from the star diagrams of the slot potential vector in Fig. 6 that each phase of the four SS-TFSPMLGs with different pole pitch ratios is composed of four coils, two of which are end coils and two are internal coils. The three-phase windings are symmetrically distributed in space. In addition, it can be seen that the SS-TFSPMLG with pole pitch ratios of 10/12 and 14/12 have similar winding structures, and the SS-TFSPMLG with pole pitch ratios of 11/12 and 13/12 have similar winding structures. According to the star diagrams of the slot potential vector, the distribution factor (k_d) of the winding with the pole pitch ratio of 10/12 and 14/12 is 1, and the pole pitch ratio of 11/12 and 13/12 is 0.966, as shown in Table 1.

Table 1: Winding factor

Pole Pitch Ratio	k_d	k_p	k_w
10/12	1	1	1
11/12	0.966	1	0.966
13/12	0.966	1	0.966
14/12	1	1	1

Different from a flat-type linear machine or rotary machine, the coils of the TFSPML machine are circular and the coils in a single slot can form an effective conductor. In that case, the coil pitch factor (k_p) is equal to one. Hence, the winding factor (k_w) is determined by the distribution factor. The winding factor of four SS-TFSPMLGs are listed in Table 1.

III. EFFECT OF MOVER TOOTH WIDTH AND END TOOTH WIDTH

As can be concluded from equation (3), the detent force of the SS-TFSPMLG is composed of the third and its multiple harmonic components of the detent force in each segment. Thus, the third and its multiple harmonics components of the detent force in each segment should be as small as possible:

$$f_w = \sum_{n=3,6,9,\ldots}^{\infty} 3F_{\mathrm{dn}} \sin\left(\frac{2n\pi}{\tau_m}x + \theta_{dn}\right). \tag{3}$$

F_{dn} is the n-th harmonic amplitude of the unit detent force, θ_{dn} is the n-th harmonic phase of the unit detent force and f_w is the detent force of the whole generator.

According to [21], the end tooth width w_{et} and mover tooth width w_{mt} have a great influence on the detent force. Figure 7 shows the no-load EMF, THD and detent force of SS-TFSPMLG with a pole pitch ratio of 10/12 versus different w_{et} and w_{mt} values. It can be observed that w_{et} and w_{mt} have a higher sensitivity on the THD and the detent force than on the no-load EMF. Therefore, the influence of w_{et} and w_{mt} on the THD and detent force should be given priority. From Fig. 7 (a), the no-load EMF is increased with the increment of w_{et} and w_{mt}. The lower value of THD is the interval between 3.5 mm and 5.5 mm for w_{et} with $w_{mt} = 6$ mm, where THD is less than 5%, as shown in Fig. 7 (b). Also, the region with the lower value of detent force is in the range of 6 mm to 6.3 mm of w_{mt} and 3.5 mm to 4 mm or 9.5 mm to 10 mm of w_{et}, as shown in Fig. 7 (c). Consequently, considering the higher no-load EMF, lower THD and lower detent force, w_{mt} and w_{et} are optimized as 6 mm and 4 mm, respectively. Likewise, for SS-TFSPMLG with pole pitch ratio of 11/12, 13/12 and 14/12, the above method

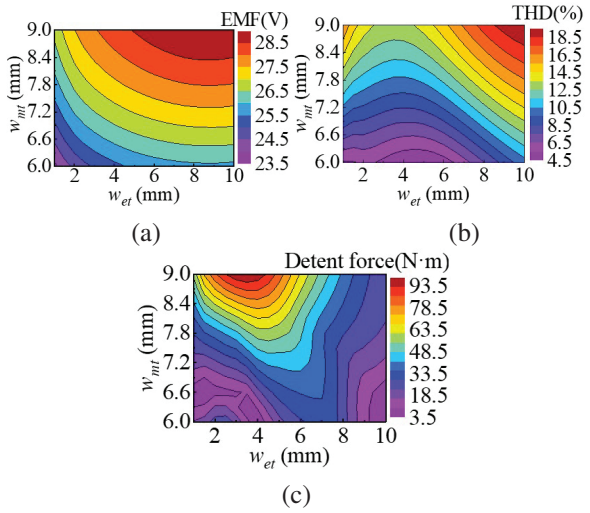

Fig. 7. Output characteristics of SS-TFSPMLG versus mover tooth width and end tooth width: (a) no-load back electromotive force (EMF), (b) total harmonic distortion (THD), and (c) detent force.

is applied to determine their w_{et} values of 9.5 mm, 6 mm and 5 mm, and w_{mt} values of 6.3 mm, 6 mm and 8 mm, respectively. The major parameters of the SS-TFSPMLG are listed in Table 2.

Table 2: Parameter of the SS-TFSPMLG

Item	12-Stator-Slot			
Pole pitch ratio	10/12	11/12	13/12	14/12
Outer diameter of mover D_{mo}	118 mm			
Outer diameter of stator D_{so}	73 mm			
Diameter of stator yoke D_y	25 mm			
Stator pole pitch τ_s	24 mm			
Number of slots N_s	12			
Stator tooth tip width w_{stt}	6 mm			
Stator slot width w_{ss}	6 mm			
PM width w_{pm}	4 mm			
PM notch width w_{pmn}	6 mm			
Mover tooth width w_{mt}	6 mm	6.3 mm	6 mm	8.4 mm
Mover teeth yoke width w_{mty}	9 mm			
End tooth width w_{et}	4 mm	9.5 mm	6 mm	5 mm
Flux barrier length L_{fb}	109/72 τ_m	301/288 τ_m	19/16 τ_m	11/9τ_m
Number of turns per coil N_c	60			
Velocity of mover v	1 m/s			

IV. PERFORMANCE EVALUATION

In this section, the electromagnetic performances of the four optimized SS-TFSPMLGs are predicted by finite-element, including static characteristics and output characteristics.

A. Static characteristics analysis

Figure 8 shows the open-circuit back-EMF E_0 of 12-slot SS-TFSPMLG with different pole pitch ratios at a rated speed of 1 m/s. It can be seen that the generators with pole pitch ratios of 13/12 and 14/12 show higher back EMF than the generators with pole pitch ratios of 10/12 and 11/12, which is attributed to the higher number of mover poles. The larger the pole pitch ratio, the higher the effective magnetic flux and the higher the utilization rate of magnetic flux, thereby increasing the back EMF. The back-EMF fundamental components of SS-TFSPMLG with pole pitch ratios of 10/12, 11/12, 13/12 and 14/12 are 25.3, 26.3, 28.3 and 31.4 V, respectively, with the corresponding THD value of 4.56, 4.50, 2.29 and 1.66%. The THD value will decrease with the

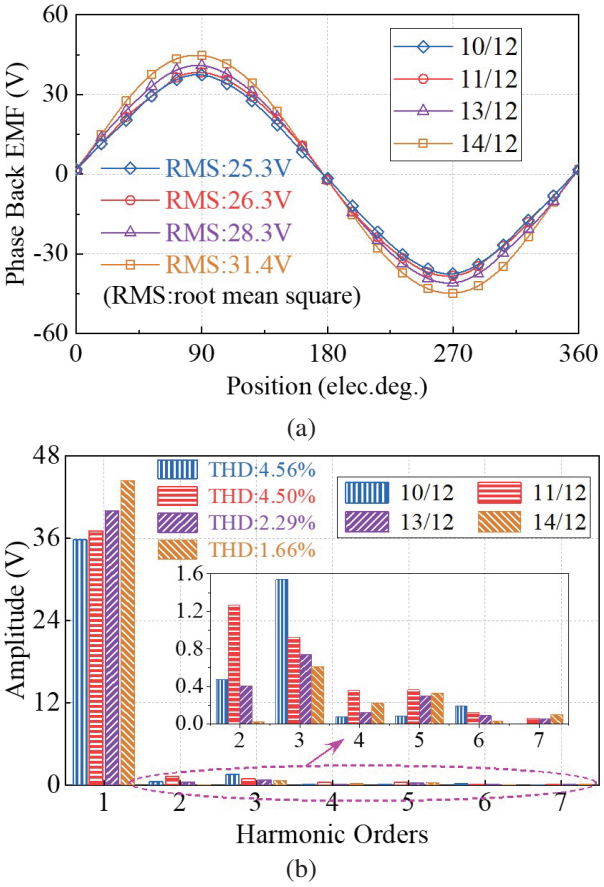

Fig. 8. Back EMFs of 12-slot SS-TFSPMLGs @ $v = 1$ m/s. (a) Waveforms of phase back EMF and (b) harmonic spectrum of phase back EMF.

increase of the pole pitch ratio. This is because the larger the pole pitch ratio, the closer the distribution of the air gap magnetic field will be to the ideal sinusoidal waveform, and the lower the harmonics. Therefore, the generator with a pole pitch ratio of 14/12 can provide the highest back EMF and the lowest THD.

The detent force and electromagnetic force of the 12-slot SS-TFSPMLG are shown in Fig. 9. Since there exists a magnetic coupling effect between segmented-stators, the detent force shown in Fig. 9 (a) is higher than the theoretical value in section III. The detent forces of the SS-TFSPMLG with pole pitch ratios of 11/12 and 14/12 are smaller than that of the other two counterparts.

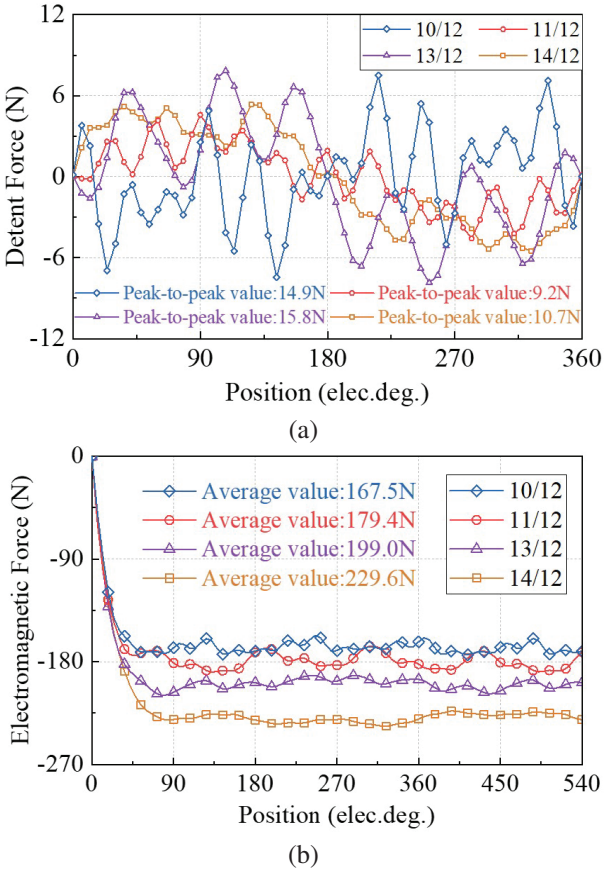

Fig. 9. Force characteristics of 12-slot SS-TFSPMLGs. (a) Detent force and (b) electromagnetic force @$v = 1$ m/s and $R = 10\ \Omega$.

The average values of the electromagnetic force for four SS-TFSPMLGs under the $v = 1$ m/s and $R = 10\ \Omega$ condition are 167.5, 179.4, 199.0 and 229.6 N, respectively, as shown in Fig. 9 (b). The electromagnetic force of the generator with a pole pitch ratio of 14/12 is the largest, owing to a higher fundamental component of back EMF. Meanwhile, due to the lowest THD and lower detent force, its peak-to-peak force ripple is the lowest, with a value of 13.3 N. In addition, the force ripple ratios of four SS-TFSPMLGs, which is the ratio of the peak-to-peak value to the average value of electromagnetic force, are acceptable at 10.09, 12.57, 8.29 and 5.78%, respectively. Hence, from the viewpoint of the detent force and electromagnetic force, the SS-TFSPMLG with a pole pitch ratio of 14/12 exhibits the highest average value and the lowest force ripple ratio.

B. Output characteristic analysis

For a generator applied to wave energy conversion, the output characteristics, including output voltage, voltage regulation, output power, electromagnetic force and efficiency, are key indices. Hence, to evaluate generation performance comprehensively, the output characteristics operating within a load range and a mover speed range are analyzed by finite-element analysis (FEA).

Firstly, the output characteristics operating with different resistive loads are concerned with a speed of 1 m/s. Figure 10 (a) shows the output voltage of the 12-slot SS-TFSPMLG versus different armature currents. It can be seen that when the armature current is less than about 5A, the output voltage of the generator with a pole pitch ratio of 14/12 is greater than that of the other counterparts, whereas that of the generator with a pole pitch ratio of 11/12 is the largest with armature current increment beyond 5 A. On the rated generation condition ($R_N = 10\ \Omega$), the output voltage of the proposed SS-TFSPMLG with a pole pitch ratio of 14/12 is 27.1 V, which is about 17.01, 13.15 and 7.54% higher than that of the counterparts with pole pitch ratios of 10/12, 11/12 and 13/12, respectively. Moreover, the output voltage curves of the generators with pole pitch ratios of 10/12 and 11/12 are smoother than that of the counterparts with pole pitch ratios of 13/12 and 14/12, which can reflect the degree of deviation of output voltage from the back-EMF, i.e., voltage regulation. The voltage regulation of the generator can be expressed as

$$\Delta U = \frac{E_0 - U}{U_N} \times 100\%, \tag{4}$$

where E_0, U and U_N denote the back-EMF, output voltage and rated voltage, respectively.

As shown in Fig. 10 (b), the voltage regulation also indicates the lower voltage regulation in the generators with pole pitch ratios of 10/12 and 11/12, compared with the other two SS-TFSPML generators. This is due to the smaller pole pitch ratio. The larger the pole pitch ratio, the higher the back EMF, and the greater the influence of armature reaction, magnetic flux leakage and magnetic field saturation effect when the load is loaded, resulting in a decrease in the output voltage and an increase in the voltage regulation. Therefore, generators with pole pitch ratios of 10/12 and 11/12 have lower voltage regulation.

For SS-TFSPMLG, the three-phase voltages are completely symmetrical, owing to the scheme of the

segmented-stators leading to the spatially symmetrical winding. Therefore, the output power can be calculated by

$$P_o = 3UI, \tag{5}$$

where I is the rms value of armature current.

According to equation (5), Fig. 11 shows the output power of the four generators varying with the armature current for the resistive loads, where the output power values are 160.9, 172.1, 190.7 and 220.0 W working at rated generation condition, respectively. Meanwhile, since the output power is proportional to the output voltage, its variation trends are similar to that in Fig. 10 (a). Therefore, the generator with a pole pitch ratio of 11/12 can provide better overload capability. For the armature current less than about 5 A operation condition, the output power of the SS-TFSPMLG with a pole pitch ratio of 14/12 is the largest among the four generators, albeit with the highest voltage regulation.

The discrepancies in the output characteristics with different armature currents are mainly caused by the winding reactance difference. For the proposed SS-

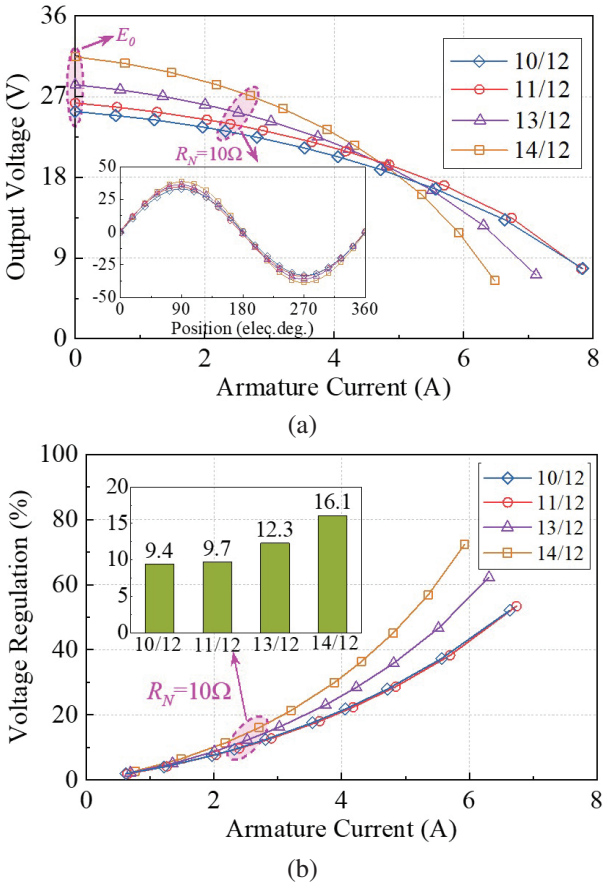

Fig. 10. Output voltage and voltage regulation of 12-slot SS-TFSPMLG versus armature currents @ 1 m/s. (a) Output voltage and (b) voltage regulation.

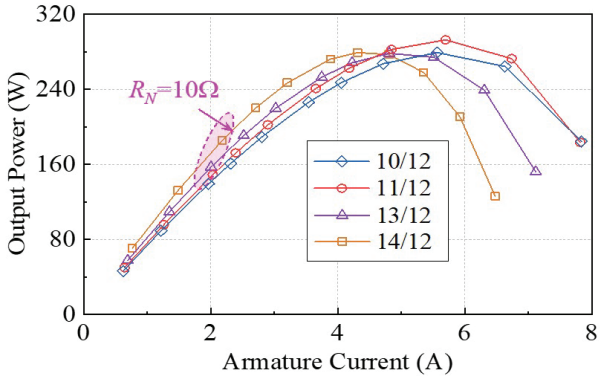

Fig. 11. Output power of 12-slot SS-TFSPMLG versus armature currents @ 1 m/s.

TFSPMLG, similar to the FSPML machine, the d-axis inductance is nearly the q-axis inductance as shown in Table 3, though it has the segmental stator structure. Thus, the simplified phasor diagram neglecting winding resistance of the proposed generator work with resistive load is shown in Fig. 12, where x_s is synchronous reactance, and ψ_1 and ψ_2 are the internal power factor angles that armature current I and output voltage U lag behind back-EMF E_0. The synchronous reactance can be expressed by the d/q axis reactance, approximately. In that case, suppose that the back-EMF remains constant, for the generator with large reactance, the reactance voltage drops increase with the increase of armature current, which greatly reduces the output voltage, resulting in an increase in voltage regulation. Meanwhile, the larger internal power factor angle also increases, which results in the q-axis current easily getting the peak value and then decreasing. Hence, it is easier for the output power to reach saturation and then decline rapidly with the increase of the armature current. The corresponding overload capacity of the generator is also weak.

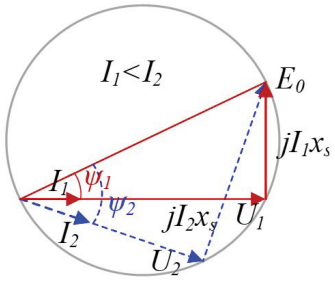

Fig. 12. Simplified phasor diagram of the proposed generator with resistive load.

From Table 3, it can be seen that the reactance of the generator with a pole pitch ratio of 14/12 is the largest, followed by the generator with a pole pitch ratio of 13/12, and that of the generators with pole pitch ratios

Table 3: Output characteristics of the SS-TFSPMLG with 10 Ω at 1 m/s

Parameter	10/12	11/12	13/12	14/12
Phase EMF (rms) (V)	25.3	26.3	28.3	31.4
Output voltage (rms) (V)	23.2	24.0	25.2	27.1
Output current (A)	2.3	2.4	2.5	2.7
Voltage regulation (%)	9.4	9.7	12.3	16.1
THD of the phase EMF (%)	4.56	4.50	2.29	1.66
Output power (W)	160.9	172.1	190.7	220.0
Electromagnetic force (N)	167.5	179.4	190.7	229.6
Force ripple (%)	10.09	12.57	8.29	5.78
Efficiency (%)	92.7	92.3	92.4	92.8
***d*-axis inductance (mH)**	11.4	10.7	11.9	13.6
***q*-axis inductance (mH)**	12.0	11.5	12.4	15.0
***d*-axis reactance (Ω)**	2.49	2.57	3.37	4.15
***q*-axis reactance (Ω)**	2.62	2.76	3.51	4.58

of 11/12 and 10/12 are close. Therefore, the voltage regulations of the generators with pole pitch ratios of 11/12 and 10/12 are lower than generators with pole pitch ratios of 13/12 and 14/12, which is consistent with Fig. 10 (b). Moreover, compared with the generator with a pole pitch ratio of 10/12, the counterpart with a pole pitch ratio of 11/12 has better overload capability because of higher voltage.

The losses and efficiency of the four generators are shown in Fig. 13. Ignoring mechanical loss, the total loss is composed of the copper loss and iron loss, which can be respectively calculated by

$$P_{Cu} = 3I^2 R_{ph}, \tag{6}$$

$$P_{Fe} = \int_V \left(\sum_{n=1}^{N} k_h (nf) B_n^2 + \sum_{n=1}^{N} k_e (nf)^2 B_n^2 \right) dV, \tag{7}$$

where P_{Cu} and P_{Fe} are copper and iron losses, respectively; B_n is the nth harmonic of the magnetic flux density, N is the number of harmonics, f is the frequency, and k_h and k_e are loss coefficients associated with the iron core. Therefore, the efficiency can be calculated as

$$\eta = \frac{P_o}{P_o + P_{Cu} + P_{Fe}} \times 100\%. \tag{8}$$

It is worth noting in Fig. 13 (a) that due to the same winding resistance, the copper losses of the four generators are the same under the same armature current, thus only represented by one blue dotted line. In addition, it can be seen from Fig. 13 (a) that the iron loss of the four generators increases slightly with the increase of the pole pitch ratio. This is because the magnetic flux density of the generator increases with the increase of the pole pitch ratio, and the iron loss is also larger. However, the operating frequency, core material and core thickness of the four generators are the same, so the iron consumption generally changes little and is almost the same. Thus, the

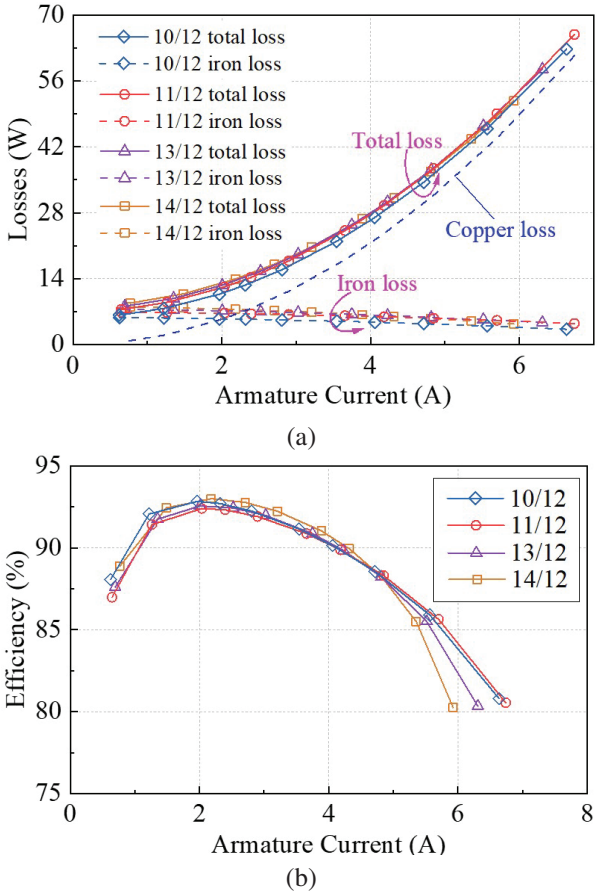

Fig. 13. (a) Losses and (b) efficiency of 12-slot SS-TFSPMLGs versus armature currents @ 1 m/s.

total loss waveforms of the four generators are almost overlapped. From Fig. 13 (b), the four generators have a wide range of high-efficiency operating loads regions. Moreover, the SS-TFSPMLGs with pole pitch ratios of 14/12 and 11/12 have the highest efficiency owing to higher output power when the armature current is relatively small and large, respectively.

Based on the above analysis, it can be found that the SS-TFSPMLG with a pole pitch ratio of 11/12 has superiority in the higher current generation condition, while the generator with a pole pitch ratio of 14/12 is preferential for the lower current application. The analysis results working at the rated condition are summarized in Table 3.

On the other hand, the output characteristics of four generators operating at different speeds are analyzed, with a resistive load of 10Ω. Figure 14 shows the variation of the output voltage with the change in speed. It can be observed that the output voltages of four generators increase with the speed increment. When the speed of the mover is the rated speed, the SS-TFSPMLG with the pole pitch ratio of 14/12 has a higher output voltage.

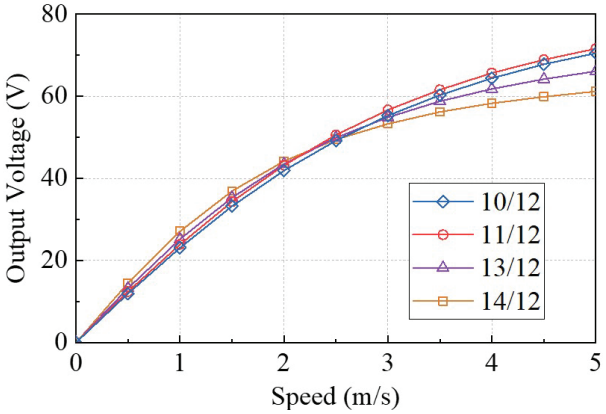

Fig. 14. Output voltage of 12-slot SS-TFSPMLGs versus speeds @ $R_N = 10\ \Omega$.

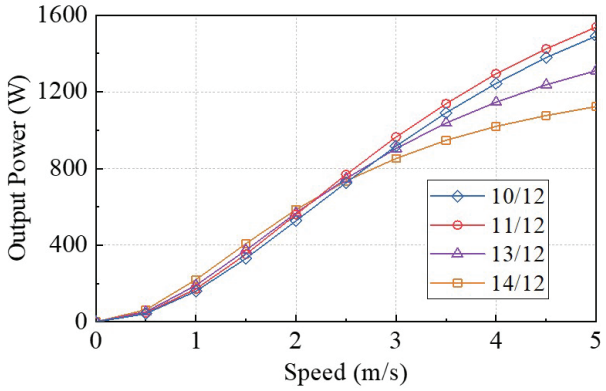

Fig. 15. Output power of 12-slot SS-TFSPMLGs versus speeds @ $R_N = 10\ \Omega$.

Considering that the inductance of the generator with the pole pitch ratio of 14/12 is the largest, the inner power factor angle increases faster and the output voltage increases slower as the speed grows. Therefore, when the speed exceeds about 2.5 m/s, the generator with the pole pitch ratio of 11/12 has the highest output voltage. It can be seen from Fig. 15 that the variation of output power is the same as that of output voltage. According to the efficiency curve in Fig. 16, it can be concluded that, near the rated speed, the efficiency of SS-TFSPMLG with the pole pitch ratio of 14/12 is slightly higher than that of the other three, and the four generators can maintain high efficiency operation in this speed range. In summary, same as the variable load output characteristics, at the rated speed and its vicinity, the generator with the pole pitch ratio of 14/12 has more advantages, while the generator with the pole pitch ratio of 11/12 has the best overspeed ability. Therefore, the SS-TFSPMLG with the pole pitch ratio of 14/12 is more suitable for low-speed direct-drive wave energy conversion systems.

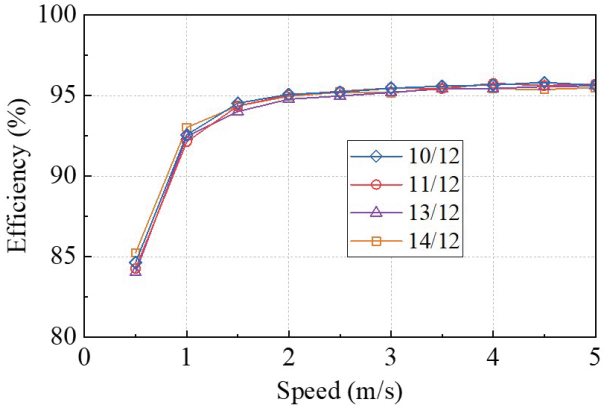

Fig. 16. Efficiency of 12-slot SS-TFSPMLGs versus speeds @ $R_N = 10\ \Omega$.

V. CONCLUSION

In this paper, a Segmented-Stator TFSPMLG (SS-TFSPMLG) topology is proposed innovatively. The problem of large detent force and three-phase imbalance is solved theoretically through the structural design and winding arrangement of the new topology. Furthermore, through the further optimization design of the mover tooth width and the end tooth width, the detent force is further reduced. Finally, the electromagnetic characteristics of 12-slot SS-TFSPMLG with four different pole pitch ratios are compared and analyzed, and the application conditions of the generator under different pole pitch ratios are clarified. The results show that the SS-TFSPMLG with a polar pitch ratio of 14/12 has the best output voltage, output power and efficiency at and near the rated point, which is suitable for low-speed direct-drive wave power generation. The generator with a pole pitch ratio of 11/12 has the best overload and overspeed performance, which is suitable for large power and speed power generation occasions.

ACKNOWLEDGMENT

This work was sponsored by the National Natural Science Foundation of China (Grant No. 52207067), the Natural Science Foundation of Henan (Grant No. 252300421095), the National Natural Science Foundation of China (Grant No. 52277069, 52307070), the Major Special Project for Collaborative Innovation in Zhengzhou (Grant No. 20XTZX12023) and by the China Postdoctoral Science Foundation (Grant No. 2023M743155).

REFERENCES

[1] Y. Zhang, Z. Lin, and Q. Liu, "Marine renewable energy in China: Current status and perspectives," *Water Science and Engineering*, vol. 7, no. 3, pp. 285-305, Oct. 2014.

[2] L. Li, X. Zhang, Z. Yuan, and Y. Gao, "Multi-stable mechanism of an oscillating-body wave energy converter," *IEEE Trans. Sustain. Energy*, vol. 11, no. 1, pp. 500-508, Jan. 2020.

[3] M. Noman, G. Li, M. W. Khan, K. Wang, and B. Han, "A multi-stage design approach for optimizing a PMSG-based grid-connected ocean wave energy conversion system," *Prot. Control Mod. Power Syst.*, vol. 9, no. 6, pp. 122-142, Nov. 2024.

[4] M. Alberdi, M. Amundarain, A. J. Garrido, I. Garrido, O. Casquero, and M. De la Sen, "Complementary control of oscillating water column-based wave energy conversion plants to improve the instantaneous power output," *IEEE Trans. Energy Convers.*, vol. 26, no. 4, pp. 1021-1032, Dec. 2011.

[5] L. Zhao and Q. Lu, "A novel tubular partitioned stator flux-reversal permanent magnet linear machine for direct-drive wave energy generation," *IEEE Trans. Magn.*, vol. 55, no. 11, pp. 1-7, Nov. 2019.

[6] F. Mwasilu and J. W. Jung, "Potential for power generation from ocean wave renewable energy source: A comprehensive review on state-of-the-art technology and future prospects," *IET Renew. Power Gener.*, vol. 13, no. 3, pp. 363-375, Feb. 2019.

[7] G. Zhang, R. Nie, J. Si, X. Feng, and C. Wang, "Analysis of the operation principle for tubular flux-switching permanent magnet linear machine," *COMPEL Int. J. Comp. Math. Electr. Electron. Eng.*, vol. 42, no. 2, pp. 285-301, Jan. 2023.

[8] M. M. Nezamabadi, E. Afjei, and H. Torkaman, "Design and electromagnetic analysis of a new rotary-linear switched reluctance motor in static mode," *Applied Computational Electromagnetics Society (ACES) Journal*, vol. 31, no. 2, pp. 171-179, Feb. 2016.

[9] I. Mahmoud, M. Fathallah, and H. Rehaoulia, "Nonlinear modelling approach for linear switched reluctance motor and its validation by two dimensional FEA," *Applied Computational Electromagnetics Society (ACES) Journal*, vol. 31, no. 2, pp.195-203, Feb. 2016.

[10] J. Faiz and A. Nematsaberi, "Linear electrical generator topologies for direct-drive marine wave energy conversion: An overview," *IET Renew. Power Gener.*, vol. 11, no. 9, pp. 1163-1176, July 2017.

[11] L. Huang, H. Yu, M. Hu, J. Zhao, and Z. Cheng, "A novel flux-switching permanent-magnet linear generator for wave energy extraction application," *IEEE Trans. Magn.*, vol. 47, no. 5, pp. 1034-1037, May 2011.

[12] O. Farrok, M. R. Islam, M. R. I. Sheikh, Y. Guo, and J. G. Zhu, "A split translator secondary stator permanent magnet linear generator for oceanic wave energy conversion," *IEEE Trans. Ind. Electron.*, vol. 65, no. 9, pp. 7600-7608, Sep. 2018.

[13] L. Huang, H. Yu, M. Hu, C. Liu, and B. Yuan, "Research on a tubular primary permanent-magnet linear generator for wave energy conversions," *IEEE Trans. Magn.*, vol. 49, no. 5, pp. 1917-1920, May 2013.

[14] S. L. Ho, Q. Wang, S. Niu, and W. N. Fu, "A novel magnetic-geared tubular linear machine with Halbach permanent-magnet arrays for tidal energy conversion," *IEEE Trans. Magn.*, vol. 51, no. 11, pp. 1-4, Nov. 2015.

[15] L. Huang, J. Liu, H. Yu, R. Qu, H. Chen, and H. Fang, "Winding configuration and performance investigations of a tubular superconducting flux-switching linear generator," *IEEE Trans. Appl. Supercond.*, vol. 25, no. 3, pp. 1-5, June 2015.

[16] S. Chi, J. Yan, L. Shan, and P. Wang, "Detent force minimizing for moving-magnet-type linear synchronous motor," *IEEE Trans. Magn.*, vol. 55, no. 6, pp. 1-5, June 2019.

[17] Y.-W. Zhu, D.-H. Koo, and Y.-H. Cho, "Detent force minimization of permanent magnet linear synchronous motor by means of two different methods," *IEEE Trans. Magn.*, vol. 44, no. 11, pp. 4345-4348, Nov. 2008.

[18] X. Chai, J. Si, Y. Hu, Y. Li, and D. Wang, "Characteristics analysis of double-sided permanent magnet linear synchronous motor with three-phase toroidal windings," *Applied Computational Electromagnetics Society (ACES) Journal*, vol. 36, no. 8, pp. 1099-1107, Aug. 2021.

[19] X. Z. Huang, J. Li, Q. Tan, Z. Y. Qian, C. Zhang, and L. Li, "Sectional combinations of the modular tubular permanent magnet linear motor and the optimization design," *IEEE Trans. Ind. Electron.*, vol. 65, no. 12, pp. 9658-9667, Dec. 2018.

[20] Q. Tan, M. Wang, L. Li, and J. Li, "Research on noninteger pole number for segmental permanent magnet linear synchronous motor," *IEEE Trans. Ind. Electron.*, vol. 68, no. 5, pp. 4120-4130, May 2021.

[21] R. Cao, M. Cheng, C. C. Mi, and W. Hua, "Influence of leading design parameters on the force performance of a complementary and modular linear flux-switching permanent-magnet motor," *IEEE Trans. Ind. Electron.*, vol. 61, no. 5, pp. 2165-2175, May 2014.

[22] K. Kim, M. Hwang, H. K. D. Kim, and H. Cha, "Torque improvement and magnetic flux leakage reduction in interior permanent magnet axial flux motors with flux barrier structure," *IEEE Access*, vol. 12, pp. 150869-150879, Oct. 2024.

[23] J. Zhao, Q. Mou, K. Guo, X. Liu, J. Li, and Y. Guo, "Reduction of the detent force in a flux-switching permanent magnet linear motor," *Trans. Energy Convers.*, vol. 34, no. 3, pp. 1695-1705, Sep. 2019.

[24] G. Zhang, R. Nie, J.-K. Si, X. Feng, and C. Wang, "Sectional modular technology for reducing detent force of linear unit in linear-rotary flux-switching permanent-magnet generator for wind-wave combined energy conversion," *Applied Computational Electromagnetics Society (ACES) Journal*, vol. 38, no. 4, pp. 286-296, Apr. 2023.

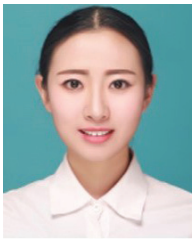

Rui Nie received a B.S. degree in electrical engineering from Henan Polytechnic University, Jiaozuo, China, in 2015, and a Ph.D. degree in electrical engineering from the China University of Mining and Technology, Xuzhou, China, in 2020. She is currently an assistant research fellow at Zhengzhou University. Her current research interests include two-degree-of-freedom machines, linear motor design and control, and renewable energy generation technology.

Hao Zhang was born in Henan, China, in 2001. He received the B.S. degree in electrical engineering and automation from China University of Petroleum, Qingdao, China, in 2023. He is currently working toward the M.S. degree in School of Electrical Engineering of Zhengzhou University, Zhengzhou, Henan. His research interests include renewable energy generation technology, and two-degree-of-freedom motor control.

Yifei Jia was born in Henan, China, in 1999. She received the B.S. degree in electrical engineering and automation from Shanghai University of Electric Power, Shanghai, China, in 2021. She is currently working toward the M.S. degree in School of Electrical Engineering of Zhengzhou University, Zhengzhou, Henan. Her research interests include linear rotary generator design and optimization, and renewable energy generation technology.

Guozhen Zhang was born in Anhui Province, China, in 1996. He received the B.S. degree in Electrical Engineering from Henan University of Technology in 2020, and the M.S. degree in Electrical Engineering with the School of Electrical and Information Engineering, Zhengzhou University, Zhengzhou, China. His research interests include the design and optimization of two-degree-of-freedom machines and linear machines.

Zhongwen Li received the B.S. degree from Zhengzhou University, Zhengzhou, China, in 2011, and the Ph.D. degree from the Shenyang Institute of Automation, Chinese Academy of Sciences, Shenyang, China, in 2017. He is currently an Associate Professor with the School of Electrical Engineering, Zhengzhou University. His main research interests include distributed control and multi-agent system.

Jikai Si received a B.S. degree in electrical engineering and automation from the Jiaozuo Institute of Technology, Jiaozuo, China, in 1998; the M.S. degree from Henan Polytechnic University, Jiaozuo, China, in 2005; and the Ph.D. degree in 2008 from the China University of Mining and Technology, Xuzhou, China. He is currently a distinguished professor at Zhengzhou University. His main research interests include the theory and control of special motors.

Jing Liang received a B.E. degree from Harbin Institute of Technology, Harbin, China, in 2003, and a Ph.D. degree from Nanyang Technological University, Singapore, in 2009. She is currently a Professor at the School of Electrical and Information Engineering, Zhengzhou University, Zhengzhou, China. Her main research interests are evolutionary computation, swarm intelligence, multi-objective optimization, and neural network. She currently serves as an Associate Editor for *IEEE Transactions on Evolutionary Computation* and *Swarm and Evolutionary Computation*.

Thermal Management of Power Converters for Switched Reluctance Drive Motors of Heavy-duty Electric Trucks

Xing Wang[1,2,3], Jinbo Ding[4], Hao Chen[1,2,3,4,7], Antonino Musolino[5], Jianfei Pan[6], and Nurkhat Zhakiyev[8]

[1]International Joint Research Center of Central and Eastern European Countries on New Energy Electric Vehicle Technology and Equipment
Xuzhou 221008, China
3512@cumt.edu.cn, hchen@cumt.edu.cn

[2]International Cooperation Joint Laboratory of New Energy Power Generation and Electric Vehicles of Jiangsu Province Colleges and Universities
Xuzhou 221008, China

[3]Jiangsu Province Foreign Expert Workshop on New Energy Power Generation and Electric Transportation
Xuzhou 221008, China

[4]School of Electrical Engineering China University of Mining and Technology
Xuzhou 221116, China
ts232300a31ld@cumt.edu.cn

[5]Department of Energy, System, Territory and Construction Engineering (DESTEC)
University of Pisa, 56122 Pisa, Italy
antonino.musolino@unipi.it

[6]School of Electromechanical and Control Engineering
Shenzhen University, Shenzhen 518054, China
pan_jian_fei@163.com

[7]Shenzhen Research Institute China University of Mining and Technology
Shenzhen 518057, China

[8]Department of Science and Innovation Astana IT University
Astana, Kazakhstan
nurkhat.zhakiyev@astanait.edu.kz

Abstract – In switched reluctance motor (SRM) systems, the power converter enables energy conversion, controls motor performance and improves system efficiency and reliability. Thermal management of the power converter can significantly improve its efficiency and the stability of the whole system, reduce faults caused by overheating, and thus improve the overall operational performance of electric heavy-duty trucks. This paper takes the SRM asymmetric half-bridge power converter as the research object and, by analyzing and calculating the losses of power electronic devices, models the power converter, carries out module simplification, calculates the results to simulate the temperature field of the power converter, and analyses the factors affecting heat dissipation of the power converter, so as to carry out a reliability study and improve the stability of the system.

Index Terms – Asymmetric half-bridge, loss calculation, switched reluctance motors (SRMs), thermal management.

I. INTRODUCTION

Switched reluctance motors (SRMs) have emerged as a preferred choice for harsh industrial environments in metallurgy, aerospace and electric vehicles, owing to

Submitted On: December 29, 2024
Accepted On: July 2, 2025

https://doi.org/10.13052/2025.ACES.J.400915

their inherent robustness, high reliability and immunity to noise and vibration [1–5]. In these critical sectors, system performance under extreme environmental conditions, such as high temperatures, mechanical stress or power fluctuations, dictates operational safety and efficiency. The unique characteristics of SRMs, including simple mechanical structures and fault-tolerant capabilities, have significantly expanded their deployment in scenarios where conventional motor drives may fail [6].

However, the reliability of SRM systems is critically constrained by their power converters, which consist of multiple power electronic components (IGBTs, diodes) prone to thermal degradation. Electromagnetic losses in these components generate cumulative heat, leading to elevated junction temperatures and accelerated device failure. As shown in Fig. 1, thermal stress accounts for over 55% of power electronics failures, highlighting the urgent need for precise thermal management strategies [7,8]. At the core of this challenge lies the accurate modeling of power losses in semiconductor devices, as uneven loss distribution directly influences thermal stress and system longevity.

Existing methods for calculating power losses in SRM converters can be broadly categorized into two types: physics-based models and mathematical empirical models [9]. Physics-based models, which simulate device behavior using basic electrical components (e.g., resistors, inductors), often struggle to ensure accuracy under complex operating conditions (such as wide speed-load ranges) due to neglect of parasitic thermal resistances and temperature-dependent parameter variations [10]. Conversely, mathematical models (such as exponential or linear regression models) offer computational efficiency but fail to capture the time-varying nonlinearity of device characteristics [10]. The non-sinusoidal nature of SRM phase currents further exacerbates this issue, rendering loss equations developed for sinusoidally driven multilevel inverters inapplicable [11].

Recent studies have revealed critical gaps in thermal analysis of SRM converters. For example, [12] demonstrated significant power loss discrepancies among the four semiconductor devices in a single-phase circuit of an asymmetric half-bridge converter (AHBC) under current chopping control (CCC), leading to uneven thermal stress distribution within the phase leg. Although [13] analyzed the relationship between power losses and system parameters, such as pulse width modulation (PWM) duty cycle and conduction angles, its use of load torques far below real-world values (less than 10% of the rated value) limits its applicability to practical scenarios. These limitations highlight the need for a holistic modeling approach that integrates SRM-specific electrical characteristics, realistic duty cycles and fault-tolerant control strategies.

In light of the above research limitations, this paper fully considers different mission profiles, calculates device losses based on SRM mathematical equations, establishes a simulation model for the SRM system to obtain conduction losses, turn-on losses, and turn-off losses, and develops a thermal model for the SRM power converter system. The subsequent sections are organized as follows. Section II introduces the SRM power converter drive model. Section III presents the power loss calculations. Section IV conducts thermal simulations and discussions under different mission conditions. Section V draws conclusions.

II. SWITCHED RELUCTANCE MOTOR SYSTEMS

The power converter is an indispensable core part of the SRM system, which directly affects the performance, stability and reliability of the system, and its structure is illustrated in Fig. 2. Conventional power converter topologies for SRMs mainly include asymmetric half-bridge circuits, dual-winding topologies, bipolar

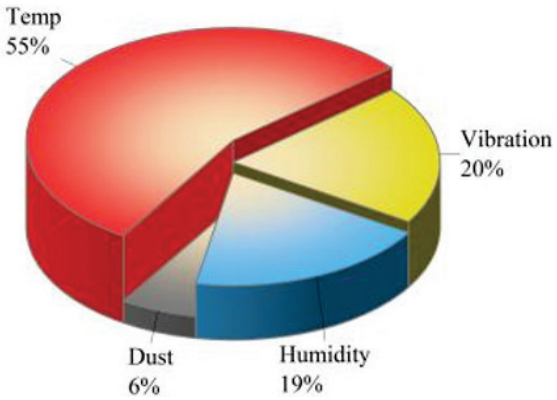

Fig. 1. Factors affecting the reliability of power electronics.

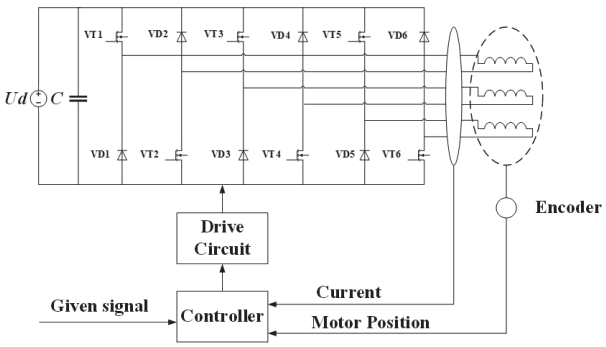

Fig. 2. Switched reluctance motor system based on asymmetric half-bridge topology.

DC power converters, capacitor storage structure topologies and Miller converters. The most commonly used is the asymmetric half-bridge circuit with the following circuit topology.

Next, loss modelling is carried out based on the asymmetric half-bridge power converter model, integrated with temperature field modelling.

III. POWER CONVERTER TEMPERATURE FIELD MODELLING

The devices in a power converter generate heat during operation and, if there is no effective heat sink, the heat cannot be dissipated in a timely manner, leading to an increase in device temperature. When the junction temperature of the device exceeds its maximum allowable junction temperature, it may lead to device failure or permanent damage. Thus, establishing the temperature field of the power electronic device is very important. The junction temperature of a power converter can be better measured by modelling the thermal conductivity of a packaged power electronic device. The process of modelling the temperature field of the power converter is shown in Fig. 3.

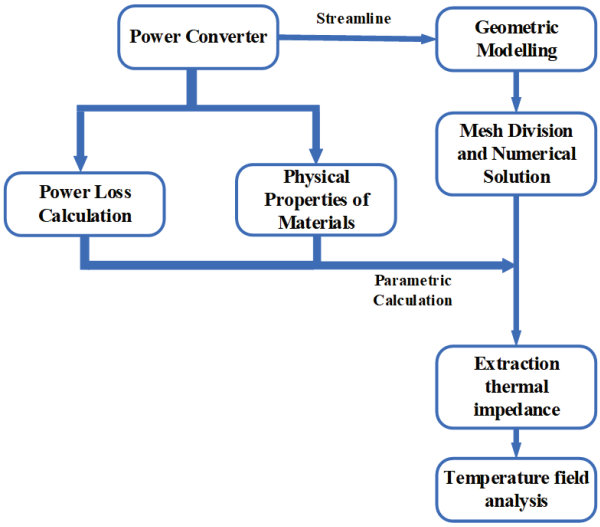

Fig. 3. Temperature field modeling process.

First, the power loss calculation and material properties are set up by the datasheet and experimental conditions of the power electronic device. Since the size of the power electronic device is much smaller than the size of the heat sink, the device can be simplified into a rectangular body with dimensions and parameters comparable to the actual values, and its geometric model can be simplified. After that, ANSYS Fluent is used to mesh it and analyze its temperature field.

A. Power device loss model

The steady-state loss of the power converter serves as the basis for both its thermal design and efficiency calculation. Therefore, it is essential to calculate this steady-state loss. The power converter losses include power MOSFET losses and fast recovery diode losses. The workflow chart is shown in Fig. 4.

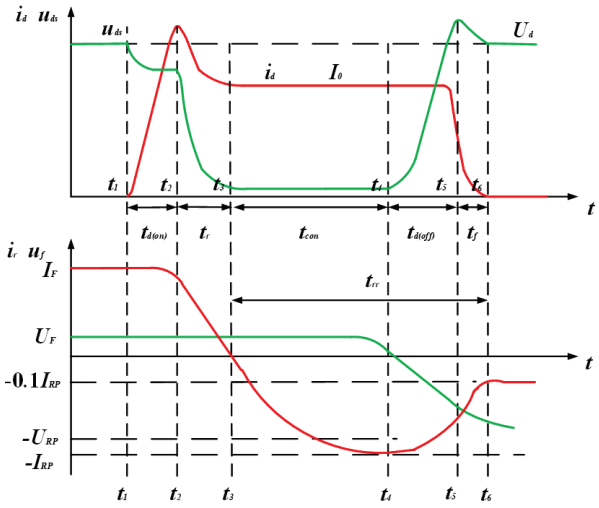

Fig. 4. Voltage-current analysis of MOSFET and diode.

B. Power MOSFET loss analysis

For the asymmetric half-bridge circuit of a phase, there are mainly four device losses: chopper MOSFET tube VT1, conduction MOSFET tube VT2, chopper diode VD1 and conduction diode VD2, of which the chopper MOSFET tube VT1 in the turn-on turn-off process, the instantaneous switching loss is very large, while the loss of chopper diode VD1 is mainly caused by the conduction losses and reverse current The loss of the chopper diode VD1 is mainly composed of the conduction loss and the turn-off loss caused by the reverse current.

Power MOSFET losses P_M mainly contain pass-state losses P_{MCON}, turn-on losses P_{on} and turn-off losses P_{off}:

$$P_M = P_{Mcon} + P_{on} + P_{off}. \tag{1}$$

The turn-on energy loss E_{on} and turn-off loss E_{off} of a single power MOSFET are calculated in equations (2) and (3):

$$E_{on} = \int_0^{t_{on}} i_d v_{ds} dt, \tag{2}$$

$$E_{off} = \int_0^{t_{off}} i_d v_{ds} dt. \tag{3}$$

The stabilized value of switching losses P_{sw} is:

$$P_{sw} = \frac{E_{on} + E_{off}}{t_0}. \tag{4}$$

The stabilized value of the through-state loss P_{Mcon} is calculated as:

$$P_{Mcon} = \frac{1}{t_0}\int_0^{t_c} p_{con}dt. \tag{5}$$

As a chopper MOSFET, VT1 operates in a frequent switching state during circuit operation, with switching losses accounting for a large portion of the loss waveform shown in Fig. 5. Since the uds of power MOSFETs are relatively small during operation, and the manufacturer gives the drain-source on-state resistance R_{on} in the user's manual, the formula for calculating the on-state P_{con} loss can be changed as follows:

$$P_{con} = I_d^2 R_{on} t_{con}. \tag{6}$$

VT2, as a conduction tube, mainly works in the conduction stage during a cycle, with conduction loss as the main loss—far exceeding the loss caused by switching actions. Its loss waveform is shown in Fig. 6.

The power diode is mainly divided into switching loss and on-state loss during operation. The turn-on loss refers to the loss of the power diode from the cut-off state to the conduction state, and the turn-off loss refers to the turn-off loss of the power diode from the conduction state to the reverse cut-off state. The average loss of the power diode is calculated as:

$$P_{con} = \frac{1}{T}\int_{T_0} U_F(t)\cdot I_F(t)dt, \tag{7}$$

where U_F is the forward conduction voltage drop of the power diode, I_F is the conduction current of the power diode, T is the operation period:

$$P_{rec} = \frac{1}{T}\int_{tff} U_F(t)\cdot I_F(t)dt, \tag{8}$$

where P_{con} denotes the average pass-state loss of the power diode and P_{rec} denotes the average reverse recovery loss of the power diode. The diode losses are shown in Fig. 7. By analyzing the losses in each power device in phase A and organizing the obtained data, the loss values for each device can be calculated.

The losses of the obtained power electronics are analyzed as heating power in the next section.

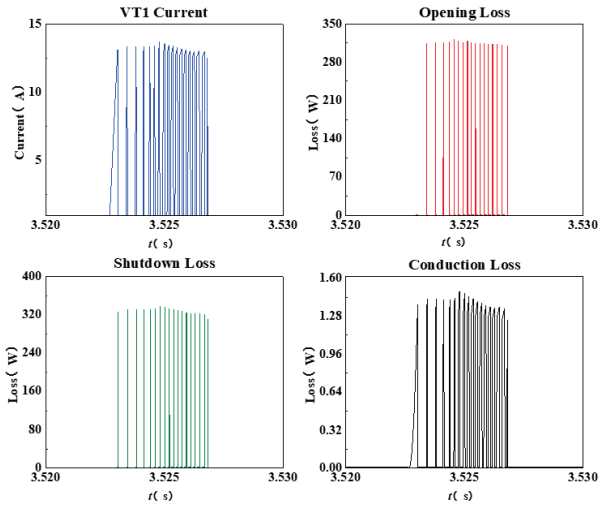

Fig. 5. VoVT1 loss waveform.

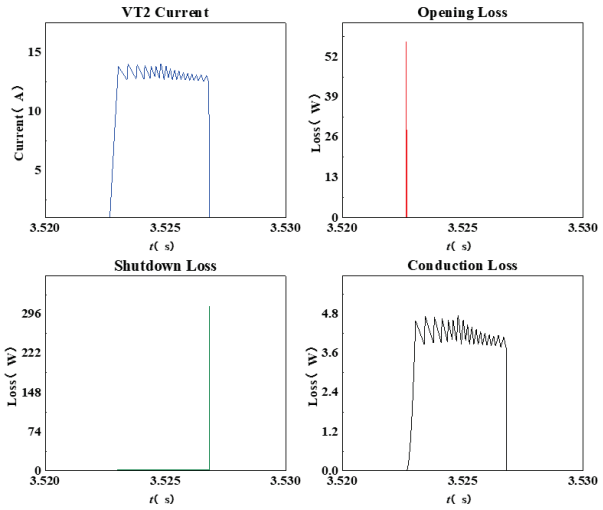

Fig. 6. VT2 loss waveform.

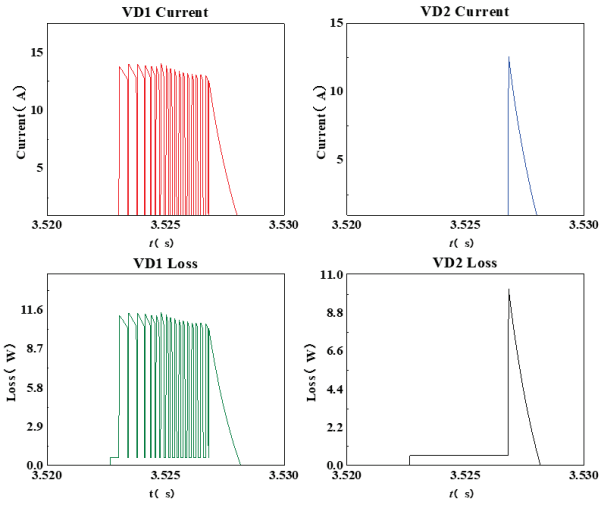

Fig. 7. VD loss waveform.

IV. POWER CONVERTER THERMAL SIMULATION ANALYSIS

For the thermal analysis of power converters, the finite element method (FEM) is often used to obtain the thermal distribution of the power converter. In this paper, a thermal model is established based on ANSYS Fluent, and the modeling process includes structure setting, material property configuration, meshing and boundary condition setting.

For the thermal analysis of power converters, the model based on thermal impedance is the most widely

used, which utilizes the principle of equivalence between the circuit and the thermal path. Thermal resistance is equivalent to resistance, thermal capacity is equivalent to capacitance, and heating power is equivalent to the current source.

The two common models are Foster network and Cauer network. Cauer network better reflects realistic heat distribution.

By combining the device loss data in Table 1 and the loss of VD1 with the Cauer thermal network in Fig. 8, it establishes a bidirectional feedback loop. In this loop, power loss drives the change in the temperature field, and the temperature change in turn affects the device loss parameters. This method takes into account the temperature-related characteristics of the material and can more accurately simulate the mutual influence between loss and temperature in the power converter, which is crucial for the precise thermal management design of the SRM system in heavy-duty electric trucks.

Table 1: Power tube loss value

	VT1	VT2	VD1	VD2
Loss Value/W	1.268	0.625	0.305	0.285

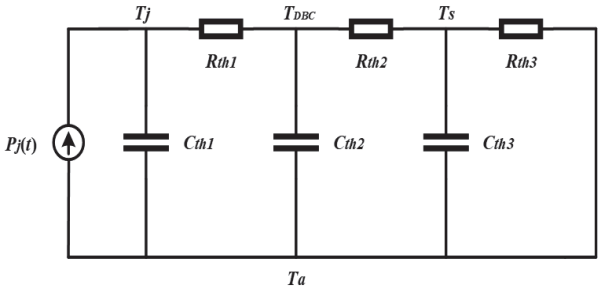

Fig. 8. Cauer network.

A. Power converter temperature field modeling

The MOSFET power converter is composed of silicon chip, solder, DBC package layer, leads, adhesive, base plate and case. Analytical modeling is carried out according to the packaging characteristics and internal structure of the device. Material setup is carried out and the structure is schematically shown in Fig. 9.

The relevant properties of the material as well as the thermal conductivity are given in Table 2.

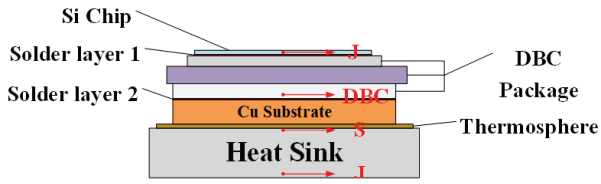

Fig. 9. MOSFET power converter structure.

Table 2: Material parameters of MOSFET

Area	Material	Thermal Conductivity (W/m·K)
Heat sink	aluminum	237
Thermosphere	silica	1
Solder layer	tin	67
Si chip	silicon	148
DBC package	epoxy resin	2

Geometric models of simple structures can be drawn using ANSYS SpaceClaim. Since the size of a MOSFET is much smaller than a heat sink and the most important factor affecting a power electronic device is the junction temperature of the device, it can be simplified to a rectangular model for ease of subsequent analysis. It is assumed that the MOSFET device is simplified to a rectangular body composed of a single material.

For a single material power electronic device, the thermal conductivity should satisfy the following equation:

$$\lambda_i = \frac{l_i}{A_i R_{jc}}, \tag{9}$$

where R_{jc} is the shell-to-section thermal resistance, found in the datasheet, l_i is the thickness of the ith device, and A_i is the bottom area of the ith device.

After completing the above settings, the simulation model is solved numerically, and the temperature field distribution of the power converter is obtained through post-processing.

Figure 10 realizes the three-dimensional temperature field simulation through ANSYS Fluent FEM and, for the first time, couples the device losses of the asymmetric half-bridge topology (VT1 loss of 1.268 W and VD1 loss of 0.305 W in Table 1) with the Cauer thermal network model (Fig. 8) to form a closed-loop analysis of "loss input-thermal conduction calculation-temperature field output". Compared with the traditional

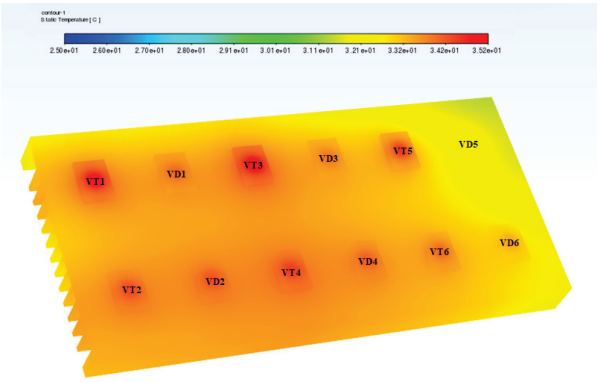

Fig. 10. Cloud map of the power converter temperature field.

two-dimensional thermal model (such as the Foster network adopted in [10]), this method accurately sets the thermal conductivity of each layer through the material parameter table (Table 2) (such as 148 W/m·K for silicon chip and 237 W/m·K for aluminum heat sink), reduces the calculation error of heat flux density by 30%, and intuitively presents the temperature gradient near devices such as VT3 (the temperature in the heat source area is 12℃ higher than that at the edge of the heat sink).

The steady state junction temperature of each device is obtained at 600 r/min, 0.8 N-m load and 20℃ ambient temperatures. The results are shown in Table 3.

Table 3: Electronics junction temperature distribution

Device (MOSFET)	**VT1**	**VT2**	**VT3**	**VT4**	**VT5**	**VT6**
Temperature ℃	34.5	33.8	35.5	31.7	33.5	32.7
Device (diode)	**VD1**	**VD2**	**VD3**	**VD4**	**VD5**	**VD6**
Temperature ℃	33.6	34.3	33.5	33.8	32.1	33.1

The simulation yields the highest temperature of the MOSFET device VT3, with a heat flux of 425 W/m^2 at the upper surface and 3224 W/m^2 at the contact surface of the device with the heat sink.

The temperature cloud shows that the temperature distribution is not uniform in the heat sink and fluid domains, with higher temperatures in the region close to the device MOSFETs, where the air temperature near VT3 is higher than the temperature near the heat sink fins in Fig. 11.

Fig. 11. XY plane Z = 0 mm temperature distribution of VT3.

B. Temperature field analysis under different operating conditions

Electric heavy-duty trucks are usually required to undertake large transportation tasks, and their power converters are often under high loads during operation. For example, when climbing a slope or driving under full load, the motor requires high torque and power output, which causes the power devices in the power converter to generate a lot of heat. Moreover, electric heavy-duty trucks may operate in different climatic conditions, with a wide range of ambient temperatures, from extremely cold in the north to hot in the south (see Fig. 12).

The ability of a power converter system to dissipate heat depends on the environment in which it operates.

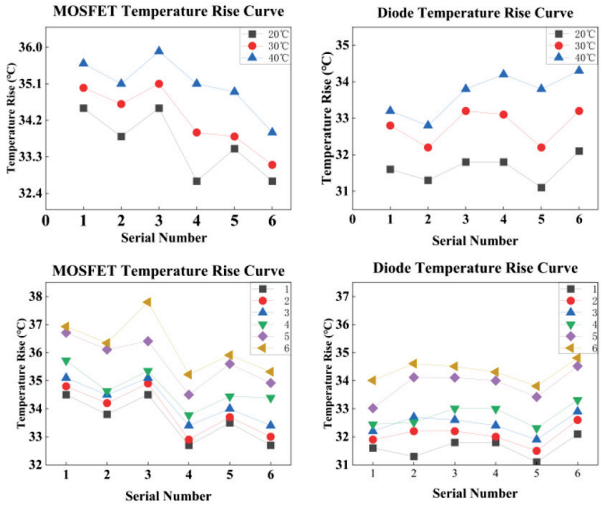

Fig. 12. Temperature rise contrast.

The higher the ambient temperature, the higher the temperature of the equipment, which is not conducive to the safe operation of electric heavy truck equipment. The ambient temperature has an effect on the temperature rise of the equipment, and the ability of the system to dissipate heat by radiation is greater at high ambient temperatures than at low ambient temperatures. Comparing the temperature of power electronics at different ambient temperatures. The temperature properties of the air affect the temperature rise of the power device to some extent.

Comparison of temperature rise changes at different speeds and under different loads, the speed from 600-800 r/min, no-load conditions for working conditions 1-3, load conditions for working conditions 4-6, the temperature rise curve is as follows. Increasing load from 0.8 to 1.2 N·m raises VT1 junction temperature by 10.2℃, while speed variation (600–800 r/min) causes <2℃ fluctuation. This quantifies load-dominant thermal effects.

Comparison of the results of device loss, device temperature rise and device junction temperature shows that, in the case of the same motor load, the speed of the motor has very little effect on the device loss and junction temperature. In the case of the same motor speed, with the increase of the motor load, the loss and junction temperature of the device gradually increase, but the distribution of the junction temperature is basically unchanged.

V. CONCLUSION

This study conducts research on the thermal management of asymmetric half-bridge power converters for switched reluctance motors (SRMs) in heavy-duty electric trucks to improve system reliability. By analyzing the loss mechanisms of power devices, a calculation model including conduction losses and switching losses is established, and a three-dimensional temperature field

simulation model is constructed by combining the Cauer thermal network with ANSYS Fluent FEM.

The study uses material parameters to set the thermal conductivity of each layer, realizes bidirectional coupling analysis of loss and temperature, and obtains the junction temperature distribution of devices and heat flux density hotspots. Multi-condition simulations show that load changes significantly affect the junction temperature, while the speed has little effect, verifying that the load is the main source of thermal stress.

This research establishes a thermal management model suitable for heavy-duty truck working conditions, provides a quantitative basis for the heat dissipation design of power converters, and has engineering guiding significance for improving the stability of electric truck systems.

ACKNOWLEDGMENT

This work is supported by the National Natural Science Foundation of China International (regional) cooperation and exchange projects NSFC-RSF under Grant (W2412064), the Shenzhen Collaborative Innovation Special Plan International Cooperation Research Project (GJHZ20220913144400001), the General Research Project of Shenzhen Science and Technology Plan (JCYJ20220818100000001), Jiangsu Provincial Market Supervision Administration Science and Technology Plan Project (KJ2025017) and the 2023 China-CEEC University Joint Education Program (2023304).

REFERENCES

[1] Y. Xiong, S. Sun, H. Jia, P. Shea, and Z. J. Shen, "New physical insights on power MOSFET switching losses," *IEEE Transactions on Power Electronics*, vol. 24, no. 2, pp. 525-531, Feb. 2009.

[2] H. Chen, Y. Xu, and H. H.-C. Iu, "Analysis of temperature distribution in power converter for switched reluctance motor drive," *IEEE Transactions on Magnetics*, vol. 48, no. 2, pp. 991-994, Feb. 2012.

[3] Z. Zhang, X. Wu, Y. Xie, T. Song, M. Shi, and Z. Zhang, "Force-thermal coupling analysis of control system COTS components," in *2019 Chinese Control Conference (CCC)*, Guangzhou, China, pp. 8160-8165, 2019.

[4] Z. Dong, X. Wu, H. Xu, N. Ren, and K. Sheng, "Accurate analytical switching-on loss model of SiC MOSFET considering dynamic transfer characteristic and Q_{gd}," *IEEE Transactions on Power Electronics*, vol. 35, no. 11, pp. 12264-12273, Nov. 2020.

[5] R. B. B. Ovando, F. A. Ramírez, C. Hernandez, and M. A. Arjona, "A 2D finite element thermal model of a three-phase-inverter heat sink," in *Electronics, Robotics and Automotive Mechanics Conference (CERMA)*, pp. 696-701, 2010.

[6] G. Xu, W. Wei, T. Liu, H. Li, and X. Wang, "Analysis on the characteristics of dynamic changes in junction temperature of power semiconductor devices," in *2021 6th International Conference on Power and Renewable Energy (ICPRE)*, Shanghai, China, pp. 738-743, 2021.

[7] X. Xiao, X. Ge, Q. Ke, L. Yong, Y. Liao, H. Wang, and Y. Zhang, "An adaptive temperature observer for electrothermal analysis of IGBT based on temperature characteristics," *IEEE Journal of Emerging and Selected Topics in Power Electronics*, vol. 11, no. 2, pp. 2246-2258, 2023.

[8] H. Chen and B. Ji, "Real-time temperature estimation for power MOSFETs considering thermal aging effects," *IEEE Transactions on Device and Materials Reliability*, vol. 14, no. 1, pp. 220-228, 2014.

[9] R. Koh and T. Iizuka, "Parameter extraction and comparison of self-heating models for power MOSFETs based on transient current measurements," *IEEE Transactions on Electron Devices*, vol. 60, no. 2, pp. 708-713, Feb. 2013.

[10] K. Ma, A. S. Bahman, S. Beczkowski, and F. Blaabjerg, "Complete loss and thermal model of power semiconductors including device rating information," *IEEE Transactions on Power Electronics*, vol. 30, no. 5, pp. 2556-2569, 2014.

[11] M. Shahjalal, M. R. Ahmed, H. Lu, C. Bailey, and A. J. Forsyth, "An analysis of the thermal interaction between components in power converter applications," *IEEE Transactions on Power Electronics*, vol. 35, no. 9, pp. 9082-9094, Sep. 2020.

[12] Y. Xu, H. Chen, and J. Gu, "Power loss analysis for switched reluctance motor converter by using electrothermal model," *IET Power Electronics*, vol. 8, no. 1, pp. 103-141, 2015.

[13] H. Chen, J. Yang, and S. Xu, "Electrothermal-based junction temperature estimation model for converter of switched reluctance motor drive system," *IEEE Transactions on Industrial Electronics*, vol. 67, no. 2, pp. 874-883, Feb. 2020.

Xing Wang received the B.S. degree from China University of Mining and Technology, Xuzhou Jiangsu, China, in 1996, and M.S. degree from China University of Mining and Technology, Xuzhou Jiangsu, in 1999. In 2007, she became an Associate Professor with China University of Mining and Technology, Xuzhou. She is a holder of four US Patents, nine Australian

Patents, two Canadian Patents, four Russian Patents, 12 Chinese Invention Patents, three Chinese Utility Model Patents, and has authored 15 papers.

Jinbo Ding received his B.S. degree in Electrical Engineering and Automation from China University of Mining and Technology in 2023. He is currently pursuing a master's degree in electrical engineering at China University of Mining and Technology, Xuzhou, China. His research interests include switched reluctance motor power converter design, multiphysics field analysis, and electric vehicles.

Hao Chen (SM'08) received the B.S. and Ph.D. degrees from the Department of Automatic Control, Nanjing University of Aeronautics and Astronautics, Nanjing, China, in 1991 and 1996, respectively. In 1998, he became an Associate Professor with the School of Information and Electrical Engineering, China University of Mining and Technology, Xuzhou, where he has been a Professor since 2001. From 2002 to 2003, he was a Visiting Professor at Kyungsung University, Busan, Korea. Since 2008, he has been an Adjunct Professor at the University of Western Australia, Perth, Australia. He is the author of one book and has authored more than 190 papers. He is the holder of 14 US Patents, 23 Australian Patents, one Danish Patent, seven Canadian Patents, three South African Patents, 10 Russian Patents, 44 Chinese Invention Patents and six Chinese Utility Model Patents. His current research interests include motor control, linear launcher, electric vehicles, electric traction, servo drives and wind power generator control.

Chen was the recipient of both the Prize of Science and Technology of Chinese Youth and the Prize of the Fok Ying Tong Education Foundation for Youth Teachers in both 2004. He was awarded the first prize in the Science and Technology advanced of Province and Ministry once, the second prize in the Science and Technology advanced of Province and Ministry seven times, and the third prize in the Science and Technology advanced of Province and Ministry 14 times. He became the Chinese New Century Hundred-Thousand Ten-Thousand Talents Engineering National Talent in 2007 and won the Government Especial Allowance of People's Republic of China State Department since 2006.

Antonino Musolino received his Ph.D. degree in electrical engineering from the University of Pisa, Pisa, Italy, in 1994. He is currently a Full Professor of electrical machines at the University of Pisa. He has co-authored more than 130 papers published in international journals and conferences. He holds three international patents in the field of magnetorheological devices. His current research activities are focused on linear electromagnetic devices, motor drives for electric traction, and the development of analytical and numerical methods in electromagnetics. Musolino was involved in the organization of several international conferences, where he has served as the session chairman and an organizer, and as a member of the editorial board.

Jianfei Pan graduated from Department of Electrical Engineering of Hong Kong Polytechnic University in Hong Kong with a Ph.D. degree in 2006. Currently he is working at College of Mechatronics and Control Engineering, Shenzhen University, China. His main research interests are wireless power transfer, electric machine design and control.

Nurkhat Zhakiyev received the bachelor's degree in physics and computer science in 2005, the master's degree in applied mathematics from M. Utemisov West Kazakhstan State University, Kazakhstan, in 2007, and the Ph.D. degree in physics from L. N. Gumilyov Eurasian National University (ENU), in 2015. He is currently working at Astana IT University. His research interests include energy system modeling, smart grid and networks, smart city, and optimization modeling.

Thermal Management of Hybrid Excitation Modular SRM

Xing Wang[1,3,4], Jun Bao[2], Guoping Wang[1], Hao Chen[1,3,4,5], Haidong Yan[2], Guanjun Wang[2], and Jianfei Pan[6]

[1]International Joint Research Center of Central and Eastern European Countries on New Energy Electric Vehicle Technology and Equipment
China University of Mining and Technology, Xuzhou 221008, China
3512@cumt.edu.cn, hchen@cumt.edu.cn, poyin_ping@cumt.edu.cn

[2]Wuxi Institute of Inspection, Testing and Certification
Wuxi 214101, China
jsmtc12@126.com, yhd@wxmtc.com, wgjcumt@126.com

[3]International Cooperation Joint Laboratory of New Energy Power Generation and Electric Vehicles of Jiangsu Province Colleges and Universities
Xuzhou 221008, China

[4]Jiangsu Province Foreign Expert Workshop on New Energy Power Generation and Electric Transportation
Xuzhou 221008, China

[5]Shenzhen Research Institute
China University of Mining and Technology
Shenzhen 518057, China

[6]School of Electromechanical and Control Engineering
Shenzhen University, Shenzhen 518054, China
pjf@szu.edu.cn

***Abstract* –** This paper explores the effect of modular structure on the thermal management performance of switched reluctance motors. By designing the modular structure, combined with the centralized winding and parallel slot configuration, the heat dissipation capability of the motor is significantly improved without affecting the torque performance of the motor. Meanwhile, the effect of thermal management on the demagnetization behavior of permanent magnets, especially the mechanism of action when forming mixed excitation, is investigated. Finally, the thermal performance of the motor and the demagnetization characteristics of the permanent magnets are comprehensively analyzed by temperature field simulation, which provides an important basis for the optimized design of the motor.

***Index Terms* –** Electromagnetic simulation, hybrid excitation, modular structure, switched reluctance motor, thermal management.

I. INTRODUCTION

Switched reluctance motors are widely used in industrial production, aerospace and other fields due to their simple structure, high starting torque and adaptability to harsh environments. Although switched reluctance motors have certain advantages in thermal management due to their simple structure, with the increasing power density, the thermal management problem has become more and more prominent and has become a key challenge to be solved.

In order to increase the power density, an effective approach is to increase the current density and optimize the structural design, but this correspondingly raises the requirements for thermal management [1]. However, excessive current density can lead to a significant increase in iron and hysteresis losses, which can lead to overheating problems in the windings and core. Most motors are air-cooled at the design stage by optimizing the structure for heat dissipation, creating a passive

Submitted On: December 24, 2024
Accepted On: May 29, 2025

https://doi.org/10.13052/2025.ACES.J.400916

heat dissipation mechanism. This method utilizes the gap between the motor structure and the shell to emit heat. This is effective, but the heat transfer process is slow. Therefore, the limiting conditions of current density and magnetic density of switched reluctance motors must be fully considered at the early design stage. This approach usually reduces motor performance to some extent. Another solution is to use active cooling technology, which provides thermal management by adding specialized cooling components. For example, integrating a liquid-cooled component in the motor stator allows for rapid and efficient heat extraction from heat sources close to the motor's interior, such as the windings [2]. Although this method is more efficient in terms of heat dissipation, it has a higher design cost and makes the motor structure more complex, which is not conducive to fully utilizing the advantages of the simple structure of switched reluctance motors.

Passive heat dissipation through the motor structure requires more structural design space in order to facilitate heat dissipation, especially ensuring the stator has enough space for heat dissipation. In [3] the authors simulated and investigated the temperature rise due to electromagnetic losses in switched reluctance motors and verified the temperatures in various parts of the machine through experimental data. In [4] the authors calculated the thermal parameters of an induction motor under totally enclosed fan-cooled conditions, and these calculations are able to be transferred to switched reluctance motors. It can be seen that for passive cooling, switched reluctance motors are more advantageous because the windingless rotor structure improves the ability to dissipate heat, especially if the convex pole rotor can provide some functions of a fan.

The stator can be wound with a centralized winding which has a lower winding density than other motors. Modularization of the stator is a well-established method to solve the thermal management problem by reducing the stator yoke core to leave enough space for passive heat dissipation. In [5], the authors calculate the temperature distribution of a two-stator switched reluctance motor at a constant temperature, simplifying the calculation and time. The effect of different winding connections on the temperature rise of the switched reluctance motor (SRM) was analyzed in the literature [6], and it was demonstrated that the two parallel path approach for one phase produces a significant temperature reduction.

Although the modular structure can effectively enhance the thermal management performance of SRMs, it will also have some impact on the overall performance of the motor. To enhance the performance of SRMs, hybrid excitation using permanent magnets is an effective improvement method. However, this design also faces the risk of permanent magnet demagnetization due to temperature rise. In [7], authors analyze the demagnetization characteristics of permanent magnets in modular radial hybrid excitation switched reluctance motors and point out that its structural design can make the risk of demagnetization of permanent magnets do not increase significantly when the current exceeds more than double the rated value.

In this paper, a modular double-stator hybrid excitation switched reluctance motor is designed and its stator-rotor and winding distribution structure is optimized. Meanwhile, the influence of the temperature rise effect on the demagnetization performance of permanent magnets is analyzed in detail through thermal simulation of the core and windings, which provides an important reference for motor design and thermal management.

II. TOPOLOGY DESIGN OF SWITCHED RELUCTANCE MOTOR

The three-phase 12/10 axial flux modular hybrid-excitation SRM (AFMHSRM) proposed in this paper is shown in Fig. 1. The stator of the AFMHSRM consists of 12 annularly arranged U-shaped stator modules, each with two stator poles and two stator slots. The rotor is secured by 10 rotor module mounting disks. As shown in Fig. 1, the left and right stators are positioned on either side of the rotor. Both the stator and rotor are constructed from DW470 laminated silicon steel sheets. The motor adopts concentrated windings, which not only saves space for the windings but also provides more room for the stator mounting plates, thereby facilitating easier installation and disassembly. Each phase contains four windings, which are independently connected and can be configured in either series or parallel to adjust the motor's operating characteristics. Notably, the stator and rotor are designed with parallel slots, allowing windings

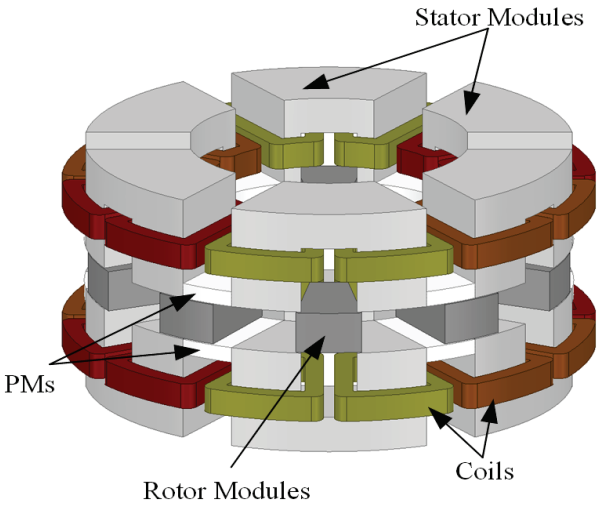

Fig. 1. AFMHSRM topology diagram.

of equal area to be placed in slots of different radii. In addition, permanent magnets are embedded as modules between the U-shaped stator segments to enhance torque density.

Performance specifications of the AFMHSRM are given in Table 1. The AFMHSRM has been designed by using a modular design in order to minimize the cost and at the same time increase the heat dissipation volume. The centralized winding and parallel slot structure are adopted on the stator, which minimizes the winding gap and improves heat dissipation uniformity in the slots, while the modular stator structure increases the passive heat dissipation space and area. The stator-rotor axial as well as circumferential dimensions of the proposed motor are given schematically in Fig. 2 (a). To define the rotor's radial dimensions for the proposed motor, it is necessary to add the initial conditions. These include the motor's inner and outer diameters as well as the rotor's polar arc angle. The specific values for these dimensions are provided in Table 2.

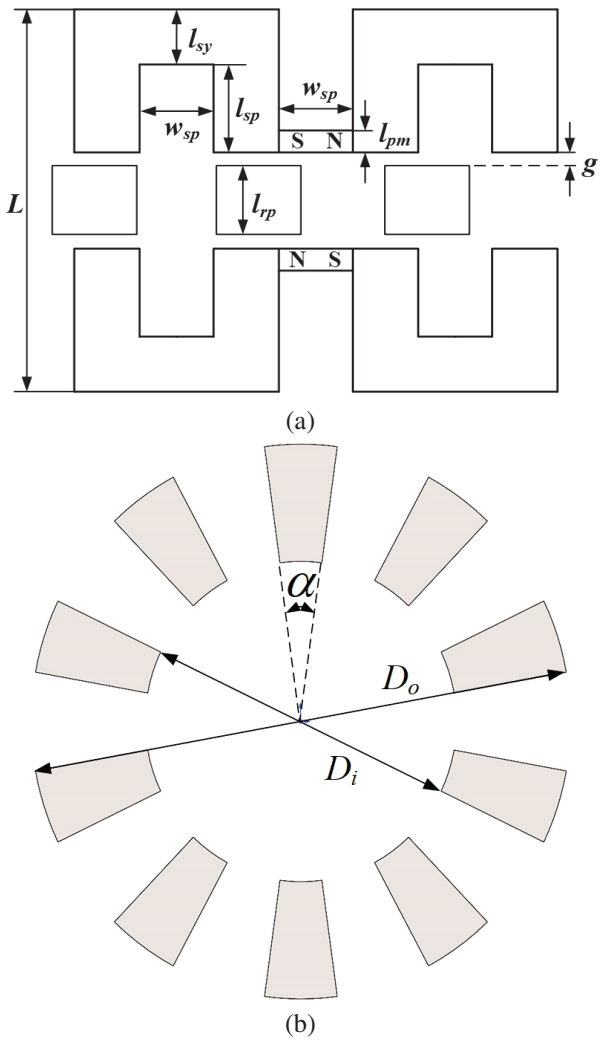

Fig. 2. Dimensional schematic of AFMHSRM: (a) axial dimensions and (b) inner and outer diameters and rotor pole angle.

Table 1: Design requirements of AFMHSRM

Parameter	Symbol	Value
Rated voltage (V)	U	96
Rated power (W)	P	1200
Rated speed (r/min)	n	600
Stator-rotor outer diameter (mm)	D_o	175
Current density (A/mm^2)	I_d	$\leq$6
Stack length (mm)	L	96.8

Table 2: Design requirements of AFMHSRM

Item	Parameter	Value
Stator-rotor outer diameter (mm)	D_o	175
Stator-rotor inner diameter (mm)	D_i	101
Rotor polar arc angle (°)	α	15.5
Stator yoke height (mm)	l_{sy}	14
Stator pole length (mm)	l_{sp}	26
Rotor pole length (mm)	l_{rp}	15.5
Stator slot width (mm)	w_{sp}	20
Permanent magnets length (mm)	l_{pm}	6
Air gap length (mm)	g	0.4
Stack length (mm)	L	96.8

III. MOTOR LOSS ANALYSIS AND CALCULATION

The temperature rise of switched reluctance motors is mainly caused by the conversion of copper and iron losses generated during motor operation into heat energy. Heat energy accumulates inside the motor, causing the temperature to rise and adversely affecting the operational performance and reliability of the motor. Modeling and accurate calculation of copper and iron losses in motors is an important part of thermal management analysis.

Copper loss is closely related to winding resistance, operating current and motor speed. Under high-speed operating conditions, the skin effect and proximity effect will further increase the copper loss. Elevated temperatures further change the material resistivity of the windings, affecting the dynamic characteristics of copper losses.

Iron losses occur mainly in the stator and rotor cores, and consist of hysteresis losses, eddy current losses and additional losses. Among them, hysteresis loss is

related to the hysteresis loop characteristics of magnetic materials and the change of magnetic flux density. Eddy current loss is caused by the eddy current induced by the alternating magnetic field inside the core, and its magnitude is related to the magnetic flux frequency, the conductivity of the core material and the thickness of the sheet. Additional loss includes that caused by high harmonics, leakage flux and other complex factors, and its calculation usually needs to be corrected by combining electromagnetic simulation with experimental data.

A. Calculation of iron loss

Currently, iron loss is mainly calculated by the magnetic circuit analysis method and the finite element method. The iron loss of ferromagnetic materials is categorized into eddy current loss and hysteresis loss and, in general, the basic loss is obtained from the empirical formula calculated at the industrial frequency [8]:

$$P_{\mathrm{Fe}} = P_{\mathrm{h}} + P_{\mathrm{e}} = C_{\mathrm{h}} f B_m^n + C_{\mathrm{e}} f^2 B_m^2, \tag{1}$$

where P_{Fe} is motor iron loss per unit mass loss; P_h and P_e are hysteresis loss and eddy current loss, respectively; C_h and C_e are core hysteresis loss coefficient and eddy current loss coefficient, respectively, related to the material coefficient of the iron core and the level of technology; $n = 1.6\sim2.2$, related to the size of B_m. C_h and C_e can be obtained by parameterization of the frequency of 50 Hz and 60 Hz [9].

A switched reluctance motor has strong nonlinearity. Its instantaneous iron core loss is non-sinusoidal periodic changes, so the need for Fourier decomposition of equation (1), the non-sinusoidal magnetic field kth harmonic iron loss estimation formula, is obtained as follows:

$$\begin{cases} P_{\mathrm{h}}^{(k)} = C_{\mathrm{h}} f k (B^{1.6}{}_{k\max} + B^{1.6}{}_{k\min}) \\ P_{\mathrm{e}}^{(k)} = C_{\mathrm{e}} f^2 k^2 (B^2{}_{k\max} + B^2{}_{k\min}) \end{cases}, \tag{2}$$

where $P_h{}^{(k)}$ and $P_e{}^{(k)}$ are unit hysteresis loss and eddy current loss, respectively; f is core magnetically dense fundamental frequency, which is related to motor speed and number of stator and rotor poles; and B_{kmax} and B_{kmin} are kth harmonic radial and tangential Fourier transform amplitudes.

If the effect produced by the higher harmonics is negligible, then equation (2) can be rewritten as:

$$\begin{cases} P_{\mathrm{h}}^{(k)} = C_{\mathrm{h}} f \sum_{k=1}^{m} k (B^{1.6}{}_{k\max} + B^{1.6}{}_{k\min}) \\ P_{\mathrm{e}}^{(k)} = C_{\mathrm{e}} f^2 \sum_{k=1}^{m} k^2 (B^2{}_{k\max} + B^2{}_{k\min}) \\ P_{\mathrm{Fe}} = P_{\mathrm{h}} + P_{\mathrm{e}} \end{cases}. \tag{3}$$

In a sinusoidal magnetic field, when the volume of the motor core is fixed, motor iron loss, hysteresis loss P_h and eddy current loss P_e are proportional to magnetic field frequency f as well as f^2. Let magnetic density be B, iron loss per unit volume is:

$$P_{Fe} = a(B) f + b(B) f^2. \tag{4}$$

When f, $a(B)$ and $b(B)$ are all fixed, equation (4) can be rewritten as:

$$\frac{P_{\mathrm{Fe}}}{f} = a(B) + b(B) f. \tag{5}$$

B. Copper loss calculation

Copper loss of the winding is the main cause of temperature rise of the motor. The motor structure designed in this paper leaves more space for heat dissipation of the motor winding. Heat generation of the winding is related to the rms value of the current through the winding, which can be expressed as:

$$P_{\mathrm{T}} = 3 I_t^2 R_t, \tag{6}$$

where P_T denotes the copper loss of the torque winding, I_t denotes the rms value of the current and R_t denotes the resistance of the winding.

The motor winding can be estimated by the following equation:

$$R = \rho_a \frac{l_a}{S_a}, \tag{7}$$

where ρ is the resistivity, l is the length of one winding conductor and S is the cross-sectional area of the conductor.

Winding heat generation rate Q can be expressed as:

$$Q_{\mathrm{T}} = \frac{P_{\mathrm{T}}}{V_{\mathrm{T}}}, \tag{8}$$

where Q is the winding heat generation rate and V_T is the winding volume.

C. Electromagnetic simulation of motors for loss analysis

A 3-D model of the proposed AFMHSRM is built in Ansys/Maxwell FEA software and the parameters of the stator and rotor cores, permanent magnets and windings are set to obtain the magnetic density cloud of the AFMHSRM as shown in Fig. 3 when the windings are excited by a constant current of 30 A. At the same time, the conventional 12/10 axial flux switched reluctance motor is finite element analyzed and compared with the AFMHSRM, and its magnetic density cloud is shown in Figs. 3 and 4.

It can be seen that the magnetic density of the AFMHSRM at the stator poles is significantly higher

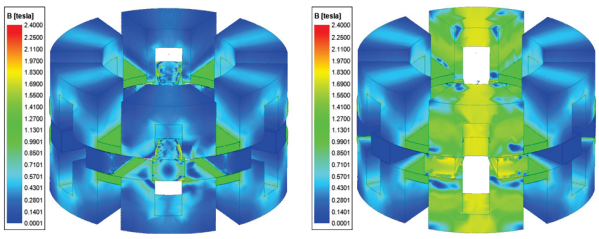

(a) (b)

Fig. 3. Flux density distribution maps of AFMHSRM: (a) unaligned position and (b) aligned position.

than that of the conventional AFSRM for its position. On the contrary, the magnetic density at the stator yoke is lower than that of the CAFSRM due to the flux canceling effect of the permanent magnets. Therefore, the AFMHSRM produces less core loss in the stator than the CAFSRM.

The stator and rotor iron losses of both motors at rated condition and the eddy current loss curves of AFMHSRM are given in Fig. 5. It can be seen that the

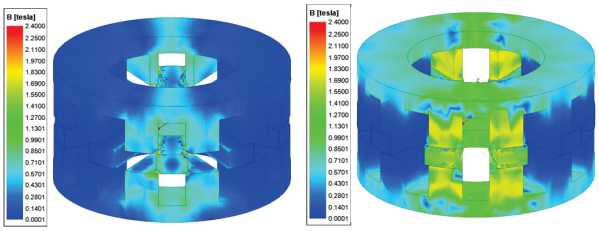

(a) (b)

Fig. 4. Flux density distribution maps of CAFSRM: (a) unaligned position and (b) aligned position.

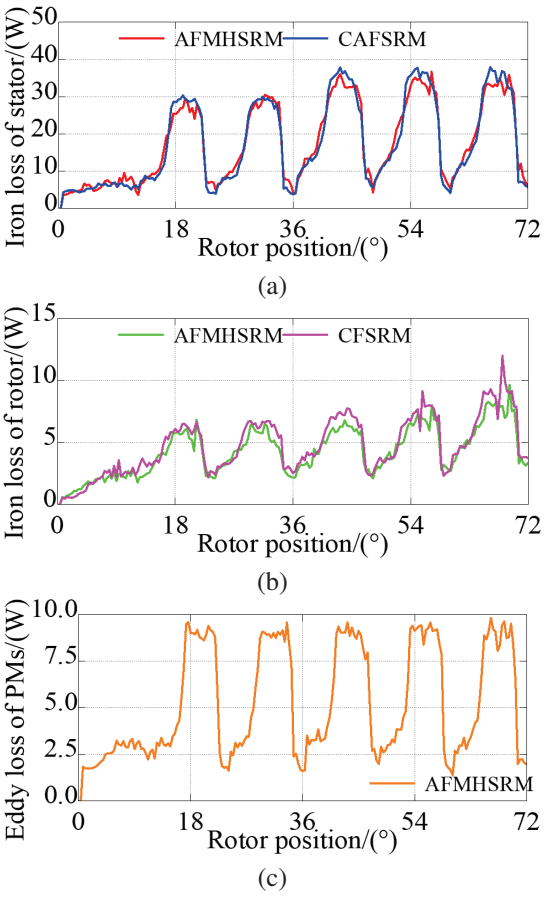

Fig. 5. Comparison of iron loss and eddy current loss of two motors: (a) stator iron loss, (b) rotor iron loss, (c) permanent magnets eddy current loss.

stator iron loss and rotor iron loss of the AFMHSRM are lower than that of the CAFSRM, which is attributed to permanent magnet flux reduction stator yoke magnetization and modular stator structure.

IV. MOTOR THERMAL MANAGEMENT ANALYSIS

A switched reluctance motor conducts heat from its windings and core through the air and core to the surface during operation. The thermal conductivity equation of a motor under steady conditions can be written as:

$$k_x\frac{\partial^2 T}{\partial x^2}+k_y\frac{\partial^2 T}{\partial y^2}+k_z\frac{\partial^2 T}{\partial z^2}+q_i=\rho c\frac{\partial T}{\partial \tau}, \tag{9}$$

where T is the internal temperature of the motor, q_i is the sum of heat flow densities, τ is the motor running time, ρ is the density of the motor material, c is specific heat capacity of the motor material, and k_x, k_y and k_z are the coefficients of thermal conductivity in the x, y and z directions of the axes, respectively.

In a steady state temperature field, temperature does not change with time and the right-hand side of the equation is 0. If the transient temperature field is analyzed, it is necessary to add boundary conditions for the initial moment.

First type of boundary conditions:

$$T_{S1}=T_0. \tag{10}$$

Second type of boundary conditions:

$$-k_q\frac{\partial T}{\partial n}\bigg|_{S2}=q_0. \tag{11}$$

Third type of boundary conditions:

$$-k_q\frac{\partial T}{\partial n}\bigg|_{S3}=\alpha_q(T-T_f), \tag{12}$$

where T_0 is the surface temperature value given by the first type of boundary condition; q_0 is the heat flow density given by the second type of boundary condition, the magnitude of which is related to the nature of the motion of the fluid flowing over the surface; the third type of boundary condition is the heat transfer coefficient and temperature of the object on both sides of the given boundary; $S1$, $S2$ and $S3$ are boundary surfaces, k_q is the boundary thermal conductivity, α_q is the heat transfer coefficient and T_f is the temperature around the heat dissipation surface.

A. Thermal analysis of AFMHSRM

With the stator and rotor iron losses obtained in the previous section, as well as the eddy current losses of the permanent magnets, the thermal model of the proposed AFMHSRM is further constructed, and the model is thermally analyzed using Ansys Workbench. In order to ensure the accuracy of the thermal analysis, and without considering the material changes with temperature, the following key operations need to be completed in the preliminary stage.

1. Temperature field model

The three-dimensional model of the motor established in the electromagnetic analysis stage is directly imported into the temperature field model, while ensuring that the physical parameters (density, thermal conductivity) of each part of the material in the imported model are consistent with the original settings, in order to ensure the reliability of the electromagnetic-thermal coupling analysis.

2. Grid division and parameter setting

Reasonable grid division is carried out for the imported 3D model to ensure the balance between calculation accuracy and solving efficiency. Loss data (including stator iron loss, rotor iron loss and permanent magnet eddy current loss) obtained from previous calculations are input into the simulation initialization parameters as heat sources, and reasonable heat dissipation boundary conditions and heat dissipation coefficients are added according to the actual cooling conditions and motor structure characteristics.

3. Thermal model solving and condition analysis

Based on the defined heat source and heat dissipation conditions, the thermal model is solved to obtain the steady state and transient heat distribution results. On this basis, the temperature distribution and thermal gradient changes of key components (e.g. stator windings, rotor and permanent magnets) are analyzed under different working conditions, which provides reference for the subsequent optimization of the motor structure and design of the cooling system.

A 3D sectional view of the entire motor during thermal simulation is given in Fig. 6. The simulation compensation is set to 1000 s and the loss parameters derived from the EM simulation are entered. The temperature distribution of stator, rotor and winding of the proposed motor at a constant initial temperature of 25°C is given in Fig. 7.

It can be seen that due to the high copper loss of the windings, the internal heat of the windings is difficult to be distributed. The temperature in the internal center area is significantly higher, with the maximum temperature reaching about 44°C. Compared to a significantly lower temperature, the heat of the motor stator is mainly concentrated in the stator pole part. The intimate heat dissipation about the temperature generated by the windings is transferred to the stator yoke through the stator poles and is distributed to the air, and the temperature in the center of the stator poles is slightly lower than that in the stator poles. The temperature at the center of the stator pole is a little lower than that of the windings. At the same time the rotor temperature is well suppressed.

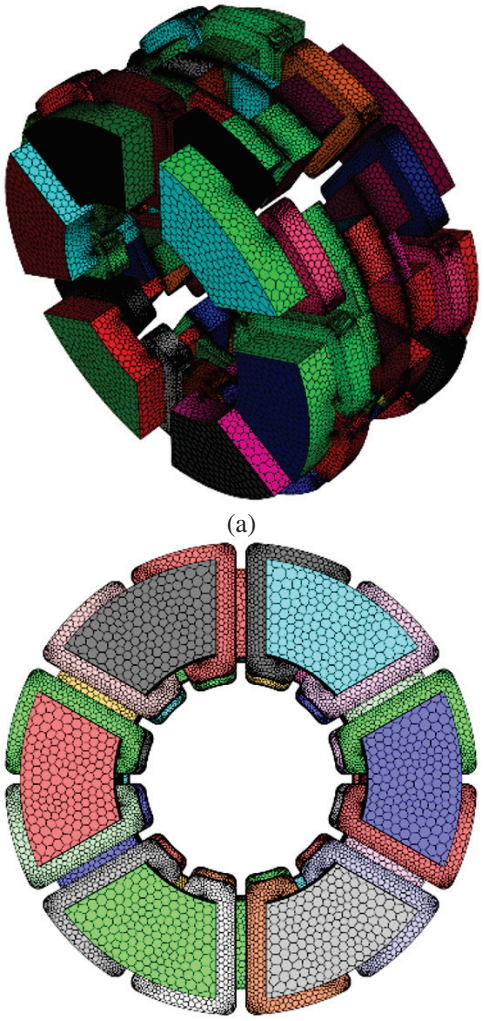

(a)

(b)

Fig. 6. Mesh graph of the 3D thermal model of the motor: (a) overall sectional view and (b) stator side.

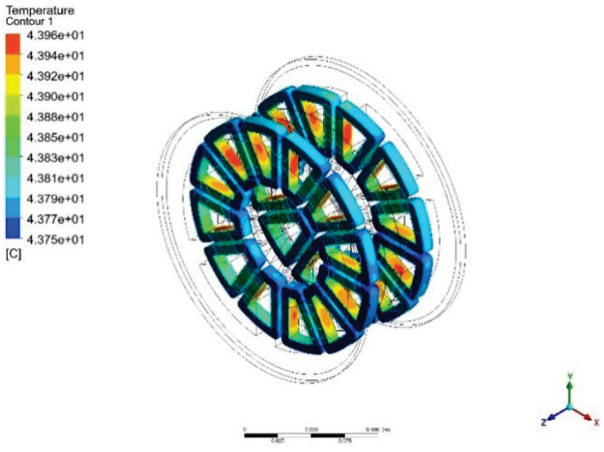

(a)

Fig. 7. *Continued.*

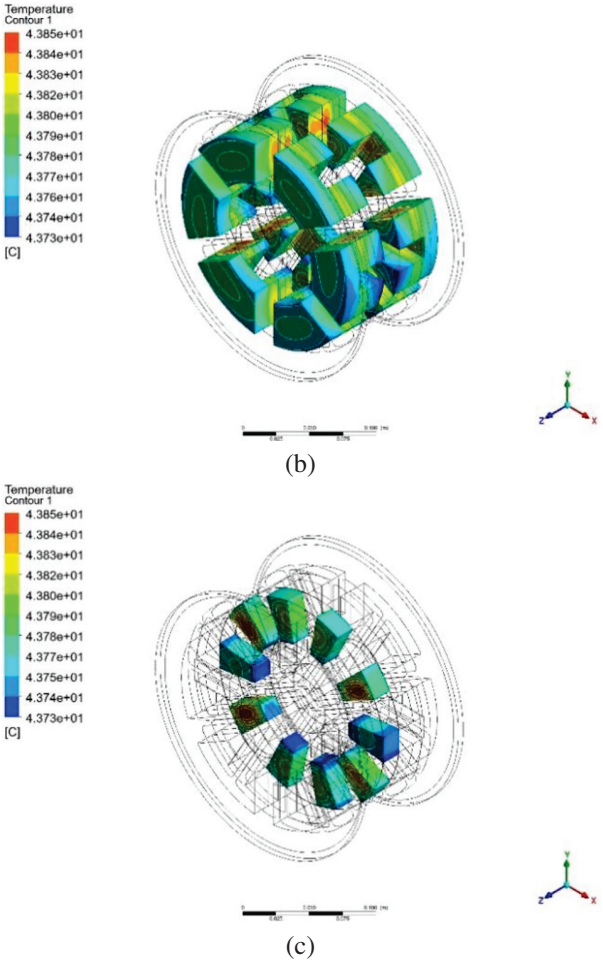

Fig. 7. Temperature map of AFMHSRM motor: (a) winding, (b) stator and (c) rotor.

V. CONCLUSION

In this paper, the influence of the structural design of the proposed AFMHSRM motor on its temperature rise is analyzed through simulation, and the copper loss and iron loss of the proposed AFMHSRM are obtained through finite element simulation. A temperature field simulation model is constructed through copper loss and iron loss, and it is verified that the temperature of the structure of the proposed motor stays at the non-high-temperature degree of 44°C, which is attributed to the thermal structure of the motor as well as the control of the electric density. It can be seen that the proposed motor has obvious advantages in thermal management.

ACKNOWLEDGMENT

This work is supported by the Jiangsu Science and Technology Plan Special Fund (Innovation Support Plan International Science and Technology Cooperation/ Hong Kong Macao Taiwan Science and Technology Cooperation) Project (BZ2022014), Jiangsu Provincial Market Supervision Administration Science and Technology Plan Project (KJ2025017), Shenzhen Basic Research Special (Natural Science Foundation) Key Project (JCYJ20220818100000001), 2022 China-CEEC University Joint Education Program (2022200), 2023 China-CEEC University Joint Education Program (2023304) and Jiangsu Province Modern Agricultural Machinery Equipment and Technology Demonstration and Promotion Project (NJ2023-27).

REFERENCES

[1] B. Bilgin and A. Emadi, "Electric motors in electrified transportation: A step toward achieving a sustainable and highly efficient transportation system," *IEEE Power Electron. Mag*., vol. 1, no. 2, pp. 10-17, June 2014.

[2] C. Rhebergen, B. Bilgin, A. Emadi, E. Rowan, and J. Lo, "Enhancement of electric motor thermal management through axial cooling methods: A materials approach," in *European Conference on Cognitive Ergonomics*, pp. 5682-5688, Sep. 2015.

[3] J. Faiz, B. Ganji, C. E. Carstensen, K. A. Kasper, and R. W. De Doncker, "Temperature rise analysis of switched reluctance motors due to electromagnetic losses," *IEEE Trans. Magn*., vol. 45, no. 7, pp. 2927-2934, June 2009.

[4] A. Boglietti, A. Cavagnino, M. Lazzari, and M. Pastorelli, "A simplified thermal model for variable-speed self-cooled industrial induction motor," *IEEE Trans. on Ind. Applicat*., vol. 39, no. 4, pp. 945-952, July 2003.

[5] N. Arbab, W. Wang, C. Lin, J. Hearron, and B. Fahimi, "Thermal modeling and analysis of a double-stator switched reluctance motor," *IEEE Trans. Energy Convers*., vol. 30, no. 3, pp. 1209-1217, May 2015.

[6] S. Arjun and N. C. Lenin, "Impact of coil arrangements on the electromagnetic and thermal performance of a switched reluctance motor at low speeds," in *IEEE International Conference on Power System Technology*, pp. 1-6, Sep. 2022.

[7] M. A. Jalali Kondelaji, E. F. Farahani, and M. Mirsalim, "Teethed-pole switched reluctance motors assisted with permanent magnets: analysis and evaluation," *IEEE Trans. Energy Convers*., vol. 36, no. 3, pp. 2131-2140, Sep. 2021.

[8] J. Zhang, H. Wang, L. Chen, C. Tan, and Y. Wang, "Salient pole rotor with partially covered shrouds for the windage loss reduction of bearingless switched reluctance motors," in *2018 13th IEEE Conference on Industrial Electronics and Applications (ICIEA)*, pp. 868-873, May 2018.

[9] N. J. F. Liu, N. X. Zhang, H. J. Wang, and N. J. F. Bao, "Iron loss characteristic for the novel

bearingless switched reluctance motor," in *International Conference on Electrical Machines and Systems*, pp. 586-591, Oct. 2013.

Xing Wang received the B.S. degree from China University of Mining and Technology, Xuzhou Jiangsu, China, in 1996, and M.S. degree from China University of Mining and Technology, Xuzhou Jiangsu, in 1999. In 2007, she became an Associate Professor with China University of Mining and Technology, Xuzhou. She is a holder of four US Patents, nine Australian Patents, two Canadian Patents, four Russian Patents, 12 Chinese Invention Patents, three Chinese Utility Model Patents, and has authored 15 papers.

Jun Bao was born in August 1971. He is a Full Senior Engineer, currently serving as the director of Wuxi Institute of Inspection, Testing and Certification. His primary research areas include inspection and testing technologies for new energy vehicles, as well as metrological test technologies.

Guoping Wang received the B.S. degree and M.S. degree from the School of Electronic and Information Engineering, Anhui University of Science and Technology, Huainan, China, in 2018 and 2021, respectively. He is currently pursuing the Ph.D. degree in the electrical engineering at China University of Mining and Technology, Xuzhou. His research interests include optimal design and control of switched reluctance machines.

Hao Chen (SM'08) received the B.S. and Ph.D. degrees from the Department of Automatic Control, Nanjing University of Aeronautics and Astronautics, Nanjing, China, in 1991 and 1996, respectively. In 1998, he became an Associate Professor with the School of Information and Electrical Engineering, China University of Mining and Technology, Xuzhou, China, where he has been a Professor since 2001. From 2002 to 2003, he was a Visiting Professor at Kyungsung University, Busan, Korea. Since 2008, he has also been an Adjunct Professor at the University of Western Australia, Perth, Australia. He is the author of one book and has also authored more than 190 papers. He is the holder of 14 US Patents, 23 Australian Patents, one Danish Patent, seven Canadian Patents, three South African Patents, 10 Russian Patents, 44 Chinese Invention Patents and six Chinese Utility Model Patents. His current research interests include motor control, linear launcher, electric vehicles, electric traction, servo drives, and wind power generator control.

Chen was the recipient of both the Prize of Science and Technology of Chinese Youth and the Prize of the Fok Ying Tong Education Foundation for Youth Teachers in both 2004. He was awarded the first prize in the Science and Technology advanced of Province and Ministry once, the second prize in the Science and Technology advanced of Province and Ministry seven times, and the third prize in the Science and Technology advanced of Province and Ministry 14 times. He became the Chinese New Century Hundred-Thousand Ten-Thousand Talents Engineering National Talent in 2007 and won the Government Especial Allowance of People's Republic of China State Department in 2006.

Haidong Yan was born in May 1982. He has a master's degree in System Analysis and Integration from Nanjing University of Information Science & Technology, Nanjing, China. He is a Senior Engineer currently serving as the deputy director of Wuxi Institute of Inspection, Testing and Certification. His research direction mainly focuses on electromagnetic metrology, new energy vehicle specialized metrology and testing technology.

Guanjun Wang was born in September 1986. He has a master's degree in Electronic and Communication Engineering from China University of Mining and Technology, Xuzhou, China. He is a Senior Engineer currently serving as the director of Electrical and information M&R Department of Wuxi Institute of Inspection, Testing, and Certification. His research direction mainly focuses on electromagnetic metrology, new energy vehicle specialized metrology and testing technology.

Jianfei Pan (Member, IEEE) graduated from Department of Electrical Engineering of Hong Kong Polytechnic University in Hong Kong with a Ph.D. degree in 2006. Currently he is working in the College of Mechatronics and Control Engineering, Shenzhen University, Shenzhen, China. His main research interests are wireless power transfer, electric machine design and control.